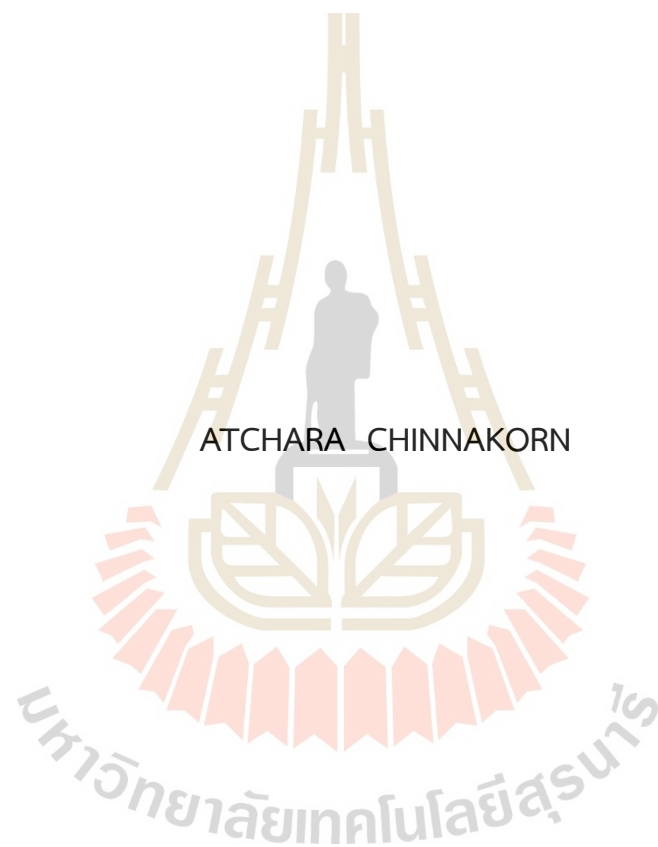


THREE-DIMENSIONAL ELECTROSPINNING OF  
POLYCAPROLACTONE-BASED NANOSTRUCTURE FOR  
BIOMEDICAL APPLICATIONS



A Thesis Submitted in Partial fulfillment of the Requirements for the  
Degree of Doctor of Philosophy in Physics  
Suranaree University of Technology  
Academic Year 2023

อิเล็กทรอนิกส์ป็นนงสามมตของครงสร้างนาโนพอลลคาโพรแลคโตน  
สำหรับการประกยกต์ใช้ทางชีวการแพทย



นางสาวอัจฉรา ชนกร

วิทยานพนธ์น้เป็นส่วนหน่งของการศกษาตามหลักสูตรปรญญาวทยาศาสตรคุษฎน้บัณฑิต  
สาขาวิชาฟลสิกส์  
มหาวิทยาลัยเทคโนโลยีสุรนารี  
ปีการศกษา 2566

THREE-DIMENSIONAL ELECTROSPINNING OF POLYCAPROLACTONE-BASED  
NANOSTRUCTURE FOR BIOMEDICAL APPLICATIONS

Suranaree University of Technology has approved this thesis submitted in partial fulfillment of the requirements for the Degree of Doctor of Philosophy.

Thesis Examining Committee

  
\_\_\_\_\_  
(Dr. Phakkhananan Pakawanit)

Chairperson  
  
\_\_\_\_\_

(Dr. Wiwat Nuansing)  
Member (Thesis advisor)  
  
\_\_\_\_\_

(Prof. Dr. Santi Maensiri)  
Member  
  
\_\_\_\_\_

(Asst. Prof. Dr. Wittawat Saenrang)  
Member  
  
\_\_\_\_\_

(Asst. Prof. Dr. Oratai Weeranantanapan)  
Member



  
\_\_\_\_\_  
(Assoc. Prof. Dr. Yupaporn Ruksakulpiwat)  
Vice Rector for Academic Affairs  
and Quality Assurance

  
\_\_\_\_\_  
(Prof. Dr. Santi Maensiri)  
Dean of Institute of Science

อัจฉรา ชินกร : อิเล็กโทรสปินนิงสามมิติของโครงสร้างนาโนพอลิคาโพรแลคโตนสำหรับการประยุกต์ใช้ทางชีวการแพทย์ (THREE-DIMENSIONAL ELECTROSPINNING OF POLYCAPROLACTONE-BASED NANOSTRUCTURE FOR BIOMEDICAL APPLICATIONS) อาจารย์ที่ปรึกษา : อาจารย์ ดร.วิวัฒน์ นวลสิงห์, 213 หน้า

คำสำคัญ : อิเล็กโทรสปินนิงสามมิติ, พอลิคาโพรแลคโตน, การปรับปรุงสมบัติความชอบน้ำด้วยพลาสมา, เทคนิคการถ่ายภาพตัดขวางด้วยเอกซเรย์จากแสงซินโครตรอน, ชีวการแพทย์

อิเล็กโทรสปินนิงเป็นเทคนิคที่ใช้กันอย่างแพร่หลายในการผลิตเส้นใยนาโนที่มีลักษณะโดดเด่นหลายประการ อย่างไรก็ตามการขึ้นรูปโครงสร้างสามมิติขนาดใหญ่ของเส้นใยอิเล็กโทรสปิน และการประเมินผลทางชีวภาพภายในโครงสร้างอิเล็กโทรสปินสามมิติ ยังคงเป็นความท้าทาย ในวิทยานิพนธ์ฉบับนี้เปิดเผยการศึกษาการพัฒนาเทคนิคอิเล็กโทรสปินนิงสามมิติ ที่รวมเทคนิคอิเล็กโทรสปินนิงเข้ากับเครื่องพิมพ์สามมิติ เพื่อแก้ไขประเด็นการขึ้นรูปโครงสร้างสามมิติขนาดใหญ่ของเส้นใยอิเล็กโทรสปิน ในส่วนของการประเมินผลทางชีวภาพ โครงสร้างอิเล็กโทรสปินสามมิติถูกทดสอบด้วยการเพาะเลี้ยงเซลล์ในห้องปฏิบัติการ และการประเมินผลด้วยเทคนิคกล้องจุลทรรศน์อิเล็กตรอนแบบส่องกราด, เทคนิคฟูเรียร์ทรานส์ฟอร์มอินฟราเรดสเปกโทรสโกปีจากแสงซินโครตรอน, และเทคนิคการถ่ายภาพตัดขวางด้วยเอกซเรย์จากแสงซินโครตรอน

ในการคิดค้นและพัฒนาเครื่องอิเล็กโทรสปินนิงสามมิติ พบว่า การประยุกต์ใช้การเคลื่อนที่แบบเดลตา สามารถลดการสะสมของเส้นใยบนบริเวณที่ไม่ต้องการให้เส้นใยตกสะสมได้ และสามารถใช้ในการควบคุมการขึ้นรูปโครงสร้างสามมิติได้ ในส่วนของการศึกษาการขึ้นรูปด้วยตัวเองของเส้นใย ผลการวิจัยแสดงให้เห็นว่าความนำไฟฟ้าของสารละลายมีบทบาทสำคัญในการขึ้นรูปด้วยตัวเองของเส้นใย ภายใต้เงื่อนไขเดียวกัน สารละลายของพอลิคาโพรแลคโตนและพอลิไวนิลิดีนฟลูออไรด์ ไม่สามารถผลิตเส้นใยที่สามารถขึ้นรูปด้วยตัวเองได้ หากไม่มีกรดพอสฟอริก อย่างไรก็ตามสารละลายพอลิอะคริลาไมด์สามารถผลิตเส้นใยที่สามารถขึ้นรูปด้วยตัวเองได้ ถึงแม้ไม่มีสารเติมแต่งใด ๆ เนื่องจากค่าการนำไฟฟ้าของสารละลายพอลิอะคริลาไมด์มีค่าสูงถึง 99.4 โมโครซีเมนส์ต่อเซนติเมตร อย่างไรก็ตาม ค่าการนำไฟฟ้าของสารละลายพอลิคาโพรแลคโตน เมื่อเติมกรดพอสฟอริกแล้วจะอยู่ที่ 0.80 โมโครซีเมนส์ต่อเซนติเมตร แต่เส้นใยยังคงสามารถขึ้นรูปด้วยตัวเองได้ แสดงว่าไม่เพียงแต่ค่าความนำไฟฟ้าเท่านั้นที่ส่งผลต่อการขึ้นรูปด้วยตัวเองของเส้นใย แต่ตัวแปรอื่น ๆ ของกระบวนการอิเล็กโทรสปินนิงก็ส่งผลต่อการขึ้นรูปเช่นเดียวกัน ดังนั้นสารละลายพอลิคาโพรแลคโตนจึงถูกใช้เพื่อตรวจสอบอิทธิพลของตัวแปรของสารละลายและกระบวนการอิเล็กโทรสปินนิง โดยพบว่าความเข้มข้นและอัตราการไหลของสารละลายมีส่วนสำคัญต่อการขึ้นรูป เนื่องจากเกี่ยวข้องกับ

ปริมาณของเส้นใยที่ใช้ในการก่อตัว นอกจากนี้ระยะห่างเริ่มต้นระหว่างหัวเข็มและแผ่นรับรองก็มีส่วนสำคัญเช่นกัน เนื่องจากระยะห่างที่ไกลเกินไปจะจำกัดความสามารถในการขึ้นรูปโครงสร้างสามมิติ และระยะห่างที่ไกลเกินไปส่งผลให้เส้นใยเกิดการสะสมแบบกระจายเชิงพื้นที่แทนการสะสมบริเวณที่เดิม ไม่เพียงแต่ตัวแปรที่กล่าวมาเหล่านี้ ตัวแปรอื่น ๆ เช่น ศักย์ไฟฟ้า และความเร็วในการเคลื่อนที่ของหัวเข็มก็ส่งผลต่อการขึ้นรูปและรูปร่างของโครงสร้างสามมิติเช่นเดียวกัน หลังจากการปรับเงื่อนไขการทดลองต่าง ๆ พบว่า อัตราการไหลที่ 4 มิลลิลิตรต่อชั่วโมง, ระยะห่างเริ่มต้นที่ 4 เซนติเมตร, แรงดันไฟฟ้าที่ 14 กิโลโวลต์ และความเร็วหัวเข็มที่ 1 มิลลิเมตรต่อวินาที เป็นเงื่อนไขที่เหมาะสมที่สุดในขึ้นรูปโครงสร้างสามมิติของพอลิคาโพรแลคโตน เงื่อนไขดังกล่าวแสดงการขึ้นรูปตามโมเดลทรงกระบอกเส้นผ่านศูนย์กลาง 6 เซนติเมตร แบบกำหนดขอบการเคลื่อนที่เป็นหนึ่ง โดยได้โครงสร้างสามมิติที่มีความสูง  $16.18 \pm 2.58$  มิลลิเมตร และความหนาของผนังของโครงสร้าง  $3.98 \pm 1.01$  มม. เส้นผ่านศูนย์กลางตำแหน่งบน กลาง และล่างของโครงสร้างสามมิติมีความแตกต่างกันแบบไม่มีนัยสำคัญ ซึ่งโดยเฉลี่ยรวมแล้วมีเส้นผ่านศูนย์กลางของโครงสร้างสามมิติเป็น  $1.40 \pm 1.10 \mu\text{m}$  สำหรับการประเมินผลทางชีวภาพ การบำบัดด้วยพลาสมาด้วย 30 และ 50 วัตต์ เป็นเวลา 5 นาที สามารถปรับปรุงสมบัติความชอบน้ำของโครงสร้างสามมิติพอลิคาโพรแลคโตนได้ ซึ่งเป็นเงื่อนไขให้การยึดเกาะของเซลล์ผิวหนัง NIH3T3 ได้ดีที่สุดในการเพาะเลี้ยงเซลล์ นอกจากนี้เทคนิคการถ่ายภาพตัดขวางด้วยเอกซเรย์จากแสงซินโครตรอน สามารถใช้ในการแสดงภาพสามมิติของการกระจายตัวของเซลล์ภายในโครงสร้างสามมิติ ซึ่งสามารถยืนยันว่าเซลล์สามารถยึดเกาะ เคลื่อนที่เข้าไปในโครงสร้างสามมิติ และเพิ่มจำนวนเซลล์ภายในโครงสร้างสามมิติได้ ปริมาตรของเซลล์ในโครงสร้างสามมิติเพิ่มขึ้นประมาณสองเท่า เมื่อเปรียบเทียบการเพาะเลี้ยงเซลล์จากวันที่ 1 และ 3 นอกจากนี้เทคนิคฟูเรียร์ทรานส์ฟอร์มอินฟราเรดสเปกโทรสโกปีจากแสงซินโครตรอน สามารถใช้วัดตำแหน่งของเซลล์บนเส้นใยอิเล็กทรอนิกส์ และประยุกต์ใช้ในการวิเคราะห์การกระจายตัวของเซลล์บนโครงสร้างเส้นใย ด้วยการวิเคราะห์กลุ่มแบบลำดับชั้น

ความก้าวหน้าของอิเล็กทรอนิกส์แบบสามมิตินี้ไม่เพียงแต่เอาชนะข้อจำกัดที่มีอยู่ในการขึ้นรูปโครงสร้างเส้นใยสามมิติเท่านั้น แต่ยังเป็นกระบวนการขึ้นรูปอีกทางเลือกหนึ่งที่สามารถนำไปประยุกต์ใช้ในสาขาต่าง ๆ เช่น อาหารแห่งอนาคต, อวัยวะเทียม, การพิมพ์โครงสร้างเส้นใยอิเล็กทรอนิกส์ เป็นต้น นอกจากนี้เทคนิคการถ่ายภาพตัดขวางด้วยเอกซเรย์และฟูเรียร์ทรานส์ฟอร์มอินฟราเรดสเปกโทรสโกปีจากแสงซินโครตรอน แสดงให้เห็นถึงความสามารถในการประเมินผลทางชีวภาพภายในโครงสร้างสามมิติ ซึ่งให้ข้อมูลเชิงลึกที่เป็นประโยชน์สำหรับการใช้งานด้านชีวการแพทย์

สาขาวิชาฟิสิกส์

ปีการศึกษา 2566

ลายมือชื่อนักศึกษา

ลายมือชื่ออาจารย์ที่ปรึกษา



ATCHARA CHINNAKORN : THREE-DIMENSIONAL ELECTROSPINNING OF POLYCAPROLACTONE-BASED NANOSTRUCTURE FOR BIOMEDICAL APPLICATIONS. THESIS ADVISOR : WIWAT NUANSING, Ph.D. 213 PP.

Keyword : 3D Electrospinning, Polycaprolactone, Plasma Treatment, Synchrotron Radiation X-ray Tomography, Biomedical applications

Electrospinning is a widely used technique producing nanofibers with a number of outstanding characteristics. However, building macroscopic 3D electrospun structures and studying the biological activity inside 3D scaffolds remain challenging. This dissertation involves the study and development of an in-house 3D electrospinning technique that combines electrospinning with a 3D printer to address the issue of macroscopic 3D fibrous structures. In a part of the biological assessments, the 3D structures are examined with *in vitro* cell culture by observing them with Scanning Electron Microscope (SEM), Synchrotron-based Fourier-transform infrared microspectroscopy (SR-FTIR), and Synchrotron Radiation X-ray Tomography (SRXTM) techniques.

In the setup of in-house 3D electrospinning, the use of a delta configuration offers the advantage of effectively minimizing undesired fiber deposition and enabling the control of 3D structures. In the section of the self-assembled formation, the findings demonstrate that solution conductivity plays a crucial role in facilitating the self-assembly of fibers. Under the same conditions, polycaprolactone (PCL) and polyvinylidene fluoride (PVDF) solutions did not exhibit self-assembled fibers stacking if there were not the addition of H<sub>3</sub>PO<sub>4</sub> additives. Nevertheless, polyacrylonitrile (PAN) solutions, without any additives, were capable of forming self-assembled stacks. It was attributed to the conductivity of the PAN solution that reached to 99.4 μS/cm. Despite the fact that the conductivity of the PCL solution with the additions of additives was around 0.80 μS/cm, it exhibited self-assembly. It implied not only did the conductivity value influence self-assembly, but it was also attributed to other variables of electrospinning. Therefore, the PCL solution was utilized to investigate the

influence of the solution and electrospinning parameters. It was observed that concentration and flow rate of solutions plays critical role because these parameters relate to the quantity of incoming fiber. Additionally, the initial distance between a nozzle and a collector is crucial for 3D formation, as a distance that is too short could hinder 3D formation and excessive length may cause fiber to spatially spread instead of depositing at the same location. Not only those mentioned earlier but other relevant parameters, including voltage, and nozzle moving speed, influent also 3D formation. Through tuning experimental conditions, 4 ml/h of flow rate, 4 cm of initial distance, 14 kV of voltage, and 1 mm/s of nozzle speed were the optimal conditions for 3D PCL fibrous constructs under the ambient environment. It provided the rapid buildup of cylinder macrostructures with 6 cm of diameter, reaching a height of  $16.18 \pm 2.58$  mm and a wall thickness of  $3.98 \pm 1.01$  mm on one perimeter with a non-significant difference in average diameter on the upper, middle, and lower parts, whose overall average diameter was  $1.40 \pm 1.10$   $\mu\text{m}$ . For biological assessment, plasma treatment with 30 and 50 W for 5 minutes improved the hydrophilicity of the PCL macrostructures, proving most suitable for *in vitro* cell culture of NIH3T3 cells. Additionally, SRXTM allowed the access to 3D images of cell distribution within the scaffolds, proving cell adhesion, migration, and proliferation within 3D PCL structures. The normalized volume of cells grown on scaffolds doubled when comparing the cultures at 1 and 3 days. In addition, SR-FTIR imaging is able to present cell localization on electrospun fibers and the cell distribution on the fibers with a hierarchical clustering analysis (HCA).

This breakthrough in 3D electrospinning not only overcomes existing limitations in scaffold fabrication but also paves the way for revolutionary applications across various fields, including future foods, artificial organs, and fibrous-based 4D printing technologies. Furthermore, SRXTM and SR-FTIR have the capability to conduct bioactivity evaluation within 3D scaffolds, providing useful insights for biomedical applications.

School of Physics  
Academic Year 2023

Student's Signature   
Advisor's Signature 

## ACKNOWLEDGEMENTS

This thesis has been successfully accomplished with the invaluable support and assistance provided by many people. I would like to extend my heartfelt gratitude to all the people who directly and indirectly encourage me.

I would like to express my sincere gratitude to my advisor, Dr. Wiwat Nuansing, for providing insightful guidance and advise during the entire duration of my academic journey. The successful completion of this work would not have been feasible without the invaluable assistance, counsel, and support based upon his expert knowledge and experience. I express my profound gratitude to Asst. Prof. Dr. Oratai Weeranantanapan for her kindly assistance and invaluable recommendations. I express my gratitude to Dr. Phakkhananan Pakawanit, Dr. Wiwat Nuansing, Prof. Dr. Santi Maensiri, Assist. Prof. Dr. Wittawat Saenrang and Asst. Prof. Dr. Oratai Weeranantanapan for their participation as my examination committees during the evaluation of my Ph.D. Their insightful feedback and suggestions have been highly beneficial to me.

I would like to express my appreciation to all members and staffs in 3D Printing and Advanced Materials Physics (AMP) laboratory, the School of Physics, Institute of Science, Suranaree University of Technology, and Synchrotron Light Research Institute (SLRI) for all assistance, support, and friendship.

I would like to gratefully acknowledge financial support to the Science Achievement Scholarship of Thailand (SAST) from Ministry of Higher Education, Science, Research and Innovation, Thailand throughout the whole period of my bachelor's and doctoral studies. In addition, I am thankful to the Fundamental Fund (FF), Suranaree University of Technology for all supports.

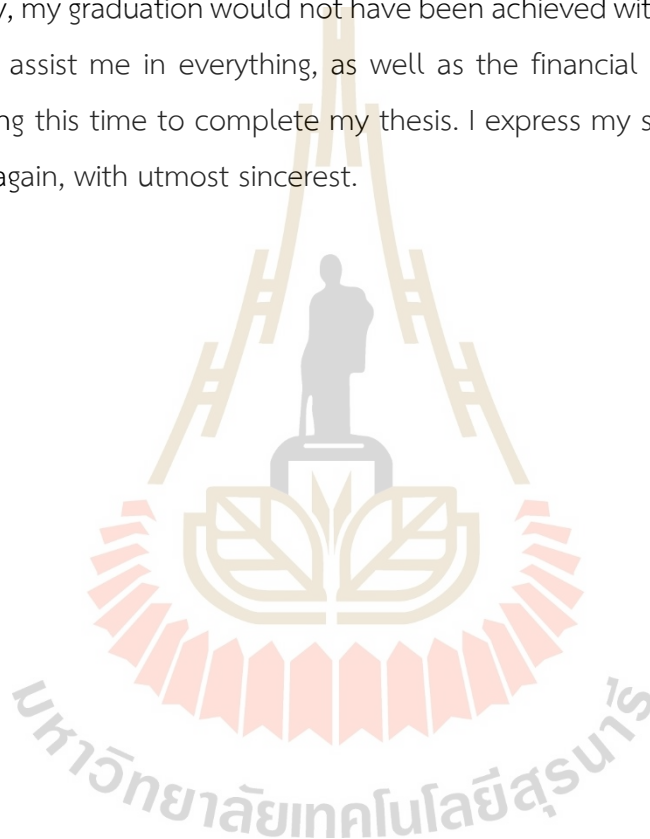
I would like to express my gratitude to Dr. Ali Zolfagharian of the 4D Printing Society Group at Deakin University's School of Engineering, Faculty of Science, Engineering and Built Environment in Australia for granting me the opportunity to engage in a short-term research project as a visiting student. Furthermore, I am grateful

for all assistance and support provide by my colleagues and staffs at Deakin University. It was an incredibly remarkable experience collaborating with you and your team.

I express my gratitude to Dr.Jessada Khajonrit, Dr. Thongsuk Sichumsaeng, Dr. Ornuma Kalawa, Miss Suphawi Chaisit, Mr. Yanwarute Soi-neong, Miss Weraporn Sukchanta, and Mr. Niwat Hema for their assistance and friendship throughout my Ph.D. study. In addition, I would like to thank Mr. Wanchaloem Khwammai for supporting me and providing suggestions on the experiment during my Ph.D. journey.

Finally, my graduation would not have been achieved without best wishes from parents, who assist me in everything, as well as the financial and mental support I received during this time to complete my thesis. I express my sincere gratitude to all of you once again, with utmost sincerest.

Atchara Chinnakorn



# CONTENTS

	Page
ABSTRACT IN THAI .....	I
ABSTRACT IN ENGLISH .....	III
ACKNOWLEDGEMENTS.....	V
CONTENTS.....	VII
LIST OF TABLES.....	XI
LIST OF FIGURES .....	XIII
LIST OF ABBREVIATIONS.....	XXVIII
<b>CHAPTER</b>	
<b>I INTRODUCTION.....</b>	<b>1</b>
1.1 Introduction and Motivation.....	1
1.2 Objectives of this work.....	9
1.3 Scope and limitations of the study.....	10
1.4 Location of research.....	10
1.5 Expected Impact.....	11
1.6 Overview of the thesis .....	11
<b>II LITERATURE REVIEWS .....</b>	<b>13</b>
2.1 Electrospinning.....	13
2.1.1 Fundamentals of electrospinning.....	15
2.1.1.1 Basics of electrostatics.....	16
2.1.1.2 Effect of electrospinning parameters .....	19
2.1.2 3D electrospun macrostructures .....	23
2.2 Additive manufacturing or three-dimensional printing.....	41
2.2.1 Types of 3D Printing.....	42
2.2.2 Delta Coordination.....	43
2.3 Surface Modification by using plasma treatment.....	46
2.4 Summary.....	48

## CONTENTS (Continued)

	Page
<b>III</b>	
<b>METHODOLOGY.....</b>	<b>49</b>
3.1 3D Electrospinning.....	49
3.1.1 Electro-mechanical parts.....	54
3.1.2 Design Calculation.....	55
3.1.3 Firmware.....	55
3.2 3D fibrous macrostructures.....	55
3.2.1 The self-assembly of electrospun fibers.....	56
3.2.2 The buildup and control of 3D fibrous macrostructures.....	56
3.2.2.1 The study of solution preparation on the buildup of 3D fibrous macrostructures.....	56
3.2.2.2 The study of electrospinning process on the buildup of 3D fibrous macrostructures.....	57
3.3 <i>In vitro</i> cell culture on the fibrous graft.....	58
3.4 Characterization Techniques.....	58
3.4.1 Digital Camera.....	58
3.4.2 Conductivity.....	59
3.4.3 X-ray Diffraction.....	59
3.4.4 Fourier transform infrared and Raman spectroscopy.....	61
3.4.5 Scanning Electron Microscopy.....	62
3.4.6 Plasma Treatment.....	63
3.4.7 Synchrotron Radiation X-ray tomography.....	64
3.4.8 Synchrotron Radiation Fourier transform infrared imaging.....	66
3.4.9 Electric field simulation.....	70
<b>IV</b>	
<b>RESULTS AND DISSCUSION.....</b>	<b>72</b>
4.1 3D Electrospinning setup.....	72
4.1.1 Coordinate system.....	73
4.1.2 Development of 3D Electrospinning.....	73
4.1.2.1 From an extrusion system to a solution feed system ..	74
4.1.2.2 Structural system.....	75

## CONTENTS (Continued)

	Page
4.1.3 3D electrospinning Troubleshooting: All problems and solutions.....	76
4.1.3.1 Firmware.....	76
4.1.3.2 Hardware .....	77
4.2 3D fibrous macrostructures .....	78
4.2.1 The self-assembly of 3D-fibrous structures.....	78
4.2.1.1 Conductivity.....	82
4.2.1.2 XRD Characterization .....	84
4.2.1.3 FTIR-Raman Characterization .....	86
4.2.2 The mechanism of buildup of 3D-fibrous macrostructures .....	90
4.2.2.1 Observation.....	90
4.2.2.2 The buildup and control of 3D-fibrous macrostructures....	93
4.2.2.3 Electric Field Simulation.....	131
4.3 Biological assessments .....	133
4.3.1 <i>In vitro</i> cell culture of osteoblast cells.....	133
4.3.2 <i>In vitro</i> cell culture of fibroblast cells.....	134
4.3.2.1 Plasma treatment.....	134
4.3.2.2 Synchrotron radiation Fourier transform infrared Microspectroscopy imaging .....	138
4.3.2.3 Synchrotron Radiation X-ray Tomography.....	144
<b>V CONCLUSION.....</b>	<b>147</b>
REFERENCE .....	154
APPENDICES .....	175
APPENDIX A 3D ELECTROSPINNING SETUP .....	176
APPENDIX B MORPHOLOGY AND DIAMETERS OF ELECTROSPUN FIBERS .....	178
APPENDIX C FTIR RESULTS AND MECHANICAL TESTS OF TREATED FIBERS .....	208
APPENDIX D SUPPLEMENTARY INFORMATION FOR SR-FTIR.....	211
APPENDIX E SUPPLEMENTARY INFORMATION FOR SRXTM .....	212

## CONTENTS (Continued)

	Page
APPENDIX F PUBLICATIONS AND PRESENTATIONS.....	213
CURRICULUM VITAE.....	214

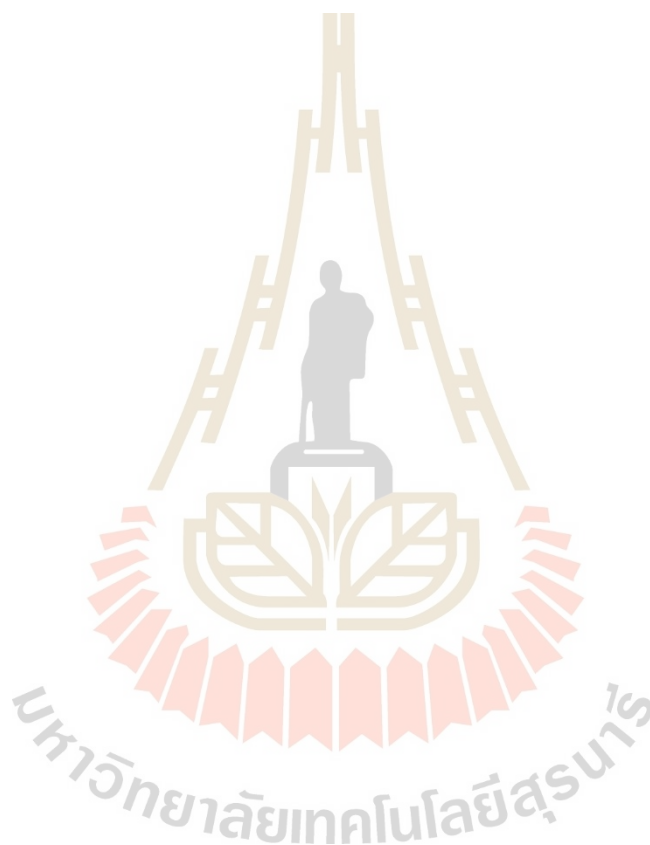


## LIST OF TABLES

Table	Page
2.1 Conclusion of possible effects of electrospinning parameter.....	19
2.2 The overview approach of 3D macrostructures based on electrospinning process .....	26
3.1 Components and supplies needed to assemble 3D electrospinning setup.....	50
3.2 Summary of all solution preparations investigated to form 3D fibrous structures with flow rates of 2, 4, and 6 ml/h at an initial distance of 6 cm and under an applied voltage of 16 kV via 3D electrospinning .....	57
3.3 Summary of all spinning parameters used to form 3D fibrous macrostructures using PCL solution via 3D electrospinning.....	58
3.4 Electrospinning setup measurement for electric field simulation .....	71
4.1 The conductivity ( $\mu\text{S}/\text{cm}$ ) of PCL, PVDF, and PAN solution with the existing $\text{H}_3\text{PO}_4$ additives.....	83
4.2 The summarization of the height, the $C_{\text{hh}}$ , the DW, the $D_{\text{out}}$ , and wall thickness of 3D structures obtained from various flow rates, including 2, 3, 4, 5, and 6 mL/h.....	115
4.3 The summarization of the height, the $C_{\text{hh}}$ , the DW, the $D_{\text{out}}$ , and wall thickness of 3D structures obtained from various flow rates, including 2, 3, 4, 5, and 6 cm .....	120
4.4 The summarization of the height, the $C_{\text{hh}}$ , the DW, the $D_{\text{out}}$ , and wall thickness of 3D structures obtained from various voltages, including 12, 13, 14, 15, and 16 kV .....	124
4.5 The summarization of the height, the $C_{\text{hh}}$ , the DW, the $D_{\text{out}}$ , and wall thickness of 3D structures obtained from various moving speeds of a nozzle including 1, 2, 3, 4, and 5 mm/s .....	129

## LIST OF TABLES (Continued)

Table	Page
4.6 The analytical results of hierarchical cluster based on the integration and cluster index .....	144
5.1 The effect of electrospinning parameters on the shape of 3D macrostructures .....	149



## LIST OF FIGURES

Figure	Page
1.1 Schematic illustration of a conventional electrospinning setup and nanofiber-formation processes: (a) a general setup; (b-d) the formation of Taylor cones from the droplet; and (e) factors affecting the formation of the jet.....	3
1.2 Examples of 3D electrospun constructs fabricated by self-assembly using electrospinning.....	4
1.3 Comparative illustrations of (a) ranges of jets used in various techniques and (b) their comprehensive concepts, including (i) conventional electrospinning, (ii) 3D printer, (iii) near-field electrospinning (NFES), (iv) melt electrowriting (MEW), and (v) 3D electrospinning.....	6
2.1 Research progress of electrospinning based on the publication over the years. Data was obtained from Scopus (Elsevier) based on the searching command “TITLE_ABS_KEY electrospinning OR electrospun OR electrospin” on 23 November 2023.....	14
2.2 Schematic images of (a) transformation of solution to nanofiber under the electric field, (b) the zoom image of the droplet transformation, and (c) the formation of electrospun nanofiber.....	15
2.3 (a) Schematic image of parallel electrode used as collector in electrospinning, (b) an electric field strength vectors calculated on STUDENT’S QUICKFIELD software, and (c) basic model of electrostatic on parallel collector consisting of two or more electrodes.....	18

## LIST OF FIGURES (Continued)

Figure	Page
2.4	(a) Jet trajectories captured by high speed camera and (b) fiber mats at different PS concentrations: (i) 10, (ii) 15, (iii) 20, (iv) 25, and (v) 30 wt%, which operated by an applied voltage of 20 kV, a distance of 20 cm, and a flow rate of 1 ml/h .....21
2.5	Schematic illustration of 2D, 3D, and 4D electrospun fibers.....24
2.6	Examples of the multilayer: (a) the fabrication process of multilayered electrospun nanocomposite membrane, (b) (i) schematic and (ii) experimental electrospinning setup for the fabrication of multilayer fibrous membranes, and (iii) schematic and (iv) cross-sectional SEM images of the multilayer fibrous scaffolds, and (c) schematic and SEM images of the 3D multilayer fabricated by electrospinning and electrospray.....25
2.7	Examples of fabrication procedure using post-processing after electrospinning: (a) schematic diagrams of (i) a unique biological structures of cotton fiber and (ii) the post-processing, which (iii) can provide various structures and (iv) can be candidates in biological applications, to obtain the (v) unique structures based on electrospun fibers and (b) (i) a schematic diagram to fabricate 3D scaffolds with controllable shapes using (ii) foaming process of 2D mat to 3D scaffold and (iii-viii) the experimental results of the foaming process .....33

## LIST OF FIGURES (Continued)

Figure	Page
2.8 Schematic illustration of mockup-assisted collectors and final products of 3D electrospun structures: (a) (i) electrospinning setup of the fabrication of 3D radially oriented nanofibrous scaffolds, (ii) modified collector by using copper wires and metal pin in the hemispherical device designed to be electrically connected to each other, and (iii) electrospun structures obtained from the modified collector with copper wires and metal pin, and (b) (i) electrospinning setup modified by using the hydrogel-based collector such as (ii) the multi-bifurcated 3D gelatin cylindrical structure and so on, which can provide (ii-vi) various shapes of hydrogel/fiber structures following the collectors, including (iv) bellow-shaped tubular, (v) human alveoli-like and (vi) brain-like shell macrostructure.....	34
2.9 Examples of the use of new platform of collector in electrospinning to achieve 3D macrostructures: (a) the use of (ii) hemisphere collector used in electrospinning compared to (i) normal collector used in conventional electrospinning, which provided (iii) 2D PCL scaffold with no depth using the conventional electrospinning and (iv-v) a 3D cotton ball-like PCL scaffold and (b) the use of liquid collector with (i-iv) various methods of depositions which provided (v-vi) various 3D macrostructures following the deposition methods.....	36
2.10 Examples of technique combinations: (a) (i) experimental illustration of the fabrication process of electrospun-based piezoresistive pressure sensors and (ii) electrospun 3D nanostructured mats and (b) Schematic illustration of the fabrication procedure for cell-laden hierarchical scaffolds by using (i) melt-dispensing, (ii) electrospinning process, and (iii) cell-dispensing process which (iv) final shape of the scaffold and (e) cross-sectional view of the scaffold .....	38

## LIST OF FIGURES (Continued)

Figure	Page
2.11	Examples of self-assembly in the 3D electrospun formation: (a) conversion between a 3D fiber stack and a 2D thin film by changing (i) 3Dstack on Al foil to (ii) 2D fiber mat by using a lucite plate and then (iii) connecting the 2D mat to an electrostatic generator to get a 3D stack, and (d) 3D stack grown on the lucite plate, (b) growth evaluation of 3D PVP-based macrostructures, and (c) photography of fiber deposition processes for (i) 2D mat and (ii) 3D scaffolds and schematic diagram of fiber deposition for (iii) 2D mat and (iv) 3D scaffolds ..... 40
2.12	A workflow diagram of 3D printing ..... 41
2.13	Schematic illustration of the categories of AM techniques ..... 43
2.14	Coordinate systems of 3D FDM printer: (a) cartesian and (b) delta coordinates ..... 44
2.15	(a) Anatomy of 3D delta printer, (b) location of towers, and (c) delta geometry with the definition in configuration.h of Marlin..... 45
2.16	A schematic illustration of typical plasma treatment used with many methods to change the surface properties ..... 47
2.17	The contact angle of glycerol droplet on the poly(dimethylsiloxane) film (a) without and with the oxygen plasma treatment using different exposure time that were (b) 6, (c) 12, (d) 18, and (e) 24 s..... 48
3.1	(a) Rostock mini and (b) parts of Rostock mini chosen to use in the 3D electrospinning setup..... 50
3.2	Printed parts used in 3D electrospinning setup, including idler end, endstop switch mount, belt end, carriages, u-joints, needle holder, tower end, collector holder, motor end, effector, and jaws..... 53

## LIST OF FIGURES (Continued)

Figure	Page
3.3	Schematic diagram of Ramp 1.4 board used in 3D electrospinning setup: (a) the connect of motors, motor drivers endstop switch, and power supply on the board, (b) the connect of variable resistor instead of bed and hotend ..... 54
3.4	Geometrical diffraction from lattice planes ..... 60
3.5	Schematic illustration of the vibrational function and the energy level transitions measured by infrared (IR), near infrared, and Raman spectroscopy ..... 61
3.6	Cryo-section of electrospun grafts using a Cryostat microtome ..... 66
3.7	(a) Electrospinning process of PLA fibers at the flow rate of 1 ml/h, the tip-to-collector distance of 6 cm, the voltage of 16 kV, (b) PLA electrospun fiber on the BaF <sub>2</sub> window, and (c) photography of PCL fiber obtained by optical microscopy ..... 67
3.8	Example of data processing, including (a) a specific region chosen for analysis and mapping using SR-FTIR in the range of 1682-1610 cm <sup>-1</sup> , (b) derivative spectra, (c) a hierarchical cluster map, and (d) an analytical method ..... 70
3.9	The configuration of a needle and a collector based on the actual scale of 3D electrospinning setup: (a) a 20G needle positioned 4 cm from a collector and at the collector's center as modeled in Fusion360 and (b) the configuration on CST studio ..... 71
4.1	Development of 3D electrospinning setup which combined an electrospinning and a delta printer: (a) Prototype 1.0, (b) Prototype 2.0, (c) Prototype 3.0, (d) Prototype 3.1, and (e) Prototype 4.0 that is the final prototype used in this work ..... 74
4.2	Structural systems of tower in (a) Rostock mini and (b) the prototype 3.0, 3.1, and 4.0 of 3D electrospinning ..... 75

## LIST OF FIGURES (Continued)

Figure	Page
4.3 The experimental results of electrospun fibers fabrication using the PCL solution (a) without and (b) with the addition of H <sub>3</sub> PO <sub>4</sub> additives under (i-v) the condition of a flow rate at 5 mL/h, a tip-to-collector distance at 10 cm, and a voltage of 18 kV and (vi-x) a flow rate at 2 mL/h, a tip-to-collector distance at 5 cm, and a voltage of 14 kV.....	79
4.4 The experimental results of electrospun fibers fabrication under the condition of a flow rate at 2 mL/h, a tip-to-collector distance at 8 cm, and a voltage of 16 kV by (a) non-moving which was used to test PVDF solution (i) without and (ii) with the addition of H <sub>3</sub> PO <sub>4</sub> additives the nozzle and (b) moving the nozzle.....	81
4.5 The experimental results of electrospun fibers fabrication by (a) non-moving nozzle under the condition of a flow rate at 2 mL/h, a tip-to-collector distance at 8 cm, and a voltage of 18 kV and (b) moving nozzle at 1 mm/s under (i-v) the condition of a flow rate at 2 mL/h, a tip-to-collector distance at 8 cm, and a voltage of 18kV and (vi-x) the condition of a flow rate at 3 mL/h, a tip-to-collector distance at 6 cm, and a voltage of 18 kV.....	82
4.6 XRD patterns of (a) PCL series, including 2D PCL mat, 3D PCL stack and PCL powder, (b) PVDF series, including 2D PVDF mat, 3D PVDF stack and PVDF powder, and (c) PAN series, including 3D PAN stack and PAN powder.....	84
4.7 Structural configuration of three phases of PVDF.....	86
4.8 FTIR spectra of PCL series, including PCL pellet, 2D PCL mat, 3D PCL stack, PVDF, including PVDF pellet, 2D PVDF mat, 3D PVDF stack, and PAN series, including PAN powder, and 3D PAN stack.....	88

## LIST OF FIGURES (Continued)

Figure	Page
4.9	Raman spectra of PCL series, including PCL pellet, 2D PCL mat, 3D PCL stack, PVDF, including PVDF pellet, 2D PVDF mat, 3D PVDF stack, and PAN series, including PAN powder, and 3D PAN stack .....89
4.10	The buildup of 3D-fibrous macrostructures at a flow rate of 6 mL/h, an initial distance of 6 cm, a voltage of 16 kV, and a nozzle speed of 1 mm/s by an in-house 3D electrospinning setup.....90
4.11	Schematic images of parameters involving 3D printing, melt electrowriting, and 3D electrospinning that are (a) the perimeters and adhesion types in 3D printing, (b) the jet lag in melt electrowriting, and (c) the electrospun structures obtained from 3D electrospinning .....91
4.12	(a-b) Diagrams and (c-d) an example of parameters used to illustrate 3D-electrospun structures in this work .....92
4.13	The top view of 2D mats and 3D constructs fabricated using various concentrations of PCL solutions, namely 10, 12, and 14 wt%. These concentrations were prepared in the DCM:DMF solvent of 6:1 with the addition of 10% H <sub>3</sub> PO <sub>4</sub> . All experiments were conducted with a flow rate of 2, 4, and 6 mL/h, an initial distance of 6 cm, a voltage of 16 kV, and a nozzle speed of 1 mm/s via 3D electrospinning for 30 minutes in the ambient environment.....94
4.14	The side view of 3D formations fabricated using various concentrations of PCL solutions, namely 10, 12, and 14 wt%. These concentrations were prepared in the solvent of 6:1 DCM:DMF with the addition of 10% H <sub>3</sub> PO <sub>4</sub> . All experiments were conducted with a flow rate of 2, 4, and 6 mL/h, an initial distance of 6 cm, a voltage of 16 kV, and a nozzle speed of 1 mm/s via the 3D electrospinning for 30 minutes in the ambient environment .....96

## LIST OF FIGURES (Continued)

Figure	Page
4.15 SEM images and diameter histograms of fibers fabricated using 10 wt% concentration solutions prepared in 6:1 DCM:DMF solvent and 10% H <sub>3</sub> PO <sub>4</sub> additives with various flow rates, including (a) 2, (b) 4, and (c) 6 mL/h, under contants of initial distance, voltage, and nozzle speed at 6 cm, 16 kV, and 1 mm/s, respectively.....	98
4.16 SEM images and diameter histograms of fibers fabricated using 12 wt% concentration solutions prepared in 6:1 DCM:DMF solvent and 10% H <sub>3</sub> PO <sub>4</sub> additives with various flow rates, including (a) 2, (b) 4, and (c) 6 mL/h, under contants of initial distance, voltage, and nozzle speed at 6 cm, 16 kV, and 1 mm/s, respectively.....	99
4.17 SEM images and diameter histograms of fibers fabricated using 14 wt% concentration solutions prepared in 6:1 DCM:DMF solvent and 10% H <sub>3</sub> PO <sub>4</sub> additives with various flow rates, including (a) 2, (b) 4, and (c) 6 mL/h, under contants of initial distance, voltage, and nozzle speed at 6 cm, 16 kV, and 1 mm/s, respectively.....	100
4.18 The side view of 3D formations fabricated by using various solvent ratios of DCM:DMF, namely 4:1, 6:1, and 8:1. These solvents were employed in the preparation of 12 wt% PCL solutions with the addition of 10% H <sub>3</sub> PO <sub>4</sub> . All experiments were conducted with a flow rate of 2, 4, and 6 mL/h, an initial distance of 6 cm, a voltage of 16 kV, and a nozzle speed of 1 mm/s via the 3D electrospinning for 30 minutes in the ambient environment.....	101

## LIST OF FIGURES (Continued)

Figure	Page
4.19	The top view of 2D mats and 3D constructs fabricated by using various solvent ratios of DCM:DMF, namely 4:1, 6:1, and 8:1. These solvents were employed in the solution preparation of a 12 wt% PCL concentration with the addition of 10% H <sub>3</sub> PO <sub>4</sub> . All experiments were conducted with flow rates of 2, 4, and 6 mL/h, an initial distance of 6 cm, a voltage of 16 kV, and a nozzle speed of 1 mm/s via 3D electrospinning for 30 minutes in the ambient environment.....102
4.20	SEM images and diameter histograms of fibers fabricated using 12 wt% concentration solutions prepared in 4:1 ratio of DCM:DMF solvent and 10% H <sub>3</sub> PO <sub>4</sub> additives with various flow rates, including (a) 2, (b) 4, and (c) 6 mL/h, under contants of initial distance, voltage, and nozzle speed at 6 cm, 16 kV, and 1 mm/s, respectively.....103
4.21	SEM images and diameter histograms of fibers fabricated using 12 wt% concentration solutions prepared in 8:1 ratio of DCM:DMF solvent and 10% H <sub>3</sub> PO <sub>4</sub> additives with various flow rates, including (a) 2, (b) 4, and (c) 6 mL/h, under contants of initial distance, voltage, and nozzle speed at 6 cm, 16 kV, and 1 mm/s, respectively.....104
4.22	The top view of 2D mats and 3D constructs fabricated by using various amounts of H <sub>3</sub> PO <sub>4</sub> additives, including 0, 5, 10, 15, and 20%. These additives were employed in the solution preparation of 12 wt% PCL concentrations in the DCM:DMF solvent ratio of 6:1. All experiments were conducted with a flow rate of 2, 4, and 6 mL/h, an initial distance of 6 cm, a voltage of 16 kV, and a nozzle speed of 1 mm/s via the 3D electrospinning for 30 minutes in the ambient environment.....105

## LIST OF FIGURES (Continued)

Figure	Page
4.23	The side view of 3D formations fabricated using various additions of $H_3PO_4$ additives, including 0, 5, 10, 15, and 20%, into 12 wt% PCL solutions in a DCM:DMF solvent of 6:1 ratio. These solutions were executed at a flow rate of 2, 4, and 6 mL/h, an initial distance of 6 cm, a voltage of 16 kV, and a nozzle speed of 1 mm/s via the 3D electrospinning for 30 minutes in the ambient environment.....107
4.24	SEM images and histograms of fiber diameters which the fibers were fabricated using 12 wt% concentration solutions prepared in 6:1 DCM:DMF solvent and 0% $H_3PO_4$ additive with various flow rates, including (a) 2, (b) 4, and (c) 6 mL/h, under contants of initial distance, voltage, and nozzle speed at 6 cm, 16 kV, and 1 mm/s, respectively.....108
4.25	SEM images and histograms of fiber diameters which the fibers were fabricated using 12 wt% concentration solutions prepared in 6:1 DCM:DMF solvent and 5% $H_3PO_4$ additive with various flow rates, including (a) 2, (b) 4, and (c) 6 mL/h, under contants of initial distance, voltage, and nozzle speed at 6 cm, 16 kV, and 1 mm/s, respectively.....109
4.26	SEM images and histograms of fiber diameters which the fibers were fabricated using 12 wt% concentration solutions prepared in 6:1 DCM:DMF solvent and 15% $H_3PO_4$ additive with various flow rates, including (a) 2, (b) 4, and (c) 6 mL/h, under contants of initial distance, voltage, and nozzle speed at 6 cm, 16 kV, and 1 mm/s, respectively.....110
4.27	SEM images and histograms of fiber diameters which the fibers were fabricated using 12 wt% concentration solutions prepared in 6:1 DCM:DMF solvent and 20% $H_3PO_4$ additive with various flow rates, including (a) 2, (b) 4, and (c) 6 mL/h, under contants of initial distance, voltage, and nozzle speed at 6 cm, 16 kV, and 1 mm/s, respectively.....111

## LIST OF FIGURES (Continued)

Figure	Page
4.28 (a) The top and (b) side views of comparative 3D PCL-electrospun constructs by varying the values of a flow rate. The flow rate of solution, 12% wt PCL solution in 6:1 DCM:DMF + 10% H <sub>3</sub> PO <sub>4</sub> , is increased from 2 to 6 mL/h, with each increment being 1 mL/h. The 3D PCL formations were performed at an initial distance of 6 cm, a voltage of 16 kV, and a nozzle speed of 1 mm/s for 30 minutes.....	112
4.29 Various situations of 3D buildups via 3D electrospinning, which were run with various flow rates of (a-b) 2, (c-d) 3, (e-f) 4, (g-h) 5, and (i-j) 6 mL/h at an initial distance of 6 cm, a voltage of 16 kV, and a nozzle moving speed of 1 mm/s for 30 minutes in an ambient environment.....	114
4.30 SEM images and histograms of fiber diameter fabricated with various flow rates, including (a) 2, (b) 3, (c) 4, (d) 5, and (e) 6 mL/h, under constants of initial distance, voltage, and nozzle speed at 6 cm, 16 kV, and 1 mm/s, respectively .....	116
4.31 (a) The top and (b) side views of comparative 3D PCL-electrospun constructs by varying the values of an initial distance. The initial distance applied to run the formation procedure of a 12% wt PCL solution in 6:1 DCM:DMF + 10% H <sub>3</sub> PO <sub>4</sub> is increased from 2 to 6 cm, subsequently raised in increments of 1 cm. The 3D PCL structures were formed at a flow rate of 4 mL/h, a voltage of 16 kV, and a nozzle speed of 1 mm/s for 30 minutes.....	117
4.32 Various situations of 3D buildups via 3D electrospinning, which were run with various initial distances of (a-b) 2, (c-d) 3, (e-f) 4, (g-h) 5, and (i-j) 6 cm at a flow rate of 4 mL/h, a voltage of 16 kV, and a nozzle moving speed of 1 mm/s for 30 minutes in an ambient environment.....	118

## LIST OF FIGURES (Continued)

Figure	Page
4.33 SEM images and histograms of fiber diameter fabricated with various initial distances, including (a) 2, (b) 3, (c) 4, (d) 5, and (e) 6 cm, under constants of flow rate, voltage, and nozzle speed at 4 mL/h, 16 kV, and 1 mm/s, respectively.....	121
4.34 (a) The top and (b) side views of comparative 3D PCL-electrospun constructs by varying the values of an initial distance. The voltage applied to run the formation procedure of a 12% wt PCL solution in 6:1 DCM:DMF + 10% H <sub>3</sub> PO <sub>4</sub> is increased from 12 to 16 kV, subsequently raised in increments of 1 kV. The 3D PCL structures were formed at a flow rate of 4 mL/h, an initial distance of 4 cm, and a nozzle speed of 1 mm/s for 30 minutes.....	122
4.35 Various situations of 3D buildups via 3D electrospinning, which were run with various voltages of (a-b) 12, (c-d) 13, (e-f) 14, (g-h) 15, and (i-j) 16 kV at a flow rate of 4 mL/h, an initial distance of 4 cm, and a nozzle moving speed of 1 mm/s for 30 minutes in an ambient environment.....	123
4.36 SEM images and histograms of fiber diameter fabricated with various voltages, including (a) 12, (b) 13, (c) 14, (d) 15, and (e) 16 kV, under constants of flow rate, initial distances, and nozzle speed at 4 mL/h, 4 cm, and 1 mm/s, respectively.....	126
4.37 (a) The top and (b) side views of comparative 3D PCL-electrospun constructs by varying the values of an initial distance The nozzle speed applied to run the formation procedure of a 12% wt PCL solution in 6:1 DCM:DMF + 10% H <sub>3</sub> PO <sub>4</sub> is increased from 1 to 5 mm/s, subsequently raised in increments of 1 mm/s. The 3D PCL structures were formed at a flow rate of 4 mL/h, an initial distance of 4 cm, and a voltage of 14 kV for 30 minutes.....	127

## LIST OF FIGURES (Continued)

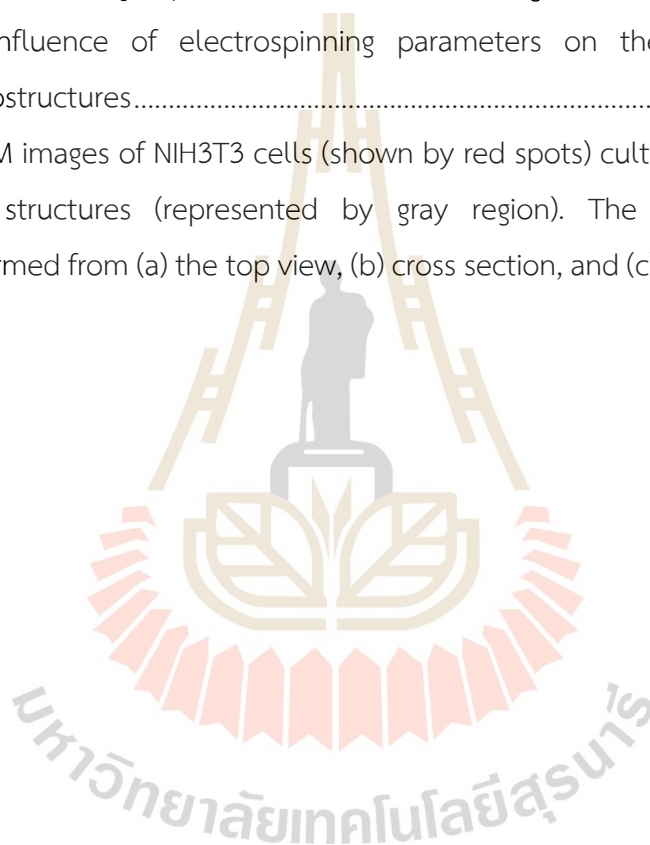
Figure	Page
4.38 Various situations of 3D buildups via 3D electrospinning, which were run with various moving speeds of a nozzle, including (a-b) 1, (c-d) 2, (e-f) 3, (g-h) 4, and (i-j) 5 mm/s at a flow rate of 4 mL/h, an initial distance of 4 cm, and a voltage of 14 kV for 30 minutes in an ambient environment.....	128
4.39 SEM images and histograms of fiber diameter fabricated with various nozzle moving speeds, including (a) 1, (b) 2, (c) 3, (d) 4, and (e) 4 mm/s, under constants of flow rate, initial distances, and voltage at 4 mL/h, 4 cm, and 14 kV, respectively.....	130
4.40 (a) The vector distribution of the electric field strength between the nozzle and collector under the applied voltage of 16 kV and an initial distance varying (i) 2, (ii) 3, (iii) 4, (iv) 5, and (v) 6 cm when the nozzle located at the center ((X, Y) = (0, 0)) which was also illustrated by a graph of electric field on (b) X, (c) Y, and (d) Z axis.....	132
4.41 The vector distribution of the electric field strength under the applied voltage of 16 kV and an initial distance of 4 cm when the nozzle located at (a) (X, Y) is (-30,-30), (b) (X, Y) is (30,30), and (c) (X, Y) is (30,0).....	133
4.42 The morphology of (a) PCL fiber cut from a 3D electrospun structure which was fabricated by a flow rate of 4 mL/h, an initial distance of 4 cm, and a voltage of 16kV, (b) PCL fiber treated by O <sub>2</sub> plasma power of 10 W for 5 minutes, (c) Saos-2 cells seeded on the glass slide (control) after 3 days of culture, and (d) Saos-2 cells seeded on treated PCL fiber after 3 days of culture .....	134
4.43 SEM images of morphological fibers with various powers of plasma treatment, namely (a) no plasma treatment, (b) 10, (c) 30, (d) 50, and 70 W, for 5 minutes.....	135

## LIST OF FIGURES (Continued)

Figure	Page
4.44 Contact angles of untreated and treated PCL-fibrous structures with 10, 30, 50, and 70 W for 5 minutes, named as 10W5MIN, 30W5MIN, 50W5MIN, and 70W5MIN, respectively.....	136
4.45 SEM images of cell morphology and adhesion on 3D PCL-electrospun structures, which were fabricated by the 3D electrospinning with conditions of 16 kV of a voltage, 4 cm of an initial distance, and 4 mL/h of a solution flow rate, viewed at 500 magnifications.....	137
4.46 SEM images of fiber morphology with the magnification of 2000X and histograms of fiber diameter distribution as follows: (a, b) pure PCL fiber, (c, d) PLA fiber with 1 wt% of cellulose, (e, f) PLA fiber with 5 wt% of cellulose, and (g, h) PLA fiber with 10 wt% of cellulose.....	139
4.47 SEM images of NIH3T3 cells on (a) the control, (b) pure PLA fiber, and (c-d) PLA-based fiber with the addition of cellulose: 1, 5, 10 wt%, respectively.....	141
4.48 Representative FTIR spectra of pure PLA fiber, PLA/cellulose fiber, NIH3T3 cells, and NIH3T3 cells on the PLA/cellulose fiber with the spectra resolution of $6\text{ cm}^{-1}$ and the scan time of 64 scans.....	142
4.49 (a-b) SEM and (d, c, e, f) SRXTM images of (a-c) pristine PCL fiber and (d-f) PCL fiber stained with $\text{OsO}_4$ . To be detailed, the SRXTM images were identified by (b, e) the intensity region of PCL polymer and $\text{OsO}_4$ -stained cells, and (c, f) the intensity region of $\text{OsO}_4$ -stained cells.....	145
4.50 SEM and SRXTM images of NIH3T3 cells seeded on PCL-fibrous structures for 1 and 3 days of the culture, which are (a) SEM image showing the surface of the cell on the fibrous structures after seeding the cells into the scaffolds for (a) 1 and (d) 3 days, SRXTM image of the NIH3T3 cells (red area) seeded into the scaffolds (a grey area) for (b) 1 and (e) 3 days, and SRXTM image of the NIH3T3 cell distribution after seeding the cell into the scaffold for (c) 1 and (f) 3 days.....	146

## LIST OF FIGURES (Continued)

Figure	Page
5.1 The current version of 3D electrospinning setup in this work.....	148
5.2 Photographs of 2D mat and 3D stack electrospun (a) using PCL solution without and with the H <sub>3</sub> PO <sub>4</sub> additives, (b) using PVDF solution without and with the H <sub>3</sub> PO <sub>4</sub> additives, (c) 3D stack using PAN solution, and (d) the influence of electrospinning parameters on the 3D fibrous macrostructures.....	150
5.3 SRXTM images of NIH3T3 cells (shown by red spots) cultivated on PCL fiber structures (represented by gray region). The imaging was performed from (a) the top view, (b) cross section, and (c) bottom view.....	152



## LIST OF ABBREVIATIONS

2D	= Two-dimensional
3D	= Three-dimensional
AM	= Additive manufacturing
BJ	= Binder Jetting
CA	= Cellulose acetate
CAD	= Computer-aided design
$C_{hh}$	= Convergence at half height
CS	= Chitosan
DLP	= Digital light processing
$D_{in}$	= Inside diameter
DMEM	= Dulbecco's modified eagle medium
DMF	= Dimethylformamide
$D_{out}$	= Outside diameter
DW	= Width of deposition
EOT	= 3,4-ethylenedioxythiophene
FBS	= Fetal bovine serum
FDA	= Food and Drug Administration
FDM	= Fused deposition modeling
FFF	= Fused filament fabrication
FT-Raman	= Fourier transform Raman
FTIR	= Fourier transform infrared
HCA	= Hierarchical clustering analysis
HV	= High voltage
HFIP	= Hexafluoroisopropanol
IR	= Infrared
LA	= Lactic acid
MEW	= Melt electrowriting

**LIST OF ABBREVIATIONS (Continued)**

MJ	= Material jetting
NFES	= Near-field electrospinning
PAN	= Polyacrylonitrile
PBS	= Phosphate buffered saline
PCL	= Polycaprolactone
PEDOT	= Poly(3,4-ethylenedioxythiophene)
PLA	= Polylactic acid
PET	= Polyethylene terephthalate
P/S	= Penicillin/streptomycin
PPy	= Polypyrrole
PS	= Polystyrene
PSS	= Poly(styrenesulfonate)
PVA	= Polyvinyl alcohol
PVDF-HFP	= Poly(vinylidene fluoride-co-hexafluoropropene)
PVDF	= Poly(vinylidene fluoride), polyvinylidene fluoride
PVP	= Poly(vinylpyrrolidone)
SA	= Sodium alginate
SEM	= Scanning electron microscope
SLA	= Stereolithography
SLRI	= Synchrotron Light Research Institute
SLS	= Selective laser sintering
SR-FTIR	= Synchrotron radiation Fourier transform infrared
SRXTM	= X-ray tomographic microscopy
THF	= Tetrahydrofuran
VDP	= Vapor deposition polymerization (VDP)
XRD	= X-ray diffraction analysis

# CHAPTER I

## INTRODUCTION

### 1.1 Introduction and Motivation

Nanofiber has attracted interest in various applications because of several advantages of nanostructured materials (Alghoraibi and Alomari, 2018; Eatemadi, Daraee, Zarghami, Melat Yar, and Akbarzadeh, 2016; Kenry and Lim, 2017). It has been prepared from various materials, such as natural polymers, synthetic polymers, and composite nanomaterials, and further fabricated by several approaches such as electrospinning (Topuz and Uyar, 2020; Wang, Kong, and Ziegler, 2019), electrohydrodynamic direct writing (Du et al., 2023; A. Nain, Wong, Amon, and Sitti, 2006), centrifugal jet spinning (Arıcan, Uzuner-Demir, Polat, Sancaklı, and Ismar, 2022; Marjuban et al., 2023; Ren, Ozisik, Kotha, and Underhill, 2015), solution blow spinning (Monsorens, Oliveira da Silva, Oliveira, Weber, and Dias, 2022; Vasireddi et al., 2019), self-assembly (Liao et al., 2016; Restuccia et al., 2019), drawing techniques (A. Nain et al., 2006; Xing, Wang, and Li, 2008), spinneret-based tunable engineered parameter method (A. S. Nain et al., 2008; A. S. Nain, Sitti, Jacobson, Kowalewski, and Amon, 2009), phase separation (Jung et al., 2022), freeze-drying synthesis (Yang, Sugita, and Nakane, 2019), sonochemical synthesis (Lee et al., 2021), polymerization of nanofibers (Guo and Zhou, 2007; Huang, 2006) and so on. Widely regarded as the nanofiber approach with great potential applications, electrospinning stands out among the other approaches because of the facilitation following the required modification and the outstanding characteristics of the obtained electrospun mesh (Abadi et al., 2022). Electrospinning provides fibers with diameters ranging from 3 nm to several micrometers, whereas other procedures create fibers ranging from 500 nm to a few microns (Eatemadi et al., 2016). Furthermore, it has been chiefly used to fabricate nanofibers (Alghoraibi and Alomari, 2018; Garg, Rath, and Goyal, 2015; Kenry and Lim, 2017).

**Electrospinning** is a simple and versatile technique for micro- and nanofiber fabrications using an electric force (Ji et al., 2024). It employs the electric force elongating the polymer droplet, resulting in the formation of nanofibers (Haider, Haider, and Kang, 2018; Radacsi and Nuansing, 2020). To be illustrated, the steps of nanofiber fabrication are shown in Figure 1.1: (i) the solution droplet is charged and then transformed to the Taylor cone; (ii) the charged jet gets more extended, which is called a straight jet, on the transition zone; (iii) the jet is thinned in the electric field, and electrical bending instability appears and increases, called a whipping jet, whose length depends on the types and properties of materials and other applied parameters (Nuansing et al., 2013; D. Sun, Chang, Li, and Lin, 2006; Topuz and Uyar, 2020; Zheng, Meng, and Xin, 2018; Zhou et al., 2019). Electrospinning allows nanofiber fabrication from various polymers and polymer-based materials, including metal, ceramic, carbon, and protein (Hwang et al., 2020; Nuansing et al., 2013; M. Vong et al., 2018). Electrospun fibers have been proposed to possess distinctive features, including a high surface-to-volume ratio, high porosity, interconnectivity, and biomimicry (Al-Abduljabbar and Farooq, 2023; Hwang et al., 2020; Islam, Ang, Andriyana, and Afifi, 2019; Jing, Li, Mi, Liu, and Tan, 2019). These features with morphology and alignment can also be easily adjusted by varying solution properties, electrospinning parameters, and modified collectors (Hwang et al., 2020; M. Vong et al., 2018). With the mentioned features, their potential has been approved in numerous applications such as tissue engineering, drug delivery, wound healing, and energy storage. Even though electrospinning is a great way to produce nanofibers with great potential, the electrospun fiber can only be spared out in space as a flat, non-woven, or two-dimensional (2D) mat. Instead of 2D mat, three-dimensional (3D) structures have presented more desirable results for some applications, such as biomedical applications (Askari et al., 2021; Cai, Xu, Jiang, and Yang, 2013; Hwang et al., 2020; Bin Sun et al., 2012), sensors (Kweon, Lee, and Oh, 2018), sound absorption (L. Cao, Si, Yin, Yu, and Ding, 2019), and energy applications (X. Li et al., 2021; M. Vong et al., 2018). In particular, the 2D mat presents low thickness and dense packs of fibrous scaffolds, resulting in too small scaffolds for cell migration and infiltration (Askari et al., 2021; Hwang et al., 2020; Bin Sun et al., 2012). Cai et al. (2013) found

that NIH3T3 cells grew better on 3D electrospun scaffolds, especially in the long term of culture. In this regard, several approaches to 3D fibrous structures based on electrospinning have been proposed, for instance, multilayering electrospinning (Chainani et al., 2013), post-processing after spinning (Gao et al., 2018; Y. Li et al., 2021), mockup-assisted collectors (Kim, Kim, and Park, 2018; Song et al., 2017), modified collectors (Binbin Sun et al., 2015), and self-assembly (Li and Long, 2011; Bin Sun et al., 2012; Michel Vong, Diaz Sanchez, Keirouz, Nuansing, and Radacsi, 2021; M. Vong et al., 2018). Almost all approaches require several steps, additional complications, and time to achieve the 3D fibrous structures, whereas self-assembly is a single step to obtain the 3D structures.

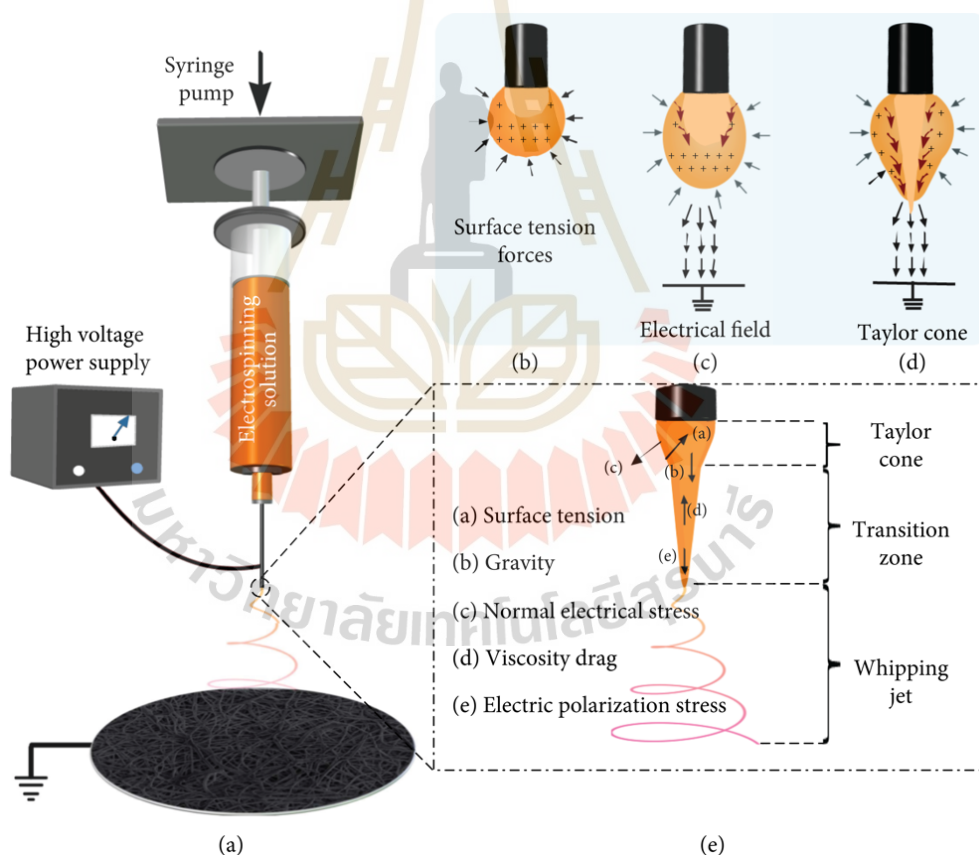


**Figure 1.1** Schematic illustration of a conventional electrospinning setup and nanofiber-formation processes: (a) a general setup; (b-d) the formation of Taylor cones from the droplet; and (e) factors affecting the formation of the jet (Topuz and Uyar, 2020).

**Self-assembly** is mentioned to describe the formations of the 3D stack by continually accumulating fiber with a spatial configuration, as seen in Figure 1.2 (Boyd, Su, Sandy, and Ireland, 2012; Li and Long, 2011; Bin Sun et al., 2012; Yousefzadeh, Latifi, Amani-Tehran, Teo, and Ramakrishna, 2012). It differs from the self-assembly mentioned in the nanofiber approaches, which is the process by which components organize themselves into patterns or structures without human involvement (Lu, Li, and Chen, 2013), such as the nanofibers causing hydrophobic and ion-ion interactions (Liao et al., 2016). Herein, the self-assembly in a field of the 3D fibrous buildup refers to the autonomous ability of the fiber to stand upright without any external support.

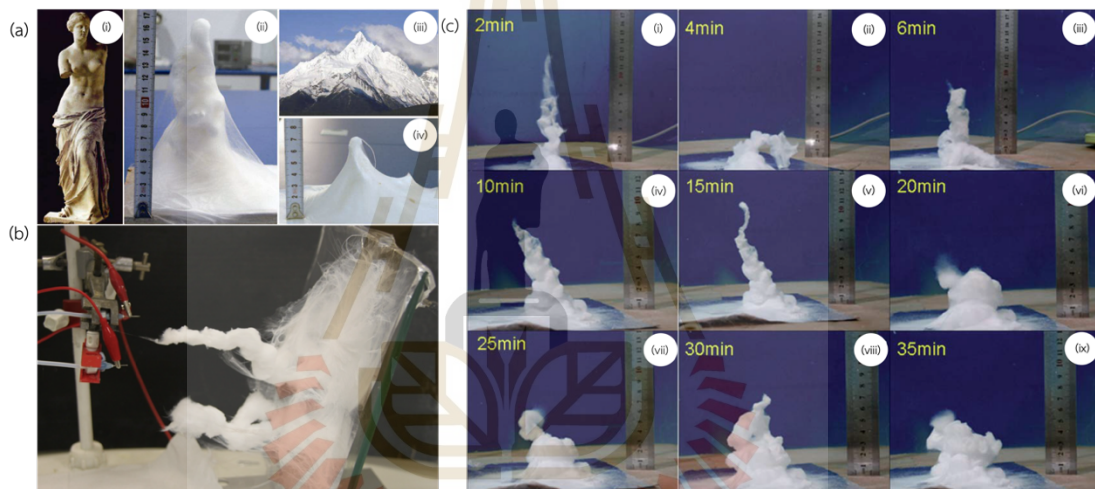


**Figure 1.2** Examples of 3D electrospun constructs fabricated by self-assembly using electrospinning (Boyd et al., 2012; Li and Long, 2011; Bin Sun et al., 2012).

**Example 1:** Li and Long (2011) reported the self-assembled 3D fibrous stacks fabricated by using conventional electrospinning (Figure 1.2(a)). The composite solution in ethanol, consisting of poly(vinylpyrrolidone) (PVP) and salts ( $\text{Fe}(\text{NO}_3)_3:\text{Co}(\text{NO}_3)_2:\text{Ni}(\text{NO}_3)_2 = 1:1:1$  by weight), had succeeded to achieve the 3D stack that reached a height of around 170 mm. In addition, the use of a polystyrene (PS) solution prepared in a mixture solvent of dimethylformamide (DMF) and tetrahydrofuran (THF) with optimal concentrations allowed for the formation of the 3D stack.

**Example 2:** Boyd et al. (2012) discovered the addition of lithium chloride into the cellulose acetate (CA) solution and modification of the spinning parameters produced 3D self-assembled nanofibre structures (Figure 1.2(b)).

**Example 3:** Bin Sun et al. (2012) revealed the quick fabrication of 3D nanofiber stacks and the controllable conversion between the 3D stack and 2D mat via conventional electrospinning. 15 wt% of PS concentration was prepared in a mixture solvent of DMF and THF with a ratio of 1:1 by weight. The solution was fed with a rate of 0.5 ml/min under the voltage of 20 kV applied between a nozzle and an aluminum foil collector placed 15 cm apart. It found that PS fiber grew upward to form a 3D self-assembled stack in a short time of as high as 100 mm (Figure 1.2(c)). The mechanism behind the stack revealed that the fibers on the collector were still negatively charged because of electrostatic induction and polarization under the strong electric field, resulting in a new collector for the coming fibers. The conversion between the 3D stack and 2D mat was achieved by inserting an insulating lucite plate on the collector to change from the 3D to the 2D mat and connecting the cathode of an electrostatic generator to the 2D mat to revert from the 2D to the 3D stack. The self-assembly mechanism has employed rapid solidification, electrostatic induction, and polarization (Hwang et al., 2020; Li and Long, 2011; Radacsi and Nuansing, 2020; Bin Sun et al., 2012).

**3D Electrospinning**, combination of electrospinning and a 3D printer, is an emerging technique used for producing 3D fibrous structures (Radacsi and Nuansing, 2020). This technique has enhanced the advance of electrospinning based on the self-assembly. M. Vong et al. (2018) successfully fabricated and controlled the shape of 3D PS structures without any auxiliary template by using 3D electrospinning, a combination of 3D printing and electrospinning, to build up a 3D macrostructure and control its shape. 3D electrospinning relies on the fiber fabrication of electrospinning, including the stretching and whipping region, to form the structures manufactured by the layer-by-layer, which is the base of 3D printing. Figure 1.3 shows schematic images of various techniques, including conventional electrospinning, 3D printing, near-field electrospinning (NFES), melt electrowriting (MEW), and 3D electrospinning. These techniques, except 3D printing, employ the voltage to stretch the droplet of melted

polymer or solution to form structures. Figure 1.3(a) illustrates the range of jets deposited on a collector or a bed for various techniques, which might influence the size or diameter of the fiber. NFES and MEW have collected the fiber from the straight jet, which differs from the 3D electrospinning. NFES achieves controllable fiber deposition by reducing the distance to eliminate whipping (Loewner et al., 2022). Similarly, the whipping zone is absent in MEW because of the high viscosity and low charge density caused by polymer melt (K. Cao et al., 2023). NFES and MEW have mainly been used in the buildup of micro- or milli-scale structures with precise positioning, while 3D electrospinning has been used to build macrostructures at a scale of centimeters (Figure 1.3(b)).

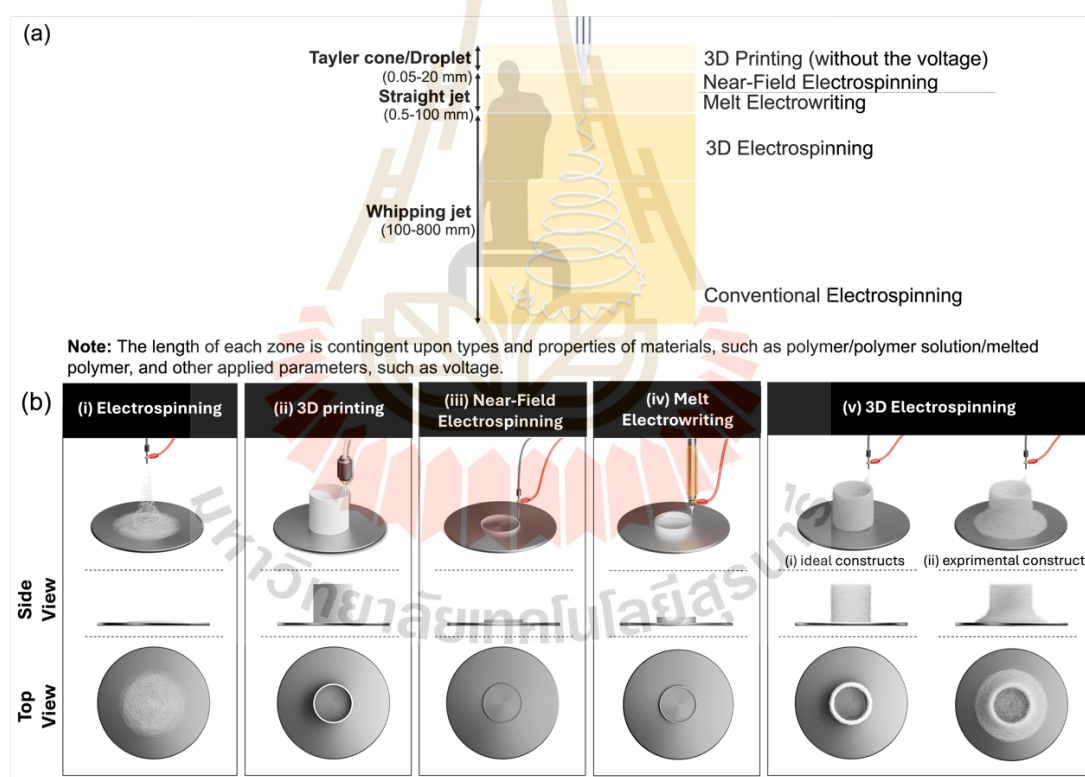


**Figure 1.3** Comparative illustrations of (a) ranges of jets used in various techniques and (b) their comprehensive concepts, including (i) conventional electrospinning, (ii) 3D printer, (iii) near-field electrospinning (NFES), (iv) melt electrowriting (MEW), and (v) 3D electrospinning.

Even though 3D electrospinning had been reported through the controllable fabrication of 3D PS structures, there is still room for improvement because there are a lot of associated factors under the building-up processes. Furthermore, the bioactivity assessment of 3D-electrospun scaffolds fabricated by self-assembly via 3D electrospinning is challenging. In this work, 3D electrospinning is designed and built in-house by combining electrospinning and a fused deposition modeling (FDM) printer. The delta configuration of the printer is chosen in this work because it is anticipated that the delta printer would be able to prevent the fibers from dispersing into undesired locations and minimize the negative impact caused by stainless steel and electric fields. For example, M. Vong et al. (2018) found that at 10 cm of spinning distance, the fiber could deposit on space between the rail of the solution feed system and the collector. In addition, Schmitt et al. (2018) reported the parts printed by the delta printer reached better surface quality; however, the difference in mass and time to print the parts between the delta and cartesian printers was insignificant. The 3D electrospinning has been used to investigate the self-assembly of electrospun stack based on polycaprolactone (PCL), CA, and polyacrylonitrile (PAN). The PCL, CA, and PAN-based solutions, mats, and stacks were chemically observed by using X-ray diffraction analysis (XRD), Fourier transform infrared (FTIR) spectroscopy, Fourier transform Raman (FT-Raman) spectroscopy. PCL has been chosen in examining the self-assembled macrostructure formations via 3D electrospinning because it provides suitable biodegradable properties and excellent mechanical strength and is approved by the Food and Drug Administration (FDA) for human medical applications (Cipitria, Skelton, Dargaville, Dalton, and Hutmacher, 2011; Hwang et al., 2020; Kim et al., 2018). The self-assembly approach for 3D-fibrous macrostructures via 3D electrospinning, without the requirement of any support, has been studied by varying solution factors (concentrations, solvent ratios, and additives) and spinning factors (flow rates, initial distances, voltages, and nozzle moving speeds) to observe on morphological characteristics and final shape of the macrostructures. Height, or thickness, is a criterion between 2D mats and 3D structures. The conductivity of solutions that can provide 2D mats and 3D structures is measured to study its effect on formations and morphology. Additionally, a simulation of the electrical field is

studied to understand the electrical field between the nozzle tip and collector when an initial distance changes or the position of the nozzle tip changes.

The optimal conditions of 3D PCL fibrous macrostructures have been modified with plasma treatment to improve the low hydrophilicity of PCL. The influence of the plasma treatment on the bioactivity is examined by scanning electron microscope (SEM). The SEM images are used to observe the cell morphology and adhesion on the surface of the PCL scaffolds; however, the cell morphology and adhesion within the scaffolds cannot be investigated. A synchrotron radiation X-ray tomographic microscopy (SRXTM) technique is a powerful tool used to collect 3D images of objects with high resolution (Bradley, Robinson, and Yusuf, 2017; Rawson, Maksimcuka, Withers, and Cartmell, 2020). It is used to assess the cell morphology and adhesion within the 3D PCL scaffolds, compared to SEM images. In addition, synchrotron radiation FTIR (SR-FTIR) mapping is another tool used to study the chemical interaction between the PCL fiber and cells.

**Conclusion:** The main goals of this research are the rapid fabrication and controllable shape of 3D PCL electrospun macrostructures using 3D electrospinning, which is designed and built in-house. The buildup of 3D PCL electrospun macrostructures is studied by varying the solution and spinning parameters to study the effect of these parameters on the 3D electrospun formations and obtain the optimal conditions of 3D PCL fibrous macrostructures. Additionally, the mechanism of self-assembly formations is confirmed. The 3D PCL electrospun macrostructures, which are examined by in vitro cell culture and assessed by the SRXTM and SR-FTIR techniques, would be investigated to be a promising scaffold in bone tissue engineering. Before the SRXTM and SR-FTIR, the optimal conditions of plasma treatment are explored because the hydrophilic property of scaffolds is necessary. Eventually, the basic requirements of the fabrication and control of fibrous macrostructures via 3D electrospinning will be discovered, and the final protocol of sample preparation for SRXTM and SR-FTIR characterizations will be reported.

## 1.2 Objectives of this work

**Motivation:** The formation and control of 3D electrospun macrostructures continue to pose difficulties, and more publications on 3D electrospun macrostructures using 3D electrospinning are needed. Additionally, the biological characterizations within the 3D macrostructure scaffolds are challenging.

**Ideas and hypothesis:** The 3D electrospinning enables the production of 3D fibrous macrostructure in a one-step process, allowing for control over the shape of the electrospun constructs and the need for additional templates. The primary scientific inquiry of this thesis is "How can the fabrication and control of 3D electrospun architectures be achieved for biomedical purposes?". Subsequently, the design and build-up of 3D electrospinning in-house are required since 3D electrospinning is currently in the developmental stage and is not readily available in the market. 'What is the suitable configuration of 3D electrospinning to build up the 3D macrostructures, which is subjected to a high voltage?' After completely tuning the solution and spinning parameters to achieve the 3D fibrous macrostructures, 'Should be the hydrophilic property of 3D PCL scaffolds concern and how to improve it'. To investigate the potential in biomedical application, 'How to observe and assess the biological activities within the 3D scaffolds' because 3D structures are composed of surface and depth spatial configurations, which typical characterization might not give the depth details.

**Hypothesis 1 (H1):** The delta printer is a compatible configuration that allows for the combination of the solution feed and voltage source of electrospinning, facilitating the formation of 3D electrospinning. The utilization of a delta printer in combination with electrospinning for 3D printing may offer more effective outcomes compared to using a cartesian printer.

**Hypothesis 2 (H2):** Conductivity and flow rate are the main parameters of self-assembly. Both spinning and printing parameters influence the formation and control of 3D fibrous macrostructures.

**Hypothesis 3 (H3):** The surface modification is required for PCL-based scaffolds before *in vitro* cell culture.

**Hypothesis 4 (H4):** The SRXTM and SR-FTIR imaging techniques are potential tools for observing the cell morphology and adhesion within 3D PCL scaffolds.

**Therefore, the objectives of this work are focused on:**

1. Developing a new system of 3D electrospinning setup suitable and convenient for forming 3D electrospun macrostructures.
2. Studying the factors of solutions, spinning, and printing parameters:
  - (a) starting from the study of a self-assembled stack by using 3D electrospinning without the nozzle movement, then
  - (b) the buildup and control of 3D electrospun macrostructures following a desired CAD file.
  - (c) the simulation based on the change of nozzle position of the 3D electrospinning procedure
3. Improving the 3D PCL-based fibrous scaffolds suitable for *in vitro* cell culture.
4. Discovering the potential tool used to observe the biological activities within the scaffolds

### 1.3 Scope and limitations of the study

1.3.1 This work focuses on designing and developing a 3D electrospinning setup based on combining a delta printer and electrospinning.

1.3.2 PCL is chosen as the primary polymer to explore the parameter effect on the fabrication and control of 3D-fibrous macrostructures using 3D electrospinning.

1.3.3 The biological assessment is carried out through *in vitro* cell culture.

### 1.4 Location of research

1.4.1 Advanced Materials Physics Laboratory (AMP Lab), School of Physics, Institute of Science, Suranaree University of Technology, Nakhon Ratchasima, Thailand.

1.4.2 The Center for Scientific and Technological Equipment, Suranaree University of Technology, Nakhon Ratchasima, Thailand.

1.4.3 Synchrotron Light Research Institute (SLRI), 111 University Avenue, Muang District, Nakhon Ratchasima 30000, Thailand.

1.4.4 Schools of Engineering, The Faculty of Science, Engineering and Built Environment, Geelong Waurm Ponds Campus, Deakin university, Waurm Ponds, Victoria 3216, Australia.

## 1.5 Expected Impact

The thesis is expected to have the following impacts: extend the ability to build 3D fibrous macrostructures based on self-assembly, the protocol to improve the cell adhesion on 3D scaffolds, and the valuable characterization to observe 3D scaffolds.

If the hypotheses are accurate, not only will a new configuration of 3D electrospinning be discovered that can be utilized to construct and control 3D electrospun macrostructures, but this finding will also enhance the potential to explore other configurations of 3D electrospinning. Moreover, it allows for exploring different materials to facilitate the study of 3D self-assembled structures.

In addition, this work primarily emphasizes the biological characterizations within 3D scaffolds. If the objectives can be achieved, the powerful and potential tools used to observe cell morphology and adhesion within scaffolds will be helpful in the characterization study of biomedical applications.

## 1.6 Overview of the thesis

This thesis is structured into 5 chapters. The first part presents background information, including Chapter I the Introduction, Chapter II literature reviews, and Chapter III methodology. The second part of the thesis includes experimental results of 3D electrospinning setup, 3D formations, and biological assessment, which are discussed in Chapter IV, and finally, the conclusion is summarized in Chapter V.

**Chapter II** will conclude with the theoretical aspects of the electrospinning process, the parameter effect of electrospinning, the approaches of 3D electrospun macrostructures, the theoretical aspect of 3D printing, and the fundamental characteristics of bone tissue engineering. This chapter guides the idea and

hypothesis: How can 3D electrospun architectures be fabricated and controlled for biomedical purposes?

**Chapter III** details the methodology containing 3D electrospinning components, solution preparation, characterization techniques, and simulation. The issues of the solution feed system, preventing unwanted fiber deposition, and nozzle-movement system are available; therefore, the 3D electrospinning setups are developed and will be presented. SRXTM and SR-FTIR additionally required specific sample preparation. Therefore, a suitable protocol will be discovered.

*Objective 1* will be mentioned in this chapter.

**Chapter IV** presents all experimental results. The first part of the experimental results on assembling and developing the 3D electrospinning prototype will be presented and discussed. After that, the self-assembly of 3D fibrous macrostructures based on PCL, PVDF, and PAN are examined. Then, the mechanism of formations and control of 3D electrospun macrostructures is illustrated. The effect of solution and spinning parameters will be explored, and the electrical field simulation will be generated to examine the electrical field change during the 3D electrospinning process. The next part of this chapter will propose biological tests and characterizations by *in vitro* cell culture of fibroblast and osteoblast cells and the techniques of SRXTM and SR-FTIR, respectively.

*Objectives 2, 3, and 4* will be mentioned in this chapter.

**Chapter V** will include a comprehensive summary of all experimental data, recommendations for potential applications of 3D electrospinning, and a characterization technique for this study.

## CHAPTER II

### LITERATURE REVIEWS

The first section of this chapter provides principle, parameters, and development of electrospinning. A brief review provides a fundamental understanding of electrospinning, the significant influence of parameters on the electrospinning process, and the development of electrospinning-based processes for the fabrication of 3D macrostructures. The second section provides principles of additive manufacturing (AM) or 3D printing. The final section gives specific information regarding tissue engineering. The offered reviews are crucial and advantageous for the implementation of this task.

#### 2.1 Electrospinning

The term of “electrospinning” is taken from the term “electrostatic spinning” (Ahirwal, Hébraud, Kádár, Wilhelm, and Schlatter, 2013; Dalton, 2017). The basic principle underlying this technique is the use of electric force to elongate a polymer solution, resulting in the formation of micro- or nanofibers. The first report of this phenomenon may be tracked back to the work reported by (Boys, 1887) in 1887, followed by subsequent a patent conducted by (Cooley, 1899) in 1902 with the patent on apparatus for electrically dispersing fluids (Tebyetekerwa and Ramakrishna, 2020). Electrospinning has garnered significant attention since the turn of the century and continues to attract a growing interest in the present day as seen in Figure 2.1. The electrospun fiber exhibits dominant characteristics such as a high surface area to volume ratio, large number of inter-/intra fibrous pores (Haider, Haider, and Kang, 2018), and biomimetic properties (Hwang et al., 2020). Moreover, this technique is easy-to-use for the nanofiber fabrication of various raw materials and additives, ranging from natural and synthetic polymer to composites, hence facilitating the enhancement of desirable qualities of fibers (Haider et al., 2018; Keirouz et al., 2023).

Due to its simplicity and versatility, electrospinning has become the most frequently used techniques for the fabrication of nanomaterials (Haider et al., 2018). This section will provide a comprehensive explanation of the fundamental principle behind this technique, the influence of electrospinning parameters, and what challenges of electrospinning remain.

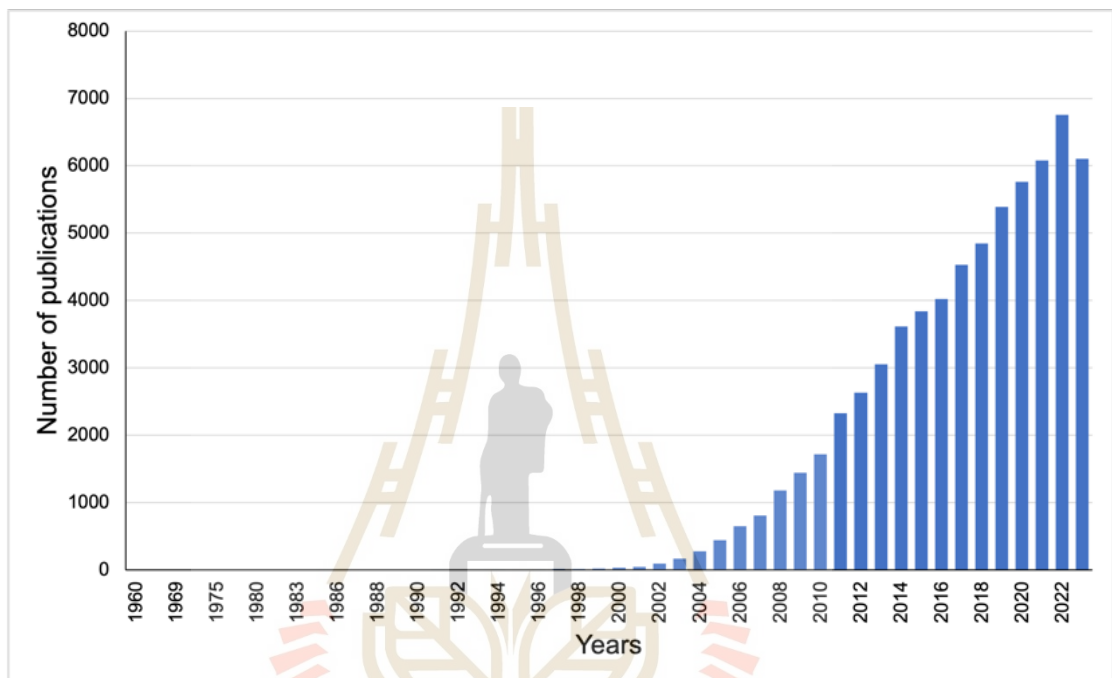


**Figure 2.1** Research progress of electrospinning based on the publication over the years. Data was obtained from Scopus (Elsevier) beads on the searching command “TITLE\_ABS\_KEY electrospinning OR electrospun OR electrospinn” on 23 November 2023.

### 2.1.1 Fundamentals of electrospinning

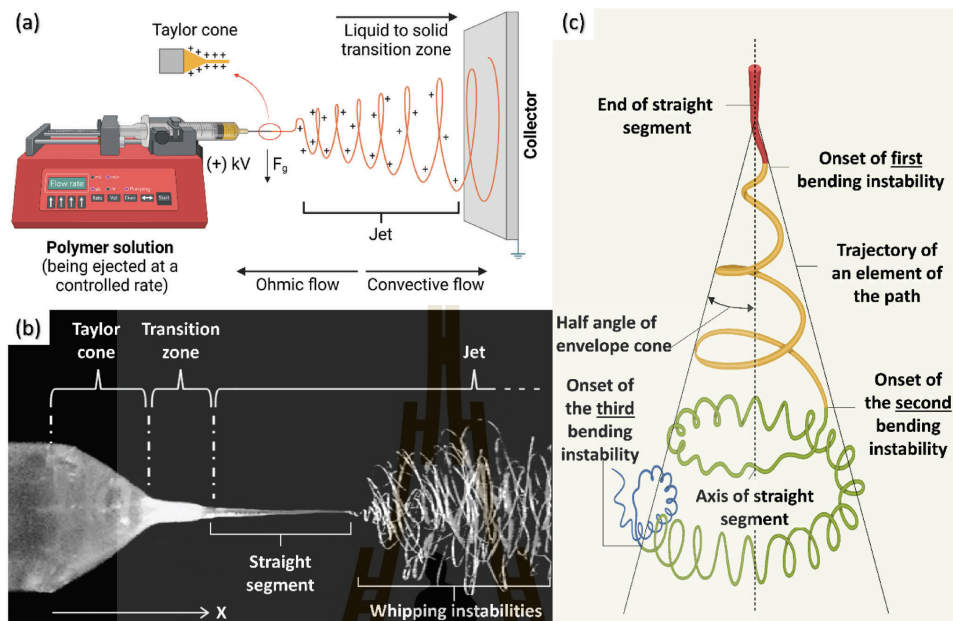


**Figure 2.2** Schematic images of (a) transformation of solution to nanofiber under the electric field, (b) the zoom image of the droplet transformation, and (c) the formation of electrospun nanofiber (Keirouz et al., 2023).

The basic electrospinning setup comprises of four main parts (Figure 2.2(a)): (i) a syringe containing a polymer solution, (ii) a metallic nozzle, (iii) a high voltage (HV) power supply, and (iv) a collector (Haider et al., 2018; Keirouz et al., 2023). To set the electrospinning experiment, the prepared polymer solution is loaded into the syringe and a metallic nozzle is added at the syringe. The collector is wrapped with an aluminum foil, or a metallic collector is used. The voltage power supply is added to generate the electromagnetic charge of opposite polarities between two conductors (Keirouz et al., 2023). Generally, a positive charge is connected to nozzle and the ground is connected to the collector. Nevertheless, it is possible to connect the negative charge to the nozzle and the positive charge to collector (Ura et al., 2020). To start electrospinning procedure, the precursor solution is extruded from the spinneret orifice at a predetermined rate, resulting in the formation of a droplet. It begins as electric charges are transported into the solution via the nozzle and collect within the solution (Haider et al., 2018; Keirouz et al., 2023). This causes instability

inside the solution as a result of the induction of charges. Simultaneously, the reciprocal repulsion between charges generates a counteracting force against the surface tension. The deformation of a spherical droplet into a conical shape, known as the Taylor cone (Figure 2.2(b)), induced by a further increase in the electric field. The accumulation of charges at the surface of droplet is intensified by the growing strength of electrical field. Eventually, the repulsive electric force becomes dominant over the surface tension of the solution, resulting in the emergence and elongation of the fibers from the conical droplet. The formation of a stable charge jet relies on the presence of adequate cohesive forces within the solution. The solidification of elongated droplet occurs by establishing a region where the charged molecules are propelled, allowing for continuous solvent evaporation, stretching the drawn polymer threads as they go toward the collector (Keirouz et al., 2023). The transition from liquid to solid is attributed to the transfer of the Ohmic current to convective flow (Figure 2.2(a, b)), resulting in an acceleration (Keirouz et al., 2023). During the process, the internal and external charge forces induce the jet whipping (Figure 2.2(b, c)). Its motion allows the polymer chains within the solution to elongate and slide past each other, leading to the formation of fibers with diameters small enough to be called nanofibers (Haider et al., 2018). In addition, the high charge density of the jet and unstable whipping motion known as bending instability contribute to form randomly oriented and nonaligned fibrous mat (Keirouz et al., 2023).

#### 2.1.1.1 Basics of electrostatics

The electrostatic field in electrospinning is based on the coulomb law and Gauss's law (Lukáš et al., 2009; Pokorny, Niedoba, and Velebny, 2010; SalehHudin, Mohamad, Mahadi, and Muhammad Affi, 2018). The Coulomb law is the fundamental principle of electrostatics, which defines the force ( $\vec{F}$ ) exerted by a charge ( $q_2$ ) on another charge ( $q_1$ ) at a distance ( $r$ ) in a medium with electric permittivity ( $\epsilon$ ).

$$\vec{F} = \frac{1}{4\pi\epsilon} \frac{q_1 q_2}{r^2} \frac{\vec{r}}{|\vec{r}|} \quad (2.1)$$

where  $q_1$  and  $q_2$  are point charges,  $r$  is the distance between charges, and in case of vacuum medium  $\frac{1}{4\pi\epsilon_0}$  or known as  $k$  is Coulomb's constant ( $k = 8.99 \times 10^9 \text{ Nm}^2/\text{C}^2$ ).

Coulomb force per unit charge is referred to as field strength or field intensity, and is typically represented as  $\vec{E}$

$$\vec{E} = \frac{\vec{F}}{q_1} \quad (2.2)$$

or the electrostatic field per unit charge is written as:

$$\vec{E} = \frac{1}{4\pi\epsilon} \frac{q}{r^2} \hat{r} \quad (2.3)$$

The superposition principle applies to the electrostatic field. The resultant or combined electrostatic field  $\vec{E}$ , generated by charges ( $q_1$ ) and ( $q_2$ ), is determined by the following summation:

$$\vec{E} = \vec{E}_1 + \vec{E}_2 \quad (2.4)$$

The superposition principle and the space dependence of intensity generated by a point charge,  $E \approx 1/r^2$ , leads to an alternative formulation of Coulomb law that is known as the Gauss theorem of electrostatics. It states that a charge ( $q$ ) trapped inside a closed surface ( $s$ ) by permittivity ( $\epsilon$ ) is equal to the scalar product of intensity,  $\vec{E}$ , with a surface area element  $d\vec{s}$ , integrated along the closed surface  $s$ . The surface area element ( $d\vec{s}$ ) is considered here as a vector normal to the surface element:

$$\oint \vec{E} d\vec{s} = \frac{q}{\epsilon} \quad (2.5)$$

Gauss's principle in electrostatics describes the electrostatic field from a macroscopic point of view. It has also a microscopic variant, given by

$$\vec{\nabla} \cdot \vec{E} = \frac{\rho}{\epsilon} \quad (2.6)$$

Where  $\vec{\nabla} = \frac{\partial}{\partial x} + \frac{\partial}{\partial y} + \frac{\partial}{\partial z}$  known as Hamilton operator and  $\rho$  is the charge density instead of the macroscopic net charge  $q$  in Gauss theorem. This equation is also known as the first Maxwell law.

Since the electrostatic field is the conservative, another Coulomb law is that a potential exists that may be used to definitively calculate the field intensity as follows:

$$\vec{E} = -\vec{\nabla}\phi \quad (2.7)$$

Considering by substitute equation (2.7) into equation (2.6), Poisson Equation is presented below.

$$\Delta\phi = -\frac{\rho}{\epsilon} \quad (2.8)$$

Where  $\Delta = \partial^2/\partial x^2 + \partial^2/\partial y^2 + \partial^2/\partial z^2$  known as Laplace operator.

**Case Study:** To be applied in electrospinning process, the basic equations are able to explain the pattern alignment of nanofiber (Pokorny et al., 2010). Pokorny et al. (2010) reported theoretical approach illustrated the dependency of transversal electrical strength on a gap width for collectors consisting of two or more grounded electrodes (Figure 2.3(a)). The modeled electric field distribution around the collector electrodes separated by void gaps shows considerable changes in electrical strength and the electrical field could be resolved into two components  $\vec{E} = (E_x, E_z)$ . The electrostatic field intensities  $E_x$  and  $E_z$  could be written as follows:

$$E_x = A \cdot \sum_i \frac{x_i}{(x_i^2 + p^2)^{3/2}} \text{ and } E_z = A \cdot \sum_i \frac{x_i}{(x_i^2 + p^2)^{3/2}}$$

Where  $A = \tau w / 4\pi\epsilon_0$ ,  $\tau$  is a linear charge density with the uniform charge distribution by  $dQ = \tau dw$ .

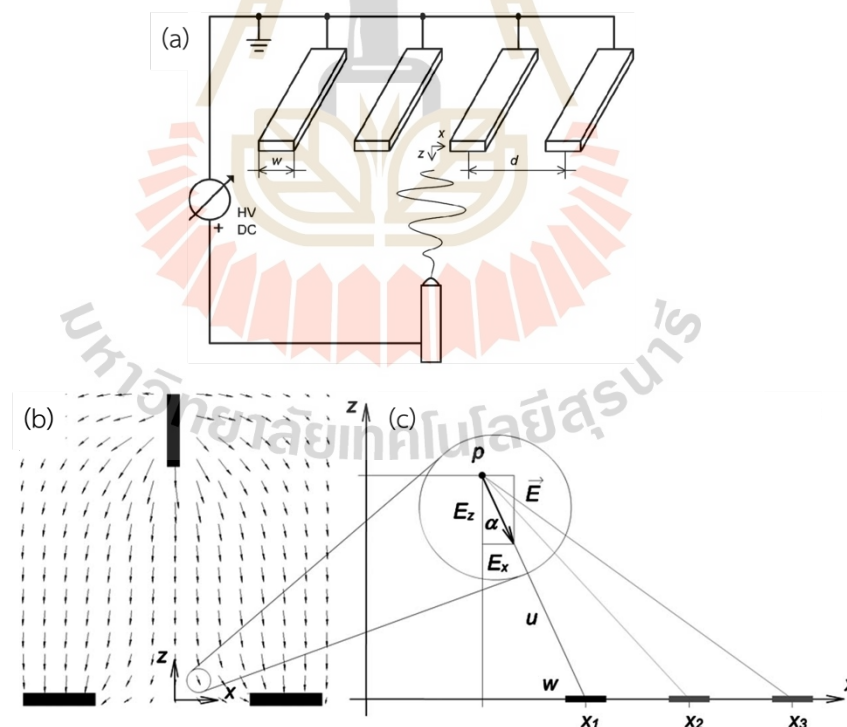


**Figure 2.3** (a) Schematic image of parallel electrode used as collector in electrospinning, (b) an electric field strength vectors calculated on STUDENT'S QUICKFIELD software, and (c) basic model of electrostatic on parallel collector consisting of two or more electrodes (Pokorny et al., 2010).

Numerical simulation was executed based on these equations, it found that the optimum spacing depends on the number of electrodes. The more electrodes required the smaller the optimum distance between electrodes. This analytical calculations of electrostatic strength around the electrodes were useful to design the practical setup of parallel electrode.

### 2.1.1.2 Effect of electrospinning parameters

Electrospinning involves to several parameters including solution concentration, solvent, flow rate, tip-to-collector distance, and voltage. The change of these parameters is review and concluded in Table 2.1.

**Table 2.1** Conclusion of possible effects of electrospinning parameters.

Parameters	Relationships	References
Concentration	- ↓ concentration ↑ formable bead	(Haider et al., 2018; Herrero-Herrero, Gómez-Tejedor, and Vallés-Lluch, 2018; Kolbuk, Guimond-Lischer, Sajkiewicz, Maniura-Weber, and Fortunato, 2015)
	- ↑ concentration ↑ viscosity	(Haider et al., 2018; Herrero-Herrero et al., 2018; Zheng, Meng, and Xin, 2018)
	- ↑ concentration ↑ surface tension	(Herrero-Herrero et al., 2018; Zhao, Wu, Wang, and Huang, 2004)
	- ↑ concentration ↓ conductivity	(Zheng et al., 2018)
	- ↑ concentration ↑ length of straight jet	(Zheng et al., 2018)
	- ↑ concentration ↓ Taylor cone's size	(Zheng et al., 2018)
	- ↑ concentration ↓ whipping frequencies	(Zheng et al., 2018)
	- ↑ concentration ↑ fiber diameters	(Gade, Nikam, Chase, and Reneker, 2021; Herrero-Herrero et al., 2018; Kolbuk et al., 2015; Zhao et al., 2004; Zheng et al., 2018)

**Table 2.1** (Continued) Conclusion of possible effects of electrospinning parameters.

Parameters	Relationships	References
Concentration	- ↑ concentration ↓ fiber diameters	(Haider et al., 2018)
Flow rate	- ↑ flow rate ↑ velocity of jet travel - ↑ flow rate ↑ fiber diameters	(Šimko and Lukáš, 2016) (Gade et al., 2021; Haider et al., 2018; O'Connor, Cahill, and McGuinness, 2021)
Tip-to-collector distance	- ↑ distance ↓ fiber diameters	(Haider et al., 2018; Zeng, Pei, and Wang, 2009; Zhao et al., 2004)
Voltage	- ↑ distance ↔ fiber diameters	(Haider et al., 2018)
	- ↑ voltage ↑↓ fiber diameters	(Haider et al., 2018; Zeng et al., 2009)
	- ↑ voltage ↓ fiber diameters	(Gade et al., 2021; O'Connor et al., 2021)
	- ↑ voltage ↑ fiber diameters	(Kolbuk et al., 2015; Zhao et al., 2004)
	- ↑ voltage ↔ fiber diameters	(Khajavi and Abbasipour, 2017)
	- ↑ voltage ↑ porosity	(Kolbuk et al., 2015)
	- ↑ voltage ↓ porosity	(H. Yousefi, Tang, Tafreshi, and Pourdeyhimi, 2019)
	- ↑ voltage ↑ velocity of jet travel	(O'Connor et al., 2021)
	- ↑ potential difference ↑ length of jet	(Šimko and Lukáš, 2016)
	- ↑ potential difference ↓ width of whipping	(Šimko and Lukáš, 2016)
	- ↑ voltage ↑ Thickness of fiber mat	(H. Yousefi et al., 2019)

## Concentration

The concentration of the solution directly influences the elongation of the electrically charged jet, which is the fundamental aspect of the electrospinning process (Haider et al., 2018). It is necessary to have a critical minimum concentration that enables enough molecular chain entanglement to overcome surface tension to prevent the jet from breaking up (Williams, Raimi-Abraham, and Luo, 2018).

At low concentrations, the combined effects of the applied electric field and surface tension cause the interconnected polymer chains to break apart into smaller pieces before reaching the collector, which leading to beads (Haider et al., 2018). The beads are also subjected by large surface tension (Kolbuk et al., 2015).

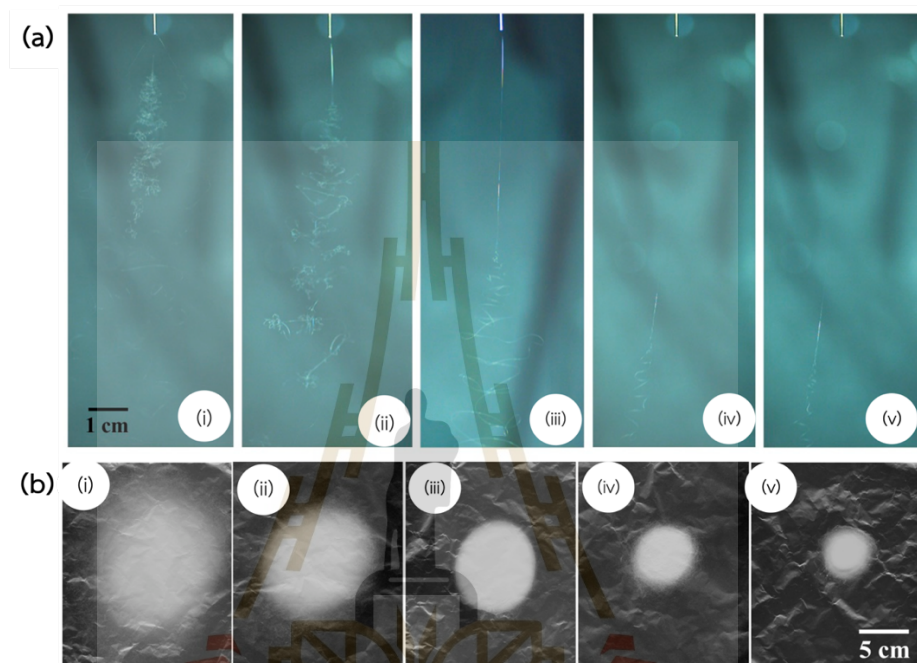


**Figure 2.4** (a) Jet trajectories captured by high speed camera and (b) fiber mats at different PS concentrations: (i) 10, (ii) 15, (iii) 20, (iv) 25, and (v) 30 wt%, which operated by an applied voltage of 20 kV, a distance of 20 cm, and a flow rate of 1 ml/h (Hwang et al., 2020).

Increasing concentration will result in a corresponding rise in viscosity, which increasing the chain entanglement among the polymer chains. These chain entanglements enable surpassing the surface tension, leading to the formation of beadless electrospun nanofibers. For example, Zheng et al. (2018) found PS solution in DMF with higher polymer concentration resulted in the increase of viscosity. The higher concentration led to down conductivity because it relates to the solvent content. In addition, the increase of PS solution concentrations resulted in longer straight jet lengths, smaller envelope cones, and lower whipping frequencies, which leading to larger diameters and smaller area of deposited fiber with more thickness

(Figure 2.4) (Zheng et al., 2018). A critical point of concentration is the range or point of concentration that provide smooth nanofiber (Haider et al., 2018). However, the increase of concentration beyond a critical value will be obstacle the flow of solution at the nozzle tip. Because the increase of concentration refers to the increase of coming polymer, the increasing of polymer solution will be incompletely spun under other constant parameters, causing the polymer solution dries at the tip of the metallic nozzle and blocks it.

### **Flow Rate**

The polymer solution will have sufficient time for polarization when the flow rate is reduced (Khajavi and Abbasipour, 2017). A critical flow rate is required to obtain the continue electrospinning process. Under conditions of low flow rate, the solution droplet is likely to retract into the nozzle. The conical droplet underwent a significant transformation into a sharp shape as a result of the electric field's strength over the surface tension (Zargham, Bazgir, Tavakoli, Rashidi, and Damerchely, 2012). Since the volumetric flow rate decreased with the increasing volume charge density, it induces to faster travel of charged jet toward the collector (Šimko and Lukáš, 2016).

At high flow rate, the droplet will be deposited instead of fiber (Zargham et al., 2012). In addition, exceeding the critical flow rate may result in the formation of beads, as well as a larger of the pore size and diameter caused by the nanofiber jet not fully drying throughout its travel from a nozzle tip to a collector (Haider et al., 2018; Khajavi and Abbasipour, 2017).

### **Tip-to-collector Distance**

The distance between a nozzle tip and a collector influent on the nanofiber morphology because it relates to the time of jet travel, the rate of evaporation, and the length/width of whipping. If the distance is too short, the solvent cannot completely evaporate before reaching the collector. Conversely, if the distance is too long, the beaded fibers has been occurred (Khajavi and Abbasipour, 2017). The larger diameter occurs when the distance is kept small whereas an increase in distance

results in a decrease in the diameter of the nanofiber (Hekmati, Rashidi, Ghazisaeidi, and Drean, 2013; Mehta and Pawar, 2018). In addition, too small distance enables defective nanofiber (Haider et al., 2018). In some instances, alterations in distance do not result in changes to the nanofiber's morphology (Haider et al., 2018).

### **Voltage**

A high voltage power supply is applied to generate the difference of potential between a nozzle tip and a collector. It has a critical role in electrospinning (Khajavi and Abbasipour, 2017). As mentioned, the current from HV supply flows into a solution via a metal nozzle, causing a droplet to deform into Taylor cone and form the nanofibers at a critical voltage. Hence it determines the initial cone shape of the polymer solution, and consequently is able to adjust to control the morphology of electrospun fibers.

Increasing voltage can result in decreasing the fiber's diameter and increasing its (Cao et al., 2023; Zeng et al., 2009). It depends on the critical point. If voltage is increased go to the critical point, the fiber will undergo greater stretching, resulting in reduce its diameter. However, the voltage is increased over the critical point, it will be likely to increase diameter because excessive voltage influences the Taylor cone shape and enhances the velocity of coming fiber to collector (Haider et al., 2018). In addition, increasing the difference in electric potentials results to increase length of jet and decrease the width of whipping zone (Šimko and Lukáš, 2016).

#### **2.1.2 3D electrospun macrostructures**

As mentioned before, the electrospun fiber has performed great potentials with outstanding characteristics including large surface area to volume and biomimicry. However, the electrospun fiber has been obtained in the spatial distribution of 2D planes and it is not easy to achieve 3D macrostructures (Eom et al., 2020). The 2D fibrous mat induced densely packed structure and small pore size which limit cellular infiltration and growth (Jing, Li, Mi, Liu, and Tan, 2019). This issue is challenging in a field of electrospinning research and industry (Eom et al., 2020; Hwang et al., 2020). To address this issue, the approaches of 3D macrostructures have

been continuously studied and improved. 3D electrospun structures have attracted notable interest in various applications such as sensors (Kweon, Lee, and Oh, 2018), energy applications (X. Li et al., 2021), tissue engineering (Hwang et al., 2020) because the 3D structures have provided higher porosity and surface area than 2D mat (Jing et al., 2019).

Figure 2.5 shows the overview of fabrication progress of electrospun fiber starting from 2D nanofiber mat obtained by conventional electrospinning to 3D electrospun structures. Generally, considering between 2D mat and 3D electrospun structures relates to thickness. Herein the approaches of 3D electrospun structures are separately considered in the scale of macroscopic scales. Additionally, it is possible to cross forward to 4D electrospun structures for specific purposes. 4D electrospun fiber is shortly mentioned to show another pathway in the structural overview of development of electrospun fabrication development. In 4D printing, 4D refers to time dimension or changes of printed structures over time, known as dynamic structures, such as color change, property changes, size changes, and shape changes (Apsite et al., 2017; W. Chen et al., 2019; Constante et al., 2021; Fang et al., 2021; Rivera and Hudson, 2019). Similarly, 4D in electrospinning is used to describe the changes of electrospun fiber in microscopic and macroscopic changes such as particle release, shape transformation (Constante et al., 2021).

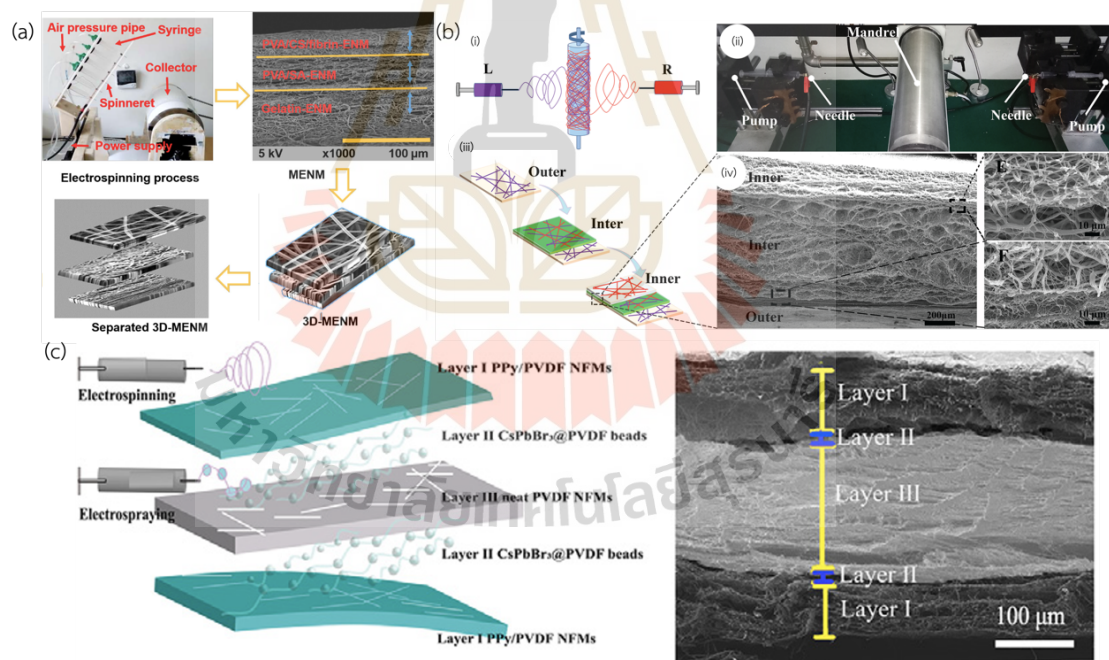


Figure 2.5 Schematic illustration of 2D, 3D, and 4D electrospun fibers.

There are several approach of 3D electrospun macrostructures, including multilayer, post-processing after spinning, collector modification, technique combination, and self-assembly. Table 2.2 conclude the overview approach of 3D electrospun macrostructures, which is detailed in Table 2.2 below.

### Multilayer

Multilayer is a simple strategies to fabricate 3D electrospun structures with the layer-by-layer stacking of electrospun layers by sequential electrospinning processes or co-electrospinning (Abadi et al., 2022). It also is based on the concept that the thickness of the electrospun mat increases with increasing electrospinning time during the conventional electrospinning (Mahesh Kumar, Rajeshwar Man, and Hem Raj, 2020; Radacsi and Nuansing, 2020). Nevertheless, the thickness is limited from tens to hundreds of microns (Radacsi and Nuansing, 2020).



**Figure 2.6** Examples of the multilayer: (a) the fabrication process of multilayered electrospun nanocomposite membrane (Talukder et al., 2021), (b) (i) schematic and (ii) experimental electrospinning setup for the fabrication of multilayer fibrous membranes, and (iii) schematic and (iv) cross-sectional SEM images of the multilayer fibrous scaffolds (F. Sun et al., 2019), and (c) schematic and SEM images of the 3D multilayer fabricated by electrospinning and electrospay (Y. Li et al., 2020).

**Table 2.2** The overview approach of 3D macrostructures based on electrospinning process.

Materials	Solvents	Approaches of 3D structures	Controllable shapes	Applications	References
<i>Multilayer</i>					
PVA, CA, SA, gelatin, fibrin powder,	water, acetic acid	Three spinneret of a melt electrospinning was used to fabricate composite fiber on each layer of scaffolds.	Not mentioned	wound dressing application	(Talukder et al., 2021)
Zein, Gelatin, Lycopene	acetic acid, water	Electrospinning with the change of spinning syringe was used to fabricated sandwich structures. The upper and bottom parts was normal electrospun while there was a round-hole plate used for the fabrication of middle part.	Not mentioned	Drug delivery system	(Charpashlo, Ghorani, and Mohebbi, 2021)
PCL	DCM:ethanol	Electrospun fiber was coated with tendon-derived extracellular matrix, fibronectin to obtain the multilayer scaffolds.	Not mentioned	Tendon tissue engineering	(Chainani et al., 2013)
PVDF, FeCl <sub>3</sub> , PbBr <sub>2</sub> , CsBr	DMF, acetone	Electrospinning and electrospraying techniques were used to fabricate multilayer structures.	Not mentioned	Piezoelectric sensor in wearable applications	(Y. Li et al., 2020)

**Table 2.2** (Continued) The overview approach of 3D macrostructures based on electrospinning process.

Materials	Solvents	Approaches of 3D structures	Controllable shapes	Applications	Ref.
<i>Post-processing after spinning</i>					
Gelatin, PLA	HFIP	The homogenization, shaping and thermal crosslinking technologies were executed to obtain 3D structures after spinning process.	Controllable	Skin tissue engineering	(Y. Li et al., 2021)
PAN, bifunctional benzoxazine, PVA, SiO <sub>2</sub>	DMF, water	The homogenization, the freeze-drying assembly and the in-situ crosslinking were employed to obtain 3D structures after spinning process.	Controllable	sensors	(Si, Yu, Tang, Ge, and Ding, 2014)
PLA	CF:DMF	CO <sub>2</sub> escaping foaming techniques was used to generate 3D porous structures.	Not mentioned	Tissue engineering	(Jing et al., 2019)
PCL	DMF:DCM	2D mat enabled expanding into 3D structures by employing the generation of H <sub>2</sub> foaming caused by the methanolysis reaction of NaBH <sub>4</sub> /methanol.	Controllable	Tissue engineering, regenerative medicine	(Gao et al., 2018)
<i>Collector Modification</i>					
PCL	HFIP	(mockup-assisted collector) The collector was adjusted by attaching copper wires and metal pins onto a nonconductive hemispherical device to obtain 3D hemispherical nanofibrous structures.	Controllable	Cornea tissue engineering	(Kim, Kim, and Park, 2018)

**Table 2.2** (Continued) The overview approach of 3D macrostructures based on electrospinning process.

Materials	Solvents	Approaches of 3D structures	Controllable shapes	Applications	Ref.
PCL, HA	DCM:DMF	(mockup-assisted collector) A stainless steel mesh was used as a collector and 3D porous scaffolds were spun by layer-by-layer assembly with a binder.	Controllable	Bone repair	(J. Song et al., 2017)
PCL	Chloroform, methanol	(mockup-assisted collector) hydrogel-assisted collector was instead of normal metal collector.	Controllable	drug/cell delivery and tissue regeneration	(Eom et al., 2020)
PVDF	Acetone:DMF	(a new platform of collector) Various collectors including pagoda-like dumbbell-, umbellar-like collectors were used to obtain 3D macrostructures.	Controllable	Tissue engineering	(Zhu et al., 2016)
PCL	DMF:Choloform	(a new platform of collector) a double-bevel collector at the peripheral area on a insulate collector was used.	Not mentioned	Tissue engineering	(Tan and Zhou, 2018)
PCL, gelatin, iron oxide	Acetic acid: formic acid	(a new platform of collector) 3D electrospun fiber was made by using a wet electrospinning with a magnetic field.	Controllable	Neural tissue engineering	(Bakhtiary, Pezeshki-Modaress, and Najmoddin, 2022)

**Table 2.2** (Continued) The overview approach of 3D macrostructures based on electrospinning process.

Materials	Solvents	Approaches of 3D structures	Controllable shapes	Applications	Ref.
<i>Technique combinations</i>					
PVDF-HFP, FeCl <sub>3</sub> , PEDOT	DMF:THF	Inkjet printing was used in the fabrication of 3D nanostructured mat together with electrospinning and vapor deposition polymerization was used to fabricate PEDOT shells.	Controllable	Piezoresistive-type pressure sensors	(Kweon et al., 2018)
PCL, alginate	methylene chloride, DMF	3D Hierarchical scaffolds containing of micro-sized struts with inter-layered nanofibers were manufactured by using a hybrid system of direct melt-dispensing and an electrospinning process	Controllable	Biomedical regeneration	(Yeo and Kim, 2014)
<i>Self-assembly</i>					
PVP, Fe(NO <sub>3</sub> ) <sub>3</sub> , Co(NO <sub>3</sub> ) <sub>2</sub> , Ni(NO <sub>3</sub> ) <sub>2</sub>	ethanol	3D formation was attributed by rapid solidification. The incorporation of Fe(NO <sub>3</sub> ) <sub>3</sub> , Co(NO <sub>3</sub> ) <sub>2</sub> , and Ni(NO <sub>3</sub> ) <sub>2</sub> is important for the formation.	Not mentioned	-	(M. M. Li and Long, 2011)
PS	DMF:THF	The concentration and humidity were main parameters which influent to form 3D electrospun structures.	Not mentioned	-	(M. M. Li and Long, 2011; B. Sun et al., 2012)

**Table 2.2** (Continued) The overview approach of 3D macrostructures based on electrospinning process.

Materials	Solvents	Approaches of 3D structures	Controllable shapes	Applications	Ref.
PCL	Acetone, DCM, Lactic acid	The addition of lactic acid enhanced the 3D formation of electrospun-sponge scaffolds.	Not mentioned	Bone tissue engineering	(Hwang et al., 2020)
CA, lithium chloride	Acetone, DMA	The incorporation of lithium chloride with optimal conditions of voltage, flow rate, and distance enhance the 3D electrospun constructs.	Not mentioned	Dental applications	Boyd, Su, Sandy, and Ireland (2012)
TEOS, PVA	Water, H <sub>3</sub> PO <sub>4</sub>	The crucial factor in achieving 3D fiber stacking was the crosslinking between hydrolyzed TEOS and PVA.	Not mentioned	Tissue engineering	(Mi et al., 2018)
PS	DMF:TH, H <sub>3</sub> PO <sub>4</sub>	The electrospinning parameters, including concentration, flow rate, and distance, played a critical role in the buildup and control of 3D macrostructures.	Controllable	-	(M. Vong et al., 2018)

Apart from the increase of time, the increasing number of syringes containing a solution is alternative to obtain the multilayer electrospun mat as shown in Figure 2.6(a,b). For instant, Talukder et al. (2021) used three spinneret of a met electrospinning to obtain hybrid multilayered electrospun nanocomposite membranes, which comprising chitosan (CS)/polyvinyl alcohol (PVA)/fibrin-based mat in the lower layer, PVA/sodium alginate (SA)-based in the middle layer, and gelatin-based mat in the top layer. The electrospinning process of these composites was executed by one by one into the same collector. Similarly F. Sun et al. (2019) reported the ability of two spinneret enabling the fabrication of trilayer structures by employing that one solution was successively electrospun after another without stopping.

Additionally, multilayer electrospinning remains characteristics of electrospun structures with interconnecting-pore (not too dense) and allows the advanced fabrication with varieties of composite and improvement (Chainani et al., 2013; Charpashlo et al., 2021; Y. Li et al., 2020). For example, Chainani et al. (2013) successfully prepared multilayered polycaprolactone scaffolds by using sequentially collecting electrospun layers onto the surface of a grounded saline solution, which was used to be a bath collector, into a single scaffold. The scaffold prepared by cutting the obtained PCL fibers into individual test strips was rehydrated, sterilized, rinsed in phosphate buffered saline (PBS), and coated with various treatments, including tendon-derived extracellular matrix, fibronectin, and PBS to improve cell attachment, which found that the multilayered electrospun scaffold incorporated with TDM show increased levels of collagen accumulation of human adipose stem cells. Similarly, Y. Li et al. (2020) employed electrospinning and electrospaying techniques to fabricate a 3D multilayer assembly of flexible organic polypyrrole (PPy) electrodes. Electrospinning was used to spin the neat poly(vinylidene fluoride) (PVDF) nanofiber and PVDF nanofibers with deposited PPy which was formed by using anhydrous  $\text{FeCl}_3$ /PVDF composites whereas electrospaying generated  $\text{CsPbBr}_3$  between the neat and deposited PVDF mats (Figure 2.6(c)). This 3D multilayer structure induced the enhanced output signals of the piezoelectric nanogenerators.

### Post-processing after electrospinning

Post-processing after spinning refer to numerous methods used to form 3D electrospun structures after completely electrospinning process. Chemical reactions including crosslinking (Y. Li et al., 2021; Si et al., 2014), gas foaming (S. Chen et al., 2020; Y. Chen et al., 2021; Gao et al., 2018; Jing et al., 2019) and so on, have been widely used to achieve 3D electrospun structures. For example, Y. Li et al. (2021) revealed the preparation steps of 3D sponge electrospun fabrication after electrospinning. A gelatin and polylactic acid (PLA) solution prepared in hexafluoroisopropanol (HFIP) was used to fabricate gelatin/PLA nanofiber meshes. The nanofiber meshes underwent four sequential procedures (Figure 2.7(a)) to transform them into 3D sponge scaffolds as follows (i) cutting nanofibers into smaller pieces; (ii) dispersing the small pieces in tert butanol through homogenization; (iii) freezing the pieces in liquid nitrogen and subsequently freeze drying them; and (iv) stabilizing the structures through thermal crosslinking. The sponge scaffolds provide the better porosity and water absorption, compared to the meshes. Moreover, the scaffolds offered a good 3D environment in *in vitro* studies, and a good 3D adhesion in *in vivo* studies. In addition, Jing et al. (2019) employed solubility difference of CO<sub>2</sub> in ethanol and water to induce 3D fluffy nanofiber scaffolds. PLA nanofiber was electrospun onto the grounded aluminum foil and into an aluminum boil containing a 70% ethanol solution. After spinning, the nanofiber was immersed in a bath of dry ice and ethanol, and subsequently moved to a water bath. This resulted in the release of CO<sub>2</sub> molecules, leading to the formations of many bubbles. When the bubbling stops, it is promptly immersed in liquid nitrogen to solidify the pores inside the scaffold, and it is then subjected to freeze drying to generate a 3D scaffold. Similarly, 3D porous scaffolds were obtained by H<sub>2</sub> gas foaming (S. Chen et al., 2020; Y. Chen et al., 2021; Gao et al., 2018). Gao et al. (2018) found 2D PCL mat enabled expanding into 3D scaffolds with the function of controllable shape by using an inner cavity of 3D mold as illustrated in Figure 2.7(b).

As mentioned, the post-process after spinning required several steps and time to reach the formation of 3D electrospun fiber. It is suitable to improve chemical characterizations and properties on specific requirement.

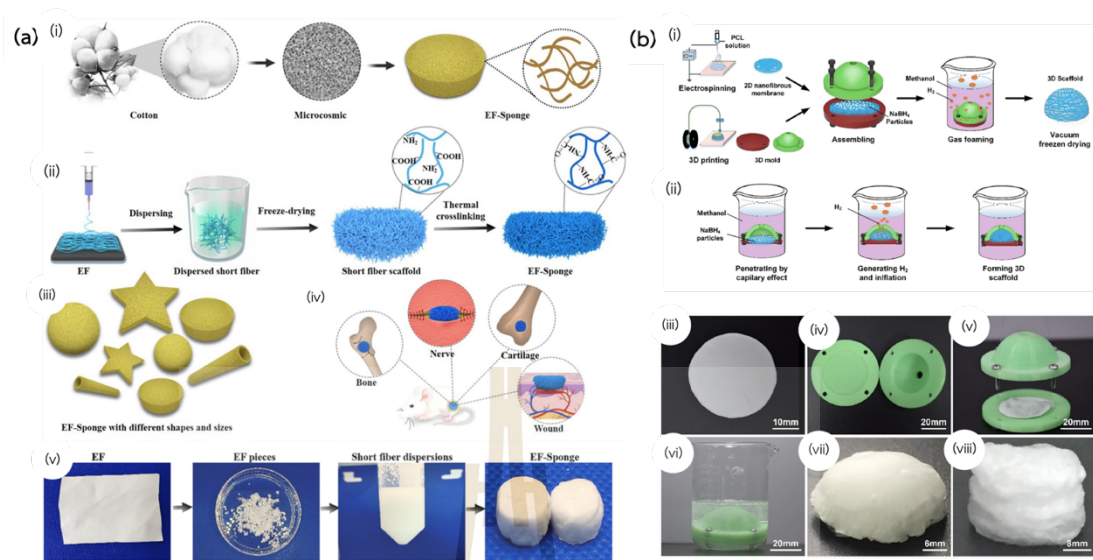


**Figure 2.7** Examples of fabrication procedure using post-processing after electrospinning: (a) schematic diagrams of (i) a unique biological structures of cotton fiber and (ii) the post-processing, which (iii) can provide various structures and (iv) can be candidates in biological applications, to obtain the (v) unique structures based on electrospun fibers (Y. Li et al., 2021) and (b) (i) a schematic diagram to fabricate 3D scaffolds with controllable shapes using (ii) foaming process of 2D mat to 3D scaffold and (iii-viii) the experimental results of the foaming process (Gao et al., 2018).

### Collector Modifications

Collector is the necessary component of electrospinning, which is used to collect the depositing fiber during the spinning process. The electrospun fiber is able to deposit and cover according to the shape of collectors. Therefore, the collector modification is another way to approach the formations of 3D electrospun macrostructures. Moreover, the customization of collectors has demanded for the alignment of electrospun fiber (Kim, Hwang, Aguilar, Park, and Kim, 2016). Due to numerous methods of the collector modifications, they are separated into two categories that are mockup-assisted collectors and new platforms of collectors as follows:

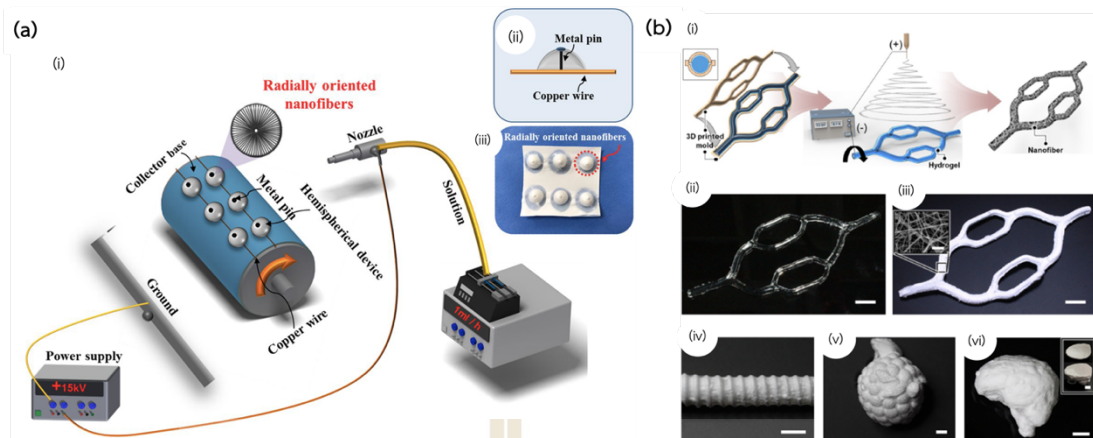


**Figure 2.8** Schematic illustration of mockup-assisted collectors and final products of 3D electrospun structures: (a) (i) electrospinning setup of the fabrication of 3D radially oriented nanofibrous scaffolds, (ii) modified collector by using copper wires and metal pin in the hemispherical device designed to be electrically connected to each other, and (iii) electrospun structures obtained from the modified collector with copper wires and metal pin (Kim et al., 2018), and (b) (i) electrospinning setup modified by using the hydrogel-based collector such as (ii) the multi-bifurcated 3D gelatin cylindrical structure and so on, which can provide (ii-vi) various shapes of hydrogel/fiber structures following the collectors, including (iv) bellow-shaped tubular, (v) human alveoli-like and (vi) brain-like shell macrostructure (J. Y. Song et al., 2021).

(i) Mockup-assisted collectors. The mockup-assisted collectors are the use of mockup instead of the normal collector in electrospinning process. There are several techniques available for constructing mockups, which vary based on intended purposes of applications, shapes, characteristics, or properties. To be simplest, the conductive mockup used to attach onto the surface of collector to achieve the desired shape. For instant, copper wires and metal pins were placed onto the nonconductive collector (Figure 2.8(a)) to obtain a 3D radially patterned nanofibrous scaffold for cornea tissue engineering (Kim et al., 2018). Additionally, 3D porous scaffolds based on PCL and HA composite was layer-by-layer fabricated by using a stainless steel mesh as a collector (J. Song et al., 2017). 3D printing, a widely utilized method for rapidly creating prototypes, is commonly employed for producing mockup collectors due to its ability to work with a variety of printable materials, offer

various design capabilities, and provide easy accessibility. Hydrogels is one of texture that can serve as a substitute for metal collectors. For example, J. Y. Song et al. (2021) manufactured 3D constructs by using a 3D ear cartilage-shaped hydrogel collector. Likewise, Eom et al. (2020) employed hydrogel structure being the collector instead of a metal collector to approach tailored configuration as seen in Figure 2.8(b).

Mockup-assisted collectors facilitated the formation of 3D structures by covering the mockup's surface. It is difficult to obtain intricate shapes and access the interior of structures. Additionally, if needed, the process of removing fiber from the collector should be realized. Specifically, a cylindrical collector was utilized to manufacture tubular scaffolds. The electrospun tube needs to be repelled from the collection.

(ii) The new platforms of collectors: it refers to the change of conventional collector like flat or drum collectors to be new platforms of collector including modified collector (Jin et al., 2014; Tan and Zhou, 2018; Zhu et al., 2016), liquid collectors (Bakhtiary et al., 2022; Yousefzadeh, Latifi, Amani-Tehran, Teo, and Ramakrishna, 2012; Zeng et al., 2009) and so on.

To achieve 3D fibrous macrostructures, modified collector with space have been widely proposed with the ability of alignment. For example, various collectors including pagoda-, dumbbell-, umbellar-like collectors were used to obtain 3D macrostructures (Zhu et al., 2016). Similarly, a double-bevel collector was attached onto the surface of the insulating plate with various angle of bevel, which this setup was used to be a collector (Tan and Zhou, 2018). Similarly, the hemisphere shape has been used as a collector to obtain 3D fluffy structures (Blakeney et al., 2011; Hwang et al., 2020). Blakeney et al. (2011) reported the fabrication of 3D electrospun nanofibrous scaffolds by using a spherical foam dish with the embedded array of stainless steel probes being the collector. The modified spherical collector provided 3D cotton ball-like structures whereas 2D mat was obtained by using a flat plat being collector as shown in Figure 2.9(a). The diameter of cotton structures was similar to one of 2D mat, but there were large pore and less dense pack, which induced cell infiltration.

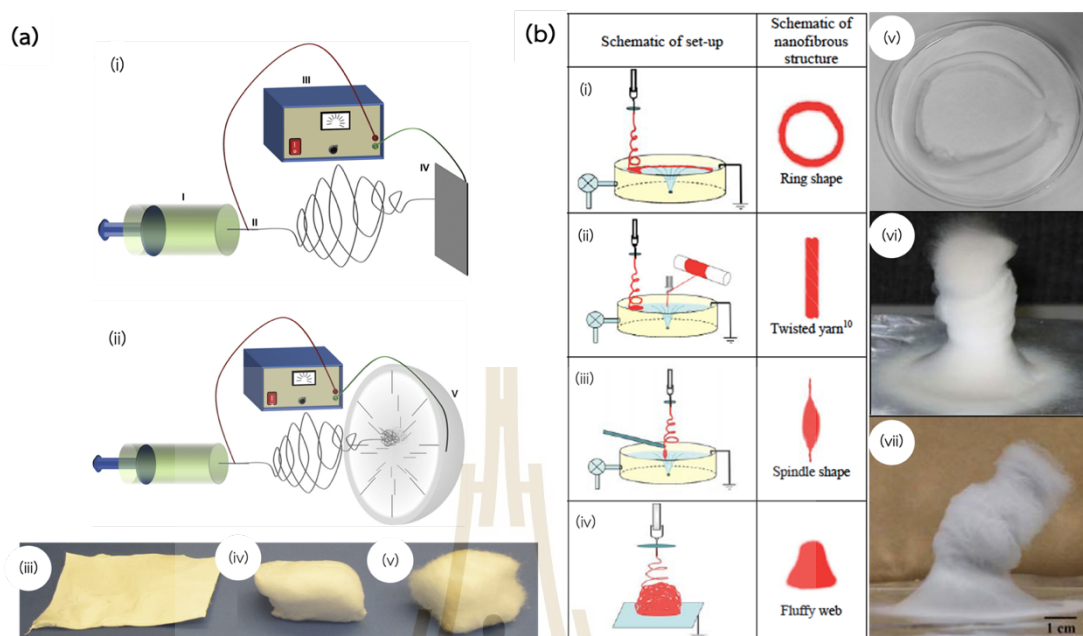


**Figure 2.9** Examples of the use of new platform of collector in electrospinning to achieve 3D macrostructures: (a) the use of (ii) hemisphere collector used in electrospinning compared to (i) normal collector used in conventional electrospinning, which provided (iii) 2D PCL scaffold with no depth using the conventional electrospinning and (iv-v) a 3D cotton ball-like PCL scaffold (Blakeney et al., 2011) and (b) the use of liquid collector with (i-iv) various methods of depositions which provided (v-vi) various 3D macrostructures following the deposition methods (Yousefzadeh et al., 2012).

The liquid collector is commonly used to create 3D structures by utilizing the gravitational force exerted by its components to manufacture the structures. The utilization of the liquid collector in electrospinning is called as wet electrospinning (Kostakova, Seps, Pokorný, and Lukas, 2014; Yousefzadeh et al., 2012) or hydrospinning (Tzezana, Zussman, and Levenberg, 2008). For liquid collector, nanofibers are being accumulated on the top of a liquid reservoir and systematically arranged layer-by-layer to construct a three-dimensional scaffold (Yousefzadeh et al., 2012; Zeng et al., 2009). Yousefzadeh et al. (2012) fabricated 3D structures with the function of controllable shape by using the incorporation of various depositions. With the swirling motion of the vortex was applied to a used water tank being a collector.

To control the shape, the movable nozzle was used, and a positive charged electrode disk was applied to around the nozzle. As seen in Figure 2.9(b), ring shape, twisted yarn, spindle shape, and fluffy web were obtained by various pattern of deposition including the circular locomotion of nozzle, the insertion of rotating collector, the addition of a grounded bar, and the flat plate.

### Technique combinations

The technique combinations refer to the use of many techniques during the fabrication process to achieve 3D electrospun-based structures such as electrospinning and 3D printer (Yeo and Kim, 2014), electrospinning and electrohydrodynamic inkjet printer (Kweon et al., 2018)

For example, the electrospinning and electrohydrodynamic inkjet printer were used to manufacture 3D structures composed of poly(vinylidene fluoride-co-hexafluoropropene) (PVDF-HFP), ferric chloride ( $\text{FeCl}_3$ ), and poly(3,4-ethylenedioxythiophene) (PEDOT) as seen in Figure 2.10(a) (Kweon et al., 2018).  $\text{FeCl}_3$  was employed as a source of  $\text{Fe}^{3+}$  ions in the construction of 3D nanostructures and as an agent that promotes the oxidation of 3,4-ethylenedioxythiophene (EDOT) during polymerization. First, the PEDOT:poly(styrenesulfonate) (PSS) solution was printed onto a polyethylene terephthalate (PET) substrate to form flexible electrodes. After printing, the electrodes were taken to an annealing process, and the residual PSS was removed by ethylene glycol. Second, PVDF-HFP/ $\text{FeCl}_3$  nanofibers were directly electrospun onto printed PEDOT:PSS/PET or indium tin oxide-coated polyethylene naphthalate substrates. Third, a vapor deposition polymerization was employed to polymerize EDOT onto the surface of the PVDF-HFP nanofibers by chemical oxidization with  $\text{FeCl}_3$ . The obtained sponge-like 3D structures were used to create piezoresistive-type pressure sensors, which provided higher pressure sensitivity than 2D mats because of their high porosity and pressure-tunable contact area. Likewise, Yeo and Kim (2014) employed the printing of melt-plotting system and electrospinning to construct 3D hierarchical scaffolds with interlayered PCL micro/nanofibers (Figure 2.10(b)). It was proposed to enhance cell infiltration and migration for tissue engineering.

Indeed, the technique combinations are the formation of electrospun-based structures. It does not perform pristine electrospun fiber of 3D structures. Similar to the new platform of collector modification or post-processing after spinning, the 3D constructs with technique combination require both time and multiple stage. However, this is suitable to create composite and detailed structures for specific applications.

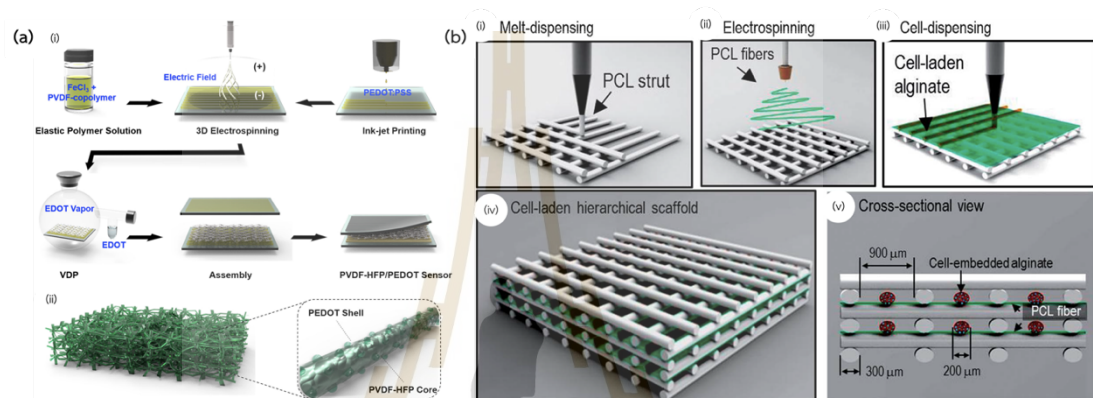


**Figure 2.10** Examples of technique combinations: (a) (i) experimental illustration of the fabrication process of electrospun-based piezoresistive pressure sensors and (ii) electrospun 3D nanostructured mats (Kweon et al., 2018) and (b) Schematic illustration of the fabrication procedure for cell-laden hierarchical scaffolds by using (i) melt-dispensing, (ii) electrospinning process, and (iii) cell-dispensing process which (iv) final shape of the scaffold and (e) cross-sectional view of the scaffold (Yeo and Kim, 2014).

### Self-assembly

Self-assembly in the research of 3D electrospun constructs refer to the self-stand-up of electrospun fiber which is able to assemble the macrostructures by itself without any auxiliary during and after spinning process (M. M. Li and Long, 2011; B. Sun et al., 2012). As mentioned in Chapter I, the rapid solidification, electrostatic induction, and polarization are necessary for self-assembly. To be illustrated, the conversion between 2D mat and 3D stack as shown in Figure 2.11(a) was investigated (B. Sun et al., 2012). It was found that the insert of an insulating lucite plate on the surface of collector, 3D stack obtained transformed to a 2D mat. It was expected that the insulate plate act as a block of the positive fibers coming through the ground.

The 3D stack backed when applying an electrostatic generator to the 2D mat. Additionally, 3D stacks enable disappearing and become 2D mats when the humidity increases (M. M. Li and Long, 2011). Indeed, the fabrication of 3D nanofiber structures involves to concentration, solvent, additives, voltage, tip-to-collector distance, and flow rate (Boyd et al., 2012; Hwang et al., 2020; M. M. Li and Long, 2011; M. Vong et al., 2018). For example, A PVP solution with  $M(NO_3)_x$  at the optimal ratio of  $Fe(NO_3)_3:Co(NO_3)_2:Ni(NO_3)_2 = 1:1:1$  by weight enabled forming a 3D electrospun stack up to as high as 17 cm (M. M. Li and Long, 2011). It was proposed that the stacking formation was attributed to the optimal condition, which can provide rapid solidification of electrospun fibers (M. M. Li and Long, 2011). As seen in Figure 2.11(b), the stack started at the center of collector where was the strongest strength of electric field, and the coming fiber would be deposited at and around the position of deposited fiber. It was found the incorporation of  $M(NO_3)_x$  content involved to the formation of 3D stack. Decreasing the  $M(NO_3)_x$  content induced 2D mats instead of 3D formations. Likewise, Boyd et al. (2012) found the incorporation of 0.5% lithium chloride with optimal conditions provided the 3D constructs and Hwang et al. (2020) found the addition of lactic acid (LA) played an important role in 3D formation of sponge scaffolds. To obtain self-assembly, apart from the incorporation of additives, crosslinking is able to induce self-assembled formation. For example, Mi et al. (2018) found free-standing silica fibers may be formed through direct self-assembly using a suitably crosslinked tetraethyl orthosilicate and PVA solution, with the process being regulated by altering the PVA content and aging time. Likewise, 3D zein and polyethylene glycol electrospun scaffolds were successfully fabricated by reducing surface resistivity and based on the principle of electrostatic repulsion (Figure 2.11(c)) (Cai, Xu, Jiang, and Yang, 2013). However, the additives are need in some polymer-based solution in fabricating 3D electrospun fiber. For example, PS solutions in DMF:THF without additives enabled forming 3D self-assembled structures (M. M. Li and Long, 2011; B. Sun et al., 2012).

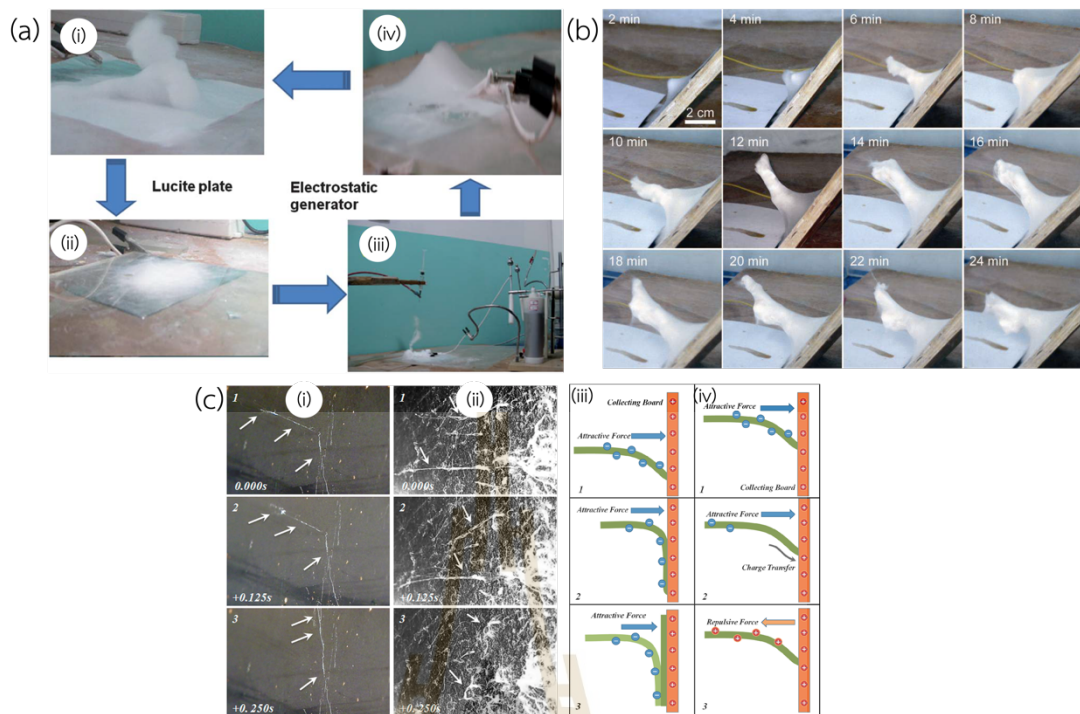


**Figure 2.11** Examples of self-assembly in the 3D electrospun formation: (a) conversion between a 3D fiber stack and a 2D thin film by changing (i) 3Dstack on Al foil to (ii) 2D fiber mat by using a lucite plate and then (iii) connecting the 2D mat to an electrostatic generator to get a 3D stack, and (d) 3D stack grown on the lucite plate (B. Sun et al., 2012), (b) growth evaluation of 3D PVP-based macrostructures (M. M. Li and Long, 2011), and (c) photography of fiber deposition processes for (i) 2D mat and (ii) 3D scaffolds and schematic diagram of fiber deposition for (iii) 2D mat and (iv) 3D scaffolds (Cai et al., 2013).

To progress the next stage, the ability of controllable shape has emerged in the formation of 3D electrospun macrostructures. 3D printing is a simple and versatile tool used to control the position of manufacturing. There was the development of electrospinning setup combining with 3D printing, called 3D electrospinning, used to fabricate 3D self-assembled fiber (Michel Vong, Diaz Sanchez, Keirouz, Nuansing, and Radacsi, 2021; M. Vong et al., 2018). The 3D PS structures could be built and controlled in one step following a CAD file of desired model by using 3D electrospinning (M. Vong et al., 2018). The 3D formation of the PS fibrous structures happened instantaneously, resulting in the 3D structures of 4 cm in height and 6 cm

in width within a 10-minute spinning procedure. All spinning and printing parameters involve to the 3D formations. The critical point of these parameters is required in building up and controlling the shape of 3D electrospun structures.

Self-assembly is the buildup of 3D electrospun structures with the outstanding characteristics of high porosity in single step. Additionally, the deposition position of self-assembled fiber can be controlled by applying a 3D printer. However, there were a few publications about materials which perform the self-assembly and the spinning parameters on the 3D formation. The insight of self-assembly is needed in the 3D formation of electrospun fiber.

## 2.2 Additive Manufacturing or Three-Dimensional Printing

AM, also known as 3D printing or rapid prototyping, is a significant advancement in human innovation that arrived in the later part of the 20th century (Gibson, Rosen, and Stucker, 2010). Starting from the first patent for stereolithography (SLA) in 1984 was obtained. It employs UV light to layer-by-layer solidify a liquid-polymer resin, resulting in the creation of 3D structures. This opened the opportunities for several innovative technological advancements in the following decades. Generally, the workflow of 3D printer starts with the design of required models by using a computer-aided design (CAD) as seen in Figure 2.12 (Manoj Prabhakar et al., 2021). It has also altered in the meshed CAD version. The model file is layer-by-layer sliced to obtain a gcode file, and also the printing parameters can be adjusted in this step. The G code file is then put into the 3D printer to start the printing process which is based on each manufacturing type of printer.

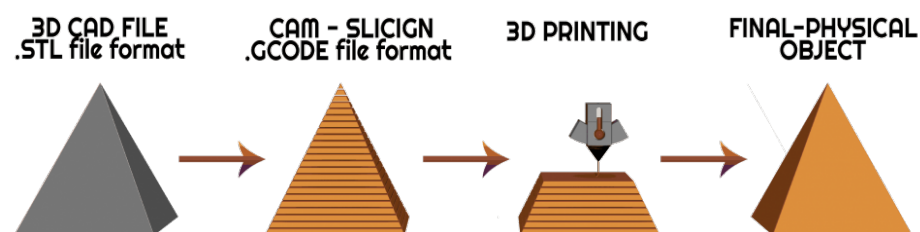


**Figure 2.12** A workflow diagram of 3D printing (from <https://fabacademy.org/2018/labs/fablabkochi/students/salman-faris/week6.html>).

### 2.2.1 Types of 3D Printing

As shown in Figure 2.13, there are several types of 3D printers, including FDM, SLA, binder Jetting (BJ), material jetting (MJ), selective laser sintering (SLS), sheet lamination, and direct energy deposition (Carew and Errickson, 2020), which listed by the ISO/ASTM 52900 standard (Ahangar, Cooke, Weber, and Rosenzweig, 2019). Briefly, the details of each type are described below:

- FDM or fused filament fabrication (FFF): It is based on the material extrusion. The meltable or thermoplastic materials are used in this technique. The materials are melted and extruded through the movable nozzle, which move following the CAD file (Gibson et al., 2010).

- Vat polymerization: It creates 3D objects by selectively curing resin through targeted light-activated polymerization in a vat with a light source selectively. There are two types of vat polymerization that are SLA and digital light processing (DLP) (Manoj Prabhakar et al., 2021). The difference of two types is the light origin utilized to heal the resin.

- BJ: It employs a jet of liquid bonding agent to selectively bond a bed of powdered materials. After printing, the layers are gradually added, fused, and the unfused powder is removed. To complete the build, postprocessing (such as heat sintering) is required (Carew and Errickson, 2020).

- MJ: This technique prints a layer of liquid resin by spraying it on and curing it with UV light at the same time. The layer is then printed over (Ahangar et al., 2019; Elkaseer et al., 2022).

- Power bed fusion like SLS: A meltable power bed is used as the base materials in this technique and a laser is used to melt selective power on a layer. A new layer of powder is placed on top of the previously melted layer, and the procedure is repeated (Ahangar et al., 2019; Chowdhury et al., 2022).

- Sheet lamination: Paper, plastic or metal sheet of material are cut either with a laser or a blade that each sheet is executed following a sliced CAD model. After all sheets are cut, the sheets are stacked and bound with a binder, and the cut parts are removed (Ahangar et al., 2019; Zhang, Jarosinski, Jung, and Zhang, 2018).

- Directed energy deposition: Layers of material, including paper, plastic, or metal composite are bonded together using an adhesive and the desired shape is obtained by cutting into each layer (Carew and Erickson, 2020).

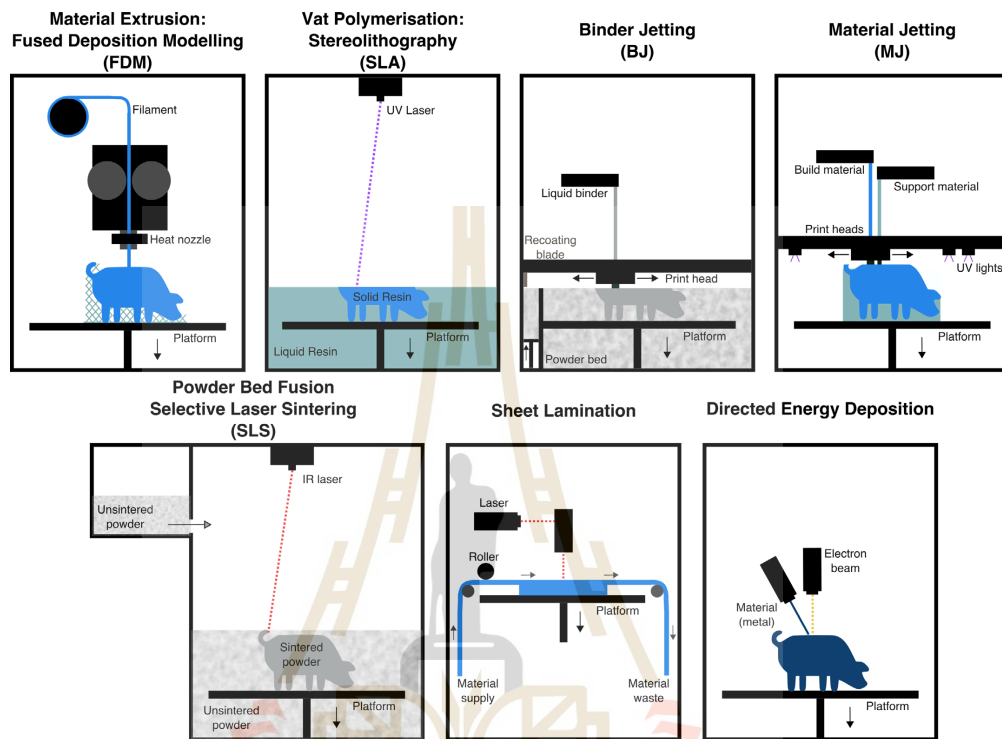
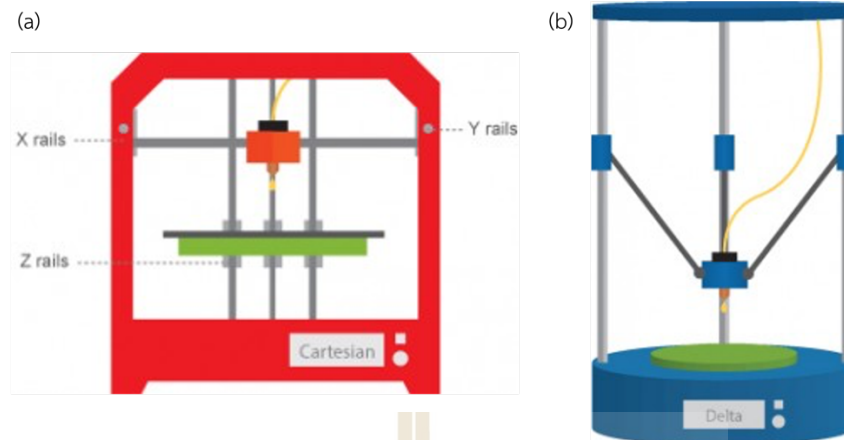


Figure 2.13 Schematic illustration of the categories of AM techniques (Carew and Erickson, 2020).

## 2.2.2 Delta Coordination

Generally, based on FDM techniques, there are two coordinate systems (Figure 2.14), including cartesian and delta coordinates, which have different ways to navigate the extruder in the build plate.



**Figure 2.14** Coordinate systems of 3D FDM printer: (a) cartesian and (b) delta coordinates (from <https://www.printspace3d.com/cartesian-vs-delta-printers-work/>).

A delta 3D printer, also known as a delta printer, is a kind of parallel robot that uses geometric algorithms to position each of three vertical axes simultaneously to move the nozzle to any position in a build area (Bell, 2015b). To understand what its components is and how it works, its anatomy is shown in Figure 2.15(a, b) and detailed below:

- Filament: it is meltable materials (mostly thermoplastics) used to insert to 3D printer.
- Extruder: it is responsible to feed the filament to the hot end.
- Build plate: it is where the printed parts are formed. Some printing process, a build plate needs to be heated.
- Axes/Towers: They are vertically arranged and labeled counter-clockwise as X, Y, and Z axis.
- Carriage: It attaches to the axis and provides a mount point for the delta arms.
- Effector: it is a base where the hot end is mounted.
- Delta arms: It attaches to the carriage and the effector using a pair of parallel arms.
- Hot end: A special heater that heats a nozzle for melting the filament.

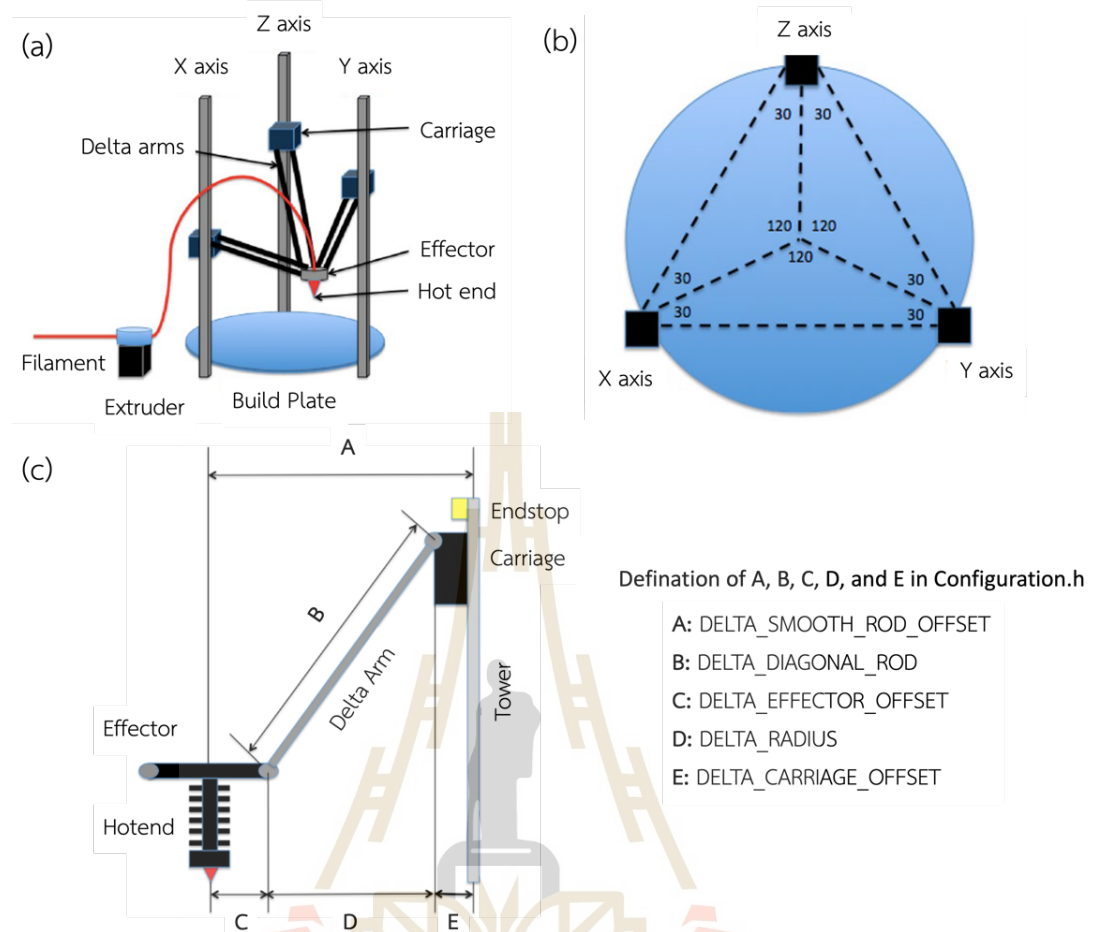


**Figure 2.15** (a) Anatomy of 3D delta printer, (b) location of towers, and (c) delta geometry with the definition in configuration.h of Marlin (Bell, 2015a).

As shown in Figure 2.15(c), the hotend is able to take the desired coordinates based on cartesian location ( $\text{cartesian}[\text{X\_AXIS}]$ ,  $\text{cartesian}[\text{Y\_AXIS}]$ ,  $\text{cartesian}[\text{Z\_AXIS}]$ ) by the calculation of carriage position ( $\text{delta}[\text{X - Axis}]$ ,  $\text{delta}[\text{Y - Axis}]$ ,  $\text{delta}[\text{Z - Axis}]$ ). Based on Marlin configuration (Bell, 2015a), the delta movement is corresponding to equation (2.9).

$$\text{delta}[\text{X - Axis}] = \frac{\sqrt{L^2 - (\text{Delta\_Tower1\_X} - \text{cartesian}[\text{X\_AXIS}])^2 - (\text{Delta\_Tower1\_Y} - \text{cartesian}[\text{Y\_AXIS}])^2} + \text{cartesian}[\text{Z\_AXIS}]}{2} \quad (2.9.1)$$

$$\text{delta}[\text{Y - Axis}] = \frac{\sqrt{L^2 - (\text{Delta\_Tower2\_X} - \text{cartesian}[\text{X\_AXIS}])^2 - (\text{Delta\_Tower2\_Y} - \text{cartesian}[\text{Y\_AXIS}])^2} + \text{cartesian}[\text{Z\_AXIS}]}{2} \quad (2.9.2)$$

$$\text{delta}[Z - \text{Axis}] = \frac{\sqrt{L^2 - (\text{Delta\_Tower3\_X} - \text{cartesian}[X\_AXIS])^2 - (\text{Delta\_Tower3\_Y} - \text{cartesian}[Y\_AXIS])^2} + \text{cartesian}[Z\_AXIS]}{(2.9.3)}$$

Where L is DELTA\_DIAGONAL\_ROD and Delta\_Tower1/2/3\_X/Y is the position of tower is considered by using the Y tower as the starting point for the calculation as following:

$$\begin{aligned} \text{Delta\_Tower1\_X} &= -\sin(60) \times \text{DELTA\_RAIUS} \\ \text{Delta\_Tower1\_Y} &= -\cos(60) \times \text{DELTA\_RAIUS} \\ \text{Delta\_Tower2\_X} &= \sin(60) \times \text{DELTA\_RAIUS} \\ \text{Delta\_Tower2\_Y} &= \cos(60) \times \text{DELTA\_RAIUS} \\ \text{Delta\_Tower3\_X} &= 0.0 \\ \text{Delta\_Tower3\_Y} &= \text{DELTA\_RAIUS} \end{aligned}$$

### 2.3 Surface Modification by using plasma treatment

Plasma treatment is a physical method of surface modification with changes of different surface chemistry (Kasoju et al., 2018; Martins et al., 2009). Plasma is regarded as the fourth state of matter, which is a blend of diverse active species such as atoms, molecules, ions, electrons, radicals, photons etc. (Kasoju et al., 2018). It can be generated by adding energy to a gas, then some of species leave their atom. These species change the physical and chemical structure of a biomaterial through interaction, leading to the change of wettability and then biological activities (Esmail et al., 2021; Kasoju et al., 2018; Martins et al., 2009; Recek et al., 2016). In fact, these plasma treatments are adding functional groups containing oxygen atoms (grafted ester, carboxyl, or carbonyl groups, for example) which significantly improves the bioactivity (Esmail et al., 2021). With the efficient results and nontoxic chemical outcomes, plasma treatment has long been widely used to modify the surface properties of biomaterials as seen in Figure 2.16.

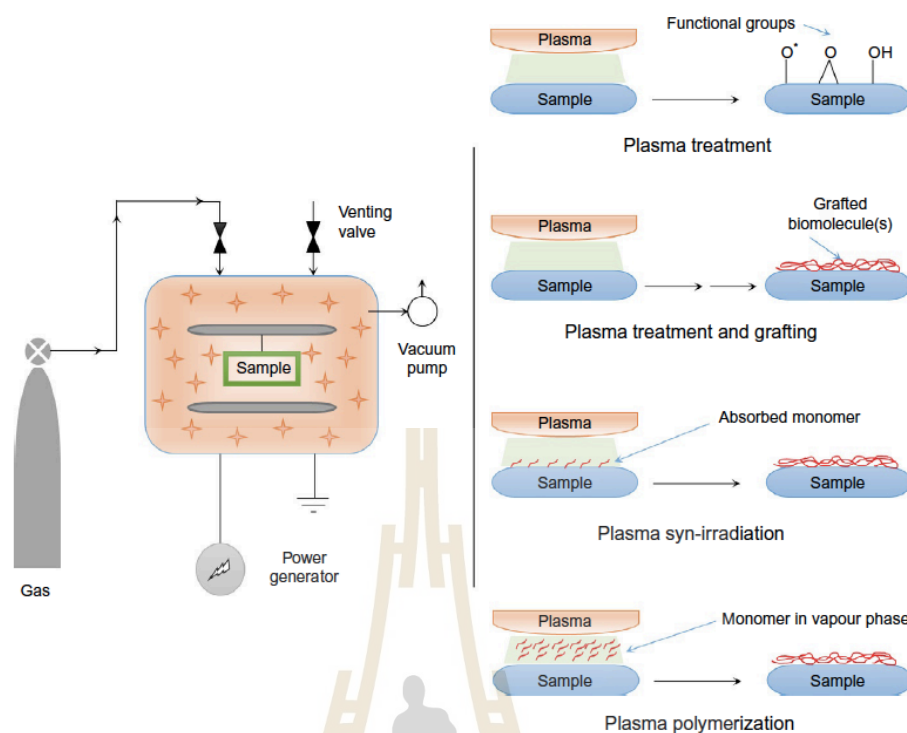


**Figure 2.16** A schematic illustration of typical plasma treatment used with many methods to change the surface properties (Kasoju et al., 2018).

Plasma treatment is applicable to materials of any size and shape and is not just restricted to flat materials (Kasoju et al., 2018). For instant, Esmail et al. (2021) discovered oxygen plasma treatment enable improving the hydrophilic property of the fibrous scaffolds based on poly(hydroxyalkanoates) and poly(3-hydroxybutyrate-co-3-hydroxyvalerate), which encouraged cell adhesion of HDFns cells on scaffolds. In other applications, Duangkanya, Kopwitthaya, Chanhorm, and Infahsaeng (2022) reported the success in the improvement of the hydrophilic property of poly(dimethylsiloxane) film by using oxygen plasma treatment for liquid lens applications. The wettability relates to the exposure time as seen in Figure 2.17. Apart from exposure time, the plasma treatment parameters, including plasma source and electric power, influent to the biological activities. PCL electrospun scaffolds were treated with different sources of plasma, exposure time, and electrical power. It was revealed the different morphology of L929 cells was observed on the scaffolds treated with  $O_2$  and Ar (Martins et al., 2009). Therefore, it is essential to apply the suitable conditions of plasma treatment to each material.



**Figure 2.17** The contact angle of glycerol droplet on the poly(dimethylsiloxane) film (a) without and with the oxygen plasma treatment using different exposure time that were (b) 6, (c) 12, (d) 18, and (e) 24 s (Duangkanya et al., 2022).

## 2.4 Summary

The first section of this chapter (Chapter 2.1) describes the electrospinning fundamental and the approach of 3D macrostructures. The electrospinning parameter enable providing various effects on the spinning process and fabrication of electrospun fiber as concluded in Table 2.1. It has emphasized the necessary of parameter effect on the process of electrospinning and the characteristic of electrospun fiber. Additionally, the overview of 3D macrostructure approach is given in Table 2.2. It has pointed out several processes and method of 3D macrostructure approach. Then the second section has explained about AM or 3D printing. All categories have been briefly presented; however, only the anatomy of delta printer based on FDM, which is another technique used in this work, has been detailed. Finally, the critical role of surface modification by using plasma treatment in this work has been demonstrated.

Some information and equations described in this chapter will be used and discussed in the further parts of thesis as set out below:

- Table 2.1 Chapter IV, V the effect of electrospinning parameters on 3D electrospun formations
- Equation 2.3 and 2.8 Chapter IV the simulation of electric field
- Figure 2.15 Chapter III the design and development of 3D electrospinning
- Equation 2.9 Chapter III the design and development of 3D electrospinning

## CHAPTER III

### METHODOLOGY

Four main steps will be undertaken to address the hypothesis of this work: (i) the design and development of 3D electrospinning setup, (ii) the study of electrospinning conditions which provide self-assembly, (iii) the buildup and control of 3D fibrous macrostructure, and (iv) the assessment of biological activities.

This chapter explains the experimental procedure for the design and assemble of 3D electrospinning setup, the buildup and characterization of 3D-fibrous macrostructures, and the protocol and characterization of bioactivities on the electrospun graft. The fundamental and procedure of characterizations with various techniques including SEM, SRXTM, XRD, FTIR, FT-Raman, SR-FTIR imaging, and electrical field simulation were also described in this chapter.

#### 3.1 3D Electrospinning

The hardware and firmware for a large number of 3D FDM printer models are currently open-sourced. The Rostock mini printer (Figure 3.1(a)) is one of the printers offered at <https://reprap.org/>, a community dedicated to creating self-replicating devices and making them publicly available for everyone's benefit. It was selected as the primary element that would be combined with electrospinning into the first 3D electrospinning prototype. A few parts of the Rostock mini were required to be adjusted in order to set up the 3D electrospinning used in this work. Since the filament and extruder were not used in the 3D electrospinning process, the extruder system, which includes the extruder, filament, fan, and hotend, were removed (Figure 3.1(b)) and replaced with the solution feed system, which consists of a spinneret with a syringe and a nozzle tip, and a syringe pump. Table 3.1 lists all of the parts and supplies needed to assemble 3D electrospinning. The printed components utilized in this project are displayed in Figure 3.2. The carriages were modified and endstop switch mount, belt end, tower end, nozzle holder, and collector holder were made

to be compatible with 3D electrospinning setup. The motor end, idler end, u-joint, jaws, and effector were borrowed from the Rostock mini model.

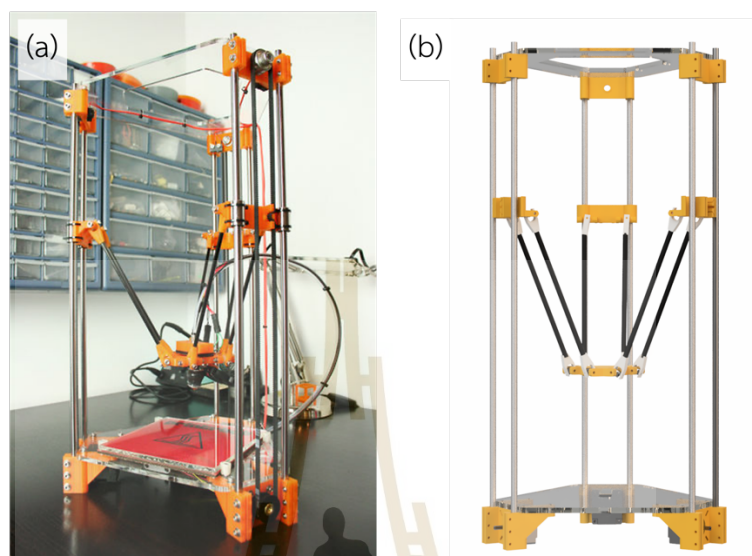


**Figure 3.1** (a) Rostock mini (from [https://reprap.org/wiki/Rostock\\_mini](https://reprap.org/wiki/Rostock_mini)) and (b) parts of Rostock mini chosen to use in the 3D electrospinning setup.

**Table 3.1** Components and supplies needed to assemble 3D electrospinning setup. Note \* is a new component that was created specifically for 3D electrospinning configuration in this work.

Items	Quantity(s)	Specification	Function
<i>Printed parts</i> (as shown in Figure 3.2)			
Motor end	3	All were made from	To holds components in place
Idler end	3	PLA and PET filament	To holds components in place
Carriage	3	by a 3D printer (Original Prusa i3).	To transport the movement to delta arms
U-joints	12		To connect carriages to delta arms
Jaws	12		and arms to an effector
Effector	1		To an appointment of delta arm
Endstop switch* mount	3		To hold the endstop switch
Belt end*	3		To prevent the belt falling from ball bearings

**Table 3.1** (Continued) Components and supplies needed to assemble 3D electrospinning setup.

Items	Quantity(s)	Specification	Function
Tower end*	3	All were made from	To cling to towers
Nozzle holder*	1	PLA and PET filament	To put a nozzle
Collector holder*	1	by the Prusa 3D printer.	To place collector
<i>Laser Cut Parts</i>			
Lower frame	1	Acrylic plates with	To serves as chassis on which
Upper frame	1	thickness of 6 mm.	components placed
Bed/Collector*	1	Copper plate with a diameter of 18 cm and a thickness of	To collect the coming and deposited fiber
<i>Electro-mechanical parts</i>			
Stepper motor	3	NEMA17s, 420N mm, 600rpm	To generate torque of the movement
Ball bearings	6	608ZZ	To support rotating belts
Linear bearings	6	LM8UU	To Carriage is mounted upon them and slides along a steel rod
Timing pulley	3	36tooth GT2 with pitch of 2 mm pitch and diameter of 12.5 diameter	To serve as an attachment point to transfer motion to the belt
Timing belt	3	GT2 timing belt with pitch of 2 mm and length of 976 mm	To transfer motor drive to move carriage along z, y, and x towers
Subminiature switch	3	LV8729 Endstop switch (Ramps based, Prusa)	To determine the highest point of towel, where the carriage can reach
Controller	1	RAMP 1.4 and Arduino	To direct the motion components based on commands sent from a computer and interprets input from the sensors
User interface and connectivity	1	LCD screen	To control the 3D electrospinning without a computer connection

**Table 3.1** (Continued) Components and supplies needed to assemble 3D electrospinning setup.

Items	Quantity(s)	Specification	Function
<i>Hardware</i>			
Delta arms	6	rigid carbon fiber tubes with outside diameter of 5 mm and length of 166 mm or as configured	To serve as a rail on which the carriage and effector
Towels	9	steel rod with diameter of 8 mm and length of 600 and 800 mm or as configured	To support rotating belts
Sheet cover on the steel	9	Flexible silicone sheet	To prevent fiber depositing to towels
<i>Electrospinning parts</i>			
Voltage*	1	A HV DC power supply (CY-DW-P503-1ACDF, Zhengzhou CY Scientific Instrument Co., Ltd., China) (50 kV of DC output voltage, 1 mA of output current)	To generate the different potential between a nozzle tip and a collector
Syringe*	1	20-ml NIPRO syringe or others which match with the syringe pump	To contain the solution
Nozzle*	1	20Gx1 ½”, NIPRO	To contain the solution
Delivery pipe*	1	polytetrafluoroethylene (PTFE) tube with inside diameter of 2 mm and an outside diameter of 4 mm	To transport the solution to the nozzle
Syringe Pump*	1	TE-331, Terumo, Terufusion	To control the flow rate of polymer solution

**Table 3.1** (Continued) Components and supplies needed to assemble 3D electrospinning setup.

Items	Quantity(s)	Specification	Function
Syringe-Teflon Connector*	1	a glass tube with an inside diameter of 4 mm, an outside diameter of 6 mm, and a length of 60 mm	To connect between a syringe and a PTFE tube

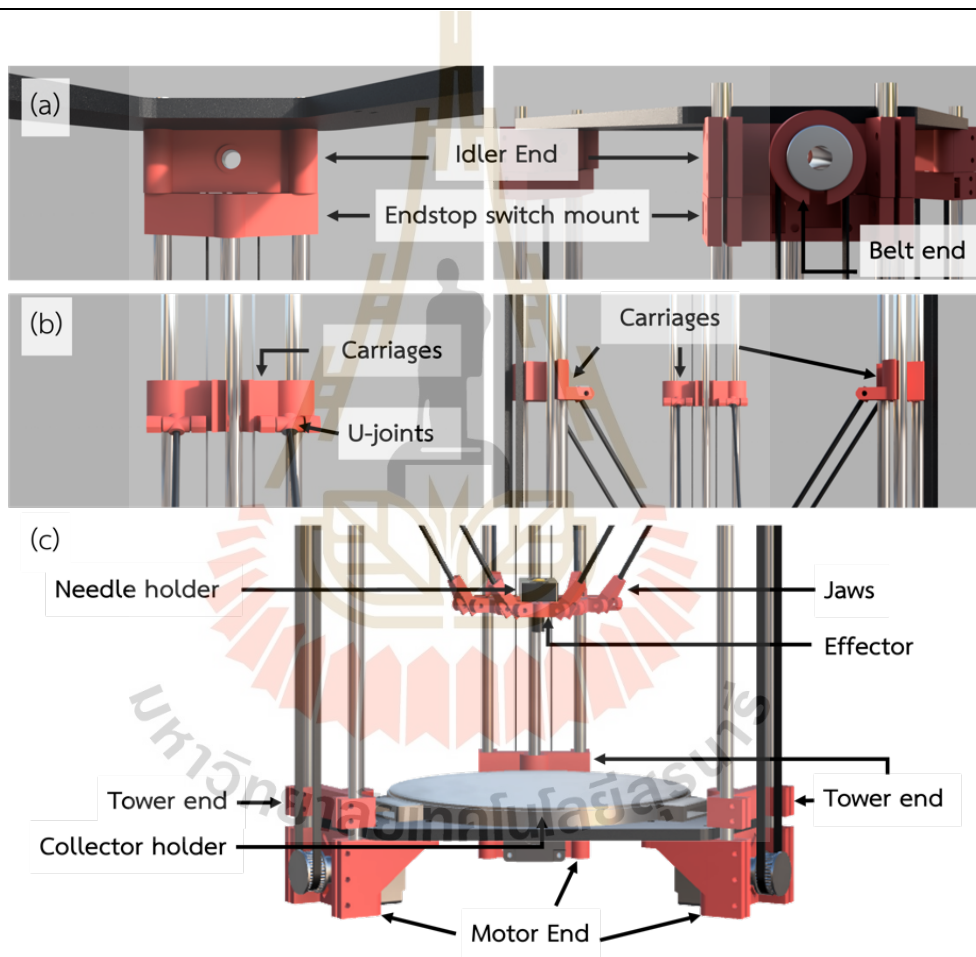


**Figure 3.2** Printed parts used in 3D electrospinning setup, including idler end, endstop switch mount, belt end, carriages, u-joints, nozzle holder, tower end, collector holder, motor end, effector, and jaws.

### 3.1.1 Electro-mechanical parts

On the ramps 1.4 board, the bed, hotend, endstop, motor drivers, motors, aux fan, and power supply are typically connected. Since the bed, hotend, and aux fan were not required for 3D electrospinning in this work, the connect on the ramps 1.4 board was made in accordance with the diagram shown in Figure 3.3. In case that connection and demand of the hotend and bed on the board and firmware cannot be ignored and adjusted on slicing software, their heating element were replaced with variable resistors in order to raise the required temperature of the hotend and bed.

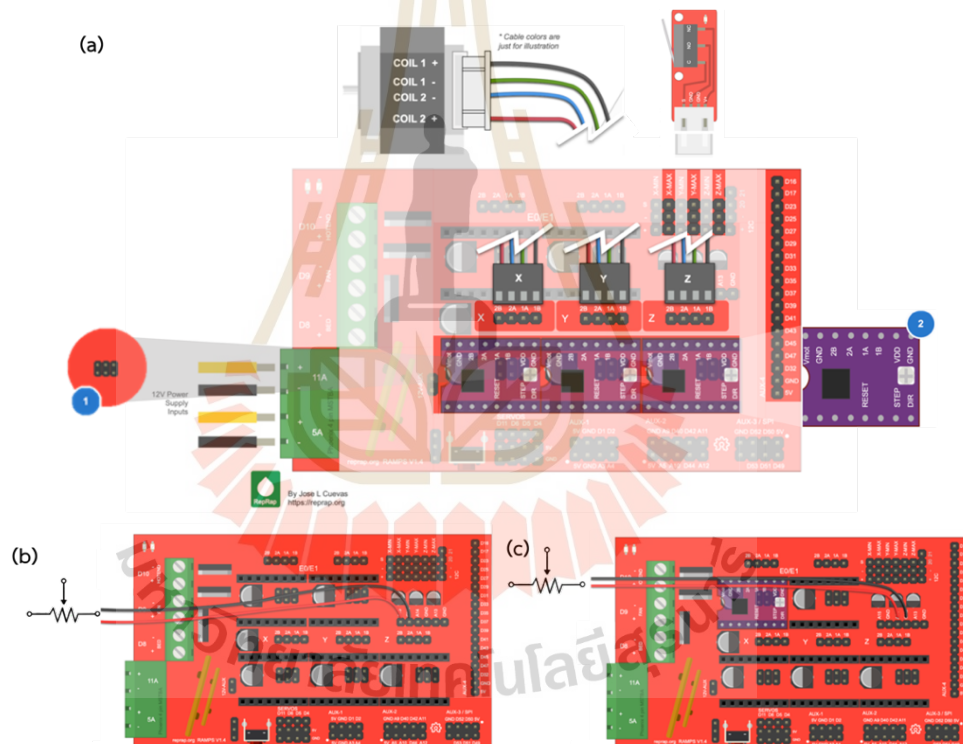


**Figure 3.3** Schematic diagram of Ramp 1.4 board used in 3D electrospinning setup: (a) the connect of motors, motor drivers endstop switch, and power supply on the board, (b) the connect of variable resistor instead of bed and hotend. (Adapted from [https://reprap.org/wiki/RAMPS\\_1.4](https://reprap.org/wiki/RAMPS_1.4)).

### 3.1.2 Design Calculation

The number of microsteps per millimeter were calculated. Using NEMA 17 motors, the formula to determine the moving mechanisms' steps per millimeter may be written as (Simons, Avegnon, and Addy, 2019)

$$\text{step (mm)} = \frac{\text{Mg x microstepping}}{\beta} \quad (3.1)$$

where **Mg** is microsteps of motor per turns,  $\beta$  is travel at one turn of the motor. The microsteps of motor per turns is given by  $\text{Mg} = \frac{360^\circ}{\text{degree step per turns}}$ . NEMA 17 stepper motors in this work have  $1.8^\circ$  per step. So, the corresponding steps/mm could be calculated by  $\text{Mg} = \frac{360^\circ}{1.8^\circ \text{ step per turn, microstepping}}$  in this work is 128 microsteps, and the travels of turns are given by

$$\beta = \text{Pitch of belt x Pulley Teeth} \quad (3.3)$$

which pitch of belt in this work = 2 mm, number of teeth of pulley in this work = 36. Herein, travels of turns in this work =  $2 \times 36 = 72$  mm. Since  $\text{step (mm)} = \frac{200 \times 128}{72} = 355.56$ , the required steps of the motor at every mm are 355 steps.

### 3.1.3 Firmware

Given the public accessibility of 3D printing, the firmware for the Rostock mini is also accessible. In this work, firmware from Repetier which is generated via <https://www.repetier.com/firmware/v092/> was utilized. Equation (2.9) indicates that the firmware was modified to be compatible with 3D electrospinning setup. The modification was executed only in configuration.h such as X\_AXIS\_STEPS\_PER\_MM, X\_MAX\_LENGTH, DELTA\_DIAGONAL\_ROD and others.

## 3.2 3D fibrous macrostructures

In order to investigate the conditions of self-assembly and the formation of 3D electrospun macrostructures, this section is partitioned into the subsequent two segments: (i) the self-assembly of an 3D electrospun stack in the absence of nozzle movement was explored; and (ii) the ability to create and control 3D fibrous macrostructures by 3D electrospinning was evaluated.

PCL ( $M_n = 80,000 \text{ kg mol}^{-1}$ ), PVDF ( $M_w = \sim 534,000$ ), and PAN ( $M_w = 150,000$ ), and DMF ( $\geq 99.9\%$  purity) were purchased from Sigma-Aldrich (United Kingdom).

Acetone (99.5%) was bought from ACI Labscan. Orthophosphoric acid ( $\text{H}_3\text{PO}_4$ ) (85% solution in  $\text{H}_2\text{O}$ ) and DCM (greater than 99.5% purity) were both acquired from Loba Chemie, India. The chemicals were used without further purification.

### **3.2.1 The self-assembly of electrospun fibers**

To study the self-assembly of electrospun fibers, PCL pellet PVDF pellet, and PAN powder were prepared by dissolving in the DCM:DMF solvent, the AC:DMF solvent, and DMF solvent, respectively, without and with the addition of  $\text{H}_3\text{PO}_4$  additives. The solution was carried out by varying electrospinning parameters including a flow rate of 1-10 ml/h, a tip-to-collector distance in a range of 5-10 cm, and voltage in a range of 10-20 kV at ambient environment.

### **3.2.2 The buildup and control of 3D fibrous macrostructures**

The PCL solutions prepared in the mixture solvent of DCM:DMF were chosen to investigate the effect of solution and electrospinning on the buildup of 3D-fibrous macrostructures.

#### **3.2.2.1 The study of solution preparation on the buildup of 3D fibrous macrostructures**

PCL solutions were prepared by mixing PCL pellets with a blended solvent that contained DCM, DMF, and  $\text{H}_3\text{PO}_4$  additives, then stirring the mixture for 24 hours under ambient conditions. The solvent was prepared by various ratios of DCM:DMF that were 4:1, 6:1, and 8:1 and then added with  $\text{H}_3\text{PO}_4$  additives by stirring for at least 10 minutes. The PCL was then added to the prepared solvent as follows: 10 wt%, 12 wt%, and 14 wt%. The PCL solutions were prepared with the same amount throughout all experiments, and all solutions were rested overnight before being used to spin fibrous structures via 3D electrospinning. The different conditions of solution preparation, including PCL concentration, solvent ratio, and  $\text{H}_3\text{PO}_4$  additives, were used to investigate the 3D fibrous formation with a variety of flow rates, which were 2, 4, and 6 ml/h at 6 cm of the initial distance and under 16 kV of HV, as

summarized in Table 3.2. Each electrospinning experiment was carried out for 30 minutes.

**Table 3.2** Summary of all solution preparations investigated to form 3D fibrous structures with flow rates of 2, 4, and 6 ml/h at an initial distance of 6 cm and under an applied voltage of 16 kV via 3D electrospinning.

Parameters	Unit	Variable values
PCL concentration	wt%	10, 12, 14
Solvent (DCM:DMF)	mixture By weight	4:1, 6:1, 8:1
H <sub>3</sub> PO <sub>4</sub>	By weight compared to PCL weight	0, 5, 10, 15, 20

### 3.2.2.2 The study of electrospinning process on the buildup of 3D-fibrous macrostructures

To study electrospinning process on the buildup and control of 3D fibrous macrostructures, the optimal condition of solution preparation was tested with a variety of electrospinning process. A model used to investigate the building of 3D-fibrous macrostructures was a hollow cylinder with a diameter of 60 mm. The model file was sliced by a fixed layer height and a perimeter of 0.4 mm and 1 to gain a motion pattern on a gcode file. The 3D-electrospun structures were tested by varying flow rates, initial distances, voltages, and nozzle moving speeds, as summarized in Table 3.3. The flow rate of the solution and the voltage applied to the nozzle were separately controlled through the syringe pump and the HV source. All experiments were taken between 30-35°C, and the relative humidity was imposed between 40% and 50%. Each experiment ran for 30 minutes, similar to the solution experiment.

**Table 3.3** Summary of all spinning parameters used to form 3D fibrous macrostructures using PCL solution via 3D electrospinning.

Parameters	Unit	Variable values
Flow rate	ml/h	2, 3, 4, 5, 6
Initial distance	cm	2, 3, 4, 5, 6
HV power supply	kV	12, 13, 14, 15, 16
Nozzle speed	mm/s	1, 2, 3, 4, 5

### 3.3 *In vitro* cell culture on the fibrous graft

To assess the biocompatible abilities of the 3D electrospun graft, *in vitro* cell culture of fibroblast and osteoblast were executed. The protocol of *in vitro* cell culture depends on the purpose of study and characterization. It will be detailed below in the section of plasma treatment, SRXTM, and SR-FTIR imaging.

Fibroblast (NIH3T3) and osteoblast cells used for *in vitro* cell assays were purchased from the American Type Culture Collection (ATCC) (Manassas, VA, USA). Dulbecco's modified eagle medium (DMEM), McCoy's, fetal bovine serum (FBS), penicillin/streptomycin (P/S), 0.25% Trypsin-EDTA, and 10X PBS solution were purchased from Gibco (Waltham, MA, USA). Glutaraldehyde 25% in aqueous solution and osmium tetroxide 2% in aqueous solution ( $\text{OsO}_4$ ) were obtained from Electron Microscopy Sciences and Thermo Fisher Scientific (USA), respectively.

### 3.4 Characterization Techniques

Self-assembled fibers and 3D electrospun macrostructures were investigated with various techniques to study their physical, chemical, and biological properties. Characterization techniques will be detailed in this section, including a digital camera, conductivity, XRD, FTIR spectroscopy, Raman spectroscopy, SEM, SRXTM, and SR-FTIR. Additionally, the electrical field simulation used in this work will be provided.

#### 3.4.1 Digital Camera

The conditions presenting when 3D electrospun macrostructures grow are essential. It is useful to comprehend the parameters that influence the formation of

3D macrostructures using 3D electrospinning. It is also necessary to capture the final shape of the 3D electrospun macrostructures in both top and side perspectives. A standard digital camera can be used for this purpose. Consequently, movies are made during each electrospinning operation and a snapshot is taken at the end of each procedure using a digital camera.

### 3.4.2 Conductivity

The flow of charge in response to an electric field is known as electrical conductivity. It is the term used to describe the movement of charge, or current, in solid conductors such as metals and semiconductors, which is attributed to electrons or holes. Because of the transport of ionic charge, ionic conductivity is equivalent to electrical conductivity (Balaji T and Choudhury, 2022; Owen, 1989).

Basically, the two electrodes of the probe can be used to measure the conductance of a solution by applying an alternating electrical current to them. While this electrical current is being supplied to the solution, the anions—ionized ions with a negative charge—move toward the positive electrode and the cations—ionized ions with a positive charge—move toward the negative electrode. The solution becomes conductive as a result of the motion ability of ionic charge.

A Mettler Seven Compact Duo S213 pH/conductivity benchtop meter at SLRI was used in this work to measure the conductivity of solutions. The instrument was calibrated using standard solutions prior to the readings. Each specimen, which was a fresh solution without any purification, was tested three times, with all measurements being conducted at room temperature.

### 3.4.3 X-ray Diffraction

XRD is frequently used to examine structural characteristics and identify the phases of a polymer (Shepelin et al., 2019). In short, if the wavelength and the periodicity of the crystals are of identical magnitude, it is based on the diffraction of X-rays caused by the interaction of waves with periodic atomic planes (Stanjek and Häusler, 2004). X-ray photons can interact with matter in a number of interactions, including the absorption and, scattering effect, and dispersion of energy. Between the

photons and electrons surrounding the atom, there is a coherent scattering also called Rayleigh scattering. Owing to the periodicity of crystalline structures, scattered radiation will result, leading to characteristic diffraction phenomena which is able to be studied to investigate the crystal structure of materials (Epp, 2016; Stanjek and Häusler, 2004). Figure 3.4 illustrates the diffraction, which had been given by W.L. Bragg. A constructive interference and subsequently the so-called Bragg's law are obtained as follows Equation (3.2), when the route of the wavelet scattered off the lower plane is longer by an integer number of wavelengths ( $\lambda$ ) than the travel of the wavelet scattered off the upper plane.

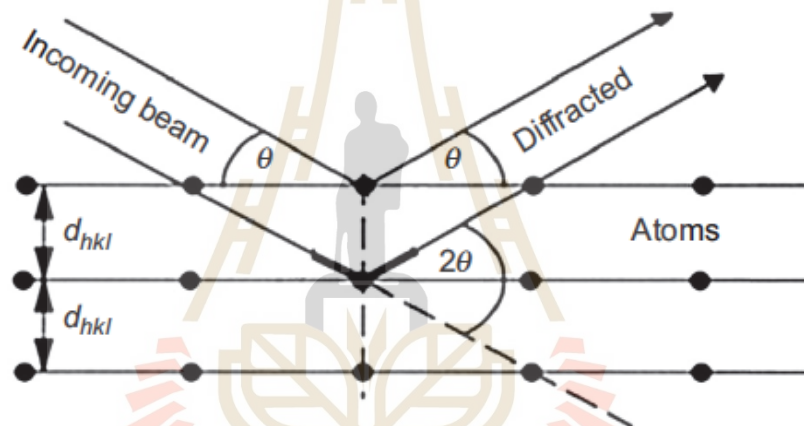


Figure 3.4 Geometrical diffraction from lattice planes (Epp, 2016).

$$n\lambda = 2d_{hkl} \sin \theta \quad (3.2)$$

where  $n$  is the order of diffraction,  $\lambda$  is the wavelength of the incident beam,  $d_{hkl}$  is the lattice spacing, and  $\theta$  is the angle of the diffracted beam in degree.

XRD analysis was used to investigate the microstructures of electrospun fiber through the drive-force of self-assembly fabrication via electrospinning and the incorporation of  $H_3PO_4$  in polymer solution on polymer electrospun fiber. XRD pattern of PCL, PVDF, and PAN in form of raw materials, including powder or pellet, and electrospun fiber, including 2D mat and 3D stack, was recorded using a Bruker diffractometer (Bruker D8 ADVANCE at the center for scientific and technological

equipment in Suranaree University of Technology) with Cu K $\alpha$  radiation ( $\lambda = 1.54 \text{ \AA}$ ) at scanning rate of 2 step per second and  $0.2^\circ/\text{step}$  in the  $2\theta$  range of  $10^\circ\text{--}40^\circ$ .

### 3.4.4 Fourier transform infrared and Raman spectroscopy

FTIR and Raman are vibrational spectroscopies in combination with microscopy techniques. It based on the interaction of specimen with light which can case vibrational transitions in the excited molecules as shown in Figure 3.5. FTIR spectra are primarily obtained directly by measuring the amount of infrared (IR) light absorbed by a specimen, which selectively absorb specific frequencies and energies of infrared radiation that passes through or is reflected off a sample (Undavalli, Ling, and Khandelwal, 2021; Wellner, 2013). Raman spectroscopy employs the Raman effect, which refers to changes in the wavelength of visible light (400–1100 nm) that is scattered inelastically, and these changes correlate to the vibrational transitions in the mid- and far infrared regions (Urban, 1993).

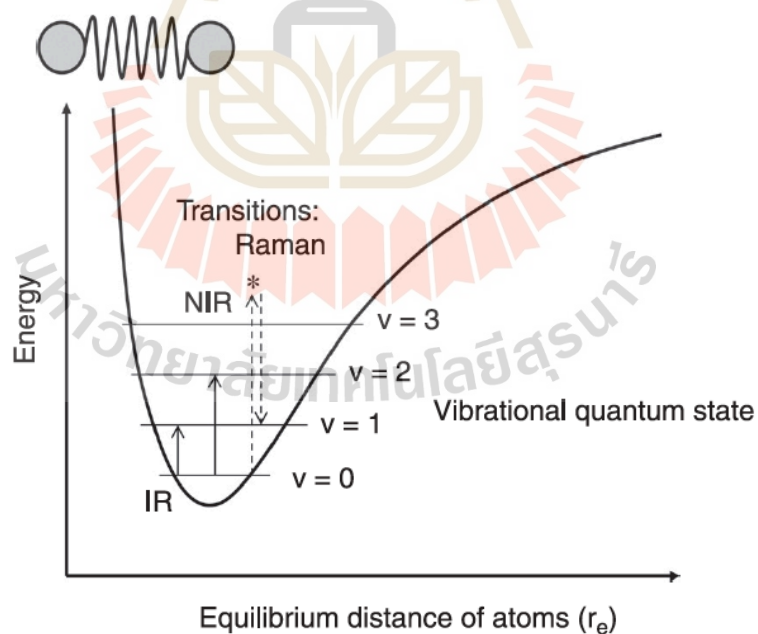


**Figure 3.5** Schematic illustration of the vibrational function and the energy level transitions measured by infrared (IR), near infrared, and Raman spectroscopy (Wellner, 2013).

In this study, the FTIR and Raman spectra of 2D mat and 3D stack based on PCL, PVDF, and PAN was investigated if the addition of  $H_3PO_4$  that resulted in the 3D build-up had any notable effects on the chemical interaction between the polymer and additives. Using FTIR and Raman spectrometers at the center for scientific and technological equipment in Suranaree University of Technology (Bruker IR spectrometer (tensor 27) linked to an IR microscope (Hyperion 3000), the spectra of PCL, PVDF, and PAN in the forms of powder/pellet, 2D mat, and 3D stack were examined. The spectra were acquired by 64 scans at a spectral resolution of  $4\text{ cm}^{-1}$  and subjected to ATR mode analysis within a scan range of  $4000$  to  $400\text{ cm}^{-1}$ . For the measurement, an average of three scans is obtained for every sample and OPUS 7.5 software was used to process the FTIR and Raman spectrum.

#### 3.4.5 Scanning Electron Microscopy

SEM is an electron microscopy technique that enable providing a detailed visual image with high-quality and spatial resolution (Akhtar, Khan, Khan, and Asiri, 2018). The creation of images in the SEM relies on the collection of signals generated by the interaction between the electron beam and the material (Zhou, Apkarian, Wang, and Joy, 2007). Briefly, it operates by utilizing primary electrons emitted from a source to energize the atomic electrons of the specimen. This energy transfer causes the release of incoming electrons, such as secondary electrons, backscattered electrons, photons (X-rays used for elemental analysis) and visible light (cathodoluminescence), which can be collected from each point of the specimen to form an image. SEM can so offer several qualitative details about the specimen, including as its topography, morphology, composition, and crystallographic information (Akhtar et al., 2018; Zhou et al., 2007).

In this work, SEM instruments and gold coaters at the center for scientific and technological equipment in Suranaree University of Technology were used to observe the morphology of 3D electrospun macrostructures and cells on the surface of electrospun fibers as following:

To observe the morphology of electrospun structures, the specimen preparation will be divided into 2 types: (i) the specimen considered as a 2D mat, a

specimen was cut and fixed on the SEM stub by a sticky carbon tape, and (ii) in the case of 3D electrospun macrostructures, containing enormous electrospun fibers with various scales of micro and nano diameter, a specimen will be cut from the upper, middle, and bottom parts of the 3D electrospun structure to observe the morphology on each part and then fixed on the SEM stub by a sticky carbon tape. Due to the height and fluffy texture of electrospun structures, drying sliver paint was used to ground whole structures in contact with the stub, which reduces the charging problem and helps in getting a good image. The specimen was coated with gold for 3 minutes (Gold (Au) Sputter Coater, Neo Coater/MP-19020NCTR). The mounted specimen was loaded into a SEM (SEM-EDS-JEOL/JSM-6010LV), and then photos were taken from three random areas on each specimen. Each area of the photo was separated into 3x3 regions, and 5 random fibers on each region were measured by Image J software. To conclude, the average diameter was measured with 45 fibers randomly selected from three areas of the specimen.

To observe the morphology of cells and cells on the electrospun fibers, a SEM instrument (FESEM-FIB/EDS - Carl Zeiss/AURIGA) was used in this work. After the cell culture fixation and dehydration, which are detailed in *in vitro* cell culture, the specimen will be paced on the stub without any cuts and coated by using gold sputter coating equipment (Sputter Coater, Leica/EM ACE600) prior to loading the specimen into the SEM instrument.

#### 3.4.6 Plasma Treatment

As mentioned in Chapter II, the hydrophilic property demands on the *in vitro* cell culture. The plasma treatment was chosen to improve the hydrophilic properties of 3D PCL fibrous macrostructures. The treatment was performed by using a plasma generator (Surface Technology HF Generators 200 W, Diener Electronics, Germany) at the SLRI in Thailand. O<sub>2</sub> gas was chosen to generate the plasma. The chamber was filled with gas prior to the treatment. The power intensity, including 10W, 30W, 50W, and 70W, was applied for 5 minutes to investigate the bioactivity of the surface modification. The pressure of the plasma chamber was kept at 0.2 mbar in all conditions by controlling the gas flow.

The untreated and plasma-treated scaffolds were prepared as 5x5 mm<sup>2</sup> scaffolds for the biological assays. The glass slide and untreated and plasma-treated scaffolds were placed in a 12-well plate (Costar, Corning, USA). The samples were sterilized under ultraviolet light for 30 minutes. Then, all were washed with cell culture media for 1 hour and further soaked in the media overnight to tune the environment onto 3D scaffolds.  $2 \times 10^4$  fibroblast NIH3T3 cells were added to the control, which was a glass slide, and all scaffolds. The media, containing DMEM, 10% FBS, and 1% P/S, were added 1 ml/well and were not changed during the 3-day culture at 37 °C with 5% humidified CO<sub>2</sub>. To assess the cell adhesion and morphology, after 3 days of cell culture, the control and scaffolds were washed twice with 1 ml of 1X PBS and then fixed with 2.5% glutaraldehyde (1 ml/well) in PBS for 2 hours at room temperature. All samples were further washed twice with 1X PBS for 10 minutes before dehydrating through a series of ethanol solutions, including 30%, 50%, 75%, and 99%, for 5 minutes. Prior to SEM examination, the dehydrated samples were kept overnight before being coated with gold sputter coating equipment (Sputter Coater, Leica/EM ACE600). SEM (FESEM-FIB/EDS-Carl Zeiss/AURIGA) was used to observe the cell adhesion and morphology. The optimized plasma condition was used to prepare scaffolds for further observation of cell morphology and adhesion with the SRXTM technique.

#### **3.4.7 Synchrotron Radiation X-ray Tomographic Microscopy**

Since SEM is mostly utilized for surface imaging of materials and does not provide any interior information (Akhtar et al., 2018), to study biological activity on an in-depth electrospun graft, the SRXTM was used to observe inside the graft. SRXTM is a powerful non-destructive technique that offers extremely high-resolution, three-dimensional insights into the internal structure for investigation and visualization (Gai and Palasiatica, 2018; Motchurova-Dekova and A.T, 2010). Briefly, it employs the differences of X-ray absorption on the density of internal structures, which allow to produce an X-ray image with positioned internal features (Landis and Keane, 2010).

The 3D-electrospun structure with the plasma treatment of 50W was prepared as 5x5 mm<sup>2</sup> to use as scaffolds in the biological assays. The glass slide (a cell control) and plasma-treated scaffolds were placed in the 12-well plates and sterilized as per

the mentioned protocol.  $2 \times 10^4$  fibroblast NIH3T3 cells were seeded on the glass slide and plasma-treated scaffolds. A plasma-treated scaffold was also put in the plates without seeded cells (used as a fiber control). The media was added into each well as 1 ml. After 1 and 3 days of culture, the controls and scaffolds were washed with the PBS solution and fixed with glutaraldehyde, as per the protocol mentioned. After the fixation, the samples were stained with a 1% osmium oxide solution for 4 hours before washing with the PBS solution and dehydration. Each sample was cut to prepare a suitable size for a 3.0 mm-diameter Kapton tube, and the tube was glued onto a pin holder.

SRXTM was used to observe a cell distribution inside fibrous scaffolds that can imply the visualization of cell migration and measure the normalization of cell volume between samples cultured for 1 and 3 days. The experiment was executed at a SRXTM beamline (BL 1.2 W: X-ray imaging and tomographic microscopy) at the SLRI in Thailand. The synchrotron radiation originated from a 2.2 Tesla multipole wiggler at the 1.2 GeV Siam Photon Source. By using a filtered polychromatic X-ray beam, the experiments were executed at a mean energy of 14 keV with a 32-m distance from source to sample. All tomographic scans with the pco.edge 5.5 detector at 5x total magnification were performed. The field of view was 3.70 mm x 3.12 mm with a pixel size of 1.44  $\mu\text{m}$ . Each sample prepared for the holder was mounted on a rotary stage. Then, a total of 2001 X-ray radiographs were obtained from  $0^\circ$  to  $180^\circ$  with an angular increment of  $0.1^\circ$ . The obtained radiographs were normalized by flat-field correction with open-beam and dark images and then reconstructed using Octopus Reconstruction software (TESCAN, Gent, Belgium) (Vlassenbroeck et al., 2006). After obtaining the reconstruction images, the 3D dataset was converted from 16-bit tiff images into 8-bit images using ImageJ software. The image processing was computed using Drishti software (Ajay, 2012). The Kapton tube seen around the scaffold material was cropped out to reduce the size of the data. The difference between the intensity of the stained cell and the polymer was used to identify cells and scaffolds. Both the original PCL fibers and the fiber control were investigated by using SRXTM with the same protocol. In addition, the measurement function of volume was used to measure the volume of the fiber and cell. Since the number of fibers was different on

electrospun scaffolds, the normalized volume of cells was calculated by comparing them with the volume of fiber.

### 3.4.8 Synchrotron Radiation Fourier transform infrared imaging

An FT-IR image is a type of chemical image created by an FT-IR microscope. Chemical images combine the digital topographical data of a sample obtained with a microscope with chemical information obtained through spectroscopy (Abadi et al., 2022). This allows us to visualize the chemical composition of a sample.

To study cell distribution on electrospun structure, SR-FTIR was utilized to track cells and electrospun fiber to create mapping based on their components. Since the SRFTIR imaging requires thickness below 7  $\mu\text{m}$ , there were two methods of sample preparation used in this work as follows:

(i) 3D PCL-based electrospun structures were required to cross section. A cryo-section was chosen to cut the electrospun graft. Tissue-Tek O.C.T. Compound (by Sakura) was added to cover the electrospun grafts placed on a substrate (Figure 3.6) and kept at  $-4\text{ }^{\circ}\text{C}$  overnight to fix the grafts on the substrate while maintaining their structure. The samples were cross sectioned to obtain a thickness in a range of 4-6  $\mu\text{m}$  using a *Cryostat* microtome (AMOS/AST500) at the center for scientific and technological equipment in Suranaree University of Technology.



Figure 3.6 Cryo-section of electrospun grafts using a Cryostat microtome.

(ii) The electrospun fiber was directly prepared on a barium fluoride ( $\text{BaF}_2$ ) window with a size of  $13 \times 1 \text{ mm}^2$  (CRYSTRAN, United Kingdom) as shown in Figure 3.7. The cryosection was not needed in this alternative. 10% wt PLA solution prepared in chloroform. The PLA-based fibers were electrospun for 3 minutes under the electrospinning conditions at the flow rate of 1 ml/h, the tip-to-collector distance of 6 cm, the voltage of 16 kV and directly deposited on the window. Before doing the in vitro cell culture, the window (control) and electrospun fiber on the window (samples) were cleaned via UV sterilization for 30 minutes and soaking in medium for 24 hours.  $4 \times 10^5$  NIH3T3 cells were seeded on the surface of control and samples and cultivated for 24 hours. After the cell culture, the control and samples were fixed by 2.5% glutaraldehyde for 2 hours and washed using DI water three time and 0.9% NaCl w/v, respectively.

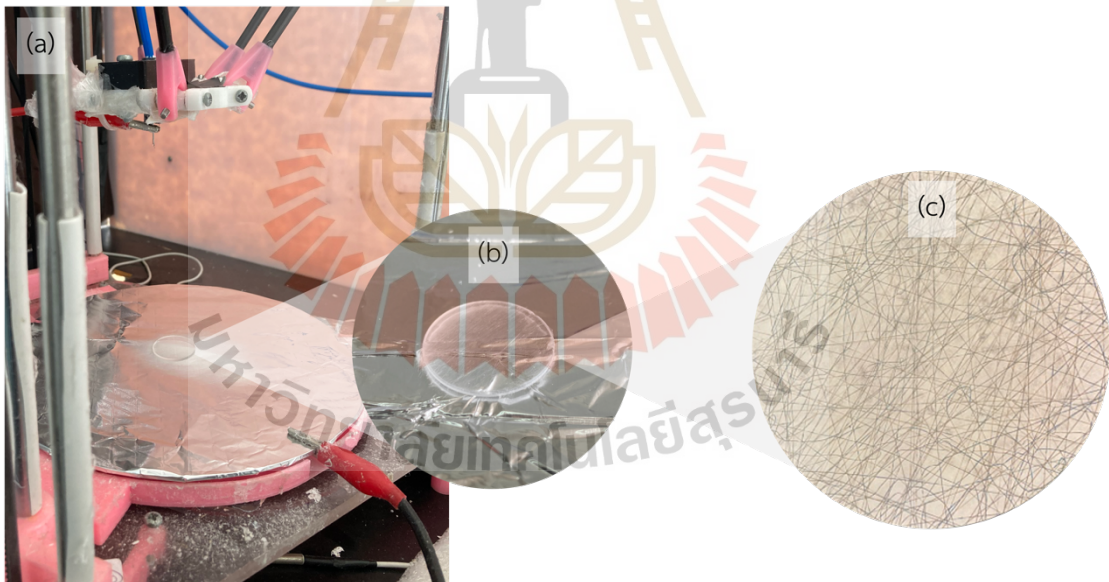


**Figure 3.7** (a) Electrospinning process of PLA fibers at the flow rate of 1 ml/h, the tip-to-collector distance of 6 cm, the voltage of 16 kV, (b) PLA electrospun fiber on the  $\text{BaF}_2$  window, and (c) photography of PCL fiber obtained by optical microscopy.

The window consisting of electrospun fibers was placed in the 12-well plate and subsequently sterilized using the following steps: 30-minute UV light cleaning, 1-hour media washing, and overnight media soaking for environmental adjustment. A

glass slide was employed as a control to assess and contrast the cellular structure on electrospun fibers. NIH3T3 cells were cultured on the electrospun fibers at a density of  $4 \times 10^5$  cells per sample and incubated for 24 hours. Following a 24-hour period, the cells on the glass slide and electrospun fibers were rinsed with a PBS solution and then fixed with 2.5% glutaraldehyde for 2 hours. Subsequently, the glass slide and electrospun fibers underwent a series of washing steps. First, they were rinsed with DI water. Following this, they were washed three times with a 0.9%w/v NaCl solution, and another round of DI water washing was performed to eliminate any remaining salts. Finally, the samples were subjected to overnight vacuum drying. Prior to commencing SR-FTIR microspectroscopy, the samples were stored in a desiccator. The samples were then subjected to analysis using the SR-FTIR technique and subsequently observed using SEM.

The SR-FTIR measurements were conducted at an infrared microspectroscopy beamline (BL4.1 IR Spectroscopy and Imaging) at the Synchrotron Light Research Institute. The spectra data was obtained using a Vertex 70 spectrometer (Bruker Optics, Ettlingen, Germany) that was connected to an IR microscope (Hyperion 2000, Bruker Optics, Ettlingen, Germany). The microscope was equipped with a nitrogen-cooled MCT (HgCdTe) detector. It was also connected to a software-controlled microscope stage and placed in a specially designed box that was purged by dry air (Thumanu et al., 2017). The spectral acquisition was conducted using attenuated total reflectance mode in mapping mode. It was collected by 64 scans with an aperture size of  $20 \mu\text{m} \times 20 \mu\text{m}$ , covering an area of  $200 \times 200 \mu\text{m}^2$  (Figure 2(a)) for each replication. The spectra resolution was set at  $6 \text{ cm}^{-1}$ , covering the range of  $600\text{--}4000 \text{ cm}^{-1}$ . Every sample was examined by selecting three random areas for replication. The process of obtaining spectral data and controlling the instrument was carried out using OPUS 7.5 software (Bruker Optics Ltd, Ettlingen, Germany).

The SR-FTIR spectra were applied with water compensation, concave rubberband baseline correction, and vector normalization on the OPUS before performing data processing on the Cytospec. The data processing for image analysis was based on prior research (Sunthornvarabhas et al., 2014). In short, the spectra were constructed and analyzed using Cytospec 1.3.4 (Cytospec Inc., NY, USA).

The spectra were transformed into the second derivative by applying a smoothing process with 13 points. In addition, the spectra were normalized using a vector normalization to account for differences in sample thickness. The image construction was executed utilizing the univariate mode, which produces output based on peak intensity, peak area, or peak ratio to generate chemical maps or function group maps. The hierarchical clustering analysis (HCA) was then conducted using the D-values method for distance matrix calculation with a cluster number of 3 to differentiate the components of the cell and PLA on the structures. The spectral ranges of 1682-1610 and 1785-1713  $\text{cm}^{-1}$  were used to represent the cell and PLA fiber corresponding to the amide I band of NIH3T3 cells and the C=O stretching of PLA, respectively. The chemical images of all samples were acquired from SR-FTIR mapping at  $20 \times 20 \mu\text{m}^2$ . The individual 2D cluster maps were recorded as an image file, with each cluster being assigned a unique color (Figure 3.8(b, c)). The HCA spectra (Figure 3.8(b)) were conducted by integrating the area of cell and PLA using a B type of integration method in OPUS. According to Figure 3.8(d), a cluster index for each color was obtained by dividing the integrated area of the cell over the PLA components. In order to evaluate the distribution of cells on electrospun fibers, the cluster index was multiplied by the corresponding number of color grids and then divided by the total number of grids to obtain a normalized value. Subsequently, the data was aggregated across all replicates to calculate an average and a standard deviation for each condition to obtain a quantitative material distribution index (**Qn**) and **Qn deviation** (Sunthornvarabhas et al., 2014). The variability of cell distribution on the sample was assessed by a qualitative material distribution index (**QI**) following a below equation (Sunthornvarabhas et al., 2014). The equation is based on the equation of the coefficient of variation (Shechtman, 2013).

$$QI = \frac{100 \times Qn \text{ deviation}}{Qn}$$

According to the equation, the high **QI** value indicates poor distribution because it is relative the standard deviation of component ratios (Sunthornvarabhas et al., 2014), referring to nonuniform distribution of cells on the nanofiber.

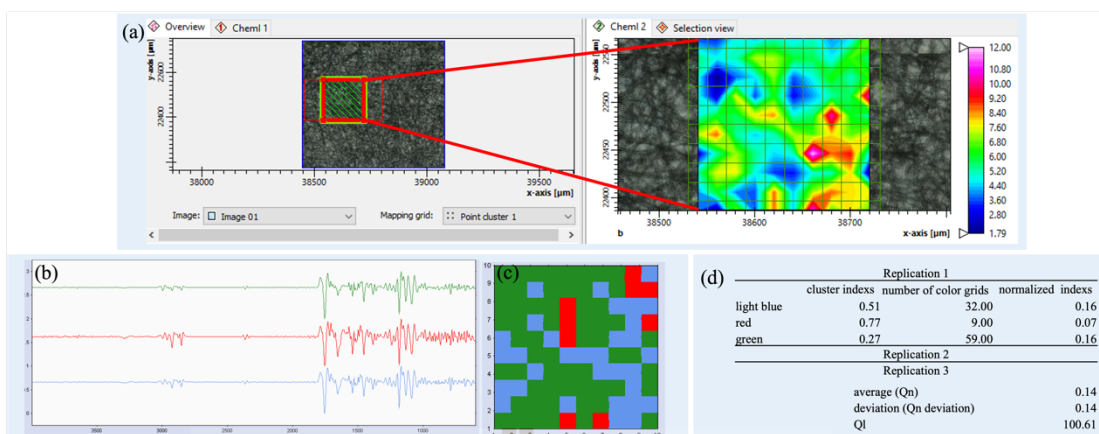


**Figure 3.8** Example of data processing, including (a) a specific region chosen for analysis and mapping using SR-FTIR in the range of  $1682\text{-}1610\text{ cm}^{-1}$ , (b) derivative spectra, (c) a hierarchical cluster map, and (d) an analytical method.

### 3.4.9 Electric field simulation

The electric field simulation was run on CST Studio (Nanospectroscopy Laboratory, Thailand Center of Excellence in Physics, Suranaree University of Technology). The electric field simulation was simulated based on real scale of 3D electrospinning as shown in Figure 3.9. There are three components as summarized in Table 3.4 that are a nozzle, a collector, and a chamber. The CAD file of a nozzle was selected from McMaster Carr (McMaster Carr, Elmhurst, IL, USA). According to McMaster Carr, the nozzle's nozzle is made of stainless steel, while the nozzle's base is composed of polypropylene (Morehouse, Ireland, and Saha, 2023). A collector was modeled using Fusion360 and a chamber was generated using the CST software. Each component was assigned its constituent material in CST studio. It allows for nozzle to be connected to the voltage of 16 kV and for the collector to be grounded without the wires. It should be noted that nozzle and collector were determined as perfect electric conductor.

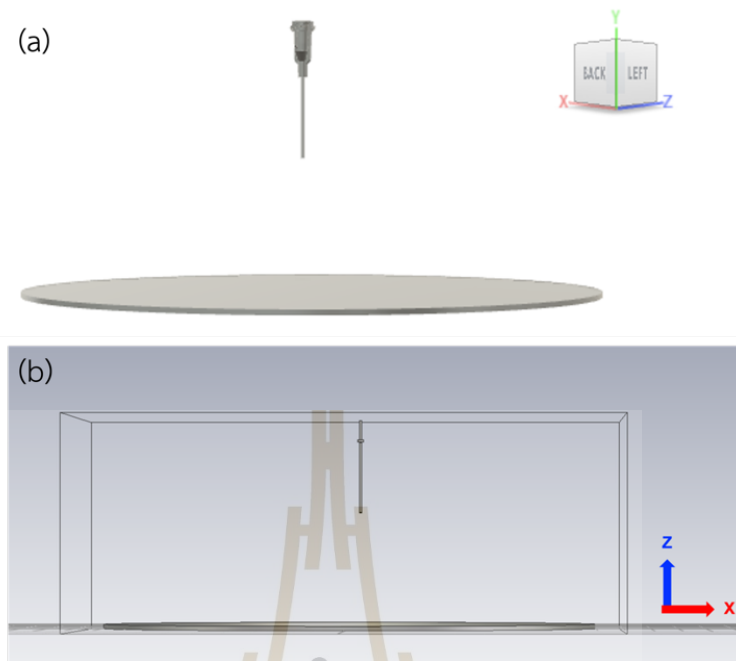


**Figure 3.9** The configuration of a nozzle and a collector based on the actual scale of 3D electrospinning setup: (a) a 20G nozzle positioned 4 cm from a collector and at the collector's center as modeled in Fusion360 and (b) the configuration on CST studio.

**Table 3.4** Electrospinning setup measurement for electric field simulation.

Components	Measurement
Collector plate diameter	180 mm
Collector plate thickness	1.6 mm
Nozzle length	2 cm
Nozzle size	20 Gauge (outer diameter of 0.908 mm)
Chamber width and length	-10 mm to 10 mm

In order to run a simulation in CST studio, mesh type was set as tetrahedral structure with accuracy of  $1 \times 10^{-12}$ . The region in chamber was defined as being filled with air. The electric field simulation was executed to study the change of electric field on the change initial distance and position of X and Y following as the model used to build up and control 3D fibrous macrostructures.

## CHAPTER IV

### RESULTS AND DISCUSSION

This chapter presents the experimental results and discussion. It is structured as follows:

- The first part will present and discuss about the design and development of 3D electrospinning setup based on the combination of the delta printer and electrospinning which include the comparative results of the electrospinning processes that were carried out using different coordinate systems in the 3D electrospinning setup (cartesian and delta coordinates), the development of 3D electrospinning prototype in this work, and 3D electrospinning troubleshooting. The last version of 3D electrospinning will be detailed and used in this work.

- The second part will present the electrospinning condition which induced self-assembly and allowed the formation of 3D stack. The effect of solution and electrospinning on 3D macrostructures will be explored. In addition, the simulation of electrical field is used to explain the effect on the formations.

- The third part will present the biological assessment with various characterizations including SEM, SR-FTIR, and SRXTM. In addition, the influence of plasma treatment on the biological activities on electrospun fiber will be explored.

#### 4.1 3D Electrospinning setup

The 3D electrospinning configuration was postulated on the basis of combining a 3D printer with electrospinning technique. It is widely known that electrospinning requires a voltage, a spinneret, and a collector; nonetheless, in the field of 3D printing, there are several types of FDM printer components. The coordinate systems of a printer that was used in combination with electrospinning were first examined. Then, the development of 3D electrospinning prototypes according to the printer

and electrospinning coordinate systems of choice is described. In end, this study provides guidance on 3D electrospinning troubleshooting, including issues and suggested solution.

#### **4.1.1 Coordinate system**

The coordinate systems are necessary in drive the printing process. Cartesian and delta coordinates are the two basic coordinate systems used in 3D FDM printers. Both cartesian and delta coordinates were combined with electrospinning to preliminarily test the printing and electrospinning process. It was found both configurations were found to be capable of producing electrospun fibers, although there were occasionally problems with the yarns falling to the stainless steel or other unintended areas as shown in Figure A.1. The delta-based configuration was chosen to be the coordinate used to drive the printing and combine with electrospinning to setup 3D electrospinning in this work. Since the delta-based configuration was able to solve the problems by attaching the silicone sheet to the stainless steel where the carriage never reaches while the carriages of cartesian-based configuration have to move the entire rail of stainless steel. In addition, all wires were covered with insulator sheet such as parafilm or silicone sheet.

#### **4.1.2 Development of 3D Electrospinning**

All prototypes of 3D electrospinning are shown in Figure 4.1. The development of 3D electrospinning involved the change and development of a solution feed system and a structural system which will be detailed in each section below.

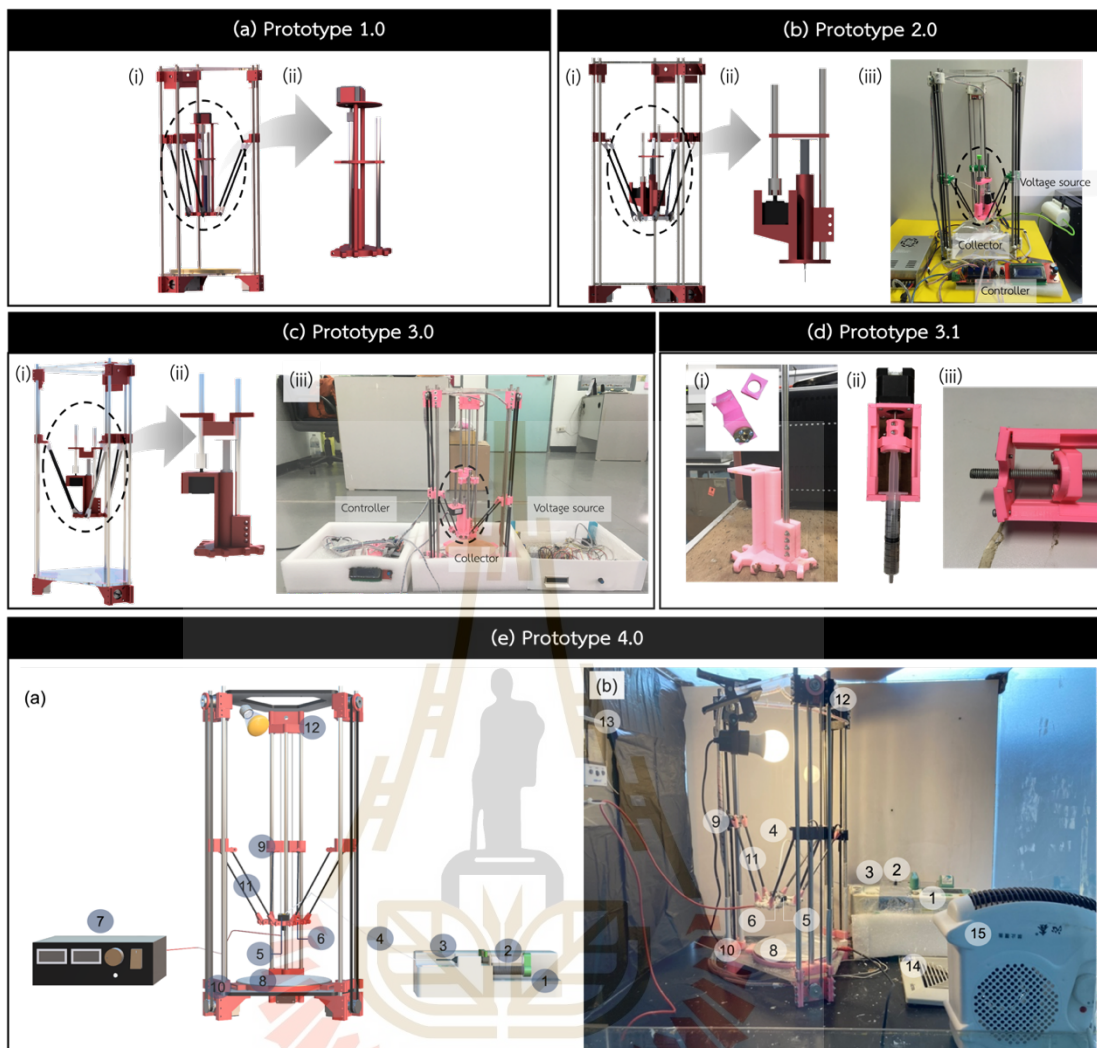


**Figure 4.1** Development of 3D electrospinning setup which combined an electrospinning and a delta printer: (a) Prototype 1.0, (b) Prototype 2.0, (c) Prototype 3.0, (d) Prototype 3.1, and (e) Prototype 4.0 that is the final prototype used in this work. These numbers refer to the following: 1 = a syringe pump, 2 = a syringe, 3 = a connector, 4 = a PTFE tube, 5 = a nozzle holder, 6 = a platform, 7 = a HV source, 8 = a collector, 9 = a carriage, 10 = a towel end, 11 = delta arms, 12 = an idler end and a limit switch, 13 = a thermometer and a hygrometer, 14 = a ventilation fan, and 15 = a heater.

#### 4.1.2.1 From an extrusion system to a solution feed system

The filament extrusion system was changed to be a solution-feed system including a syringe pump, a syringe, and a nozzle. At initial stage, the syringe pump

was set at the effector. The first model of syringe pump is presented in Figure 4.1(a)-(ii). It did not work because of too length and too heavy, which affect to the printing process. It was shorted in prototype 2.0 as seen in Figure 4.1(b)-(ii); however, the weight balance between stainless steel and motor was trouble even though their position was modified as various models in prototype 3.0 and 3.1 as demonstrated in Figure 4.1(c)-(ii) and 4.1(d)-(ii) and the motor sizes was also changed. In addition, the printed plate used to push the solution was broken as shown in Figure 4.1(d)-(i). The installation of the solution feed system apart from the effector was the optimal configuration. Teflon was chosen to carry the solution from the syringe pump to the effector's center nozzle.

#### 4.1.2.2 Structural system

As seen in Figure 4.2(a), the original model of Rostock mini used a double stainless steel of tower to propel carriages. Sometime carriage motion was seen to be unsmooth. It might be because stainless steels are susceptible to bending when the temperature fluctuates or because the nut is overly tight. A bent tower made of steel interrupted the motion of the carriages. Consequently, the double-tower system was modified in this study to resemble the single-tower system, as seen in Figure 4.2(b). The new tower was inserted between the existing tower and the double stainless-steel tower was not removed to support the structural system. In addition, it is possible for the belt, which is secured to an idler end by means of a ball bearing in motion, to slide off during the printing process. Hence, the belt holder was constructed and included into the configuration as described in Chapter III.

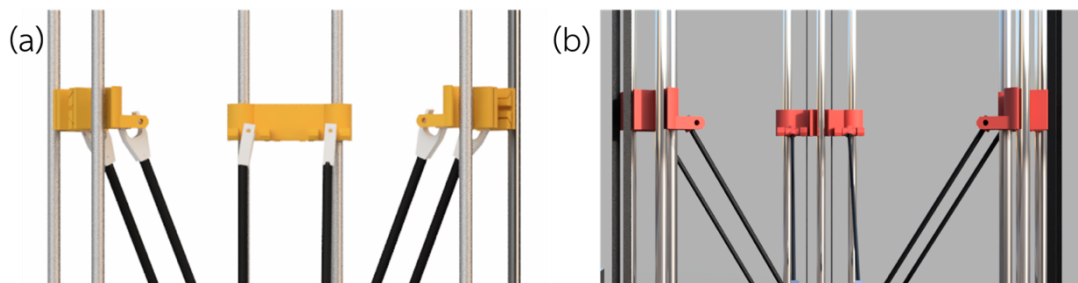


**Figure 4.2** Structural systems of tower in (a) Rostock mini and (b) the prototype 3.0, 3.1, and 4.0 of 3D electrospinning.

### 4.1.3 3D electrospinning Troubleshooting: All problems and solutions

This section reveals problems that might be happen during 3D electrospinning assemble and operation, and recommended solutions.

#### 4.1.3.1 Firmware

**Problem I:** The coding of the extruder heating cannot be removed.

**Solutions:** The temperature is able to adjust by using variable resistors. In another way, all temperature was determined on slicing software. It can be adjusted to either the LCD screen's temperature or the room temperature. It is noted temperature parameter is not used in this work. However, if temperature setting is required, the sensor and heat source will be able to add.

**Problem II:** Limit switches cannot be found.

**Solutions:** It happened after starting the 3D electrospinning process. Usually, it auto homes automatically before it starts printing, and checks endstop switch to know the endstop point or the highest distance. In this case, it cannot reach to the endstop switch and move down immediately. Checking whether the endstop settings match the connection on board is the solution. For example, the endstop switches were set at the top in this work, so position of endstop should be set as top that are `X_MAX_ENDSTOP_INVERTING`, `Y_MAX_ENDSTOP_INVERTING` and `Z_MAX_ENDSTOP_INVERTING` should be true while, `X_MIN_ENDSTOP_INVERTING`, `Y_MIN_ENDSTOP_INVERTING`, and `Z_MIN_ENDSTOP_INVERTING` should be false.

**Problem III:** A center point is not at the center of the circular collector.

**Solutions:** The determined point on the software does not match with the point on the machine. There are two parts that should be checked: check whether the bed-center setting on firmware (`BED_CENTER_AT_0_0`) and the center point on slicing software are consistent or not.

**Problem IV:** if the movement's direction differs from what the LCD panel or software is demanding.

**Solution:** The direction on `X_HOME_DIR`, `Y_HOME_DIR`, or `Z_HOME_DIR` should be checked.

#### 4.1.3.2 Hardware

**Problem I:** The printer was unable to replicate the sliced model's pattern.

**Solutions:** The distance on all axes and the current on three motor drivers should be checked

**Problem II:** Some carriage cannot move following the demand.

**Solutions:** It is important to verify that the motor, motor driver, and wiring are all operational. Basically, it can be examined by switching the working and non-working parts to see what not works. The motor driver or motor should also be checked to see if it is overheating. Please examine and adjust the voltage utilized to drive the motor driver if it is too hot. If everything seems normal, kindly check the wiring because it may be damaged.

**Problem III:** Electrical charge or spark might be on the collector (Figure A.2).

**Solutions:** The electrical charge may be between the nozzle and collector if the nozzle attached to the HV positive charge is placed too close to the collector. This could cause an electrical charge or spark on the collector, which could start a fire. The electrical charge is also caused if there are any fibers rising to the nozzle, which serve as a bridge between the nozzle and collector. As a result, it is important to determine the smallest distance that allows for safe electrospinning.

## 4.2 3D fibrous macrostructures

In order to gain insight into the self-assembly of a 3D electrospun stack and the formation of 3D electrospun macrostructures, an investigation was conducted utilizing the static nozzle of 3D electrospinning and the moving nozzle of 3D electrospinning, respectively. The influence of electrospinning and solution on 3D electrospun macrostructures was also explored.

### 4.2.1 The self-assembly of 3D-fibrous structures

To study the properties of the 3D formation of self-assembled stack required, PCL, PVDF, and PAN polymers were used to examine the condition of 3D self-assembled formation under electrospinning without the nozzle moving. The obtained

results of 2D mat and 3D stack were examined with XRD and FTIR-Raman spectroscopy to study insight change during the stacking.

The fabrication process of electrospun fiber was carried out using a PCL solution with a concentration of 12 w% in a DCM:DMF solvent with a weight ratio of 6:1. The addition of  $\text{H}_3\text{PO}_4$  additives was optional to test the self-assembly. The process parameters included a flow rate of 5 mL/h, a tip-to-collector distance of 10 cm, and a voltage of 18kV. The study discovered that the solution without additives was unable to achieve 3D formation, despite altering the electrospinning process by adjusting the flow rate within the range of 1-5 mL/h, the tip-to-collector distance of 5-10 cm and applying a voltage of 15-20 kV. Figure 4.3(a) demonstrates that the electrospun fiber maintained its mat structure after a 30-minute electrospinning procedure. The lateral expansion of the electrospun mat was clearly evident, as opposed to vertical growth. The addition of  $\text{H}_3\text{PO}_4$  additives resulted in the formation of a 3D self-assembled stack, as depicted in Figure 4.3(b). The electrospun fiber was deposited at the center of the collector and then raised in a straight path from the collector to the nozzle. Subsequently, the incoming fiber would deposit to the upper and outer surface of the raised fiber, rather than other regions on the collector. This led to the accumulation of deposited fibers in the same location, resulting in an increase in the thickness of the electrospun fiber. The significance of the additives in the development of 3D self-assembled structures was evident. In addition, the solution with additives was examined using a flow rate of 2 mL/h, a tip-to-collector distance of 5 cm, and a voltage of 14 kV (Figure 4.3(b)). This condition successfully achieved a 3D self-assembled stack with reduced height. The reason for it was attributed to the reduced distance. The influence of electrospinning parameters on the 3D PCL-based structures will be investigated in the following section.

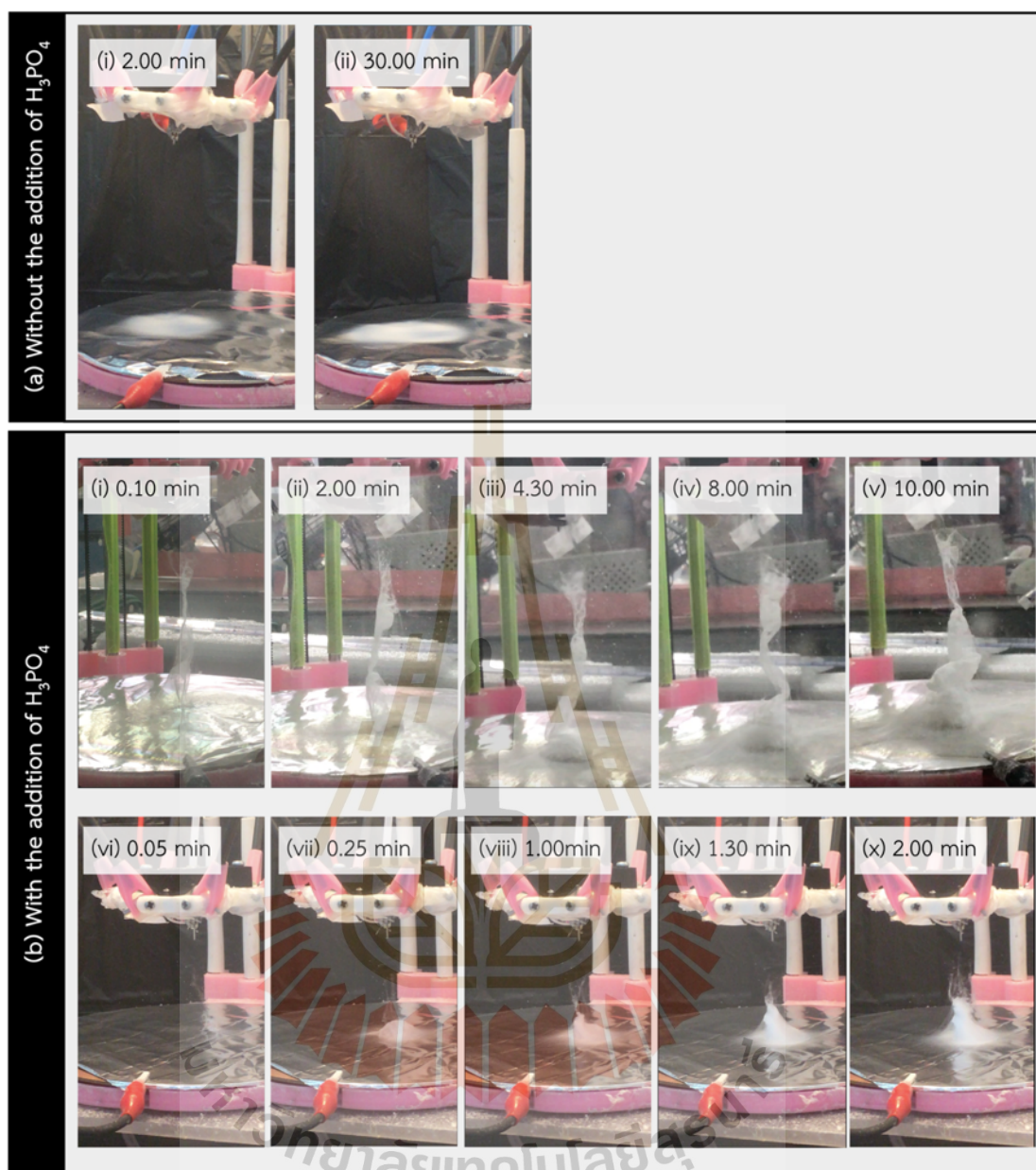


**Figure 4.3** The experimental results of electrospun fibers fabrication using the PCL solution (a) without and (b) with the addition of H<sub>3</sub>PO<sub>4</sub> additives under (i-v) the condition of a flow rate at 5 mL/h, a tip-to-collector distance at 10 cm, and a voltage of 18 kV and (vi-x) a flow rate at 2 mL/h, a tip-to-collector distance at 5 cm, and a voltage of 14 kV.

The experimental setup for the PVDF solution closely resembled that of the PCL solution. The PVDF solutions with a concentration of 15 wt% in a solvent mixture of AC:DMF in a 1:1 weight ratio without and with the addition of H<sub>3</sub>PO<sub>4</sub> additives, were

used to test self-assembly under the process parameters were a flow rate of 2 mL/h, a tip-to-collector distance of 8 cm, and a voltage of 16 kV. The addition of additives proved to play a significant role in the building of the 3D structure. Figure 4.4(a)-(i) demonstrates that the PVDF solution, without the additives, generated a 2D mat during the electrospinning process after a duration of 30 minutes. The electrospun mat exhibited prominent horizontal expansion, in contrast to its limited vertical development. The PVDF solution with additives enabled the rapid production of a 3D self-assembled stack in 1 minute as illustrated in Figure 4.4(a)-(ii). The incoming fiber deposited at the same location without any lateral expansion, which allowed the self-assembly. This corresponded to the results of the PCL.

In contrast to PCL and PVDF, which necessitated the addition of additives to solution in order to generate three-dimensional structures, the utilization of DMF-prepared PAN removed the need for additives. The performance of 3D formation under a flow rate of 2 mL/h, a tip-to-collector distance of 8 cm, and an applied voltage of 18kV was observed in Figure 4.5(a) using a PAN solution containing 10wt% in DMF solvent. The necessary conditions for this process included a flow rate of 2 mL/h, a tip-to-collector distance of 8 cm, and an applied voltage of 18 kV. There were some fibers that rose directly from the collector to the nozzle and were dragged by the nozzle's motion as shown in Figure 4.5(b). Nevertheless, the condition fails to generate 3D structures when the nozzle is in motion. In this instance, the parameters of electrospinning and printing are interdependent and crucial for 3D formation. The following section will define these parameters in accordance with PCL solutions.

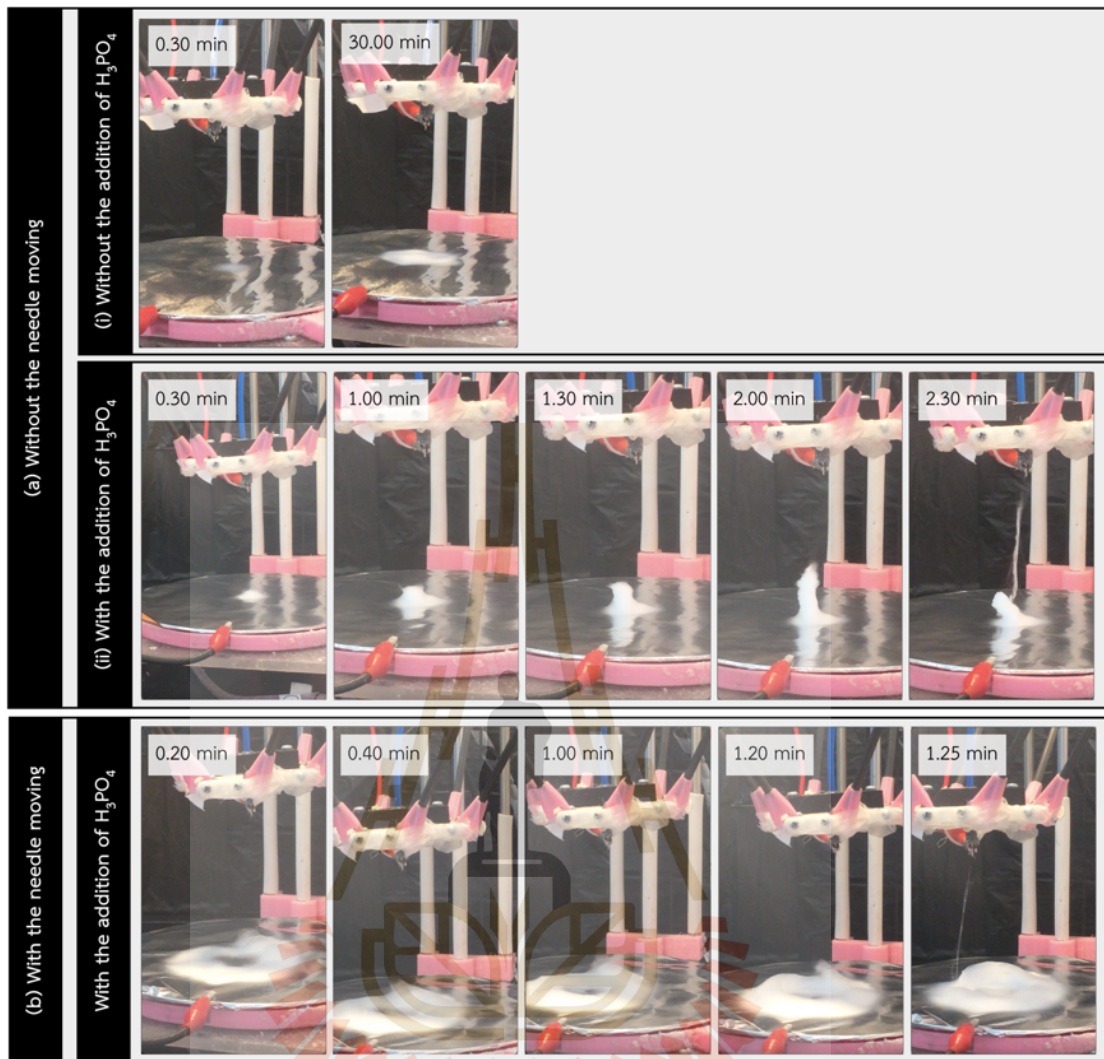


**Figure 4.4** The experimental results of electrospun fibers fabrication under the condition of a flow rate at 2 mL/h, a tip-to-collector distance at 8 cm, and a voltage of 16 kV by (a) non-moving which was used to test PVDF solution (i) without and (ii) with the addition of  $H_3PO_4$  additives the nozzle and (b) moving the nozzle.

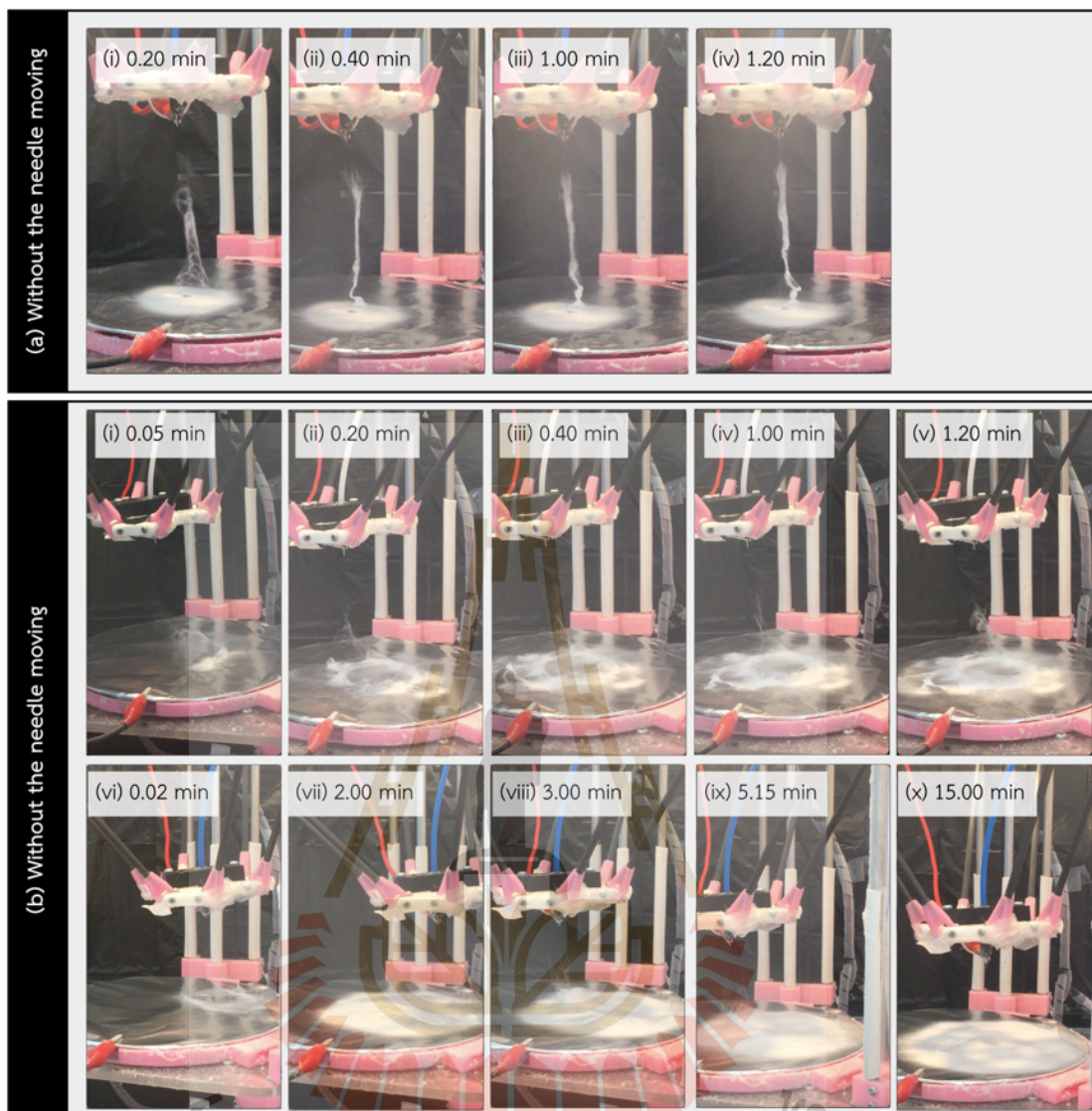


**Figure 4.5** The experimental results of electrospun fibers fabrication by (a) non-moving nozzle under the condition of a flow rate at 2 mL/h, a tip-to-collector distance at 8 cm, and a voltage of 18 kV and (b) moving nozzle at 1 mm/s under (i-v) the condition of a flow rate at 2 mL/h, a tip-to-collector distance at 8 cm, and a voltage of 18kV and (vi-x) the condition of a flow rate at 3 mL/h, a tip-to-collector distance at 6 cm, and a voltage of 18 kV.

#### 4.2.1.1 Conductivity

The ionic conductivities of PCL, PVDF, and PAN solutions were measured as a function of their concentration of  $H_3PO_4$  additives as concluded in Table 4.1. It found that the incorporation of 10%  $H_3PO_4$  enhanced the conductivity of PCL solution rose

from 0.082  $\mu\text{S}/\text{cm}$  to 0.8  $\mu\text{S}/\text{cm}$  and the conductivity of PVDF solution rose from 5.24  $\mu\text{S}/\text{cm}$  to 93.9  $\mu\text{S}/\text{cm}$  while PAN solution prepared in DMF solvent without additives had the conductivity at 99.4  $\mu\text{S}/\text{cm}$ . This was caused that PAN solution can perform 3D structures without additives. Since the PCL solution is a main polymer used to examine the buildup and control of 3D macrostructure in the next section, the quality of  $\text{H}_3\text{PO}_4$  additive on conductivity was studied by varying from 0% to 20%. The addition of  $\text{H}_3\text{PO}_4$  additives in PCL solution enhanced the conductivity of solution. As charge was carried by an increasing number of free ions produced by increasing dissociation of  $\text{H}_3\text{PO}_4$ , the total conductivity increased. Nonetheless, the tendency cannot be considered on the only increase in free ion concentration when  $\text{H}_3\text{PO}_4$  content rises. Ionic conductivity may be enhanced by additional variables, including solvent and polymer chain. Upon further increasing the concentration of  $\text{H}_3\text{PO}_4$ , the total conductivity initially reached its highest point at the 15%  $\text{H}_3\text{PO}_4$  and thereafter decreases which it was likely caused by the inhibition of ion dissociation at increased  $\text{H}_3\text{PO}_4$  concentrations (Alipoori, Torkzadeh, Mazinani, Aboutalebi, and Sharif, 2021).

**Table 4.1** The conductivity ( $\mu\text{S}/\text{cm}$ ) of PCL, PVDF, and PAN solution with the existing  $\text{H}_3\text{PO}_4$  additives. Note S1 = PCL solutions, S2 = PCL solutions + 5% $\text{H}_3\text{PO}_4$ , S3 = PCL solutions + 10% $\text{H}_3\text{PO}_4$ , S4 = PCL solutions + 15% $\text{H}_3\text{PO}_4$ , S5 = PCL solutions + 20% $\text{H}_3\text{PO}_4$ , S6 = PVDF solutions, S7 = PVDF solutions + 10% $\text{H}_3\text{PO}_4$ , and S8 = PAN solutions.

No.	S1	S2	S3	S4	S5	S6	S7	S8
1	0.082	0.614	0.825	0.850	0.728	5.261	93.920	99.780
2	0.081	0.615	0.817	0.839	0.724	5.250	93.690	99.570
3	0.084	0.621	0.770	0.844	0.748	5.209	93.960	98.750
average	0.082	0.617	0.80	0.84	0.73	5.24	93.9	99.4
SD	0.002	0.004	0.03	0.01	0.01	0.03	0.1	0.5

#### 4.2.1.2 XRD Characterization

The XRD patterns of PCL power, 2D PCL mat, 3D PCL stack, PVDF power, 2D PVDF mat, 3D PVDF stack, PAN power, and 3D PAN stack (Figure 4.6) had been analyzed to investigate that the driving force of the self-assembly was due to a change of crystallinity in the polymer fibers during spinning.

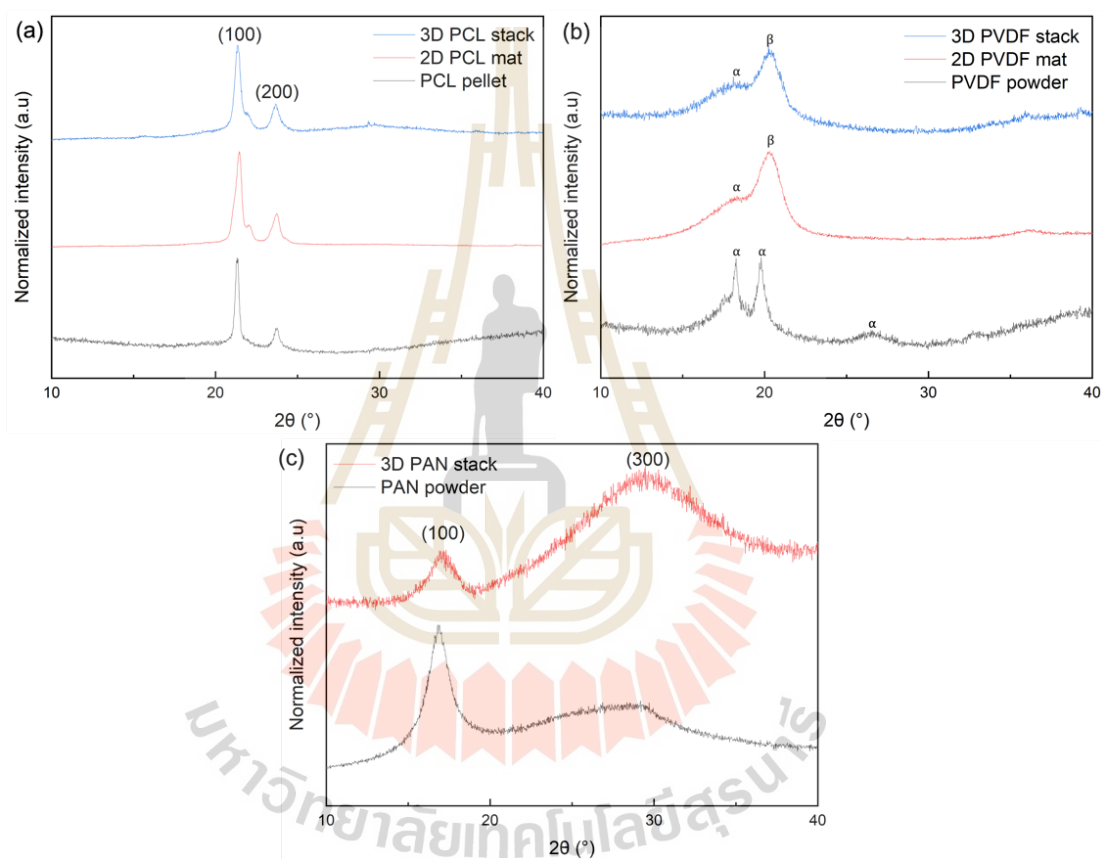


**Figure 4.6** XRD patterns of (a) PCL series, including 2D PCL mat, 3D PCL stack and PCL powder, (b) PVDF series, including 2D PVDF mat, 3D PVDF stack and PVDF powder, and (c) PAN series, including 3D PAN stack and PAN powder.

XRD patterns of PCL powder, 2D PCL mat, and 3D PCL stack is shown in Figure 4.6(a). The diffraction pattern of the crystalline PCL powder, 2D PCL mat and 3D PCL stack shows the existence of substantial crystallinity, with peaks at  $2\theta = 21.4^\circ$  and  $23.8^\circ$  corresponding to the (110) plane and overlapping 200, 013, 112, 104 reflections of the orthorhombic crystal structure (Balu, Kumar, and Ramalingam, 2011; L. Li et al.,

2011; Shkarina et al., 2018). Considering the diffraction peaks between 2D mat and 3D stack, their crystalline structure did not change with the addition of  $H_3PO_4$  additives. In addition, electrospinning process did not change the crystalline structure of PCL.

XRD pattern of PVDF powder, 2D PVDF mat, and 3D PVDF stack is given in Figure 4.6(b). In chemical structures of PVDF polymer, two fluorine atoms are linked to every second carbon atom along a vinyl backbone with three different polymorphs that are alpha ( $\alpha$ ), beta ( $\beta$ ) and gamma ( $\gamma$ ) phases as seen in Figure 4.7 (Janakiraman, Surendran, Ghosh, Anandhan, and Venimadhav, 2016; Shepelin et al., 2019). A perpendicular effective dipole is displayed by the chain substituents if the fluorine atoms are oriented in a precise way. Specifically, it has been discovered that polymers with a dipole moment perpendicular to the backbone have piezoelectric characteristics (Shepelin et al., 2019). The PVDF powder had been indexed to phase  $\alpha$ , and electrospun fiber including 2D mat and 3D stack had been indexed to a mixture of both  $\alpha$  and  $\beta$  phases. It was attributed to stretched jet at high applied voltage during electrospinning process, which orients the dipoles in the PVDF molecular chains and allows the  $\alpha$ -to- $\beta$  crystalline phase transitions (He, Rault, Lewandowski, Mohsenzadeh, and Salaün, 2021; Janakiraman et al., 2016; Lim, Kim, and Seo, 2015). The absence of the XRD pattern between 2D mat and 3D stack confirmed the  $H_3PO_4$  did not interact the molecular structures.

The XRD pattern of the PAN powder and 3D PAN stack is shown in Figure 4.6(c), where the (100) and (300) planes are represented by the broad peak at  $29^\circ$  and the strong peaks at  $2\theta = 17^\circ$  (Mahmood and Jawad, 2019; Yu, Lu, Branford-White, Yang, and Wang, 2011). Compared to the PAN powder, electrospun fiber exhibited higher intensity peaks of  $29^\circ$ ; however, the intensity peak at  $17^\circ$  decreased, suggesting the arrangement of (100) decreased with the increase in the (300) arrangement through electrospinning process.

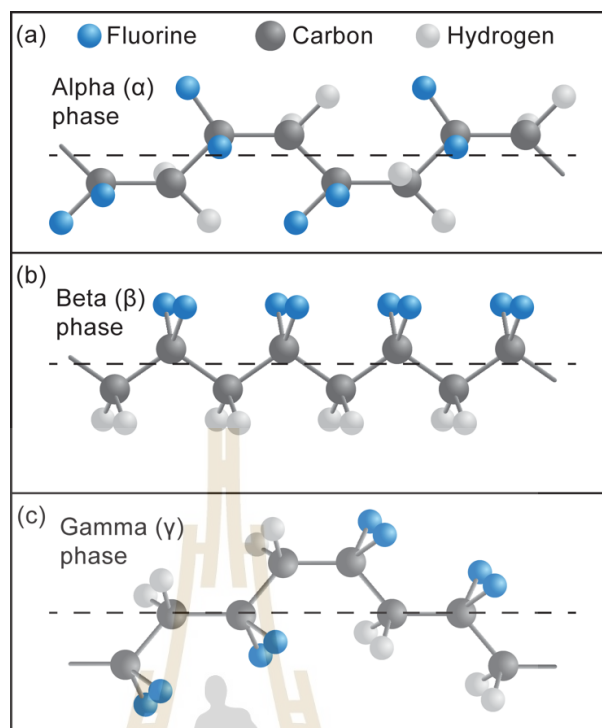


**Figure 4.7** Structural configuration of three phases of PVDF (Shepelin et al., 2019).

#### 4.2.1.3 FTIR-Raman Characterization

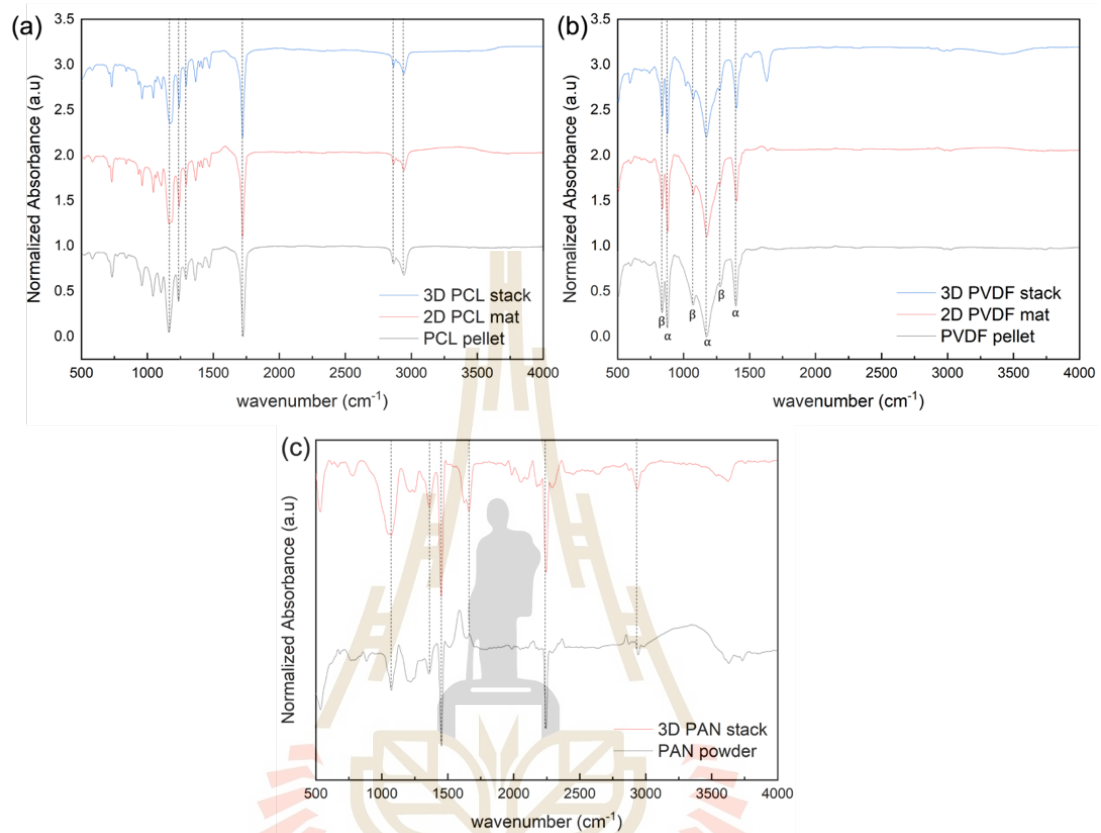
The FTIR-Raman spectra of 2D mat and 3D electrospun stack were compared in this work to whether the insertion of the additive responsible for the 3D build-up resulted in significant changes.

Figure 4.8(a) shows the FTIR peak of PCL powder, 2D PCL mat, and 3D PCL stack. The typical characteristic peaks of PCL appear in the ranges of  $1000\text{--}1800\text{ cm}^{-1}$  and  $2800\text{--}3000\text{ cm}^{-1}$  (Shkarina et al., 2018). The strong band belonging at  $1720\text{ cm}^{-1}$  is attributed to the stretching ( $\text{C}=\text{O}$ ) mode of carbonyl esters. The two peaks at  $2864\text{ cm}^{-1}$  and  $2947\text{ cm}^{-1}$  correspond to the symmetric and asymmetric stretching of the  $\text{CH}_2$  group. Moreover, the two peaks at  $1238\text{ cm}^{-1}$  and  $1163\text{ cm}^{-1}$  correspond to the symmetric and asymmetric stretching of the  $\text{C-O-C}$  group and the bands at  $1292\text{ cm}^{-1}$  are related to  $\text{C-O}$  and  $\text{C-C}$  stretching in the crystalline phase (Balu et al., 2011; Chen and Lin, 2020; Shkarina et al., 2018). These peaks of PCL pellet were able to locate at other of 2D mat and 3D stack. These results confirmed that the process of electrospinning and the incorporation of  $\text{H}_3\text{PO}_4$  did not interact the molecular bonding, according to XRD results. Additionally, FT-Raman spectra confirmed the

process of electrospinning and the incorporation of  $\text{H}_3\text{PO}_4$  did not interact the molecular bonding as shown in Figure 4.9(a). All peaks, including 912, 1020–1122, 1271–1323, 1410–1471, 1724, and 2840–3000  $\text{cm}^{-1}$  corresponding to  $\nu\text{C-COO}$ , skeletal stretching,  $\omega\text{CH}_2$ ,  $\delta\text{CH}_2$ , C=O stretching, and  $\nu\text{CH}$  (Baranowska-Korczyc et al., 2016; Taddei, Di Foggia, Causa, Ambrosio, and Fagnano, 2006), were appeared in PCL pellet, 2D mat, and 3D stack.

FTIR peaks of PVDF is shown in Figure 4.8(b). The polar  $\beta$  phase is associated with the bands at 840, and 1279  $\text{cm}^{-1}$ , while the  $\alpha$  phase is represented by the bands at 879, 1178, and 1400  $\text{cm}^{-1}$ . The peaks centered at 879  $\text{cm}^{-1}$  and 1400  $\text{cm}^{-1}$  are attributable to the C–F stretching vibration and  $\text{CH}_2$  bending while the band at 1178  $\text{cm}^{-1}$  is related to C–C bond (Kumarasinghe, Bandara, Bandara, Senadeera, and Thotawatthage, 2021; Shepelin et al., 2019). The procedure of electrospinning and self-assembly did not result in an enhancement of the  $\beta$ -phase peak. The peak of molecular bonding of 2D mat was similar to PVDF pellet; however, it found the new peak at 1635  $\text{cm}^{-1}$ , and 1016 and 1633  $\text{cm}^{-1}$  were appeared in FTIR peak of 2D mat and 3D stack respectively because of C–C and C=O stretching, which were attributed to the residual DMF solvent (Lanceros-Méndez, Mano, Costa, and Schmidt, 2001; Ren et al., 2017). These results illustrated that the increase in thickness of electrospun fiber, leading to shorter distance of electrospinning process, responded to the residual solvent on electrospun fiber. It was similar in Raman spectra as seen in Figure 4.9(b) that a new peak at 740 and 1641  $\text{cm}^{-1}$  of 2D mat and 3D stack was attributed to the residual solvent. It was clear differences between PVDF pellet and electrospun fiber including 2D mat and 3D stack that electrospinning induced the intensity of  $\beta$ -phase at 840  $\text{cm}^{-1}$  was relatively higher while the intensity of  $\alpha$ -phase at 796  $\text{cm}^{-1}$  was decreased in electrospun fiber which indicating a predominance of  $\beta$ -phase (Ma, Zhang, Lin, Zhou, and Ni, 2018; Shepelin et al., 2019; Singh, Borkar, Singh, Singh, and Kumar, 2014). The raised beta-phase content observed in electrospun fiber is believed to be the consequence of the liquid jet's stretching and drying, which induces a phase transition from  $\alpha$  to  $\beta$  phase (Gade, Nikam, Chase, and Reneker, 2021). Due to their electronegativities, the paired hydrogen and fluorine atoms in the PVDF monomer structure form a dipole. Stretching the jet in the electrical field aligns

the dipoles perpendicularly, increasing the  $\beta$ -phase content and piezoelectric response (Gade et al., 2021; X. Liu, Kuang, Xu, and Wang, 2017).



**Figure 4.8** FTIR spectra of PCL series, including PCL pellet, 2D PCL mat, 3D PCL stack, PVDF, including PVDF pellet, 2D PVDF mat, 3D PVDF stack, and PAN series, including PAN powder, and 3D PAN stack.

Figure 4.8(c) shows the characteristic FTIR peaks of PAN powder and electrospun stack. There was a strong peak located at  $2241\text{ cm}^{-1}$  and  $1359$ ,  $1450$ , and  $2939\text{ cm}^{-1}$  which corresponds to  $\text{C}\equiv\text{N}$  stretching, and the vibrations of the aliphatic CH groups ( $\text{CH}$ ,  $\text{CH}_2$ , and  $\text{CH}_3$ ) (M. K. Haider et al., 2021; Jiangling et al., 2013; Mahmood and Jawad, 2019). The skeletal vibration of PAN molecular chain in PAN powder was observed at  $1074\text{ cm}^{-1}$ . There was the new peak at  $1664\text{ cm}^{-1}$  associated to  $\text{C}=\text{O}$  stretching (Jiangling et al., 2013) which was appeared in the FTIR spectrum of PAN fiber. It was attributed to the residual DMF exists in the PAN fibers. This confirmed the existing DMF in PAN fibers due to incompletely DMF evaporation during

electrospinning (Jiangling et al., 2013). However, the existing residual of solvent was not appeared in Raman spectra as shown in Figure 4.9(c). The Raman spectra of PAN powder and electrospun fiber presented same pattern. The dominant band of PAN powder and fiber was appeared at  $2245\text{ cm}^{-1}$  corresponding to the nitrile CN (C=N) stretching band (Dorota and Malgorzata, 2021). In addition, the characteristic bands were at  $1452\text{ cm}^{-1}$  and  $2879\text{-}2979\text{ cm}^{-1}$  corresponding to  $\text{CH}_2$  bending and CH bonding, respectively.

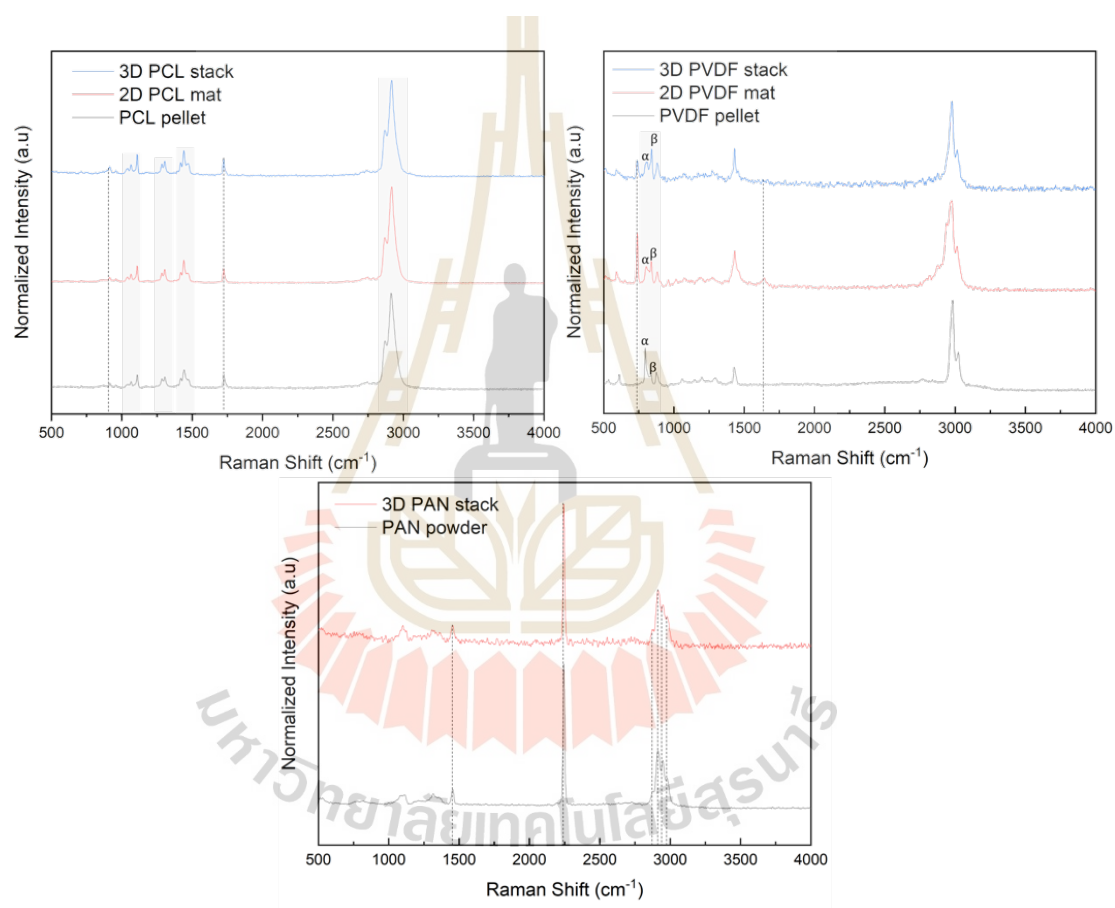


**Figure 4.9** Raman spectra of PCL series, including PCL pellet, 2D PCL mat, 3D PCL stack, PVDF, including PVDF pellet, 2D PVDF mat, 3D PVDF stack, and PAN series, including PAN powder, and 3D PAN stack.

## 4.2.2 The mechanism of buildup of 3D-fibrous macrostructures

### 4.2.2.1 Observation

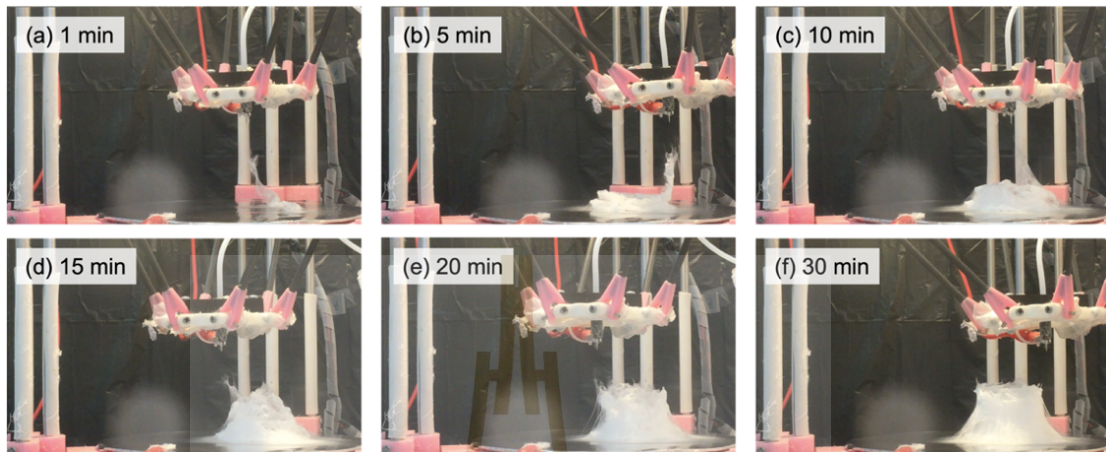


**Figure 4.10** The buildup of 3D-fibrous macrostructures at a flow rate of 6 mL/h, an initial distance of 6 cm, a voltage of 16 kV, and a nozzle speed of 1 mm/s by an in-house 3D electrospinning setup.

Figure 4.10 illustrates the 3D buildup at discrete intervals of 5 minutes. The build-up of the 3D electrospun fiber self-assembly spontaneously occurred within 1 minute after starting the process, as shown in Figure 4.10(a). Initially, a 2D mat was formed at the location that only corresponded to the nozzle for 2-3 seconds. After that the fibers started to rise up between the nozzle and collector. The raised-up fibers were able to move following the nozzle movement to build up and control a 3D structure (Figure 4.10(a-d)). There was some delay between the deposited fibers and the movement of the nozzle. This observation resembles the jet lag found in MEW (Figure 4.11(c)). As the structures were higher, the fibers fell to the edges of the structure (Figure 4.10(d-f)). It was slightly different at the initial stage from the previous report reported by Vong et al. (2018) that 3D PS formation happened after first depositing an initial layer, the flat layer of 2D fiber. It might be attributed to the different conductivity of solutions. Sun et al. (2012) remarked that a 3D PS stack made from a PS solution was generated on a fiber mat, while one made from the PS solution with an additive was more likely to get fast-growing without the mat. However, the flat layer at the bottom part of 3D-fibrous structures in this work

remains. It was generated during the 3D formation because of whipping instability, resulting in the fibers depositing at the edges of structures and surrounding areas, as demonstrated in Figure 4.10(b-f). It caused the convergent shape at the bottom part of the structures. The flat layer at the bottom resembles a raft or a brim in 3D printing, as shown in Figure 4.11(b). The raft and brim are types of adhesion that are adjustable to avoid warping. Nevertheless, it cannot be adjusted via 3D electrospinning because of the inherent whipping jet.

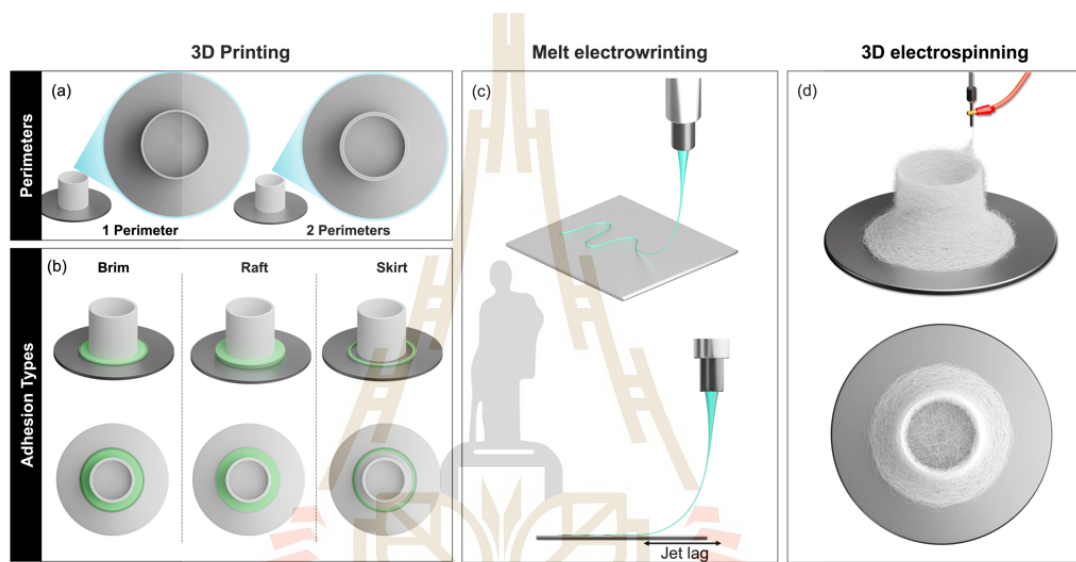


**Figure 4.11** Schematic images of parameters involving 3D printing, melt electrowriting, and 3D electrospinning that are (a) the perimeters and adhesion types in 3D printing, (b) the jet lag in melt electrowriting, and (c) the electrospun structures obtained from 3D electrospinning.

According to the self-assembly mechanism mentioned (Hwang et al., 2020; Sun et al., 2012; Vong et al., 2018), the deposited fibers, being negatively charged, act as the new collectors for the coming fibers because of polarization and electrostatic induction. It is similar to this work. As obviously seen in Figure 4.10, the raising-up fibers, attracted by the positively charged nozzle, were dragged along the pathway of the nozzle. Some fibers were then moved downward to the previously deposited area and stacked to form a 3D structure. During the electrospinning process, some collapse and overhang occur because of the weight of itself at the accumulation position and whipping instability (M. M. Li and Long, 2011).

This is how the 3D-fibrous macrostructures form via 3D electrospinning. It is unattainable to achieve an identical structure to the model due to the inherent whipping instability in the electrospinning process. To understand the associated factors, varying solution preparations and electrospinning parameters are investigated, and the final products are assessed as shown in Figure 4.12. A thickness was measured as a height to identify a 2D mat and a 3D structure. The width of deposition (DW) is measured from a length from one side at the bottom part of 3D structures to another. The wall thickness is measured by the difference between the inside diameter ( $D_{in}$ ) and the outside diameter ( $D_{out}$ ). The wall thickness is considered in the case of the perimeter to be 1. The convergence at half height ( $C_{hh}$ ) is also measured to assess the deformation in the model.

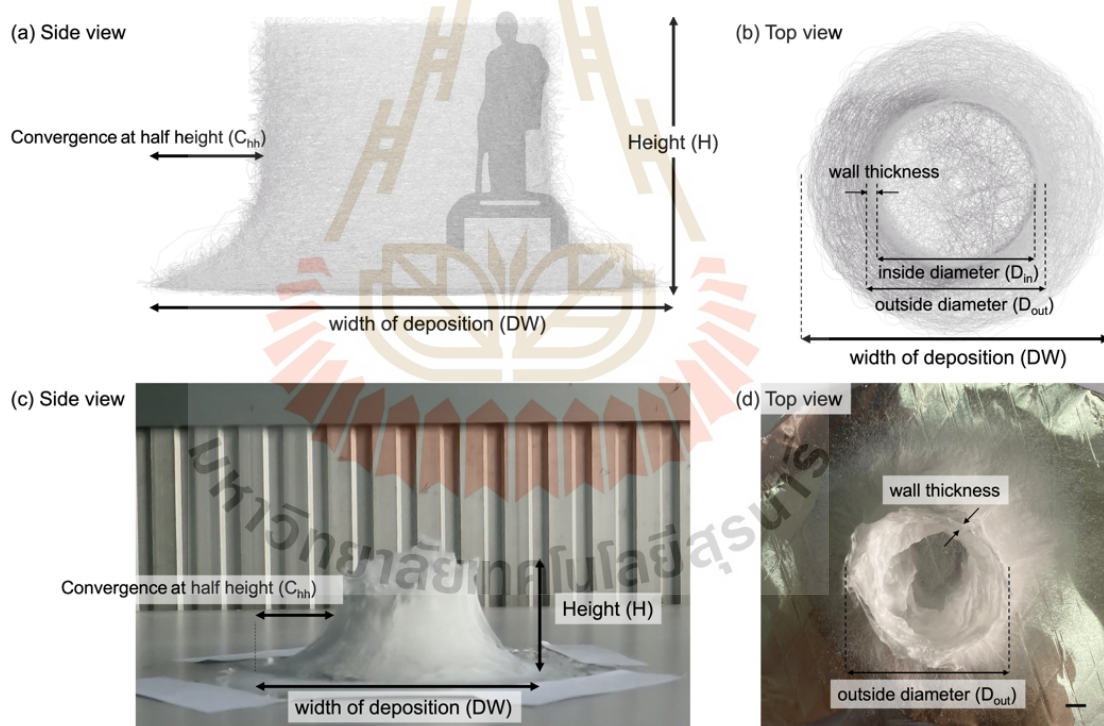


**Figure 4.12** (a-b) Diagrams and (c-d) an example of parameters used to illustrate 3D-electrospun structures in this work. The scale bar is 10 mm.

#### 4.2.2.2 The buildup and control of 3D-fibrous macrostructures

In this section, the optimal conditions for building up electrospun macrostructure via 3D electrospinning have been studied. The solution and electrospinning parameters were studied on the buildup and control of 3D electrospun macrostructures. The specific criterion required to distinguish between a 2D mat and a 3D structure is thickness or height. Generally, the electrospun fibers obtained from conventional electrospinning ranges from nano, micro, to millimeter scale. Therefore, a sample greater than 10 mm is considered an indication of 3D structures.

##### **Solution parameters**

There are several factors that affect the buildup of 3D macrostructures via 3D electrospinning. The PCL solutions with various conditions of solution preparation were investigated to explore the influence of concentrations, solvent ratios, and additives on the buildup of 3D electrospun structures. Each condition was executed for 30 minutes in order to survey the optimal condition, which presents the most opportunity for obtaining the stable buildup.

##### **Relation between solution and flow rate**

10, 12, and 14 wt% concentrations of PCL solutions prepared in a solvent containing a DCM:DMF ratio of 6:1 and an addition of 10%  $H_3PO_4$  were used to investigate the 3D buildup by using the 3D electrospinning with various flow rates, including 2, 4, and 6 mL/h, at an initial distance of 6 cm, a voltage of 16 kV, and a nozzle's moving speed of 1 mm/s under ambient conditions for 30 minutes.

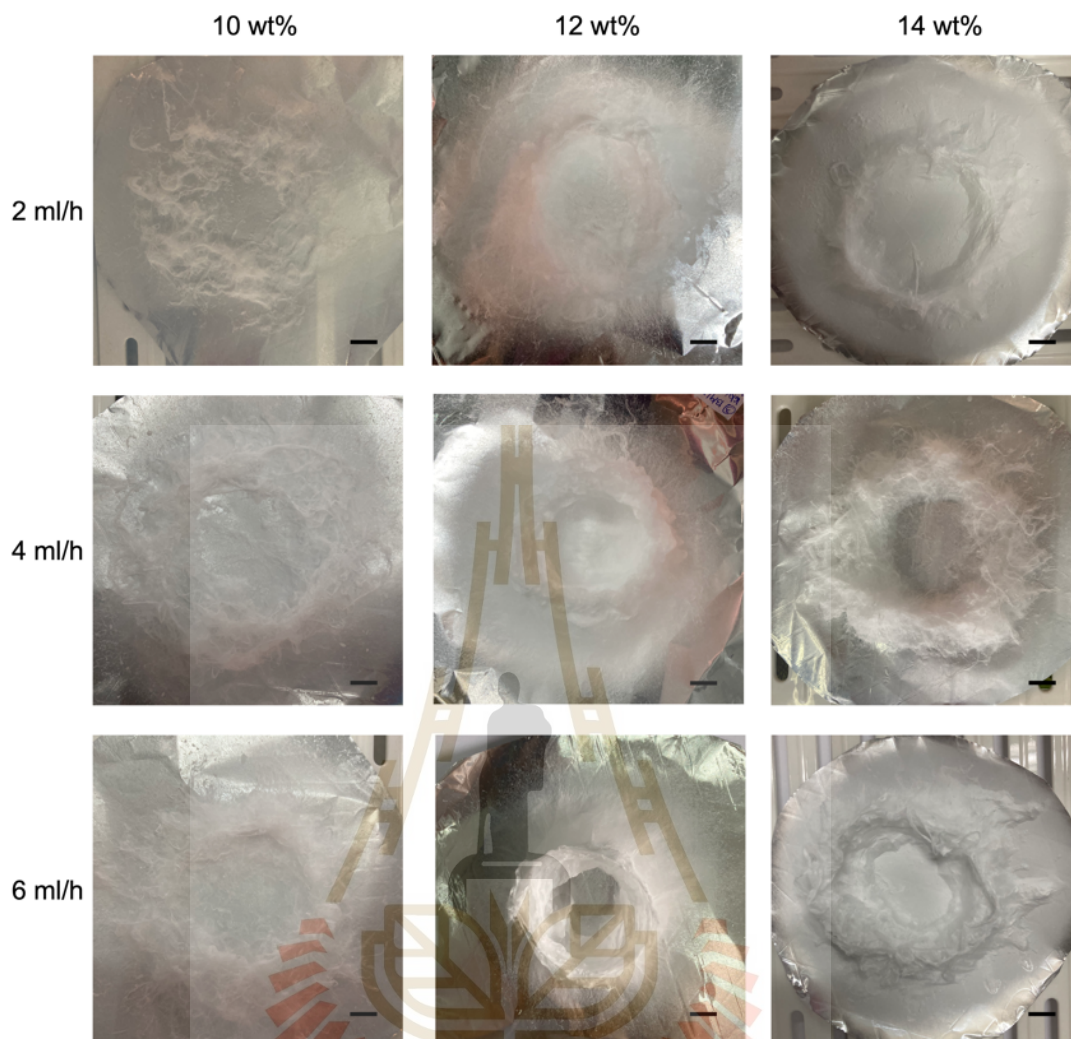


**Figure 4.13** The top view of 2D mats and 3D constructs fabricated using various concentrations of PCL solutions, namely 10, 12, and 14 wt%. These concentrations were prepared in the DCM:DMF solvent of 6:1 with the addition of 10%  $\text{H}_3\text{PO}_4$ . All experiments were conducted with a flow rate of 2, 4, and 6 mL/h, an initial distance of 6 cm, a voltage of 16 kV, and a nozzle speed of 1 mm/s via 3D electrospinning for 30 minutes in the ambient environment. The scale bar is 10 mm.

All conditions leave a trace of deposited fibers following the cylinder shape, as seen in Figure 4.13. The existing trace of a hollow cylinder might be attributed to the slow-moving speed of the nozzle. In these ranges of concentration, the 12 wt% concentration was preferred for the buildup of 3D PCL-electrospun macrostructures that resembled the model. It presented the highest structures, reaching  $32.30 \pm 3.90$

mm, as shown in Figure 4.14. No 3D-electrospun buildup was found under the 10 wt% concentration at 2, 4, and 6 mL/h and the 10-14 wt% concentration at 2 mL/h. These imply an adequate amount of solution is needed. Their formations based on 10 wt% showed that there was the raising-up fiber, which was able to drag following the nozzle locomotion at the initial stage; however, it did not continue and disappeared later when the distance was increasing. Moreover, all performances of 10 wt% had unstable electrospinning jets and solution drying, hampering the self-assembly. The fabrication of electrospun fiber had been emerged by the stretching of the charged jets in uniaxial directions; however, at low concentrations, the charged jets lose their intermolecular attractions and thus discrete into droplets from the Taylor cone due to low viscosity and high surface tension (Islam, Ang, Andriyana, and Afifi, 2019). When concentration was increased to 12 wt%, it provided stable spinning and no drying. Increasing the concentration will lead to an increase in chain entanglement among the polymer chains, resulting in stable 3D structures (A. Haider, Haider, and Kang, 2018). However, increasing the concentration beyond the threshold causes the droplet to dry at the tip. There was a little droplet remaining at the tip of the nozzle for 14 wt% concentration at a flow rate of 4 and 6 mL/h, resulting in a decrease in height. A higher concentration also has the possibility of shape-shifting effect, as seen in top views of 12 and 14 wt% at 6 mL/h in Figure 4.14. Considering the wall thickness of the 2D mat at a flow rate of 2 mL/h, it was found that wall thickness decreases with an increase in concentration. This finding is in agreement with the experiments and modeling reported by other studies (Islam et al., 2019; Šimko and Lukáš, 2016). The increase in concentration and viscosity leads to a decrease in the width of whipping and an increase in a straight jet trajectory before the bending instability, resulting in a smaller wall thickness and a closer  $D_{out}$ . However, their relationships were changed in the higher structure. The wall thickness of higher structures was less than that of 2D mats as higher structures result in a shorter distance between the nozzle and collector during electrospinning.

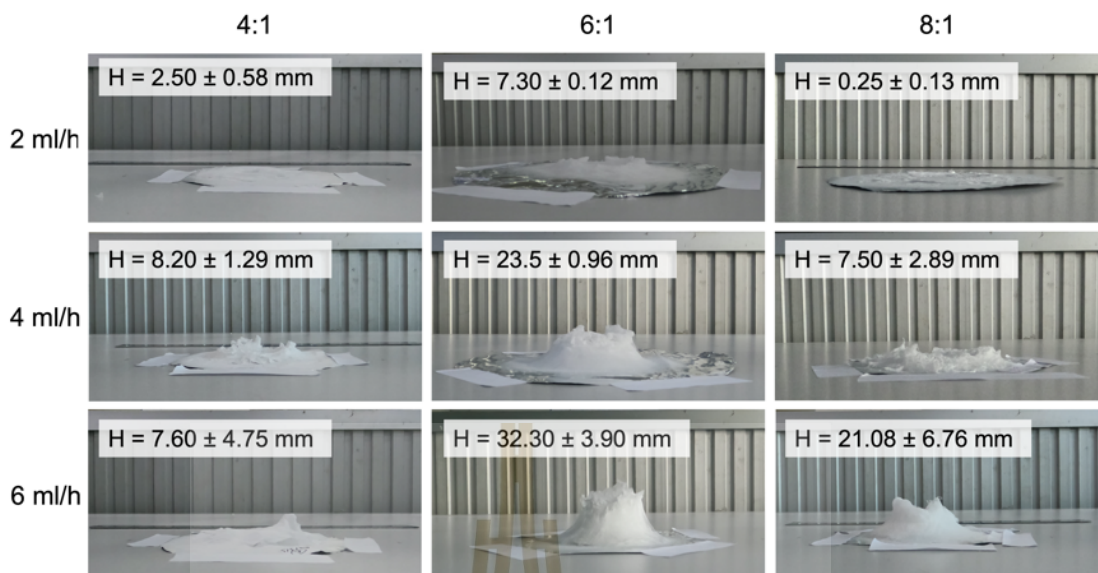


**Figure 4.14** The side view of 3D formations fabricated using various concentrations of PCL solutions, namely 10, 12, and 14 wt%. These concentrations were prepared in the solvent of 6:1 DCM:DMF with the addition of 10%  $H_3PO_4$ . All experiments were conducted with a flow rate of 2, 4, and 6 mL/h, an initial distance of 6 cm, a voltage of 16 kV, and a nozzle speed of 1 mm/s via the 3D electrospinning for 30 minutes in the ambient environment.

Generally, the increase in concentration increases the diameter of the electrospun fibers (A. Haider et al., 2018; Radacsi and Nuansing, 2020; Vong et al., 2018), but that was not the case in this study. The SEM images of all, including upper part for 2D mat and upper, middle, and lower parts for 3D structures, are presented in Figure B.1. To be illustrated, the SEM images and diameter histograms of overall electrospun fibers are demonstrated in Figure 4.15, 4.16, and 4.17 for 3D fibrous structures fabricated using 10, 12, and 14 wt% PCL concentrations, respectively, in the 6:1 DCM:DMF solvent with 10 wt%  $H_3PO_4$  additives by the flow rates of 2, 4, and 6 mL/h at an initial distance of 6 cm, a voltage of 16 kV and a nozzle speed of 1 mm/s. Furthermore, each part of 3D structures fabricated using 12 wt% concentrations at 4 and 6 mL/h flow rates and using 14 wt% concentrations at 6 mL/h flow rate is shown in Figure B.2, B.3, and B.4. An increase in concentration from 10 to 12 wt% increased diameters; however, the average diameter of 14 wt% decreased, as seen in Figure B.5. It was attributed to the regular change in electrospinning distance. If there

are conditions that cannot perform the 3D formation, it means the distance will increase gradually. In other words, the lower height of the 3D structure means a longer distance of electrospinning. Even though no higher structures of 3D formation were found at 10 wt% concentration, the dripping and drying were found and were able to explain the bigger fiber. There is branching of small fibers from large fibers, like a taproot, and broken fibers in SEM images of 10 wt% (Figure 4.15). A. Haider et al. (2018) mentioned that the low concentration causes the entangled polymer chain to break fragments before reaching the collector, resulting in thicker fiber, beaded fiber, or bead. Fibers of various sizes, tangled together or connected together, have been found in SEM images of 12 wt% (Figure 4.16). The various morphologies found in the structures might relate to the upward structures. The average diameter of 14 wt% is thinnest and smoothest due to the broader distribution of deposited fiber and the lower structure height. If the controllable function and high structures are not needed, this solution is suitable. Notably, all morphologies of 3D formation showed a wide range of diameter. It was attributed to various lengths of electrospinning distance. The upcoming fibers enable first depositing on the top of deposited fibers (shorter distance), in which their height increases over time, and second depositing around the edge of structures (higher distance).

Normally, the polymer concentration is recommended to be optimized in the electrospinning technique (Al-Abduljabbar and Farooq, 2023), which is the same for 3D electrospinning. The threshold concentration is needed to maintain polarization and electrostatic induction, along with the balance of stable electrospinning, to form 3D-electrospun structures continuously. The 12 wt% concentration was chosen to investigate other parameters further to study and tune the parameters of 3D electrospinning to achieve optimal conditions.

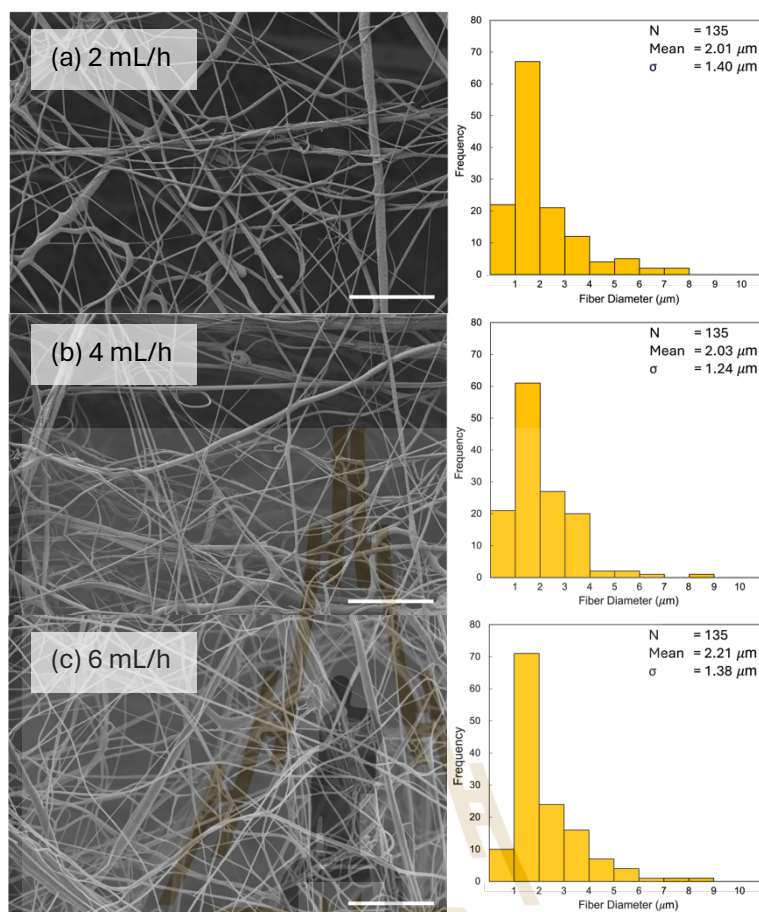


**Figure 4.15** SEM images and diameter histograms of fibers fabricated using 10 wt% concentration solutions prepared in 6:1 DCM:DMF solvent and 10% H<sub>3</sub>PO<sub>4</sub> additives with various flow rates, including (a) 2, (b) 4, and (c) 6 mL/h, under contents of initial distance, voltage, and nozzle speed at 6 cm, 16 kV, and 1 mm/s, respectively. The scale bar is 50 μm.

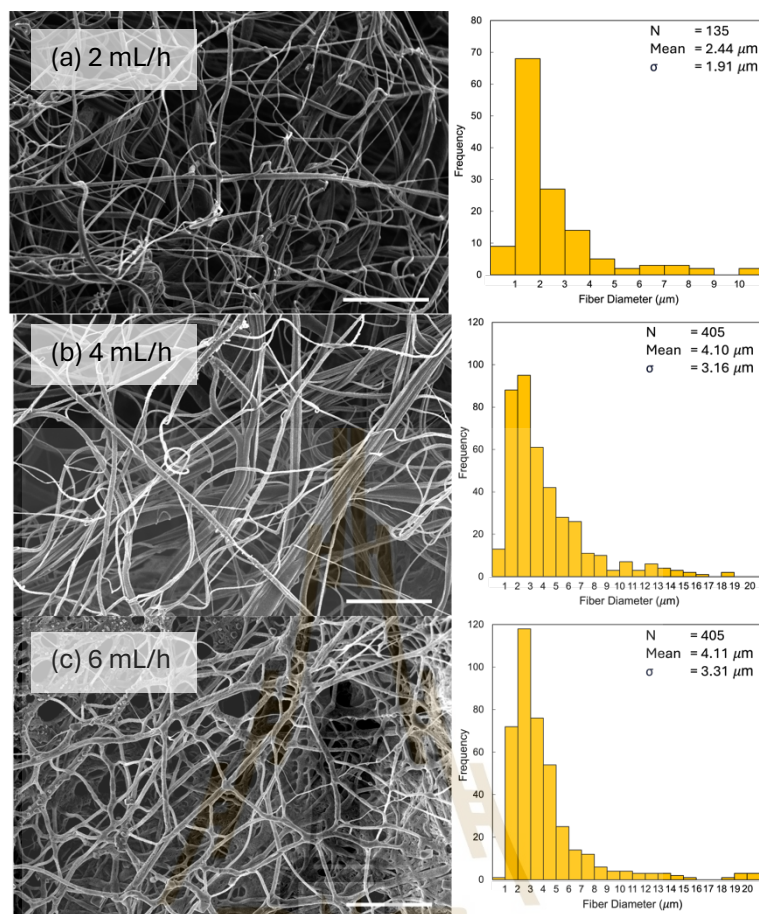


**Figure 4.16** SEM images and diameter histograms of fibers fabricated using 12 wt% concentration solutions prepared in 6:1 DCM:DMF solvent and 10%  $\text{H}_3\text{PO}_4$  additives with various flow rates, including (a) 2, (b) 4, and (c) 6 mL/h, under contents of initial distance, voltage, and nozzle speed at 6 cm, 16 kV, and 1 mm/s, respectively. The scale bar is 50  $\mu\text{m}$ .

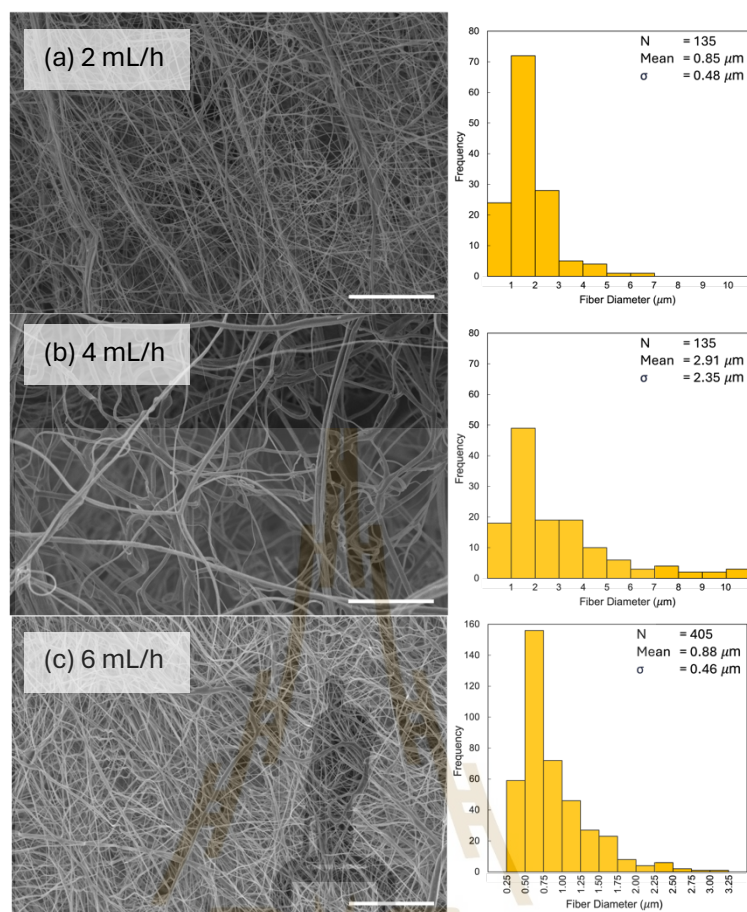


**Figure 4.17** SEM images and diameter histograms of fibers fabricated using 14 wt% concentration solutions prepared in 6:1 DCM:DMF solvent and 10%  $H_3PO_4$  additives with various flow rates, including (a) 2, (b) 4, and (c) 6 mL/h, under contents of initial distance, voltage, and nozzle speed at 6 cm, 16 kV, and 1 mm/s, respectively. The scale bar is 50  $\mu\text{m}$ .

#### Relation between solvent ratio and flow rate

The solvent is another important factor in the 3D self-assembly because the formation employs rapid solidification alongside electrostatic induction. A high evaporation rate of volatile solvent is desired; however, a high evaporation can cause the solution to dry at the nozzle tip, resulting in clogging (A. Haider et al., 2018). In this work, DCM was chosen because of its high evaporation rate, and DMF was added to decrease the issue with solution drying at the nozzle. The DCM:DMF solvent ratios of 4:1, 6:1, and 8:1 by weight were surveyed to obtain the optimal ratio for 3D buildup.

The side view of all the final structures is shown in Figure 4.18. The only solutions prepared by using the solvent of 6:1 performed stable processes of electrospinning, while there was some clogging at the tip of the nozzle and dripping to the collector for the ratios of 4:1 and 8:1 at 2, 4, and 6 mL/h and 2 and 4 mL/h, respectively. In the case of 4:1, it was expected that the slower flow rate, less than 2 mL/h, might provide more stability, and the 6 mL/h and faster flow rate could provide stable electrospinning for an 8:1 solvent mixture. It might cause the large volume of DCM and the higher volume of fast-evaporation solvent to need a faster flow rate to avoid the issue of drying and clogging, while the large volume of DMF might need a slower flow rate to complete the evaporation. The clogging at the nozzle tip represents a major problem for the 3D formation.

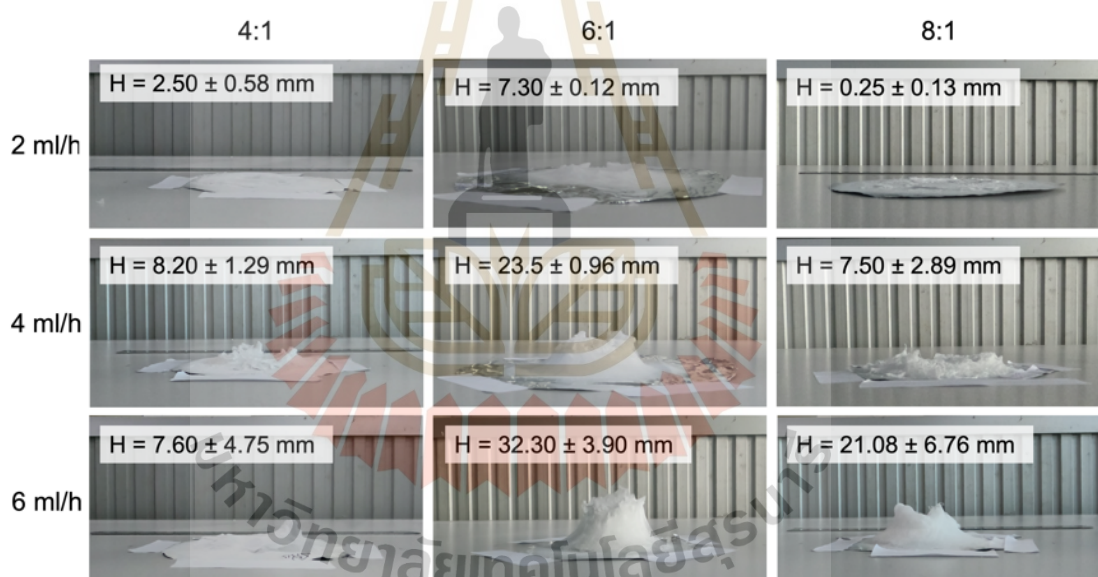


**Figure 4.18** The side view of 3D formations fabricated by using various solvent ratios of DCM:DMF, namely 4:1, 6:1, and 8:1. These solvents were employed in the preparation of 12 wt% PCL solutions with the addition of 10%  $H_3PO_4$ . All experiments were conducted with a flow rate of 2, 4, and 6 mL/h, an initial distance of 6 cm, a voltage of 16 kV, and a nozzle speed of 1 mm/s via the 3D electrospinning for 30 minutes in the ambient environment.

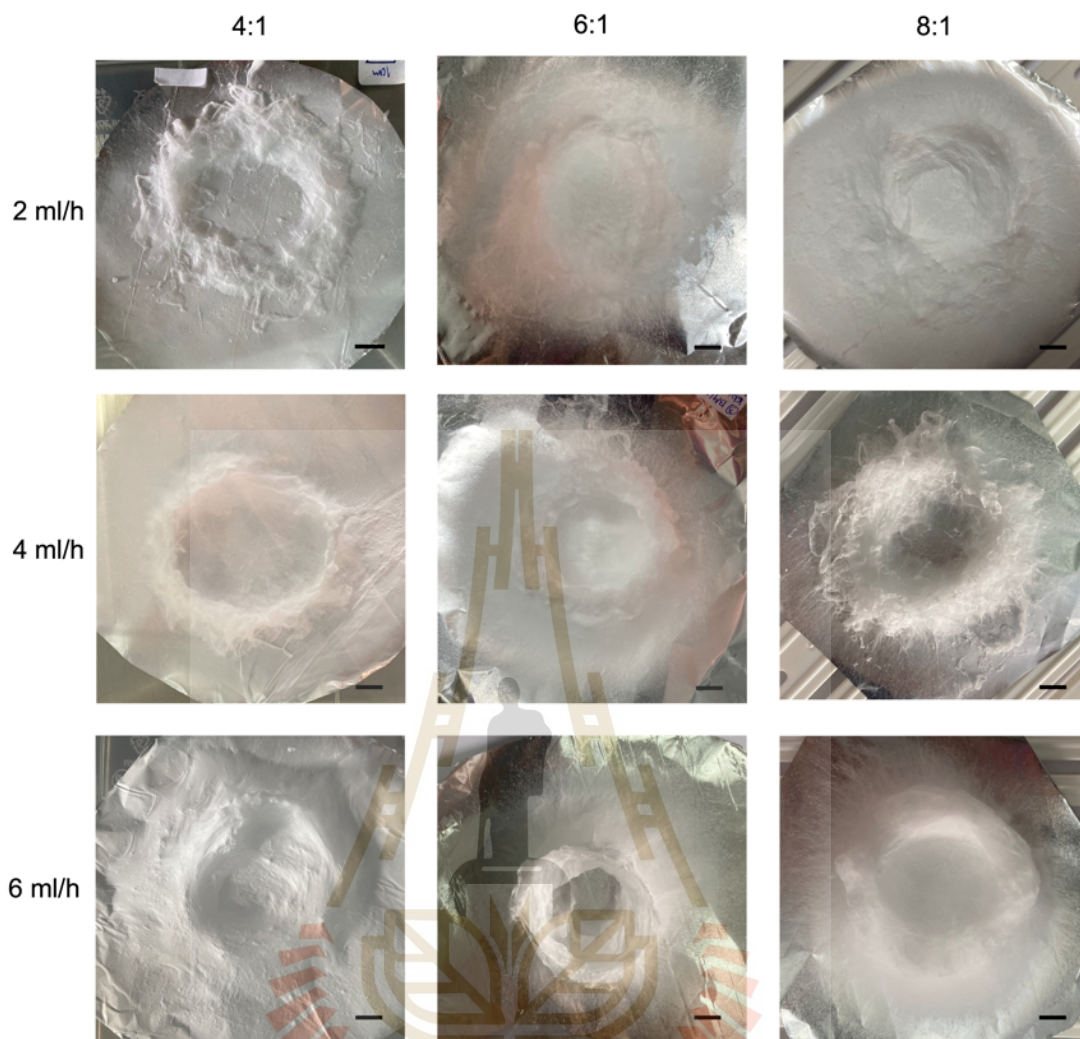


**Figure 4.19** The top view of 2D mats and 3D constructs fabricated by using various solvent ratios of DCM:DMF, namely 4:1, 6:1, and 8:1. These solvents were employed in the solution preparation of a 12 wt% PCL concentration with the addition of 10%  $\text{H}_3\text{PO}_4$ . All experiments were conducted with flow rates of 2, 4, and 6 mL/h, an initial distance of 6 cm, a voltage of 16 kV, and a nozzle speed of 1 mm/s via 3D electrospinning for 30 minutes in the ambient environment. The scale bar is 10 mm.

As seen in the top view of electrospun structures in Figure 4.19, an increase in the DCM ratio resulted in a wider wall thickness. Bain and Koomsap (2016) reported the effect of DCM/DMF solvent in the PCL solution used in NFES that a high amount of DCM performed the random deposition of PCL fibers due to the whipping effect, and a decreasing amount of DCM would offer straight fibers. Because the high evaporation rate of DCM increased surface tension on a droplet, a large amount of

charge was required to overcome the surface tension, leading to repulsive forces and the whipping effect. Similarly, an increase in the DCM ratio increased the deposition area at a flow rate of 2 mL/h. However, it was changed when the structure was moved upward because the deposition of fiber on the 3D structure was moved from the flat collector to the edge and top of the structures.

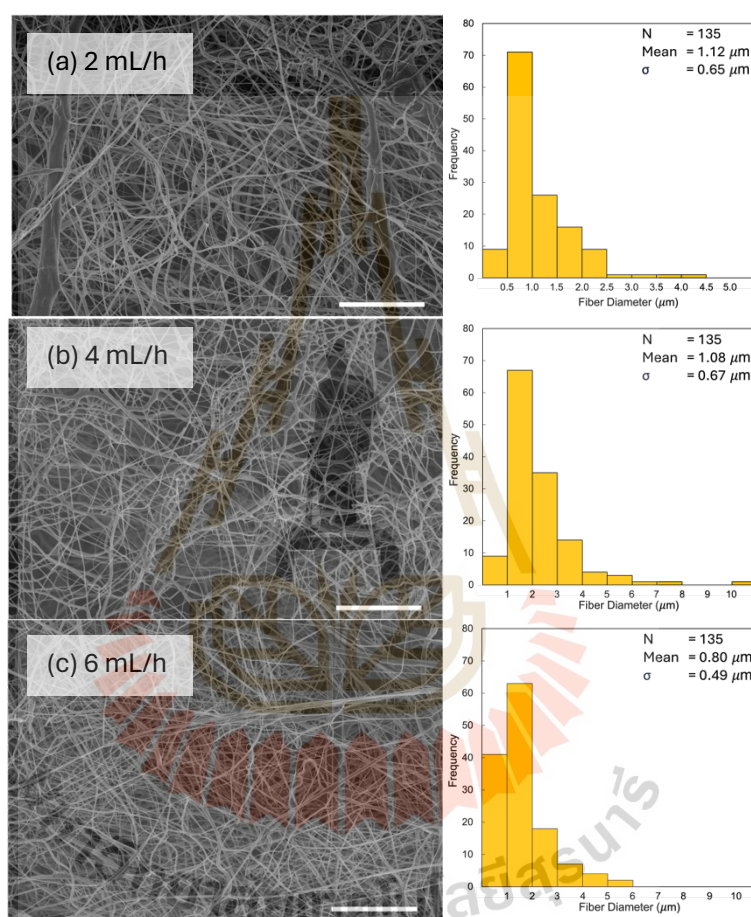


**Figure 4.20** SEM images and diameter histograms of fibers fabricated using 12 wt% concentration solutions prepared in 4:1 ratio of DCM:DMF solvent and 10%  $H_3PO_4$  additives with various flow rates, including (a) 2, (b) 4, and (c) 6 mL/h, under constants of initial distance, voltage, and nozzle speed at 6 cm, 16 kV, and 1 mm/s, respectively. The scale bar is 50  $\mu\text{m}$ .

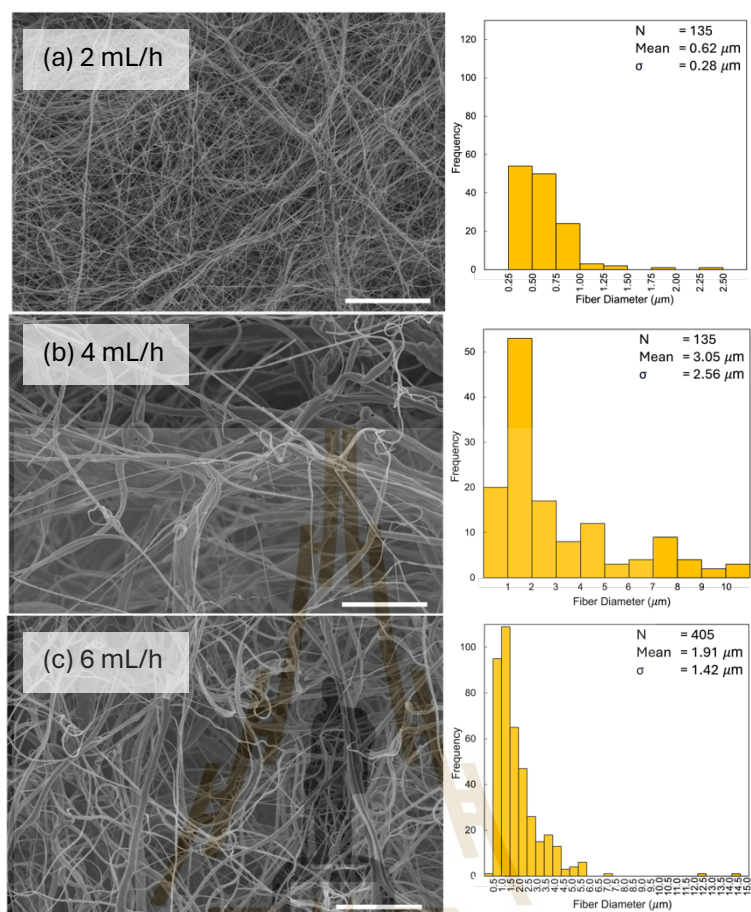


**Figure 4.21** SEM images and diameter histograms of fibers fabricated using 12 wt% concentration solutions prepared in 8:1 ratio of DCM:DMF solvent and 10%  $H_3PO_4$  additives with various flow rates, including (a) 2, (b) 4, and (c) 6 mL/h, under constants of initial distance, voltage, and nozzle speed at 6 cm, 16 kV, and 1 mm/s, respectively. The scale bar is 50  $\mu\text{m}$ .

The morphology of 2D mats and 3D structures is shown in Figure B.6. The SEM images and diameter histograms of overall electrospun fibers are demonstrated in Figure 4.20, 4.16, and 4.21 for 3D fibrous structures fabricated using 4:1, 6:1, and 8:1 ratios of DCM:DMF solvents, respectively, with 10 wt%  $H_3PO_4$  additives in 12 wt% PCL concentration by the flow rates of 2, 4, and 6 mL/h at an initial distance of 6 cm, a voltage of 16 kV and a nozzle speed of 1 mm/s. To be more detailed, each part of 3D structures fabricated using the 6:1 solvent ratio at 4 and 6 mL/h flow rates and using the 8:1 solvent ratio at 6 mL/h flow rate is shown in Figure B.2, B.3, and B.7. The average diameters fluctuated, as seen in Figure B.8, because of many associated

factors, including solvent, spinning distance, and voltage. It found that the average diameter of structures was related to the structure height. The higher structures had a larger diameter because the tops of the structures were closer to the nozzle. The 6:1 ratio of DCM:DMF was used to be the optimal solvent for 3D PCL formation through 3D electrospinning because of stable spinning.

#### Relation between additives and flow rate

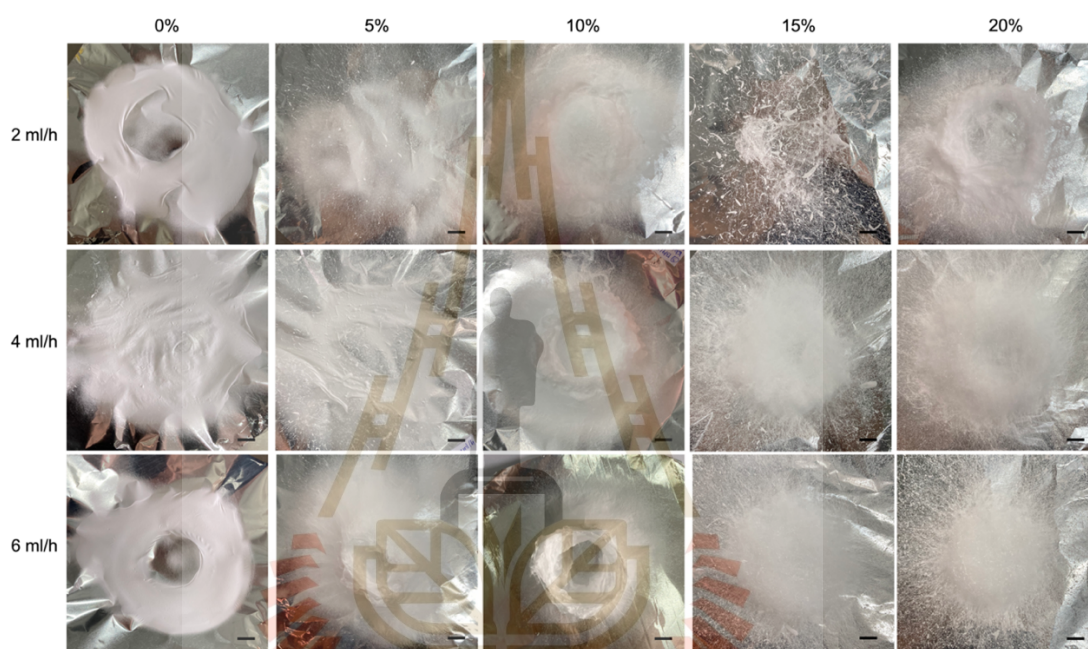


**Figure 4.22** The top view of 2D mats and 3D constructs fabricated by using various amounts of  $\text{H}_3\text{PO}_4$  additives, including 0, 5, 10, 15, and 20%. These additives were employed in the solution preparation of 12 wt% PCL concentrations in the DCM:DMF solvent ratio of 6:1. All experiments were conducted with a flow rate of 2, 4, and 6 mL/h, an initial distance of 6 cm, a voltage of 16 kV, and a nozzle speed of 1 mm/s via the 3D electrospinning for 30 minutes in the ambient environment. The scale bar is 10 mm.

The addition of additives, including 0, 5, 10, 15, and 20%, was added to the 12 wt% PCL solution, which was prepared in 6:1 of DCM:DMF solvent, to investigate 3D buildup of 3D structures with the flow rate of 2, 4, and 6 mL/h at the initial distance of 6 cm, the voltage of 16 kV, and the moving speed of 1 mm/s. Among the solution

parameters, including concentration, solvent ratio, and additives, the number of additives directly affects the existing hollow shape of 3D-electrospun structures under the constant parameters of flow rate, initial distance, voltage, and moving speed, as shown in Figure 4.22. The change of concentration and solvent ratio still showed the traces of deposited fiber as cylinder paths, while the increase of additives beyond a critical point led to the fluffy structures without the controllable ability of shape. It was because the increase in additives increases the repulsive forces of fibers, leading to a wider length of raising-up fiber. Therefore, the additives affect the potential control position.

The evolution of existing additives in the buildup of 3D-electrospun macrostructure is shown in Figure 4.23. The PCL solutions without  $\text{H}_3\text{PO}_4$  additives did not perform 3D-fibrous formations. When 5%  $\text{H}_3\text{PO}_4$  was added to the solution, the 3D formation happened. Similarly, PCL solutions with 10, 15, and 20%  $\text{H}_3\text{PO}_4$  additives were able to form a 3D structure when applying a flow rate of 4–6 mL/h. It is in accordance with the results reported in previous studies (Hwang et al., 2020; Lee et al., 2021). The pure PCL solution can only produce a 2D fibrous membrane, and the incorporation of lactic acid into the PCL solution aims to form 3D sponge-like structures (Hwang et al., 2020). The existing  $\text{H}_3\text{PO}_4$  additives in PS solution supported the control and formation of 3D structures (Vong et al., 2018). The mechanism behind the self-assembled formations of electrospun fibers relates to polarization and electrostatic induction of the deposited fibers. It has been confirmed that adding additives is another important part of 3D self-assembly. However, adding too many additives changes the final shape of 3D-electrospun structures and can lead to the formation of beads. As seen in Figure 4.22, the 5 and 10% additive concentrations still maintain the shape of the hollow cylinder, while 15 and 20% concentrations were not able to provide the hollow shape. At 6 mL/h, the raised-up fibers, which was the first step that allowed 3D self-assembled fiber, began to form in about 40 seconds, and 2 seconds for the addition of 5 and 10%  $\text{H}_3\text{PO}_4$ , respectively. While the raised-up fiber had occurred since the first second when using the solutions with addition of 15 and 20%  $\text{H}_3\text{PO}_4$ . Nonetheless, the existing 2D mat at the bottom part formed from the accumulation of depositing fiber during the formation. Adding the additive causes the

wider raised-up fibers, resulting in the spreading of fiber and also the solution drying at the nozzle. Since the addition of  $H_3PO_4$  might increase the charge accumulation at the Taylor cone.

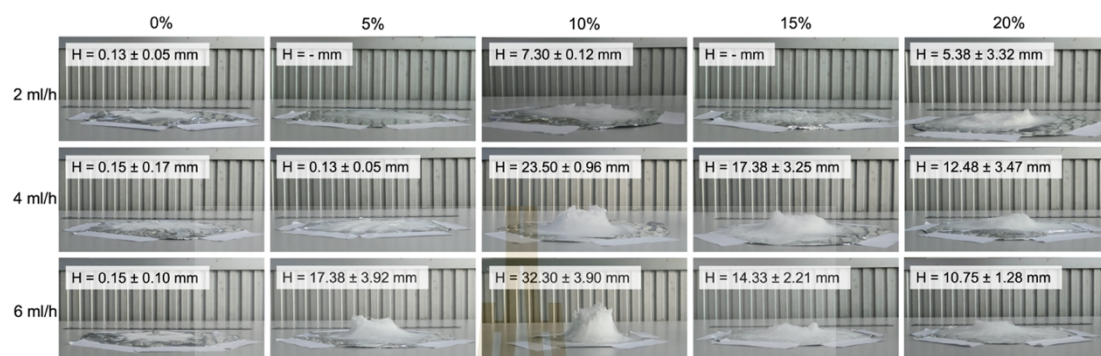


**Figure 4.23** The side view of 3D formations fabricated using various additions of  $H_3PO_4$  additives, including 0, 5, 10, 15, and 20%, into 12 wt% PCL solutions in a DCM:DMF solvent of 6:1 ratio. These solutions were executed at a flow rate of 2, 4, and 6 mL/h, an initial distance of 6 cm, a voltage of 16 kV, and a nozzle speed of 1 mm/s via the 3D electrospinning for 30 minutes in the ambient environment.

The SEM images shown in Figure B.9 demonstrated an increase in the pore size, corresponding to the increasing proportion of  $H_3PO_4$ . Similarly, Hwang et al. (2020) reported that the pore size of 3D-fibrous scaffolds varies according to LA contents. The increase in LA content resulted in higher conductivity and lower viscosity of solution, leading to a number of fibers coming down onto the collector at the same time. This is also another reason why the shape of the 3D PCL formation cannot be controlled in the hollow cylinder when increasing the additives to 15 and 20%. Higher additives induced a wider area of deposition (Figure 4.22). To be illustrated, the SEM images and diameter histograms of overall electrospun fibers are demonstrated in Figure 4.24, 4.25, 4.16, 4.26, and 4.27 for 3D fibrous structures fabricated using 0, 5, 10, 15, and 20 wt%  $H_3PO_4$  additives in the 12 wt% PCL concentration in the 6:1 DCM:DMF solvent by the flow rates of 2, 4, and 6 mL/h at an initial distance of 6 cm, a voltage of 16 kV and a nozzle speed of 1 mm/s. Each part of 3D structures fabricated using 5 wt%  $H_3PO_4$  at 6 mL/h flow rate, 10 wt%  $H_3PO_4$  at 4 and 6 mL/h flow rates, 15 wt%  $H_3PO_4$  at 4 mL/h flow rate, and 20 wt%  $H_3PO_4$  at 4 mL/h flow rate is shown in Figure B.10, B.2, B.3, B.11

and B.12. An increase in additives had an increasing trend in diameter, as shown in Figure B.13. Furthermore, the excessive additives, including the  $\text{H}_3\text{PO}_4$  contents of 15% and 20%, obviously resulted in the formation of beads. The suitable solvent ratio for making PCL solutions in which the impact of spinning parameters was examined was determined to be 10%  $\text{H}_3\text{PO}_4$ .

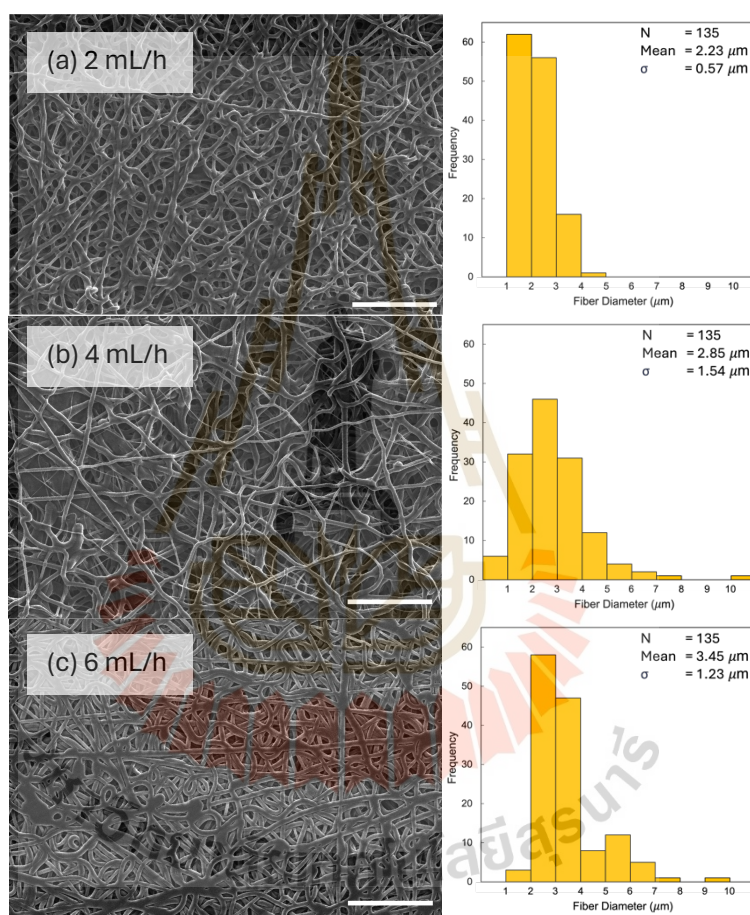


**Figure 4.24** SEM images and histograms of fiber diameters which the fibers were fabricated using 12 wt% concentration solutions prepared in 6:1 DCM:DMF solvent and 0%  $\text{H}_3\text{PO}_4$  additive with various flow rates, including (a) 2, (b) 4, and (c) 6 mL/h, under constants of initial distance, voltage, and nozzle speed at 6 cm, 16 kV, and 1 mm/s, respectively. The scale bar is 50  $\mu\text{m}$ .

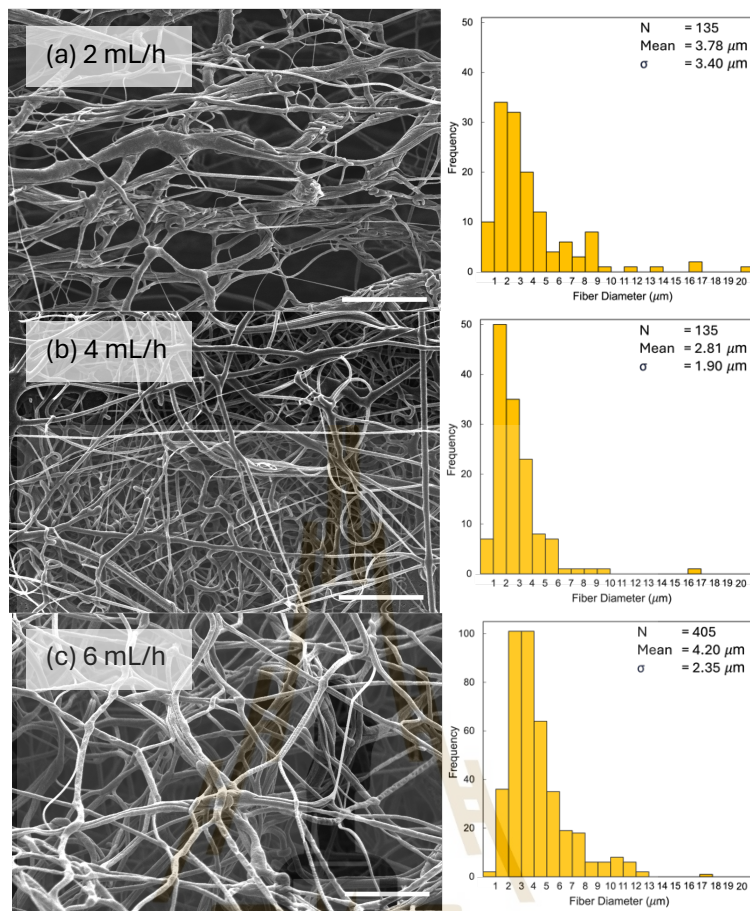


**Figure 4.25** SEM images and histograms of fiber diameters which the fibers were fabricated using 12 wt% concentration solutions prepared in 6:1 DCM:DMF solvent and 5%  $H_3PO_4$  additive with various flow rates, including (a) 2, (b) 4, and (c) 6 mL/h, under constants of initial distance, voltage, and nozzle speed at 6 cm, 16 kV, and 1 mm/s, respectively. The scale bar is 50  $\mu\text{m}$ .

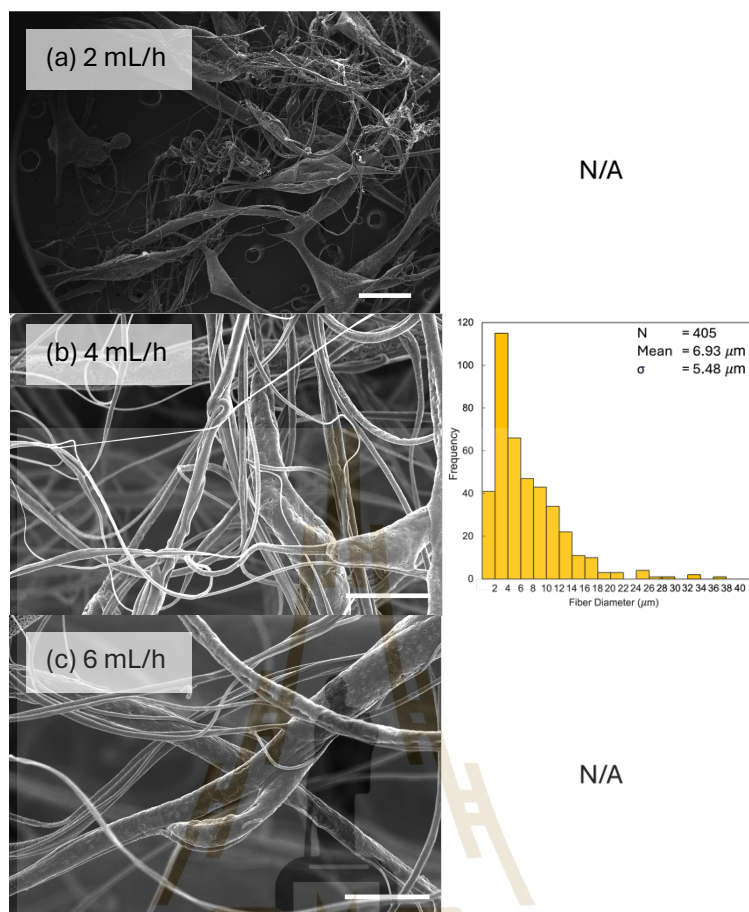


**Figure 4.26** SEM images and histograms of fiber diameters which the fibers were fabricated using 12 wt% concentration solutions prepared in 6:1 DCM:DMF solvent and 15%  $\text{H}_3\text{PO}_4$  additive with various flow rates, including (a) 2, (b) 4, and (c) 6 mL/h, under constants of initial distance, voltage, and nozzle speed at 6 cm, 16 kV, and 1 mm/s, respectively. The scale bar is 50 μm.

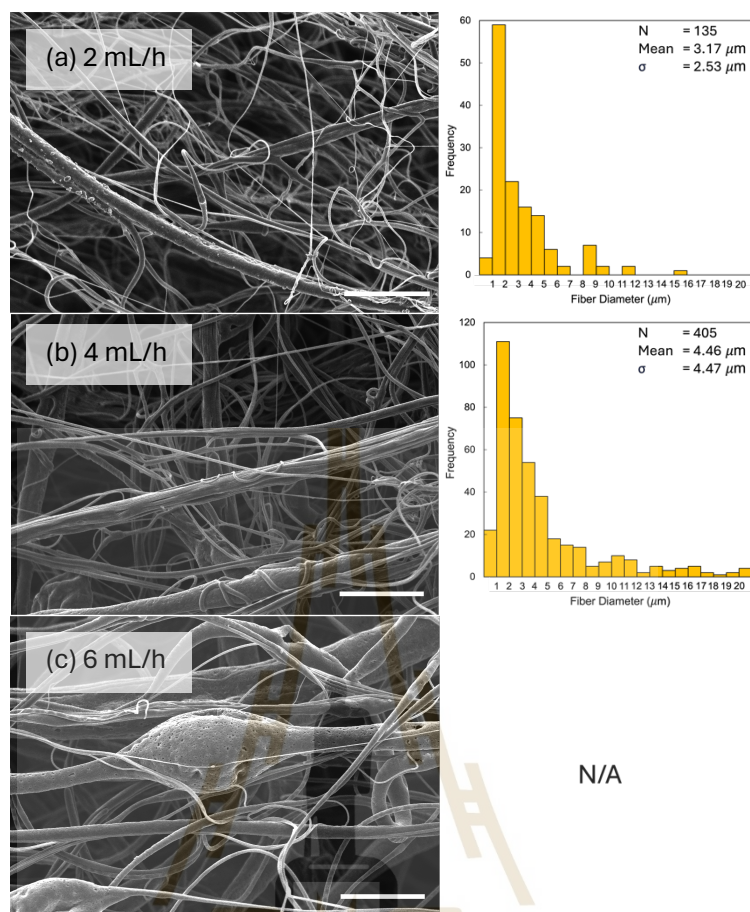


**Figure 4.27** SEM images and histograms of fiber diameters which the fibers were fabricated using 12 wt% concentration solutions prepared in 6:1 DCM:DMF solvent and 20%  $\text{H}_3\text{PO}_4$  additive with various flow rates, including (a) 2, (b) 4, and (c) 6 mL/h, under contents of initial distance, voltage, and nozzle speed at 6 cm, 16 kV, and 1 mm/s, respectively. The scale bar is 50  $\mu\text{m}$ .

### Electrospinning parameters

The PCL solution with a 12% wt concentration in 6:1 by weight DCM:DMF was used to investigate the electrospinning factors, including the flow rate of solution, the initial distance between a nozzle and a collector, the HV applied between the nozzle and the collector, and the nozzle moving speed, on the buildup of 3D PCL-electrospun macrostructures.

### Flow rate

Knowing a minimum flow rate is necessary for sufficient depositing fibers to perform the 3D buildup (Radacsi and Nuansing, 2020). A balance between the amount of the extruded solution and the replacement of the new solution during electrospinning is needed. The flow rate in a range of 2, 3, 4, 5, and 6 mL/h was used to study the 3D buildup under an initial distance of 6 cm, a voltage of 16 kV, and a nozzle moving speed of 1 mm/s.

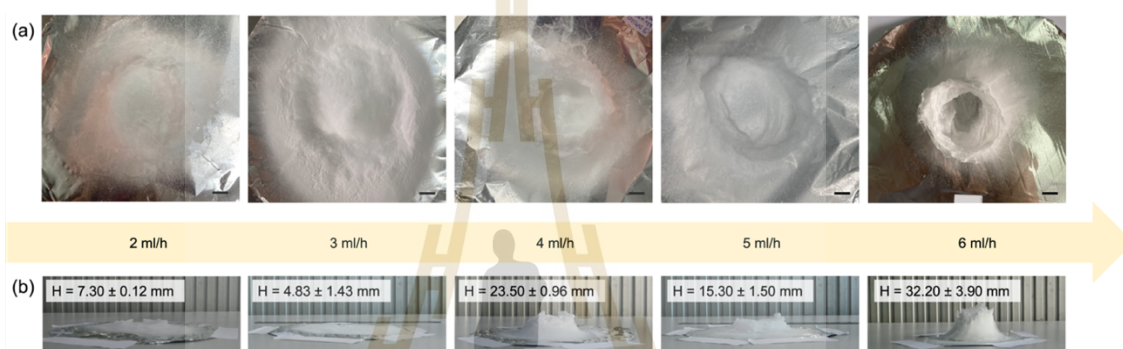


**Figure 4.28** (a) The top and (b) side views of comparative 3D PCL-electrospun constructs by varying the values of a flow rate. The flow rate of solution, 12% wt PCL solution in 6:1 DCM:DMF + 10% H<sub>3</sub>PO<sub>4</sub>, is increased from 2 to 6 mL/h, with each increment being 1 mL/h. The 3D PCL formations were performed at an initial distance of 6 cm, a voltage of 16 kV, and a nozzle speed of 1 mm/s for 30 minutes.

As shown in Figure 4.28, the 3D buildup occurred when using the flow rate of 4 mL/h, and the height of structures is likely to increase following an increase in the flow rate. The increase in flow rate relates to a higher amount of polymer solution extruded from the tip of the nozzle. As seen in Figure 4.29, an increasing amount of the raising-up fibers deposited onto the collector following an increase in flow rate was observed. However, the appearance of the depositing fiber changed from the vertically raised-up fibers to the horizontally widespread fibers when the 3D structures were unable to grow up in response to the rising distance between the nozzle and collector, as shown in Figure 4.27(b, d). This resulted in losing the position control of depositing fiber and a wider fiber deposition, finally achieving a 2D mat. The flow rate of 4 mL/h showed enough depositing fibers to enable being dragged

following the model throughout the 3D buildup. At the flow rate of 5 mL/h, the solution was drying and clogging at the nozzle's tip, resulting in discrete 3D buildup. Although it performed normal self-assembly formations after the dripping, the height of the obtained structures was decreased. At a flow rate of 6 mL/h, the raising-up fiber was drawn following the model at the initial stage. When the structure was higher, the raising-up fiber was shorter, and the coming fiber was deposited at the edge of the structure. It was attributed to the increasing amount of coming fiber, resulting in faster buildup than 4 mL/h. Interestingly, a faster flow rate at the flow rates of 5 and 6 mL/h induced some shape-shifting, as seen in Figure 4.28. A sufficient amount of coming fiber is necessary to obtain charge induction, polarization effect, and repulsive force between fibers to build up; however, the excessive amount at the high flow rate decreases printing quality (Radacsi and Nuansing, 2020; Vong et al., 2018). This work uses the flow rate of 4 mL/h as the optimal condition for the 3D buildup of 12 wt% PCL solution.

As mentioned before, an increase in flow rate enables the rapid buildup of 3D macrostructures and is likely to result in an increase in their height. However, above a certain flow rate, shape-shifting, structure collapse, and solution clogging was observed. The height of the structure starts to decrease at a flow rate of 5 mL/h due to the discontinued accumulation resulting from the drying of the solution. The increase in flow rate performed a wider deposition area in the range of 2-3 mL/h, in which a 2D mat was obtained. It is in agreement with Vong et al. (2018). The DW at 2 mL/h was  $80.88 \pm 1.33$  mm and increased to  $93.55 \pm 7.10$  mm when the flow rate was increased to 3 mL/h. Nevertheless, the DW decreased as the structures were higher, as indicated in Table 4.2. The deposition width of the first layer was caused by the deposition of the electrospun mat at the initial stage. It was attributed to the continuous positioning of depositing fiber on the top and at the edge of structures during electrospinning. As the structures rise, some depositing fibers will deposit onto the edge of the structures instead of the collector. This results in increased  $C_{hh}$  and decreased  $D_{out}$  when height is higher. The wall thickness measured at the top of structures was thinner with an increase in flow rate of  $8.28 \pm 0.61$  mm,  $6.05 \pm 1.10$  mm, and  $2.69 \pm 0.57$  mm for the applying flow rate at 4, 5, and 6 mL/h. An increase

in flow rate induces a longer straight jet (Joy, Anuraj, Viravalli, Dixit, and Samavedi, 2021), and an increased structure's height enables balancing the electrospinning distance, resulting in no increase in the length of the whipping jet.

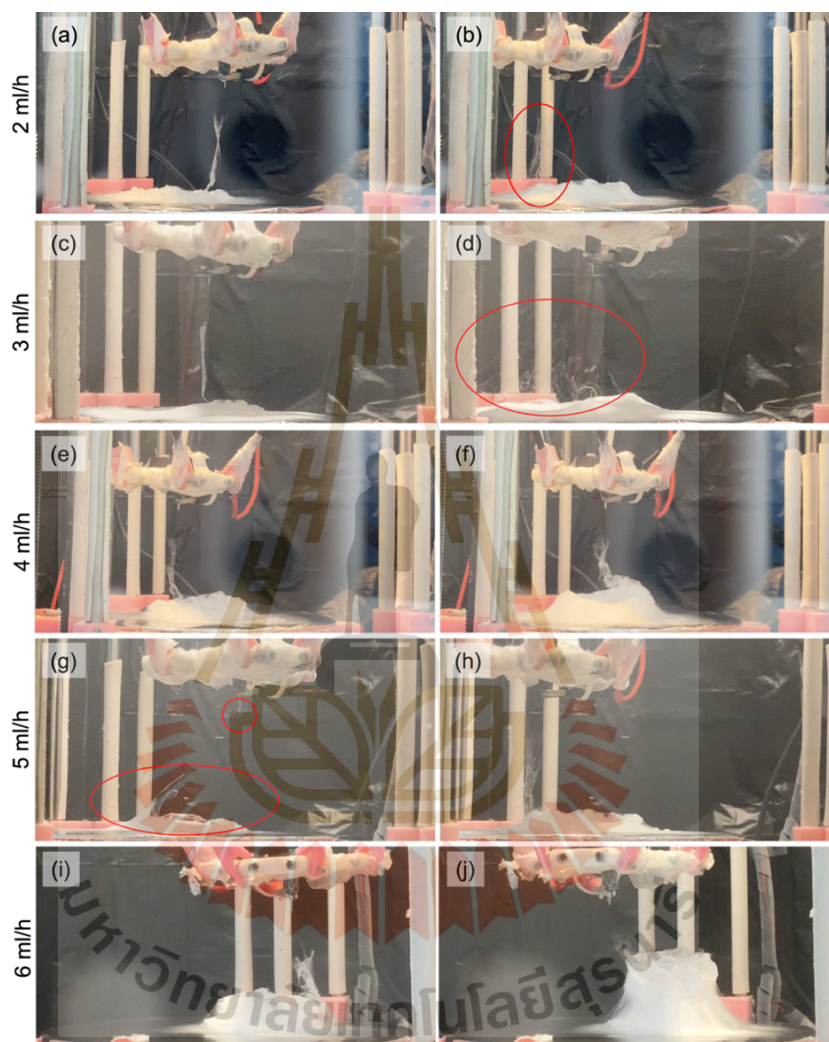


**Figure 4.29** Various situations of 3D buildups via 3D electrospinning, which were run with various flow rates of (a-b) 2, (c-d) 3, (e-f) 4, (g-h) 5, and (i-j) 6 mL/h at an initial distance of 6 cm, a voltage of 16 kV, and a nozzle moving speed of 1 mm/s for 30 minutes in an ambient environment. The images were captured at different times that were 9.56, 24.11, 9.58, 23.59, 10.02, 27.01, 10.42, 24.12, 9.50, and 24.16 minutes, respectively.

**Table 4.2** The summarization of the height, the  $C_{hh}$ , the DW, the  $D_{out}$ , and wall thickness of 3D structures obtained from various flow rates, including 2, 3, 4, 5, and 6 mL/h. The experimental conditions, including a voltage, an initial distance, a flow rate, and a nozzle moving speed applied in the 3D buildup, were named voltage-initial distance-flow rate-moving speed.

Experimental conditions [kV-cm-mL/h-mm/s]	Height [mm]	$C_{hh}$ [mm]	DW [mm]	$D_{out}$ [mm]	Wall thickness [mm]
16-6-2-1	$7.30 \pm 0.12$	$3.88 \pm 0.44$	$80.88 \pm 1.33$	$61.68 \pm 2.58$	$11.55 \pm 3.10$
16-6-3-1	$4.83 \pm 1.43$	-	$93.55 \pm 7.10$	-	-
16-6-4-1	$23.50 \pm 0.96$	$12.69 \pm 1.09$	$81.10 \pm 4.69$	$52.70 \pm 1.56$	$8.28 \pm 0.61$
16-6-5-1	$15.30 \pm 1.50$	$10.61 \pm 0.23$	$81.20 \pm 2.74$	$55.40 \pm 2.13$	$6.05 \pm 1.10$
16-6-6-1	$32.25 \pm 3.86$	$20.09 \pm 2.78$	$71.88 \pm 3.82$	$41.72 \pm 0.88$	$2.69 \pm 0.57$

The SEM images and diameter histogram of fibers varying flow rates is shown in Figure 4.30. The morphological characteristics of electrospun mat at flow rates of 2 and 3 mL/h were similar. Thinner fibers were intertwined with larger fibers. The average diameter at 2 mL/h was  $2.40 \pm 1.90 \mu\text{m}$  and decreased to  $1.80 \pm 1.30 \mu\text{m}$  when applying 3 mL/h. The small decrease in diameter at 3 mL/h might correspond to the slight decrease in the structure's height, resulting in a little increase in the distance. A decrease in volumetric flow rate resulted to an increase in volume charge density and faster travel of the charged jet toward the collector, leading to thicker fiber (Šimko and Lukáš, 2016). The SEM image of 3D fibrous structures in Figure B.14 displays numerous intricate and sizable fibers. The lower part of 3D structures at flow rates of 4, 5, and 6 mL/h had the lowest average diameter (Figure B.2, B.15, B.3, respectively). As a result, the middle and/or top parts that were closer to the nozzle had a larger diameter. The average diameter of the upper part at 4 mL/h was significantly different from the middle and lower parts. When the flow rate increased to 6 mL/h, the average diameter of the lower part was significantly different from other parts. This was consistent with what happened during the 3D formation: the high flow rate resulted in faster buildup. The average diameter did not exhibit a rise with the increase in solution flow rate due to the wide range of diameter, as seen in Figure B.16(b).

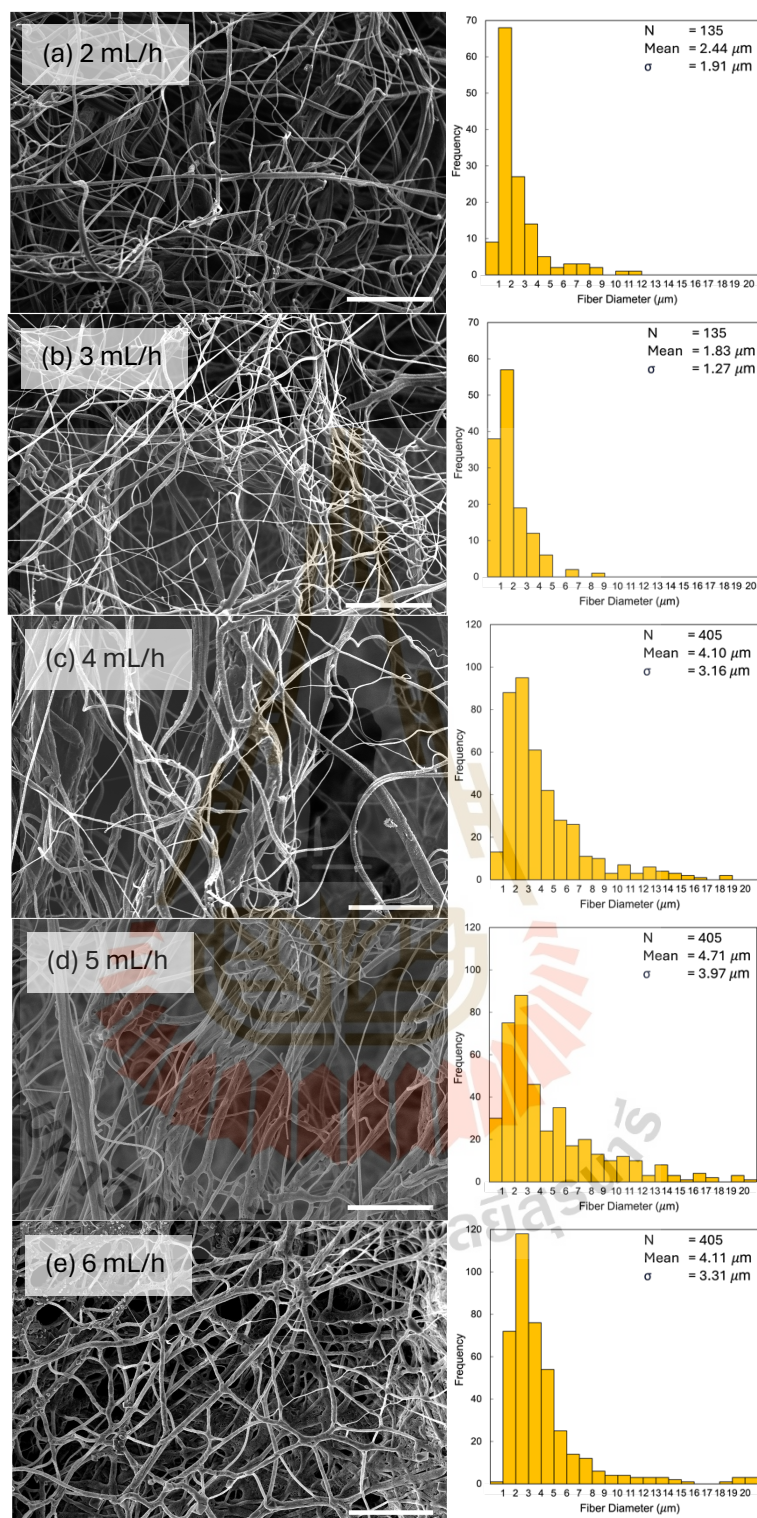


**Figure 4.30** SEM images and histograms of fiber diameter fabricated with various flow rates, including (a) 2, (b) 3, (c) 4, (d) 5, and (e) 6 mL/h, under contants of initial distance, voltage, and nozzle speed at 6 cm, 16 kV, and 1 mm/s, respectively. The scale bar is 50  $\mu\text{m}$ .

### Initial distance

An initial distance is one of the necessary parameters in 3D-electrospun buildup since it relates to the determination of buildup height (Vong et al., 2018). The electrospinning distance changes over time following the nozzle movement. The 12 wt% PCL solution prepared in 6:1 DCM:DMF solvent was used to investigate a varying initial distance of 2 to 6 cm under a flow rate of 4 mL/h, a voltage of 16 kV, and a nozzle moving speed of 1 mm/s. All experiments were carried out for 30 minutes in an ambient environment. Figure 4.31 shows the evolution of the 3D buildup by varying the initial distance.

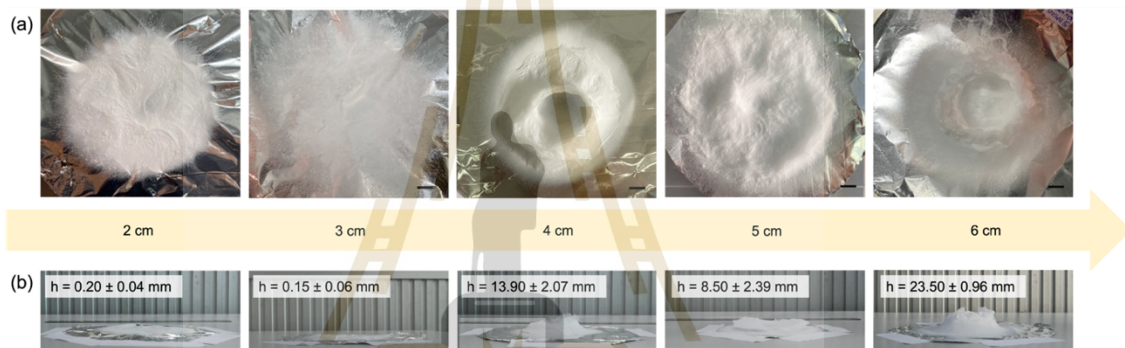


**Figure 4.31** (a) The top and (b) side views of comparative 3D PCL-electrospun constructs by varying the values of an initial distance. The initial distance applied to run the formation procedure of a 12% wt PCL solution in 6:1 DCM:DMF + 10% H<sub>3</sub>PO<sub>4</sub> is increased from 2 to 6 cm, subsequently raised in increments of 1 cm. The 3D PCL structures were formed at a flow rate of 4 mL/h, a voltage of 16 kV, and a nozzle speed of 1 mm/s for 30 minutes.

At initial distances of 2 and 3 cm, the 2D mat was finally obtained. As seen in Figure 4.32(a–d), the deposition of rising-up fibers was scattered in various positions. At the initial stage, the deposition pathway of spun fiber remained the hollow cylinder (Figure 4.32(a–c)); however, it finally disappeared because of the widespread deposition, resulting in the circle mat (Figure 4.31(a)). There were also some drips and drying at the tip of the nozzle due to the short distance. It showed the initial distance at 2 and 3 cm is too short to form 3D fibrous macrostructures.

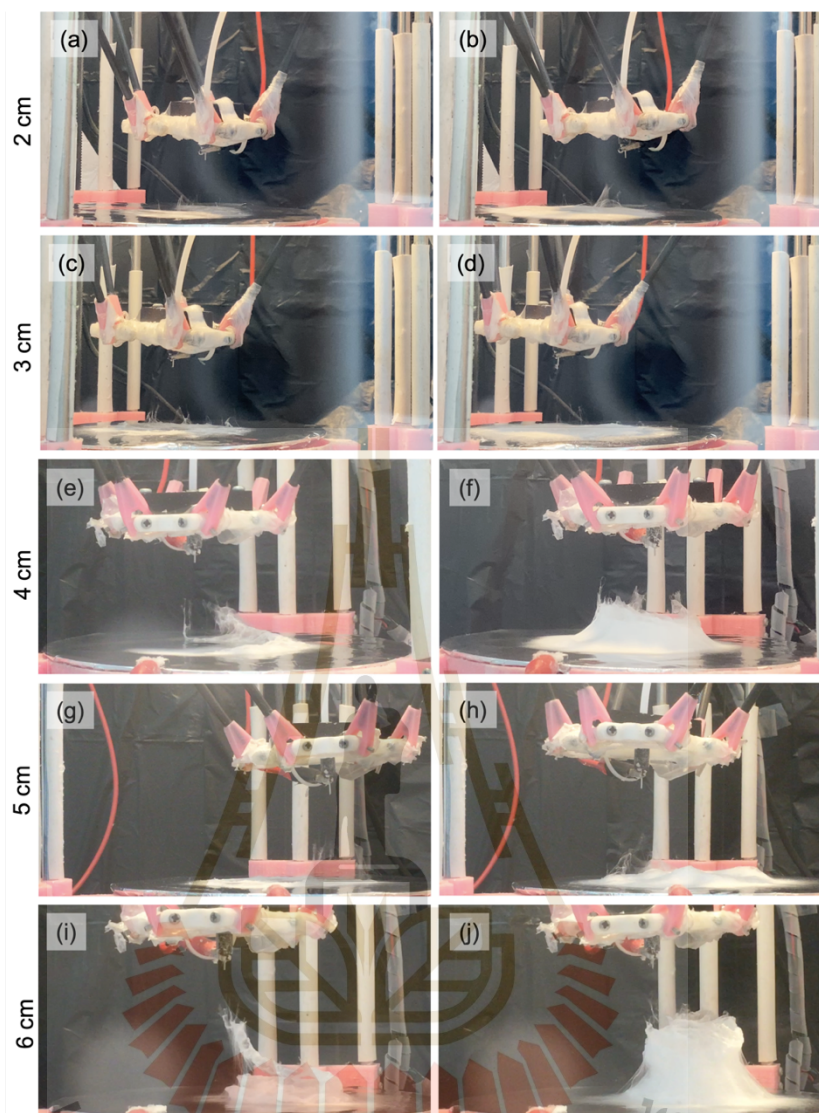


**Figure 4.32** Various situations of 3D buildups via 3D electrospinning, which were run with various initial distances of (a-b) 2, (c-d) 3, (e-f) 4, (g-h) 5, and (i-j) 6 cm at a flow rate of 4 mL/h, a voltage of 16 kV, and a nozzle moving speed of 1 mm/s for 30 minutes in an ambient environment. The images were captured at different times: 1.02, 24.46, 2.22, 22.00, 1.36, 25.32, 1.50, 24.34, 6.02, and 24.00 minutes, respectively.

The 3D buildup started at the initial distance of 4 cm. The raising-up fiber, which enabled moving along the nozzle, was observed at the initial stage. It was worth mentioning that there were rising-up fibers in two directions on previously fiber-deposited structures, as seen in Figure 4.32(e-f). This effect was attributed to the multi-jet ejection of electrospinning. Joy et al. (2021) revealed the multi-jet regime was found

when decreasing the distance at a constant voltage, and a decreasing distance was likely to increase the number of multi-jet splits. With this situation, it may be another reason for the widespread deposition at 2 and 3 cm. Likewise, the multi-jet ejection was found at the initial stage under the initial distance of 5 cm and disappeared when the nozzle moved upward. The unbalance of upward height between nozzles and structures resulted in widespread deposition and finally obtaining mat for the initial distance of 5 cm. Nevertheless, the multi-jet ejection was not found at the initial distance of 6 cm. The raising-up fiber containing many electrospun fibers enables nozzle movement in one position instead of wide deposition, leading to 3D buildup.

The increase in the initial distance allows for higher structures; however, it might risk being inconsistent and unstable because of the longer length of the whipping jet. The increase in the initial distance increased the deposition areas, similar to the results reported by Vong et al. (2018). Separately considering the 2D mat and 3D structures, the DW of the initial distance of 2, 3, and 5 cm was  $85.76 \pm 3.59$ ,  $91.37 \pm 4.72$ , and  $93.30 \pm 2.53$  mm. Similarly, the DW increased from  $78.95 \pm 2.28$  to  $81.10 \pm 4.69$  mm when increasing the initial distance from 4 to 6 cm. Likely, the increase in the initial distance allowed for a larger wall thickness, which was increased from  $4.50 \pm 2.26$  to  $8.28 \pm 0.61$  mm when increasing the distance from 4 to 6 cm. It is attributed to the longer jet in the whipping zone. The  $C_{hh}$  increased with the increase in the initial distance, and the  $D_{out}$  was wider with the increase of the initial distance, as concluded in Table 4.3.

**Table 4.3** The summarization of the height, the  $C_{hh}$ , the DW, the  $D_{out}$ , and wall thickness of 3D structures obtained from various initial distances, including 2, 3, 4, 5, and 6 cm. The experimental conditions, including a voltage, an initial distance, a flow rate, and a nozzle moving speed applied in the 3D buildup, were named voltage-initial distance-flow rate-moving speed.

Experimental conditions [kV-cm-mL/h-mm/s]	Height [mm]	$C_{hh}$ [mm]	DW [mm]	$D_{out}$ [mm]	Wall thickness [mm]
16-2-4-1	$0.20 \pm 0.08$	-	$85.76 \pm 3.59$	-	-
16-3-4-1	$0.15 \pm 0.06$	-	$91.37 \pm 4.72$	-	-
16-4-4-1	$13.90 \pm 2.07$	$7.74 \pm 3.19$	$78.95 \pm 2.28$	$48.03 \pm 2.66$	$4.50 \pm 2.26$
16-5-4-1	$8.50 \pm 2.39$	-	$93.30 \pm 2.53$	-	-
16-6-4-1	$23.50 \pm 0.96$	$12.69 \pm 1.09$	$81.10 \pm 4.69$	$52.70 \pm 1.56$	$8.28 \pm 0.61$

The morphology and diameter histogram of electrospun fibers are shown in Figure 4.31 and B.17. SEM images of upper, middle, and lower parts of 3D structures fabricated at 4, 5, and 6 cm of initial distances are shown in Figure B.18, B.19, and B.2, respectively. The dense pack of fibers and beaded fibers were found in the electrospun mat fabricated at 2 and 3 cm. There was a significant difference between the lower and middle parts under the initial distance of 4 cm in Figure B.20(a); however, it was changed to be the upper part, which was significantly different from others. It was probably because the short initial distance caused more deposited fiber and limited the height of rising-up fiber, resulting in dense-pack fiber on the lower parts of structures under the initial distance of 4 cm. When the initial distance was higher, it allowed for a faster buildup. However, if the distance between the upward-moving nozzle and the rising height of structures were not balanced, it would result in a significantly different size of the upper part. For the 2D mat, although there was an increase in diameter between 2 and 3 cm, there was a slight decrease when the initial distance increased to 5 cm. The large fiber in the range of 2 to 3 cm might relate to the solution dripping. The overall average diameter of 3D structures shows that the increase in the initial distance is likely to increase the average diameter (Figure B.20(b)). It was attributed to the upward height of structures over time.

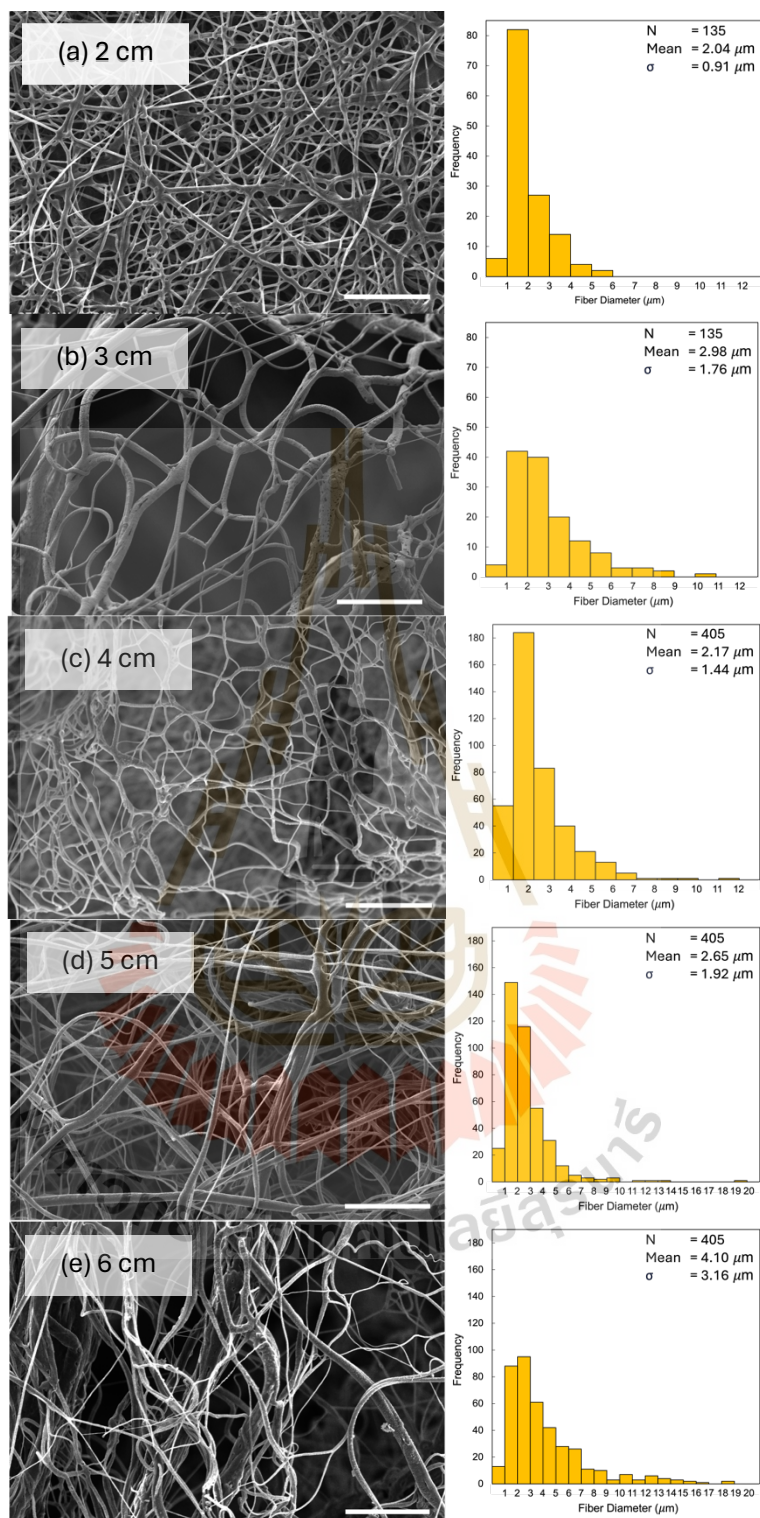


**Figure 4.33** SEM images and histograms of fiber diameter fabricated with various initial distances, including (a) 2, (b) 3, (c) 4, (d) 5, and (e) 6 cm, under contants of flow rate, voltage, and nozzle speed at 4 mL/h, 16 kV, and 1 mm/s, respectively. The scale bar is 50 μm.

## Voltage

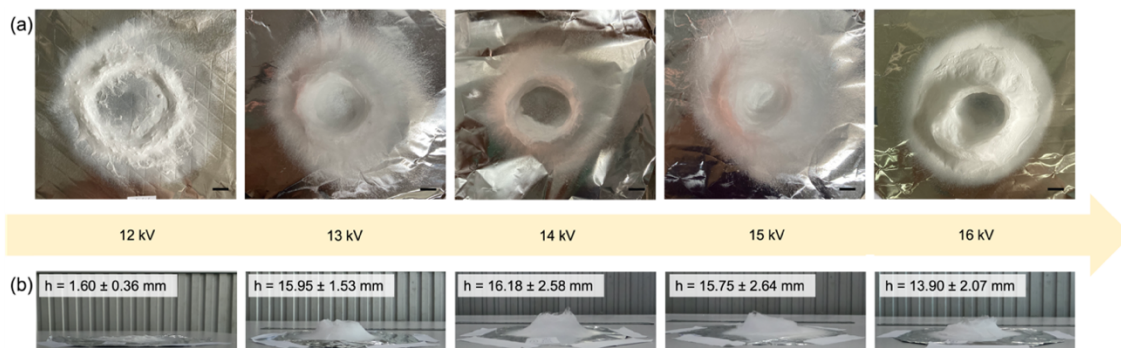


**Figure 4.34** (a) The top and (b) side views of comparative 3D PCL-electrospun constructs by varying the values of an initial distance. The voltage applied to run the formation procedure of a 12% wt PCL solution in 6:1 DCM:DMF + 10%  $H_3PO_4$  is increased from 12 to 16 kV, subsequently raised in increments of 1 kV. The 3D PCL structures were formed at a flow rate of 4 mL/h, an initial distance of 4 cm, and a nozzle speed of 1 mm/s for 30 minutes.

The study of various voltages applied to build up the 3D PCL-electrospun structures was executed by applying a flow rate of 4 mL/h, an initial distance of 4 cm, and a nozzle moving speed of 1 mm/s for 30 minutes. The influence of voltage on the 3D buildup is shown in Figure 4.34 and Figure 4.35. All conditions were able to perform the pathway of the hollow cylinder (Figure 4.34(a)). At the applied voltage of 12 kV, the 2D mat with a thickness of  $1.60 \pm 0.36 \mu\text{m}$  was obtained with a controllable deposition shape, even though some raising-up fibers occurred and enabled the deposition following the nozzle locomotion. Due to the low voltage, some accumulation of droplet drying, which caused the prolonged droplet at the tip, and the dripping on the collector was observed (Radacsi and Nuansing, 2020; Vong et al., 2018). The 3D buildup started at an applied voltage of 13 kV. As seen in Figure 4.34(b), the structure rose to  $15.95 \pm 1.53 \text{ mm}$  at 13 kV and reached its highest value at 14 kV. When increasing voltage to 15 and 16 kV, the height of structures decreased. It might cause an increase in the jet velocity when applying a stronger voltage. An increase in applied voltage will result in a decrease in the size of the Taylor cone and an increase in the jet velocity (A. Haider et al., 2018; Radacsi and Nuansing, 2020). The multi-jet ejection was observed when increasing the applying voltage to 15 and 16

kV, as seen in Figure 4.35. An increase in the voltage at a constant distance induces multi-jet ejection since increasing voltage beyond the threshold results in the disappearance of a protruding droplet and electric field concentration on the tube edge, resulting in more than one jet (Fromager et al., 2023; Joy et al., 2021).

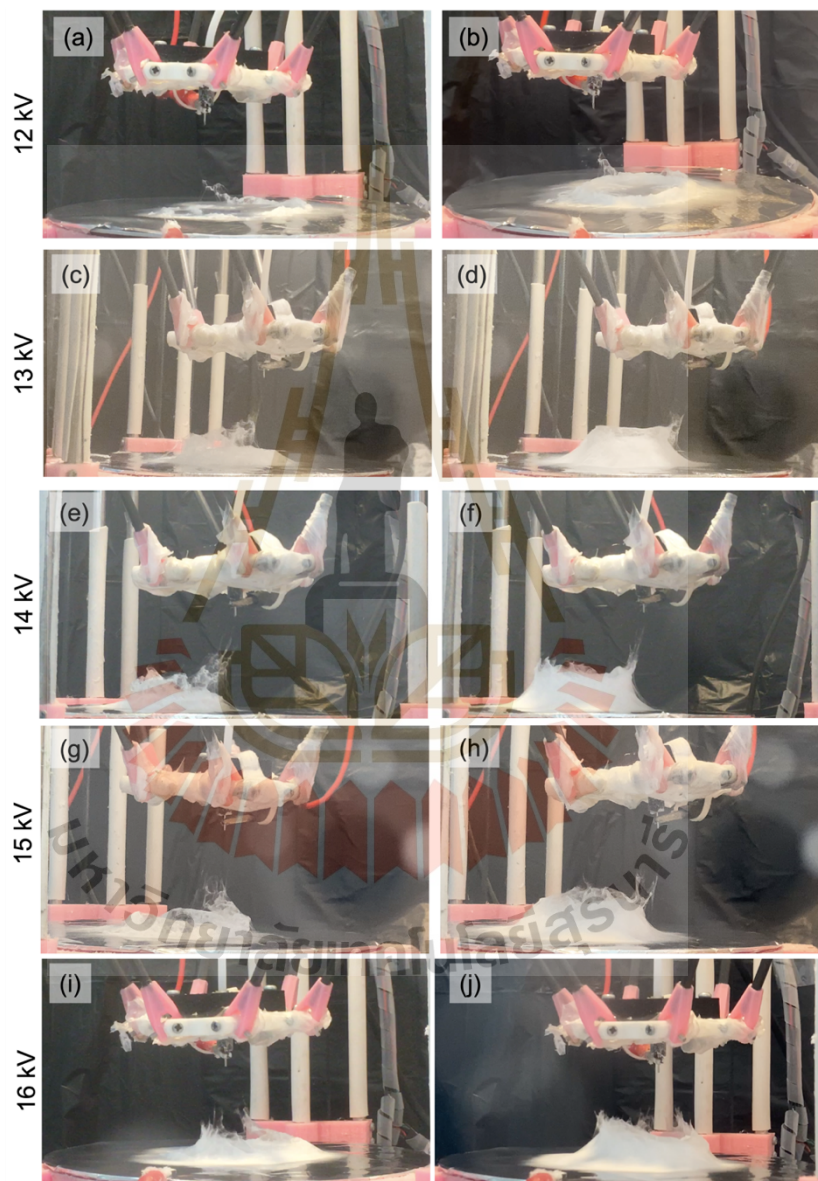


**Figure 4.35** Various situations of 3D buildups via 3D electrospinning, which were run with various voltages of (a-b) 12, (c-d) 13, (e-f) 14, (g-h) 15, and (i-j) 16 kV at a flow rate of 4 mL/h, an initial distance of 4 cm, and a nozzle moving speed of 1 mm/s for 30 minutes in an ambient environment. The images were captured at different times: 5.00, 19.05, 5.24, 21.03, 5.30, 24.54, 5.26, 17.55, 5.58, and 24.10 minutes, respectively.

The potential difference applied between the nozzle and collector relates to the force used to stretch the droplet. An increase in the voltage increases the velocity of the jet onto the collector. An increase in applied voltage up to a certain point allows for a higher structure, but a voltage greater than that point leads to a decrease in the height of structures. Likewise, the  $C_{hh}$  corresponds to the height. For DW,  $D_{out}$ , and wall thickness (Table 4.4), these decrease with an increase in voltage. It was attributed to the shorter length of the whipping jet. An increase in voltage results in an increase in the length of the straight jet and a decrease in the width of the whipping zone (Šimko and Lukáš, 2016). This caused a trend to decrease the wall thickness, which was  $14.42 \pm 1.36$ ,  $7.70 \pm 1.75$ , and  $3.98 \pm 1.01$  for the conditions of 12, 13, and 14 kV; however, the increase in wall thickness at 15 and 16 kV was  $8.63 \pm 4.02$  and  $4.50 \pm 2.26$  mm, which might be attributed to the multi-jet ejections observed. Likewise, the  $D_{out}$  decreased with an increase in voltage; however, an increase in  $D_{out}$  was observed in the range of multi-jet ejection observed.

**Table 4.4** The summarization of the height, the  $C_{hh}$ , the DW, the  $D_{out}$ , and wall thickness of 3D structures obtained from various voltages, including 12, 13, 14, 15, and 16 kV. The experimental conditions, including a voltage, an initial distance, a flow rate, and a nozzle moving speed applied in the 3D buildup, were named voltage-initial distance-flow rate-moving speed.

Experimental conditions [kV-cm-mL/h-mm/s]	Height [mm]	$C_{hh}$ [mm]	DW [mm]	$D_{out}$ [mm]	Wall thickness [mm]
12-4-4-1	$1.60 \pm 0.36$	-	$84.41 \pm 11.46$	$67.59 \pm 3.05$	$6.67 \pm 1.06$
13-4-4-1	$15.95 \pm 1.53$	$11.95 \pm 0.39$	$82.60 \pm 2.27$	$46.55 \pm 2.04$	$7.70 \pm 1.75$
14-4-4-1	$16.18 \pm 2.58$	$15.49 \pm 4.60$	$72.93 \pm 2.70$	$43.85 \pm 1.58$	$3.98 \pm 1.01$
15-4-4-1	$15.75 \pm 2.64$	$9.94 \pm 5.40$	$82.26 \pm 4.50$	$52.98 \pm 7.80$	$8.63 \pm 4.02$
16-4-4-1	$13.90 \pm 2.07$	$7.74 \pm 3.19$	$78.95 \pm 2.28$	$48.03 \pm 2.66$	$4.50 \pm 2.26$

The morphology and diameter histogram of electrospun mats and 3D structures are shown in Figure 4.36 and B.21. To be illustrated, SEM images and diameter histogram of upper, middle, and lower parts of 3D fibrous structures built up

at 13, 14, 15, and 16 kV are demonstrated in Figure B.22, B.23, B.24, and B.18, respectively. The average diameter fluctuated. An increase in voltage was able to increase or decrease the diameter of the fiber (A. Haider et al., 2018; Vong et al., 2018). The influence of voltage is dependent on the threshold or critical point of voltage varying from condition to condition. As seen in Figure B.25(a), the average diameter at the lower part of applying 13 kV was a little thinner than at 12 kV; however, the middle and upper parts of 13 kV were increased when the structure was upward, which resulted in a closer deposition area to the nozzle. It causes the overall average diameter of 13 kV to be greater than 12 kV, as seen in Figure B.25(b). The unstable electrospinning at 12 and 13 kV causes dripping and clogging, resulting in thicker fiber. When voltage was increased to reach stable electrospinning, smooth fiber was obtained at 14, 15, and 16 kV. The average diameter of 14 kV is dramatically decreased and the thinnest. Furthermore, only the structure at the applied voltage of 14 kV provided no significant difference in electrospun diameter on the upper, middle, and lower parts. After increasing the voltage to 15 and 16 kV, the greater diameters were found. Z. Liu et al. (2019) revealed that the increased jets share a limited electrical field, resulting in a weakened electrical field for each jet. An increase in voltage increases the interconnective pore or space between each fiber, as seen in Figure 4.34. Since the repulsive force of fiber increases with an increase in voltage, at 16 kV, an oily flat was found in the lower parts of structures. It was attributed to increasing jet velocity with an increase in voltage (Vong et al., 2018). When decreasing the voltage to 14 and 15 kV, this characteristic disappeared. The voltage of 14 kV was chosen to be the optimal condition in the 3D buildup of the PCL solution and used to further investigate the moving speed of the nozzle.

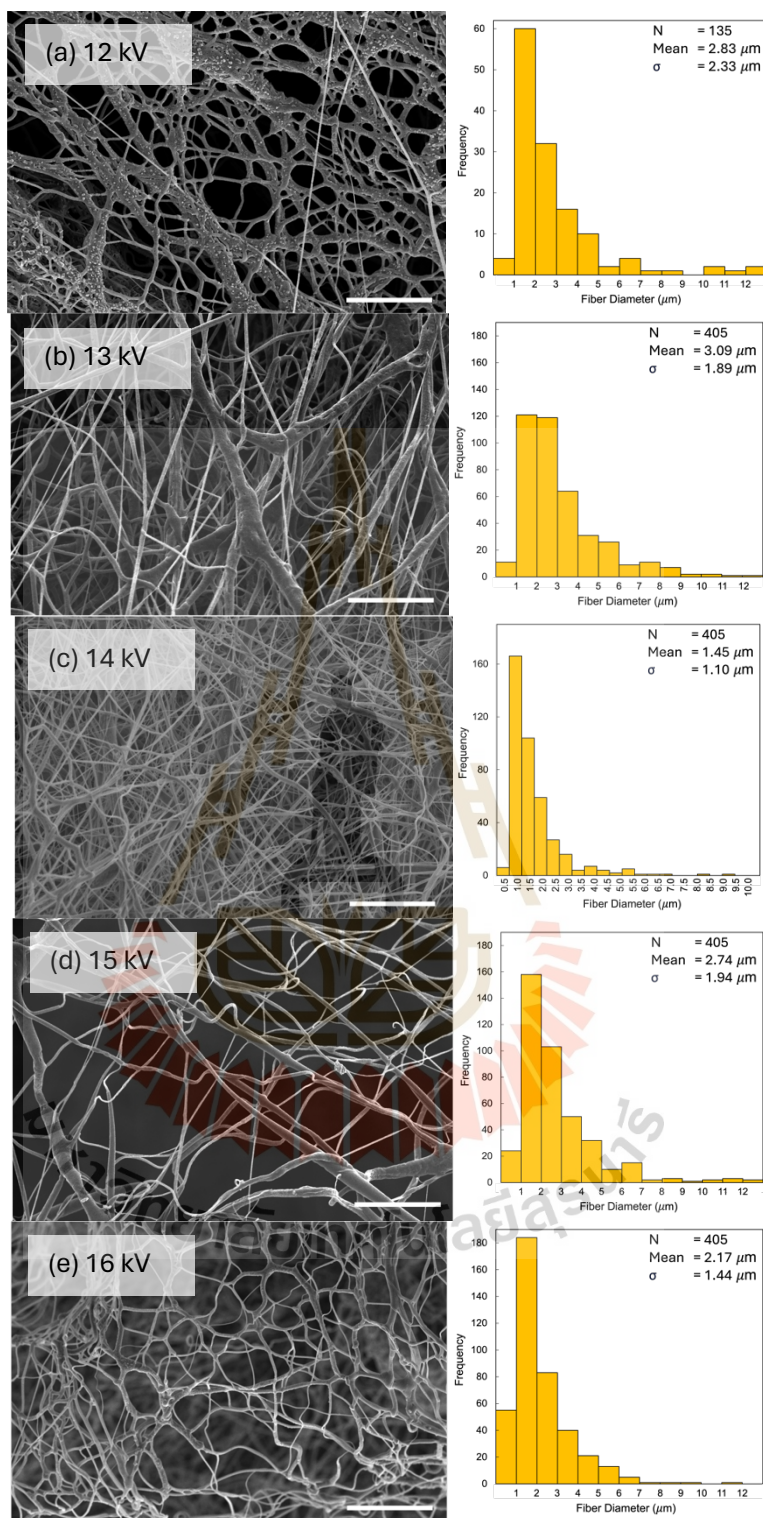


**Figure 4.36** SEM images and histograms of fiber diameter fabricated with various voltages, including (a) 12, (b) 13, (c) 14, (d) 15, and (e) 16 kV, under contants of flow rate, initial distances, and nozzle speed at 4 mL/h, 4 cm, and 1 mm/s, respectively. The scale bar is 50  $\mu\text{m}$ .

### Nozzle Moving Speed

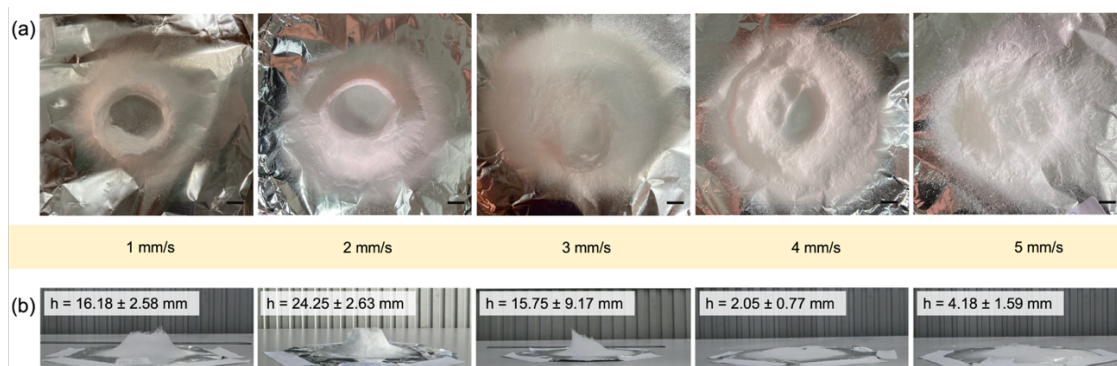


**Figure 4.37** (a) The top and (b) side views of comparative 3D PCL-electrospun constructs by varying the values of an initial distance. The nozzle speed applied to run the formation procedure of a 12% wt PCL solution in 6:1 DCM:DMF + 10%  $\text{H}_3\text{PO}_4$  is increased from 1 to 5 mm/s, subsequently raised in increments of 1 mm/s. The 3D PCL structures were formed at a flow rate of 4 mL/h, an initial distance of 4 cm, and a voltage of 14 kV for 30 minutes.

The moving speed of a nozzle at 1, 2, 3, 4, and 5 mm/s was investigated using the optimal conditions of 12 wt% PCL solution in the 6:1 DCM:DMF solvent and the addition of 10%  $\text{H}_3\text{PO}_4$  at a flow rate of 4 mL/h, an initial distance of 4 cm, and a voltage of 14 kV (Figure 4.37 and 4.38). An increase in the nozzle speed causes the 3D formation to rise faster over time, but it also causes the printing quality to change from a hollow cylinder to a filled circular. The speed relates to the exact position of the fiber deposition, which results in the final shape. Due to discontinuous deposition at faster speeds, the structure deformed into a filled and slanting structure at the speeds of 3, 4, and 5 mm/s. Moreover, it was discovered that the solution dried at the tip at 4 and 5 mm/s. It was attributed to the fast changes in electrospinning parameters and evaporation. The increased evaporation might be explained by a faster nozzle, which allows faster air flow around the solution droplet.

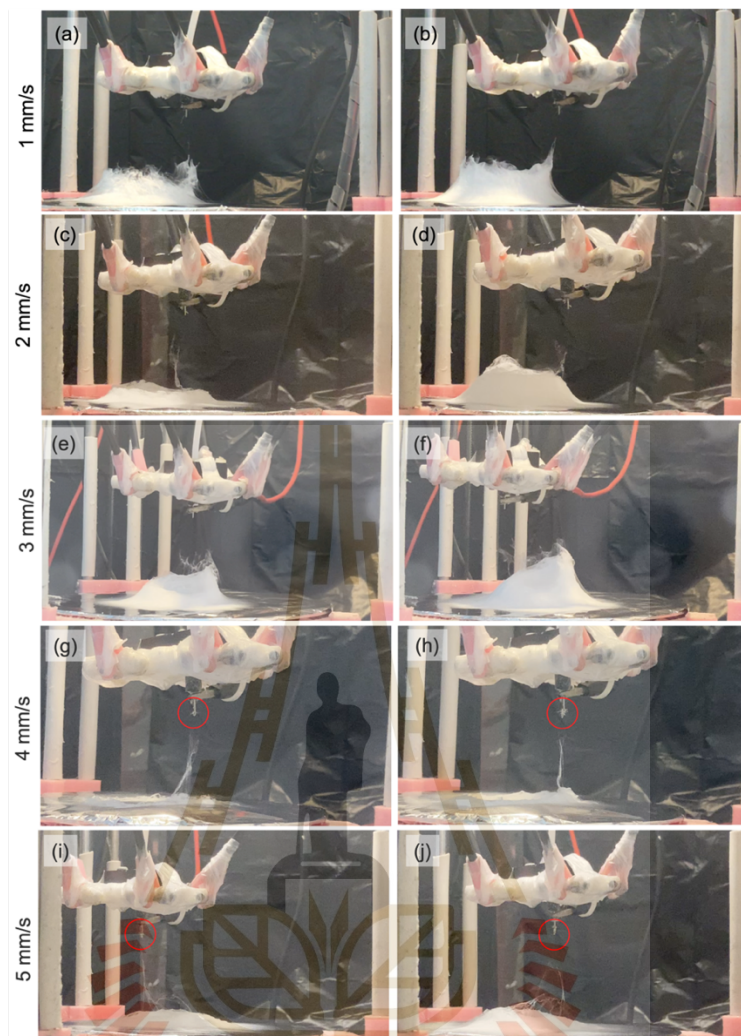


**Figure 4.38** Various situations of 3D buildups via 3D electrospinning, which were run with various moving speeds of a nozzle, including (a-b) 1, (c-d) 2, (e-f) 3, (g-h) 4, and (i-j) 5 mm/s at a flow rate of 4 mL/h, an initial distance of 4 cm, and a voltage of 14 kV for 30 minutes in an ambient environment. The images were captured at different times: 10.00, 20.00, 10.53, 25.09, 10.49, 22.54, 5.01, 13.00, 10.07, and 21.55 minutes, respectively.

As concluded in Table 4.5, an increase in the nozzle speed allows for higher structures; however, it also poses a risk of deformation. In the case of slower nozzle speeds, it provides the precise position of deposition; however, the accumulation of incoming fibers at single position increases, which may lead to unstable constructs. The DW increases with an increase in the speed. Nevertheless, the DW decreases when the shape is not controlled, resulting in the fiber accumulating at the center

and filling the hollow shape. It corresponds that the  $C_{hh}$  increases with an increase in the speed and the wall thickness increases until no wall thickness occurs. The increase in the nozzle speed results in low printing quality for hollow cylinders.

**Table 4.5** The summarization of the height, the  $C_{hh}$ , the DW, the  $D_{out}$ , and wall thickness of 3D structures obtained from various moving speeds of a nozzle including 1, 2, 3, 4, and 5 mm/s. The experimental conditions, including a voltage, an initial distance, a flow rate, and a nozzle moving speed, applied in the 3D buildup were named voltage-initial distance-flow rate-moving speed.

Experimental conditions [kV-cm-mL/h-mm/s]	Height [mm]	$C_{hh}$ [mm]	DW [mm]	$D_{out}$ [mm]	Wall thickness [mm]
14-4-4-1	16.18 ± 2.58	15.49 ± 4.60	72.93 ± 2.70	43.85 ± 1.58	3.98 ± 1.01
14-4-4-2	24.25 ± 2.63	20.92 ± 2.47	78.56 ± 1.88	46.08 ± 0.95	4.30 ± 1.18
14-4-4-3	15.75 ± 9.18	20.57 ± 0.81	-	-	10.32 ± 5.08
14-4-4-4	2.05 ± 0.77	-	84.83 ± 1.55	-	22.33 ± 3.60
14-4-4-5	4.18 ± 1.59	-	76.65 ± 6.01	-	-

The morphology and diameter histogram of 2D electrospun fibers and 3D fibrous structures varying the nozzle moving speed is presented in Figure 4.39 and B.26. To be illustrated, each part of 3D structures fabricated using 1, 2, and 3 mm/s is shown in Figure B.23, B.27, and B.28. In the speed of 1-2 mm/s, the average fiber diameters remained within a similar range. Larger fiber diameters were found at the top part of the 2 mm/s sample, whereas the lower and middle parts' fiber diameter remained comparable to the 1 mm/s sample's fiber diameter. It was attributed to the higher structures, which allowed the top to be closer to the nozzle. The overall average diameter of fibers at the speed of 1 and 2 mm/s was similar (Figure B.29). The nozzle speed in that range does not have a direct impact on the elongation and drying of the jet (Vong et al., 2018). However, when the speed exceeds 2 mm/s, the average diameter of the fiber increases according to the speed. This could be attributed to the drying of the solution at the nozzle that occurred during the experiment. It might be the result of solution drying when the speed increased.

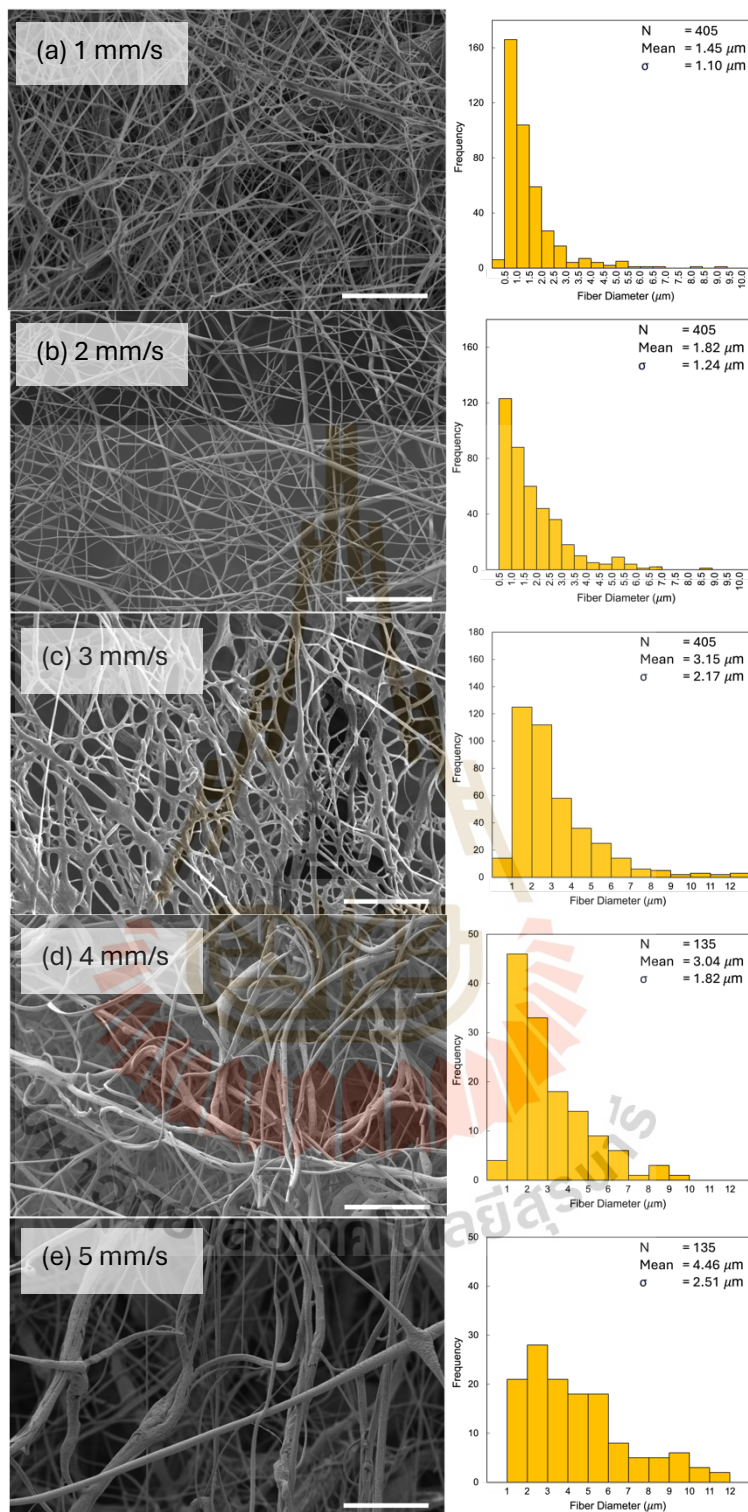


**Figure 4.39** SEM images and histograms of fiber diameter fabricated with various nozzle moving speeds, including (a) 1, (b) 2, (c) 3, (d) 4, and (e) 4 mm/s, under constants of flow rate, initial distances, and voltage at 4 mL/h, 4 cm, and 14 kV, respectively. The scale bar is 50  $\mu\text{m}$ .

### 4.2.2.3 Electric Field Simulation

#### The change of initial distance between the nozzle and collector

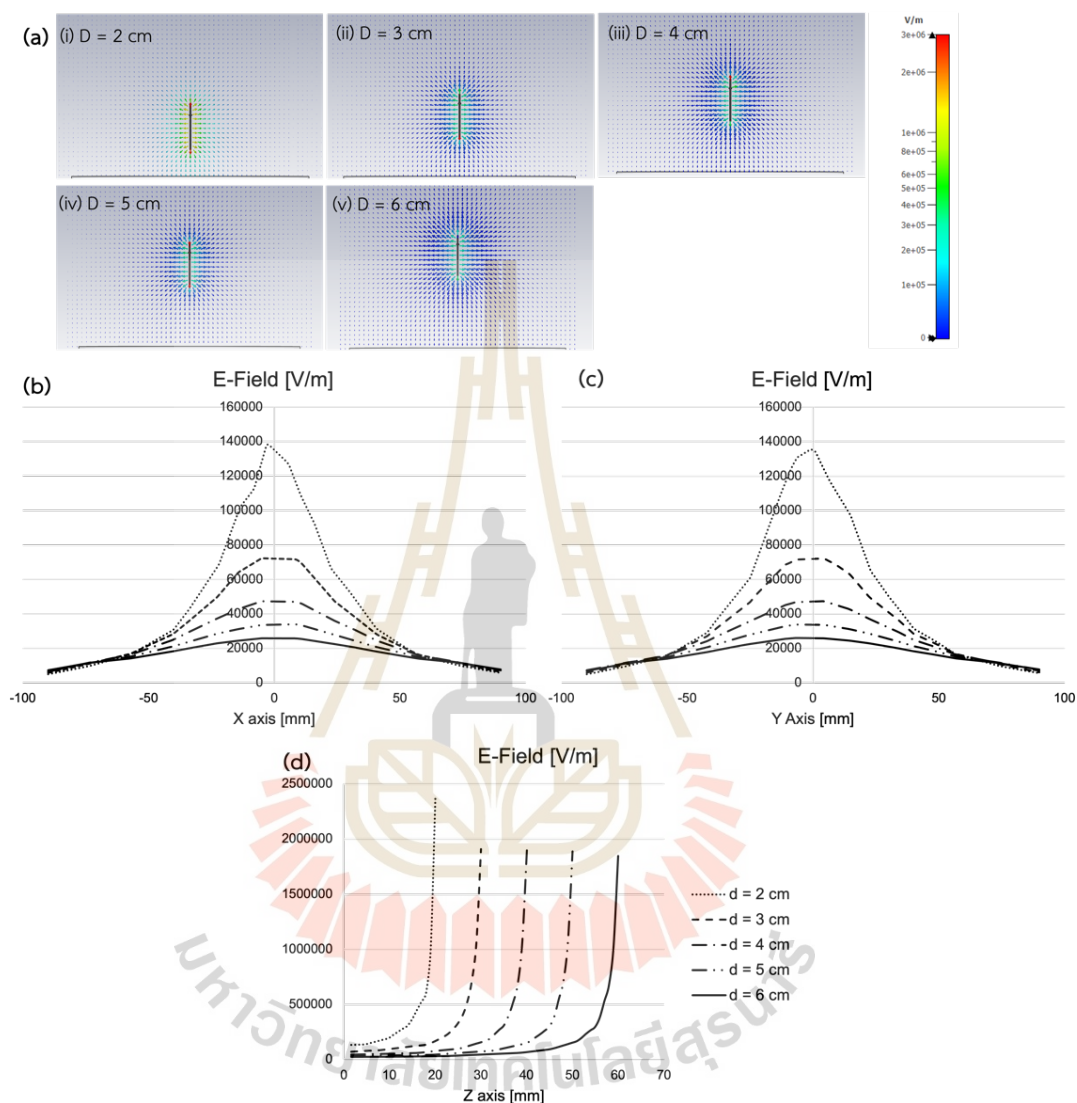
It is obvious that there is a main direction of electrostatic field gradient ranging from charged nozzle to grounded collector as illustrated in Figure 4.40. It presents the distribution of electric-field vector and the graph of electric field when the initial distance was changed from 2 to 6 cm with interval of 1 cm. The strength of electric field decreased with an increase in initial distance, which was expected. It is apparent in Figure 4.40(a)-(i-v) that the electric field that was generated in the 3D electrospinning configuration was highly non-uniform corresponding to conventional electrospinning of a nozzle to plate (Jiang, He, Duan, and Li, 2014). The non-uniformity was attributed to the electric field generating at a point and a plane, and then expanding towards a large collector. It was noticed that the electric field reached a point of uniformity to the collection plate when initial distance was 2 cm while the strength of the field of other distances dropped significantly before reaching to collector.

As seen in Figure 4.40(b-d), the graphs of electric field were corresponded to the Gauss's law. The electric field at the nozzle tip of 2 cm provided the highest strength and the most board peak as shown in Figure 4.40(d), which it might be cause that 2 cm cannot perform 3D formation. The electric fields of other conditions on Z axis were slightly decreased following the decrease in the distance. The electric field on Z axis dramatically increased when the position was approximately 10 mm closer to the nozzle.

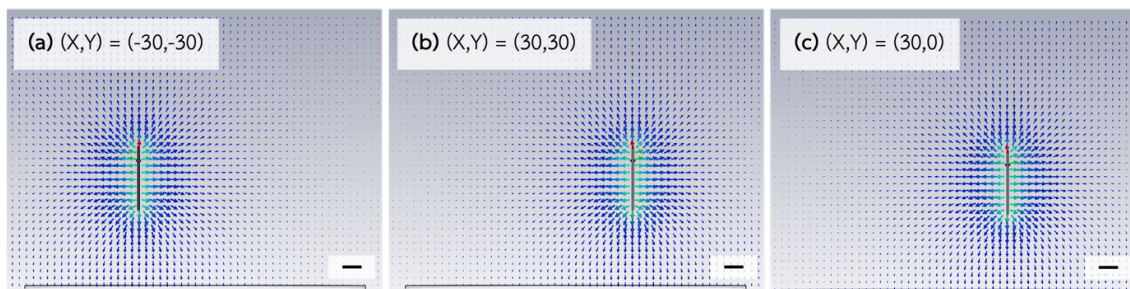
#### The change of point on X-Y plane

Figure 4.41 shows the movement of nozzle to position  $(X,Y) = (-30,-30)$ ,  $(30, 30)$ , and  $(30,0)$ . the distribution of electric-field vector was similar. It was expected that the elector-field vector of  $(X,Y) = (0,30)$  was equal to one of  $(X,Y) = (-30,0)$ . It presented the change of XY plane did affect to the strength and direction of electric field on the nozzle to the collector. However, there were some differences of electric field around the nozzle, which imply the change of electric field over time when the

nozzle will be moving. If the movement of the nozzle does not exceed 12 mm per movement, the electric field on the nozzle should be stable.



**Figure 4.40** (a) The vector distribution of the electric field strength between the nozzle and collector under the applied voltage of 16 kV and an initial distance varying (i) 2, (ii) 3, (iii) 4, (iv) 5, and (v) 6 cm when the nozzle located at the center ( $X, Y = (0, 0)$ ) which was also illustrated by a graph of electric field on (b) X, (c) Y, and (d) Z axis.



**Figure 4.41** The vector distribution of the electric field strength under the applied voltage of 16 kV and an initial distance of 4 cm when the nozzle located at (a)  $(X, Y)$  is  $(-30,-30)$ , (b)  $(X, Y)$  is  $(30,30)$ , and (c)  $(X, Y)$  is  $(30,0)$ . The scale bar is 10 mm.

### 4.3 Biological assessments

#### 4.3.1 *In vitro* cell culture of osteoblast cells

To evaluate the biocompatibility, the 3D PCL macrostructure (Figure 4.42(a)) fabricated with the following parameters: 4 mL/h flow rate, 4 cm initial distance, 16 kV voltage, and 1 mm/s nozzle moving speed was chosen. In order to prepare electrospun grafts for an *in vitro* cell culture test, it was cut from the 3D macrostructures into a  $5 \times 5 \text{ mm}^2$  area. The  $\text{O}_2$  plasma treatment was applied to the electrospun grafts for 5 minutes at a power of 100W. The grafts were sterilized using UV light and immersed in media prior to cell culture.  $5 \times 10^5$  cells/sample of Saos-2 cells were seeded on the surface of electrospun grafts and a glass slide (control, Figure 4.42(c)). The cells were then incubated for 3 days without changing media. The study revealed that exposing the plasma to a power of 100W for a duration of 5 minutes resulted in the formation of melted fibers as shown in Figure 4.42(b). Nevertheless, Saos-2 cells appeared on the surface of the electrospun graft, as depicted in Figure 4.42(d). The change of the porous fiber into the melt fiber after plasma treatment can be seen clearly in Figure 4.42(a)-(iii) and (b)-(iii). The heat generated during the plasma treatment was attributed to the cause. The influence of plasma treatment on electrospun grafts was observed. In the following section, we will examine and clarify this issue.

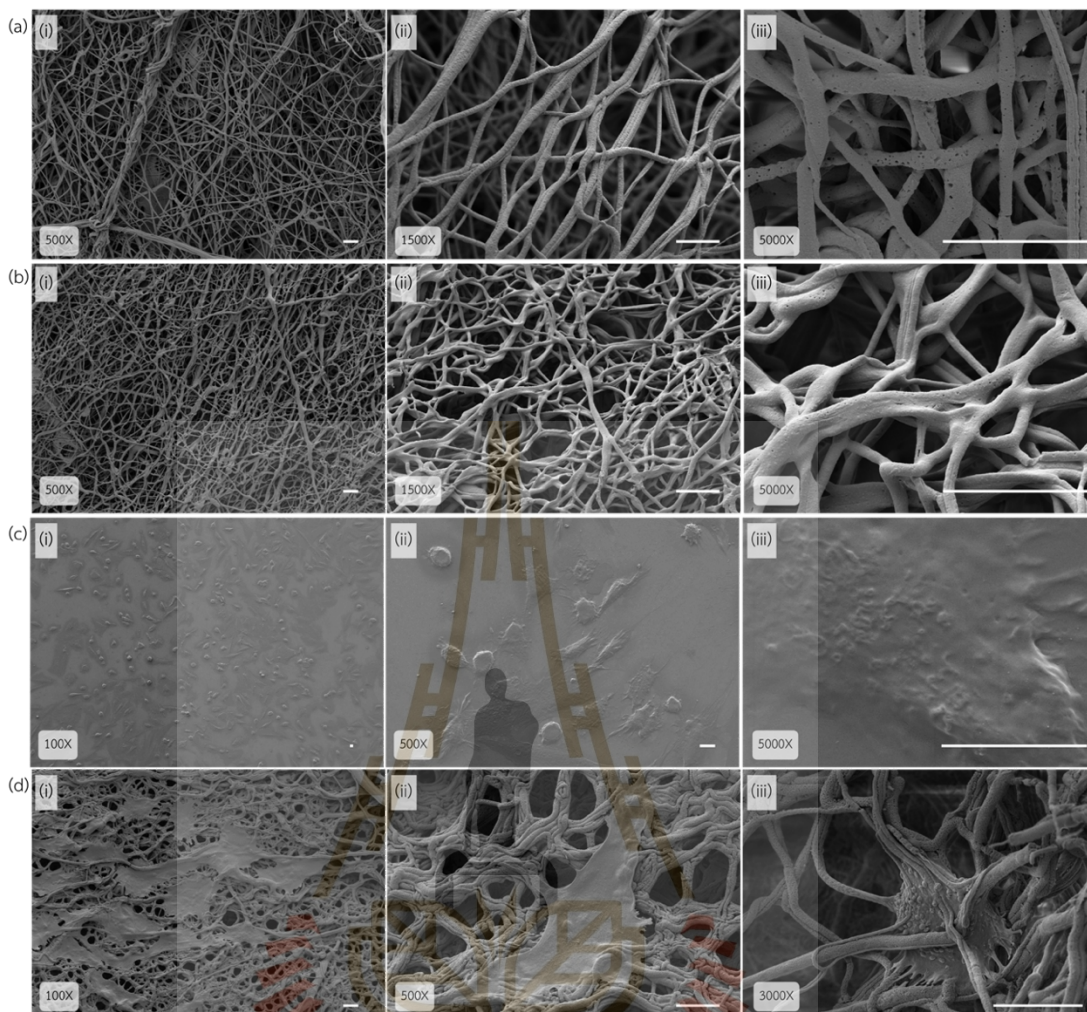


**Figure 4.42** The morphology of (a) PCL fiber cut from a 3D electrospun structure which was fabricated by a flow rate of 4 mL/h, an initial distance of 4 cm, and a voltage of 16kV, (b) PCL fiber treated by O<sub>2</sub> plasma power of 10 W for 5 minutes, (c) Saos-2 cells seeded on the glass slide (control) after 3 days of culture, and (d) Saos-2 cells seeded on treated PCL fiber after 3 days of culture. The scale bar is 10 mm.

### 4.3.2 *In vitro* cell culture of fibroblast cells

#### 4.3.2.1 Plasma treatment

The morphology of the untreated and plasma-treated electrospun PCL fibers exhibited little difference, as observed in the SEM images (Figure 4.43). An incremental rise in diameter was shown to coincide with an increase in the power of plasma treatment. The average diameters of PCL fibers were  $0.97 \pm 0.39$ ,  $1.03 \pm 0.57$   $\mu\text{m}$ ,  $1.41 \pm 0.82$ ,  $1.43 \pm 0.74$ , and  $1.28 \pm 0.47$   $\mu\text{m}$  for untreated fiber and plasma-treated

fibers with 10, 30, 50, and 70 W, respectively. In addition, the pore space between the fibers exhibited a greater width when subjected to the powers of 30 and 50 W. This is in agreement with the result reported by Arabi et al. (2014). They showed that O<sub>2</sub>-plasma treatments with a power of 30 W for a duration of 10 min resulted in the induced melting of the thinner diameters of PCL nanofibers, leading to an increased gap between the individual fibers. Moreover, it should be noted that greater powers or longer exposure times were able to result in a more refined surface texture of the treated fibers

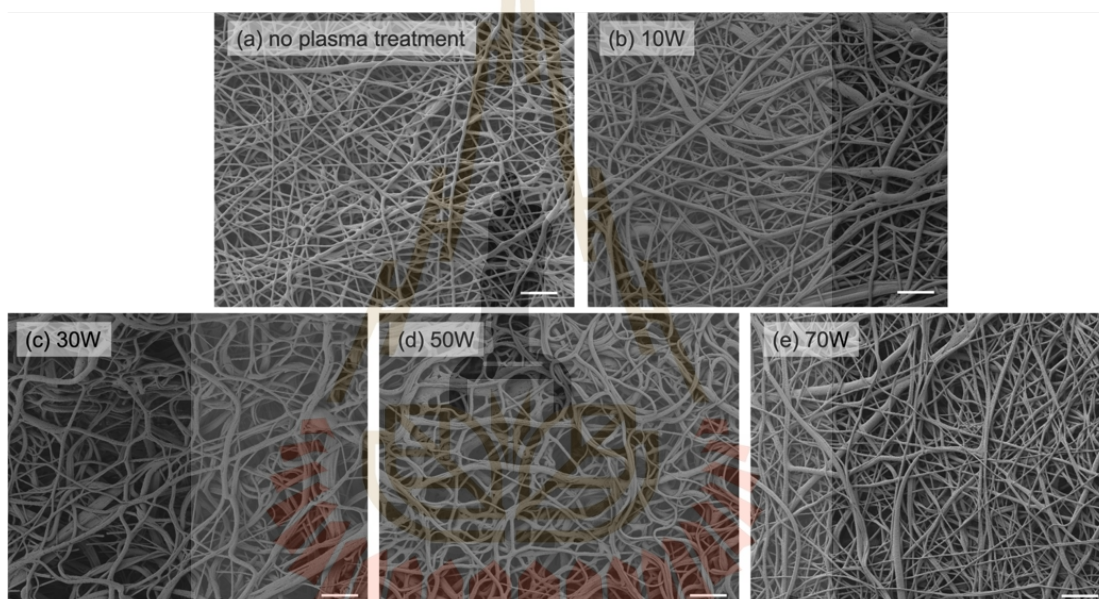


**Figure 4.43** SEM images of morphological fibers with various powers of plasma treatment, namely (a) no plasma treatment, (b) 10, (c) 30, (d) 50, and 70 W, for 5 minutes. The scale bar is 10  $\mu\text{m}$ .

The functional group of PCL-fibrous structures, both untreated and treated with O<sub>2</sub> plasma were examined by FTIR, as seen in Figure C.1. The typical characteristic peaks of PCL fiber appear in the ranges of 1000–1800 and 2800–3000  $\text{cm}^{-1}$  (Shkarina et al., 2018). The strong band at 1727  $\text{cm}^{-1}$  is attributed to the stretching (C=O) mode of carbonyl esters. The two peaks at 2867 and 2944  $\text{cm}^{-1}$  correspond to the symmetric and asymmetric stretching of the CH<sub>2</sub> group. Moreover, the two peaks at 1185 and 1241  $\text{cm}^{-1}$  correspond to the stretching of the C-O-C group, and the bands

at  $1295\text{ cm}^{-1}$  are related to backbone C-O and C-C stretching in the crystalline phase (Balu et al., 2011; Chen and Lin, 2020; Gorodzha, Surmeneva, and Surmenev, 2015; Shkarina et al., 2018). These peaks were able to be located in both untreated and treated PCL-fibrous structures. There were new peaks shown in Figure C.1 that only appeared on the treated PCL structures, which were  $3000\text{--}3400$  and  $1670\text{ cm}^{-1}$ . The  $3000\text{--}3400\text{ cm}^{-1}$  was attributed to OH stretching vibration modes, and  $1670\text{ cm}^{-1}$  may be the bending mode of adsorbed water (Choi et al., 2015) or the amide I band (Mecozzi and Sturchio, 2017). It was confirmed that hydrophilic groups can be introduced to the surface by oxygen plasma treatment. To confirm the hydrophilic property of PCL-fibrous structures was improved. The wettability was investigated by a customized setup of contact angle measurements. As shown in Figure 4.44, the contact angles of untreated and treated structures with 10 W for 5 minutes were  $99.34 \pm 8.63$  and  $95.71 \pm 0.13$  degrees, respectively, while the contact angles of treated structures with 30, 50, and 70 W for 5 minutes, respectively, cannot be measured because of the fast absorption of water droplets into the surface. The time of complete absorption on the surface of PCL-fibrous structures was  $21.00 \pm 6.08$ ,  $8.76 \pm 1.15$ , and  $1.63 \pm 1.11$  seconds for untreated, treated with 10, and 30 W conditions, respectively, and less than 1 second for 50 and 70 W conditions.



**Figure 4.44** Contact angles of untreated and treated PCL-fibrous structures with 10, 30, 50, and 70 W for 5 minutes, named as 10W5MIN, 30W5MIN, 50W5MIN, and 70W5MIN, respectively.

As mentioned in Chapter III, the glass slide and scaffolds were examined with *in vitro* cell culture to obtain the suitable condition of surface modification for 3D fibrous scaffolds. The morphology of NIH3T3 cells that were cultivated for 3 days on three different substrates: the glass slide (control), untreated electrospun PCL scaffolds, and plasma-treated electrospun PCL scaffolds, was observed by SEM as seen

in Figure 4.45. It was observed that the wettability of plasma-treated PCL fiber was better than that of untreated fiber. The hydrophilic property of PCL-electrospun scaffolds was improved with the plasma treatment, consistent with previous results reported (Arabi et al., 2014; Ghobeira, Geyter, and Morent, 2017; Sankar, Mony, and Rangasamy, 2021). This led to cell adhesion to the surface of plasma-treated fibers, which was found to be more probable compared to untreated fibers. The plasma treatments obviously enhanced cell adhesion. However, an increase in plasma treatment power greater than 50W did not enhance NIH3T3 cell adhesion on scaffolds. The plasma-treated electrospun scaffold subjected to 30 and 50 W treatments for 5 minutes provided the optimal cell morphology and adhesion of NIH3T3 cells on the scaffolds. It needs further the investigation to assess the biological difference between the 30 and 50 W conditions. In this work, the condition of a 50W treatment has been selected as the optimal plasma treatment condition for the PCL-electrospun scaffolds.

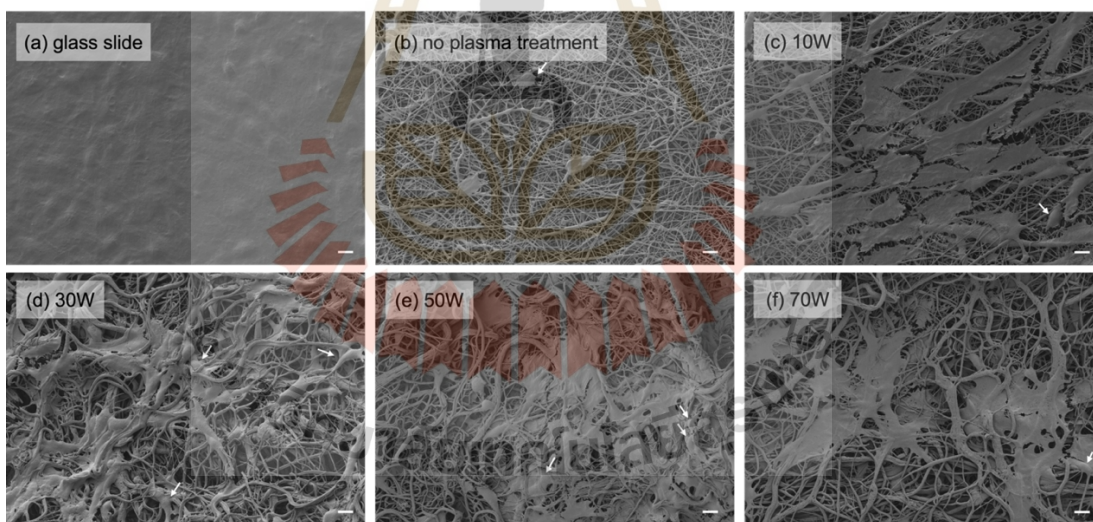


**Figure 4.45** SEM images of cell morphology and adhesion on 3D PCL-electrospun structures, which were fabricated by the 3D electrospinning with conditions of 16 kV of a voltage, 4 cm of an initial distance, and 4 mL/h of a solution flow rate, viewed at 500 magnifications. The scale bar is 10  $\mu\text{m}$ .

#### 4.3.2.2 Synchrotron radiation Fourier transform infrared microspectroscopy imaging

As described in Chapter III, two techniques were used to prepare the samples for SR-FTIR imaging. First, electrospun graft was fabricated by using 3D electrospinning and then it was cut by using a cryo-section. Second, electrospun fiber was directly deposited onto the BaF<sub>2</sub> window surface, which serves as the SR-FTIR imaging substrate. The cryo-section proved ineffective for the electrospun-based construction due to the fact that the cut electrospun fiber did not form a single sheet and may have dispersed. Additionally, as seen in the Figure D.1, optical microscopy presented considerable difficulty in determining the precise position of the cells.

In preparation for SR-FTIR imaging, therefore, samples were prepared by direct deposition of electrospun fiber onto the window (Figure 3.7). Cellulose powder was added into the PLA solutions to fabricate composite fibers to enhance the biocompatible properties. The PLA and PLA/cellulose fibers were prepared to investigate cell distribution on the surface of electrospun fiber through an analytical method of SR-FTIR imaging and HCA. The incorporation of various cellulose contents, including 1, 5 and 10 wt%, enhanced the average diameter of fibers. Figure 4.46 shows the morphology and diameter distribution of the electrospun fibers. There were some flat textures in the fiber morphology that are hard to evaluate as beads. As shown in Figure 4.46(e, g), this was more noticeable in samples containing a high amount of cellulose. Nevertheless, during the electrospinning process, there was no clogging or dropping. The fiber diameter measured from pure PLA ranged from 0.20 to 2.40  $\mu\text{m}$  with an average diameter of  $0.70 \pm 0.29 \mu\text{m}$ . The addition of cellulose at 1 and 5 wt% showed a slight increase in fiber diameter to  $0.80 \pm 0.31$  and  $0.80 \pm 0.34 \mu\text{m}$ . When the amount of cellulose was increased to 10 wt%, the diameter reached  $1.37 \pm 0.78 \mu\text{m}$ , which is nearly twice as much as one of the pure PLA. It is consistent with previous study (Refate et al., 2023). Likewise, the diameter of the composite polyurethane-based fiber increased in accordance with the effect of increasing cellulose nanocrystal concentration (Redondo, Jang, Korley, Gunkel, and Steiner, 2020). All conditions of PLA/cellulose fiber were further tested with *in vitro* cell culture to examine the cell adhesion and distribution.

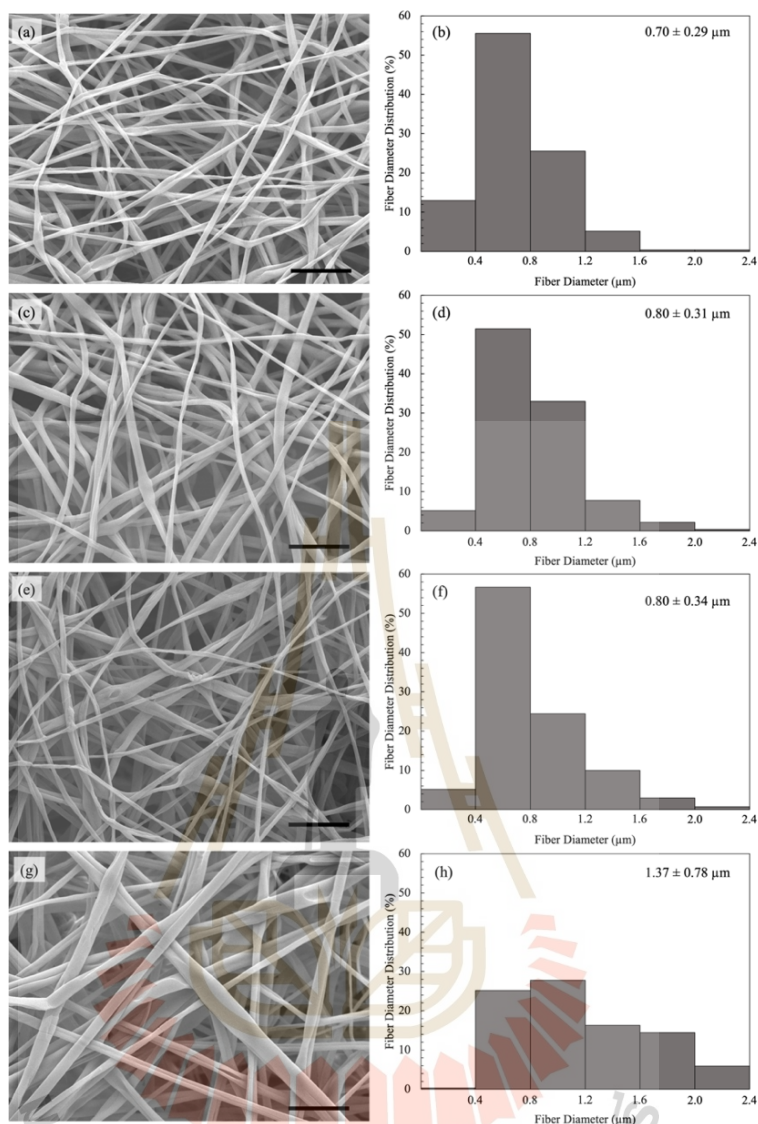


**Figure 4.46** SEM images of fiber morphology with the magnification of 2000X and histograms of fiber diameter distribution as follows: (a, b) pure PCL fiber, (c, d) PLA fiber with 1 wt% of cellulose, (e, f) PLA fiber with 5 wt% of cellulose, and (g, h) PLA fiber with 10 wt% of cellulose. The scale bar is 10  $\mu\text{m}$ .

After the 24-hour cell culture and the sample fixation, the morphology on the surface of samples was observed by SEM. Figure 4.47 presents the morphology of cell adhesion on the control, pure PLA, and PLA/cellulose fiber with 1, 5, and 10 wt%. There was cell adhesion on all samples; however, it is difficult to assess the cell growth and distribution on the sample from the SEM images.

The SR-FTIR imaging technique with HCA was utilized to assess the distribution of cells, both qualitatively and quantitatively. Moreover, it can confirm the existing cell adhesion on samples by detecting the functional group of cells and present the location of cells through SR-FTIR mapping.

Since this technique provides the data regarding the bonding vibration associated with a particular functional group (Deegan, Cinque, Wehbe, Konduru, and Yang, 2015; Pocasap et al., 2020), it can exhibit a dominant peak that allows us to accurately identify the specific area containing our desired components. Figure 4.48 shows the representative FTIR spectra of pure PLA fiber, PLA/cellulose fiber, NIH3T3 cells, and NIH3T3 cells on the PLA/cellulose fiber after 24-hour *in vitro* cell culture. The dominant peak of the PLA fiber was at  $1755\text{ cm}^{-1}$ , corresponding to carbonyl (C=O) characteristic stretching (Chi et al., 2020; Chieng, Ibrahim, Yunus, and Hussein, 2014; Gonçalves, Da Silva, Picciani, and Dias, 2015). The peaks at 1065, 1097, 1137, and  $1197\text{ cm}^{-1}$  were related to C-O stretching vibration (Chi et al., 2020; Chieng et al., 2014; Cosme, Silva, Nunes, and Picciani, 2016; de Deus et al., 2021; Elisabeta et al., 2017). These peaks were found in all samples containing the PLA component. The addition of cellulose showed a new broad region to be in the range of 3290-3532, attributed to the O-H stretching of cellulose (Abderrahim et al., 2015; Delfino, Ricciardi, and Lepore, 2022). The O-H peak of cellulose was detected in the PLA/cellulose of the sample with the addition of 10 wt% cellulose on some areas; however, it was not noticeable in the low content of cellulose in the PLA fiber. It was attributed to the low content of cellulose added inside the fiber, and the reflection mode might be difficult to detect the cellulose inside the fiber. It was similar

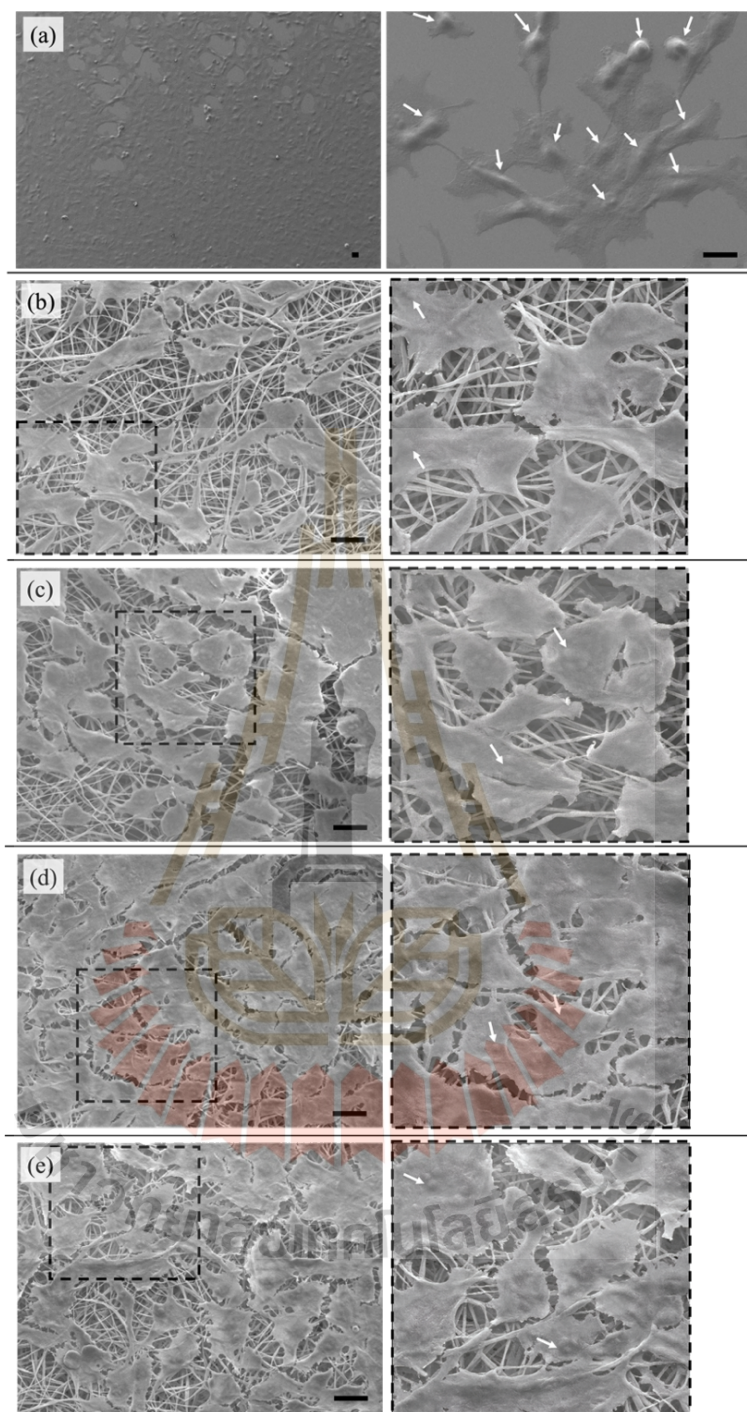


**Figure 4.47** SEM images of NIH3T3 cells on (a) the control, (b) pure PLA fiber, and (c-d) PLA-based fiber with the addition of cellulose: 1, 5, 10 wt%, respectively. The scale bar is 20  $\mu\text{m}$ .

In Elisabeta et al. (2017) that no new peaks occurred, and the additions of cellulose showed the shifted width bands of spectra of PLA/cellulose fibers due to the interaction between PLA and cellulose fiber. The FTIR spectrum of NIH3T3 cells revealed strong absorbance at 1662 and 1548  $\text{cm}^{-1}$ , consistent with the amide I (C=O stretching, C–N stretching) and II bands (C–N stretching, C–NH bending) characteristics of protein (Delfino et al., 2022; Roberts et al., 2018; Zlotnikov et al., 2023). Furthermore, the region of 3100–3600  $\text{cm}^{-1}$  of NIH3T3 was assigned to the stretching vibration of O–H (Delfino et al., 2022; Zlotnikov et al., 2023). As seen in Figure 4.48, the FTIR spectra exhibited obvious difference in spectra regions associated with the presence or absence of cells. Therefore, the C=O stretching and amide I bands were chosen as the representative fingerprints of PLA and cell characteristics to analyze the SR-FTIR imaging.

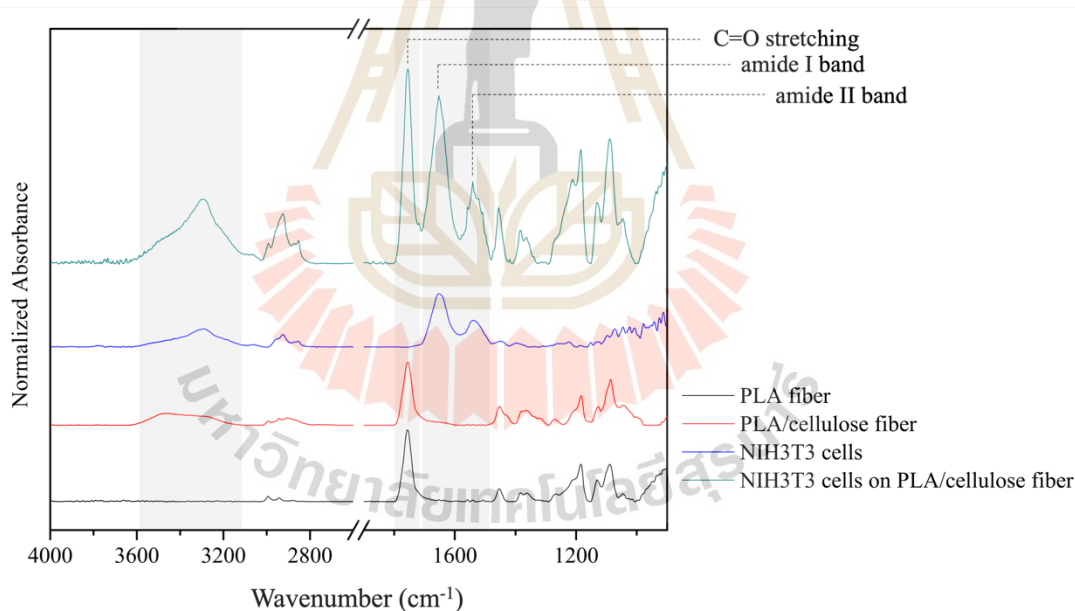


**Figure 4.48** Representative FTIR spectra of pure PLA fiber, PLA/cellulose fiber, NIH3T3 cells, and NIH3T3 cells on the PLA/cellulose fiber with the spectra resolution of 6  $\text{cm}^{-1}$  and the scan time of 64 scans.

The SR-FTIR mapping and hierarchical cluster maps of PLA and cell components based on chemically functional groups are shown in Figure D.2. It

proved the presence of cell adhesion and demonstrated the distribution in specific regions. PLA fibers was not uniform collected because it was attributed to the direct deposition on the window. It might influence to the cell distribution. The further investigation between the nonalignment and alignment of electrospun nanofiber is interesting. The spectra were processed with the second derivation and HCA to obtain the color clusters, which are able to represent the cluster index and reach the normalized index of cell on the single area as the mentioned method.

The statistical analysis presented in Table 4.6 reveals noticeable differences in the distribution of cells on the pure PLA and composite fibers. The composite fiber consisting of 5 wt% cellulose exhibited the lowest **QI** value, indicating the most uniform distribution of cells on the fiber. An increase in cellulose content promoted the uniform distribution of cells. However, when the cellulose content reached 10 wt%, it may not further improve the uniform distribution. The cause can be attributed to many factors. It was attributed to the accumulation of power or the greater diameter of fiber. Further investigation is required, such as varying content ranging from 6 to 9 wt% and the use of nanocellulose powder. Hence, the NIH3T3 cells exhibited adhesion to the PLA-based fiber surface, as confirmed by SEM images, SR-FTIR mapping, and HCA statistical analysis. Furthermore, the incorporation of cellulose into the PLA-based fiber enhanced the distribution of NIH3T3 cells. Nonetheless, further investigation on different regions of samples and an increase in replication have been requested.

**Table 4.6** The analytical results of hierarchical cluster based on the integration and cluster index.

Factors	Sample number			
	1	2	3	4
Cellulose in PLA-based nanofiber (wt%)	0	1	5	10
Average fiber diameter ( $\mu\text{m}$ )	$0.70 \pm 0.29$	$0.80 \pm 0.31$	$0.80 \pm 0.34$	$1.37 \pm 0.78$
<i>Calculated values*</i>				
Replication 1	0.13	0.14	0.19	0.05
Replication 2	0.28	0.02	0.16	0.12
Replication 3	0.00	0.04	0.17	0.08
<b>Qn</b>	0.14	0.07	0.17	0.08
<b>Qn deviation</b>	0.14	0.06	0.02	0.03
<b>QI</b>	100.61	95.58	10.74	42.64

\* The calculated values were obtained by multiplying the cluster indexes with the amount of color grid, and then statistically averaged for each replicate.

#### 4.3.2.3 Synchrotron Radiation X-ray Tomography

The SRXTM was used to observe the cell morphology and adhesion within the 3D-electrospun scaffolds cultured for 1 and 3 days. It is able to present a large field of view that allows for clear visualization of cells on the surface of the scaffolds after normalization, reconstruction, and image processing. Since the intensity distribution of the X-ray absorptance of cells and PCL polymer is overlapping, the dyeing process is needed.  $\text{OsO}_4$  was used for dyeing purposes to facilitate examination with SRXTM and validate the analysis of cell behavior on electrospun structures (Castejón et al., 2018). The distinction between cells and fibers can be determined by analyzing the disparity in X-ray absorptance intensity. The pristine PCL-electrospun scaffold without undergoing any process of cell culture and the PCL scaffold with the *in-vitro* culture, including the staining process, were examined using SRXTM. Figure 4.49 demonstrates that no signals were observed within the intensity range used to identify stained cells, ensuring this procedure for conducting bioassessment within 3D-electrospun scaffolds.

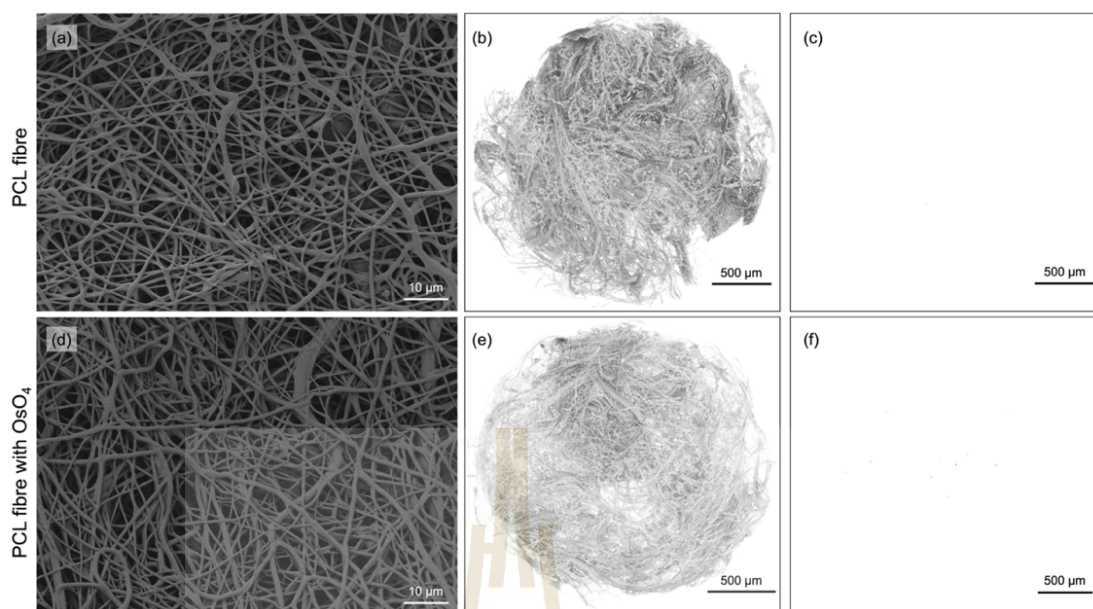
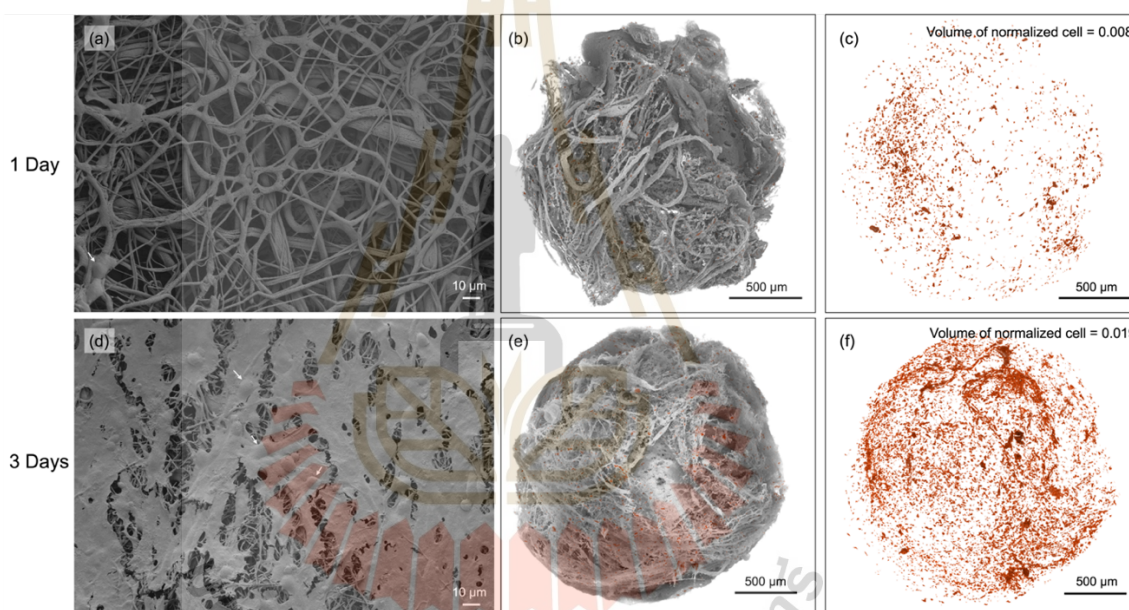


Figure 4.49 (a-b) SEM and (d, c, e, f) SRXTM images of (a-c) pristine PCL fiber and (d-f) PCL fiber stained with OsO<sub>4</sub>. To be detailed, the SRXTM images were identified by (b, e) the intensity region of PCL polymer and OsO<sub>4</sub>-stained cells, and (c, f) the intensity region of OsO<sub>4</sub>-stained cells.

The SEM and SRXTM images of cell morphology and adhesion during 1 and 3 days of culture are shown in Figure 4.50. Figure 4.50(a) shows little cell count on the electrospun surface for 1 day, even though the SRXTM reveals a discernible distribution of cells inside the scaffolds, as observed in Figure 4.50(b, c). This result highlights the potential of wide spatial and in-depth observation. The NIH3T3 cell enables growth within the electrospun scaffolds, as shown in Figure 4.50(a, d). In Figure 4.50(b, e), cells attached to the fibers were shown, and the distribution of cells appeared to be random within the scaffolds. After 3 days of cell culture, the SRXTM results significantly ensured the verification of cell migration and proliferation within the electrospun structures (Figure 4.50(c, f)), corresponding with the observations by SEM. The SRXTM images were transferred to the quantitative data by measuring the volume of components with a tool of functions in the Drishti software. Since the amount of fiber on each scaffold was different, the volume of cells was normalized by comparing with the volume of fiber to assess the cell growth on the scaffolds during 1 and 3 days of the culture. Figure E.1 shows the broader view of SEM images of cells after the culture for 3 days,

which illustrates this cell behavior almost everywhere, not only one point. It is in agreement with the SRXTM observation in Figure 4.50(d-f). To assess the cell proliferation, the volume of each component including fibers and cells was measured by considering the whole sample and the selected volume with  $300 \times 300 \times 300$  voxel as concluded in Table E.1. The normalized volumes of cells on the scaffolds considered by whole volume after 1 and 3 days of culture were 0.008 and 0.019, respectively. It implied that there was a twice increase in cell growth on the scaffolds according to the increase in culture days. Likewise, the normalized volumes of cells on the scaffolds considered by selected volumes were 0.006 and 0.012 which was the twice increase.



**Figure 4.50** SEM and SRXTM images of NIH3T3 cells seeded on PCL-fibrous structures for 1 and 3 days of the culture, which are (a) SEM image showing the surface of the cell on the fibrous structures after seeding the cells into the scaffolds for (a) 1 and (d) 3 days, SRXTM image of the NIH3T3 cells (red area) seeded into the scaffolds (a grey area) for (b) 1 and (e) 3 days, and SRXTM image of the NIH3T3 cell distribution after seeding the cell into the scaffold for (c) 1 and (f) 3 days.

## CHAPTER V

### CONCLUSION

The objectives, hypotheses, and basic principles, outlined in Chapters I and II, were amalgamated with an extensive assortment of 3D electrospinning assembly and characterizations in Chapter III, which focused on the assembly of 3D electrospinning and characterization of 3D fibrous macrostructures and biological activities. Chapter IV, specifically section 4.1, discussed the proper setup for 3D electrospinning. Additionally, it explored the conditions and characteristics necessary to produce self-assembled electrospun stacks and build 3D fibrous macrostructures, as discussed in section 4.2 of Chapter IV. Furthermore, the biocompatibilities of the 3D fibrous constructions were evaluated through *in vitro* cell culture using SEM, SR-FTIR and SRXTM techniques in section 4.3 of Chapter IV.

As stated in hypothesis I, the investigation focused on the 3D electrospinning technique using cartesian and delta coordinates. It was discovered that both coordinates face the common issue of fibers being deposited in undesirable locations. Nevertheless, the delta framework effectively avoided this issue by incorporating silicon onto the tower in areas outside of the reach of the carriages. Here, the delta coordinate was used to be the mechanical component of 3D electrospinning. Figure 5.1 showcases the most recent version of 3D electrospinning. This device allows for the buildup and control of 3D fibrous macrostructures. It has a maximum printing area of 500 mm in height and 180 mm in diameter. The flow rate can range from 0.1 to 300 ml/h, and a voltage source can be applied in a range from 1.0 to 50.0 kV.

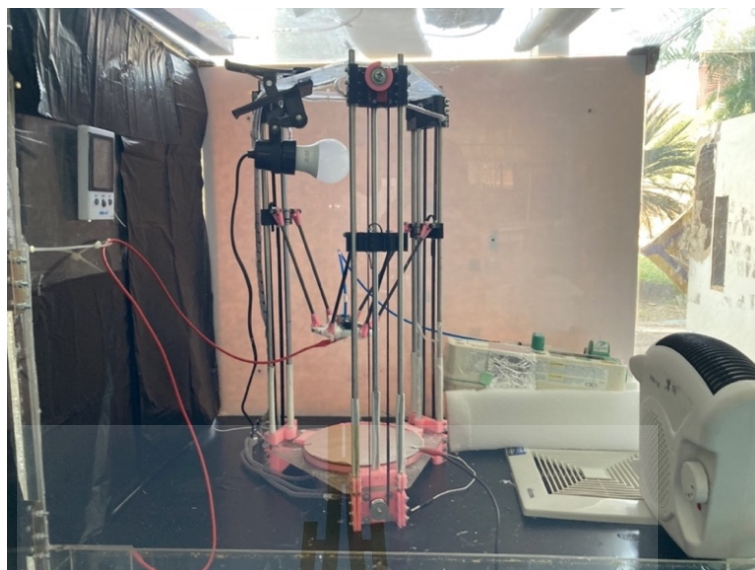


**Figure 5.1** The current version of 3D electrospinning setup in this work.

The results from Chapter 4, particularly in section 4.2 (as seen in Figure 5.2), provide confirmation that supports hypothesis II in this study. The conductivity of a solution is a significant component to facilitating the self-assembly of 3D fibrous structures. The addition of  $H_3PO_4$  additives was crucial for the 3D electrospun stack of PCL and PVDF, but the PAN solution in DMF solvent did not require the additives. The addition of  $H_3PO_4$  additives did not change the chemical bonding and crystalline structures of PCL and PVDF, as indicated in the XRD pattern, FTIR spectra, and Raman spectra. However, the process of electrospinning caused a phase change in PVDF by increasing the  $\beta$  phase on the electrospun fiber, as confirmed by the XRD pattern.

Undoubtedly, the addition of  $H_3PO_4$  in a solution provides greater potential for constructing 3D fibrous macrostructures. Nevertheless, the high presence of  $H_3PO_4$  leads to the formation of bead-like fibers and fluffy fibrous structures, making it challenging to precisely regulate the positioning of the incoming fiber during deposition. The formation of 3D fibrous macrostructures is influenced not only by conductivity but also by the concentration, which determines the number of incoming fibers. The concentration may not have an apparent impact when the nozzle is fixed, but it is essential when the nozzle is in motion. If the concentration is insufficient, the fiber being produced will not be continuous and the distance between the nozzle and the collector will progressively increase, resulting in spatial

dispersion in two dimensions. The increased concentration causes the solution at the nozzle tip to dry out and can potentially impact vertical structures due to the weight of a large amount of fiber. Furthermore, it is crucial to ensure that the solvent is properly proportioned with the concentration and flow rate in order to achieve sufficient evaporation during electrospinning, under the specified conditions. The flow rate factor provides results that closely correspond to the concentration. The building of 3D electrospun macrostructures is influenced not only by the flow rate and concentration, but also by other parameters such as initial distance, voltage, and moving speed. The insufficient starting distance hinders the development of three-dimensional macrostructures, whereas an excessive initial distance results in the construction of a two-dimensional mat instead of a three-dimensional stack. The effect of solution and electrospinning on 3D fibrous macrostructures are concluded in Table 5.1 based on the empirical tests.

**Table 5.1** The effect of electrospinning parameters on the shape of 3D macrostructures.

Parameters	Height	$C_{hh}$	DW	$D_{out}$	Wall thickness	Diameter
↑ Flow rate	≈	↑	↑↓	↓	↓	≈
↑ Initial Distance	≈	↑	↑*	↑	↑	↑*
↑ Voltage	↑↓	↑↓	↓	↓	↓	↓
↑ Nozzle's Speed	↑↓	↑	↑	-	↑	↑

Note ↑ = increase, ↓ = decrease, ≈ = fluctuation, ↑↓ = increase until the point and then decreases, \* = based on the separation of consideration between 2D mat and 3D structures.

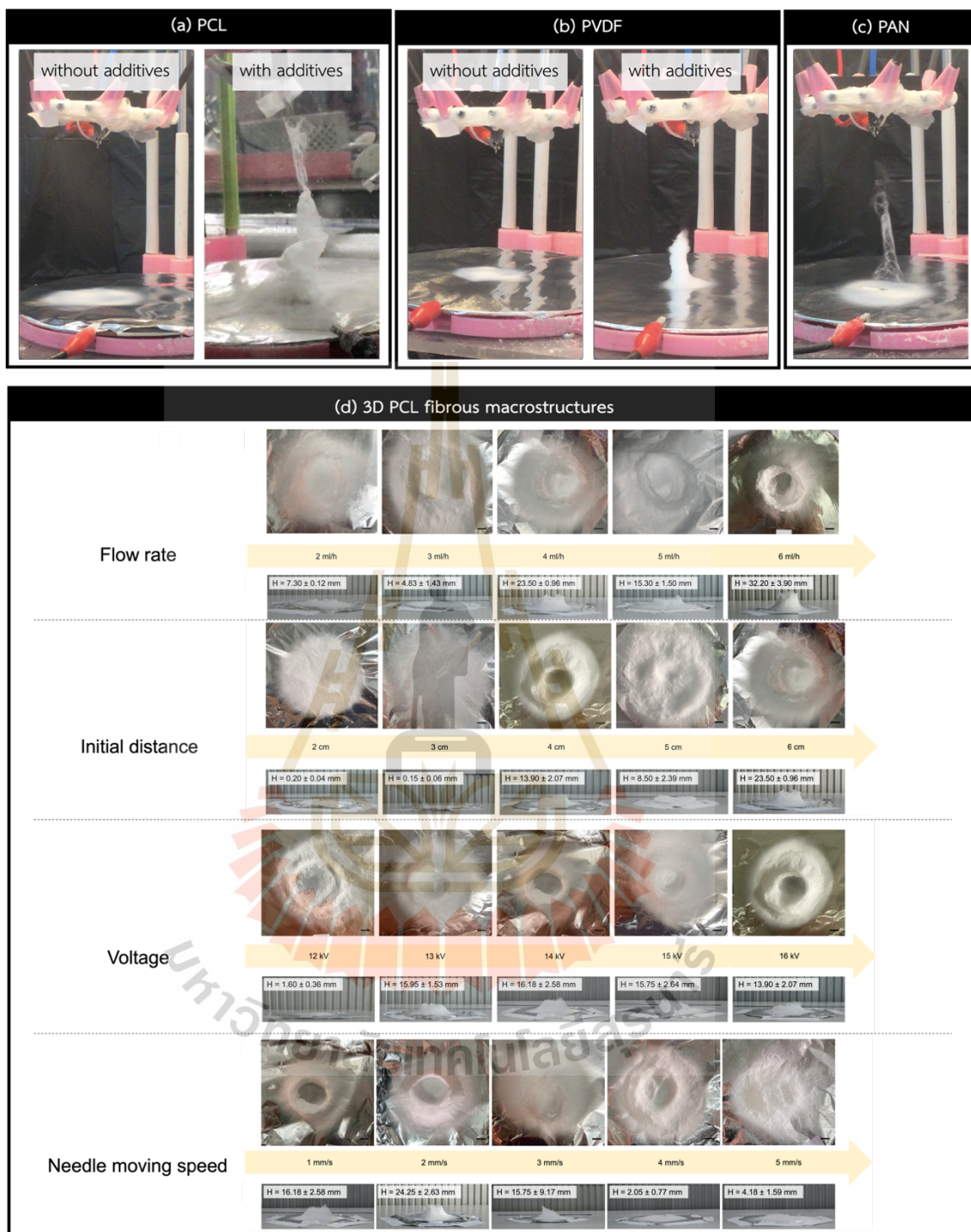


**Figure 5.2** Photographs of 2D mat and 3D stack electrospun (a) using PCL solution without and with the  $\text{H}_3\text{PO}_4$  additives, (b) using PVDF solution without and with the  $\text{H}_3\text{PO}_4$  additives, (c) 3D stack using PAN solution, and (d) the influence of electrospinning parameters on the 3D fibrous macrostructures.

The results presented in Section 4.3 of Chapter 4 provide support for Hypotheses III and IV of this work. The hydrophilic property of 3D PCL fibrous structures can be enhanced via plasma treatment, which is essential for cell culture. The optimal conditions of plasma treatment yield favorable results in *in vitro* cell culture. If the power applied in the plasma treatment was low, the hydrophilic property underwent modifications. Conversely, if excessively high power was given, it resulted in the melting and a lack of fibers, both of which were not favor to cell adhesion. In part of biological assessment, the SR-FTIR imaging techniques can provide the mapping used to track the location of cell on the fibrous sample. Furthermore, the analytical method of SR-FTIR imaging with HCA is able to provide distribution information. In this work, the results of SR-FTIR imaging with HCA implied the content of 5 wt% cellulose performed the most uniform distribution of cells on the fiber as shown in Table 4.6. The SRXTM technique is a potential tool for observing the cell morphology and adhesion within 3D PCL scaffolds. Not only the observation on the surface of electrospun graft, but also the inside of graft can be observed, as seen in Figure 5.3. In addition, the normalized volume of cell by compared to the volume of fiber can imply to the cell growth inside the electrospun graft.

As an aspect of biological assessments, the SR-FTIR imaging techniques can be utilized to generate a map that accurately traces the position of cells on the fibrous sample and assess the distribution of components. The analytical method of SR-FTIR imaging can provide quantitative results, allowing for comparable outcomes to reach the optimal condition. It is an effective technique for observing and analyzing the biochemical composition. It can not only indicate the distribution of components but also accurately monitor the location of composites. Furthermore, the SRXTM approach has the potential to be used as a tool for monitoring the cell morphology and adhesion within 3D PCL scaffolds. The top view, cross section, and bottom view of the electrospun graft can be viewed, as depicted in Figure 5.3. Furthermore, the volume of cell can indicate existing cell growth within the electrospun graft. When comparing the volume of cells cultivated for 1 and 3 days, the ratio of the

NIH3T3 cell's normalized volume to the volume of the PCL graft in this work can indicate a double rise in NIH3T3 cell growth within the PCL electrospun graft.

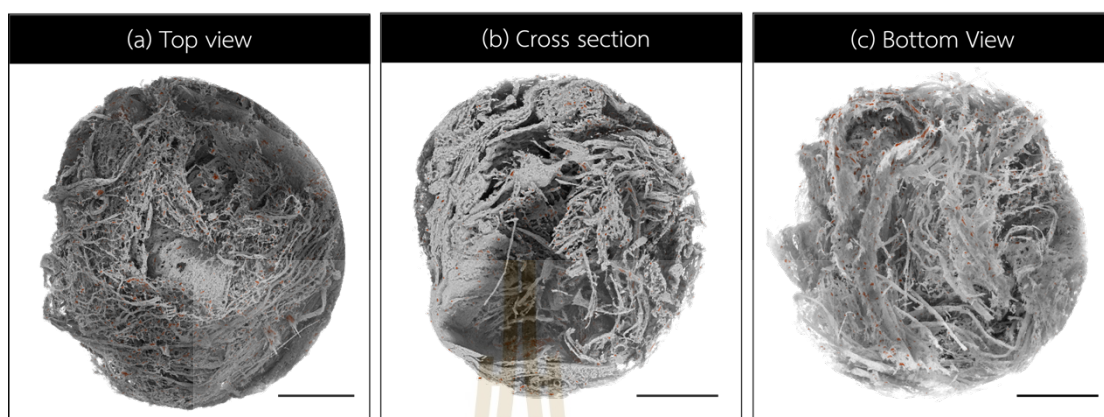


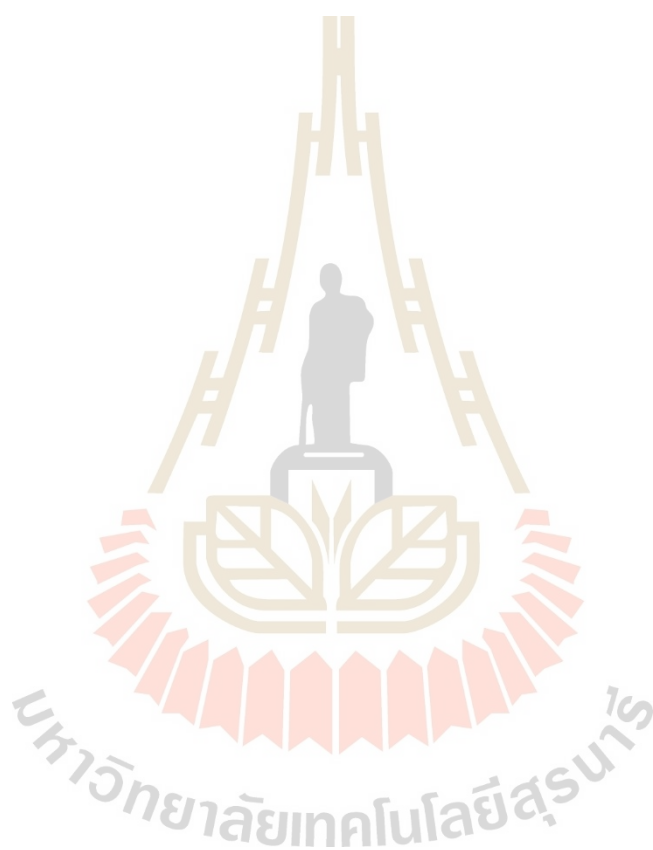
**Figure 5.3** SRXTM images of NIH3T3 cells (shown by red spots) cultivated on PCL fiber structures (represented by gray region). The imaging was performed from (a) the top view, (b) cross section, and (c) bottom view. The scale bar is 500  $\mu\text{m}$ .

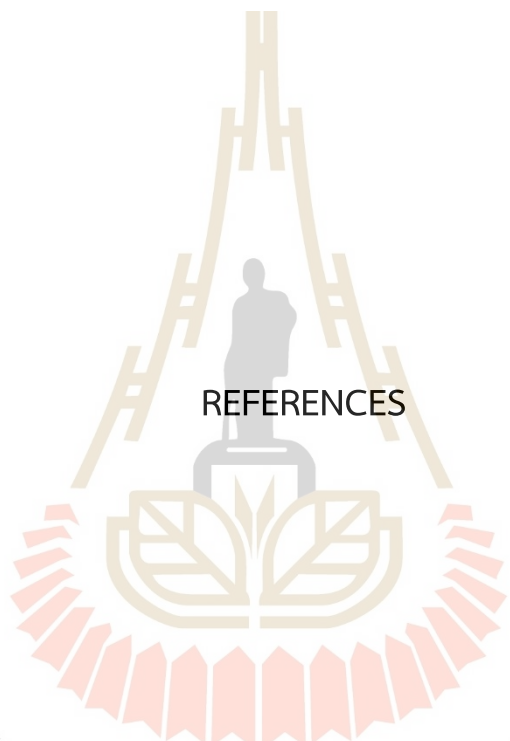
### Future Perspectives

The conclusions of this work demonstrate the capacity of 3D electrospinning to create 3D fibrous macrostructures, as well as the efficiency of the SR-FTIR and SRXTM approaches for biological evaluations. The results show that it is feasible to gather electrospun fibers during the early whipping phase in order to construct 3D electrospun macrostructures. Further, the resulting 3D macrostructures possess biocompatible abilities following the proper improvement. As stated in the expected impact outlined in section 1.5 of Chapter I, next prospects will integrate the tests, parameters, and modeling through the utilization of 3D electrospinning to produce more polymers and composites. The number of 3D self-assembled structures achieved using 3D electrospinning has the potential to significantly increase. The utilization of SR-FTIR and SRXTM techniques for observing biological activity is expected to expand and develop.

This advancement in 3D electrospinning not only overcomes current constraints in scaffold fabrication but also opens up possibilities for groundbreaking applications in various fields. The precise design and enhanced capabilities of these

large-scale structures have considerable potential for expanding the field of lab-grown organs and creating artificial tissues. Furthermore, the foundational work laid by this 3D electrospinning method sets the stage for advancements in 4D printing, particularly in the development of dynamic, responsive fibrous materials, opening new horizons in biomedical engineering and beyond.





REFERENCES

มหาวิทยาลัยเทคโนโลยีสุรนารี

## REFERENCES

- Abadi, B., Goshtasbi, N., Bolourian, S., Tahsili, J., Adeli-Sardou, M., and Forootanfar, H. (2022). Electrospun hybrid nanofibers: Fabrication, characterization, and biomedical applications. *Frontiers in Bioengineering and Biotechnology*, 10.
- Abderrahim, B., Abderrahman, E., Mohamed, A., Fatima, T., Abdesselam, T., and Krim, O. (2015). Kinetic Thermal Degradation of Cellulose, Polybutylene Succinate and a Green Composite: Comparative Study. *World Journal of Environmental Engineering*, 3(4), 95-110.
- Ahangar, P., Cooke, M. E., Weber, M. H., and Rosenzweig, D. H. (2019). Current Biomedical Applications of 3D Printing and Additive Manufacturing. *Applied Sciences*, 9(8), 1713.
- Ahirwal, D., Hébraud, A., Kádár, R., Wilhelm, M., and Schlatter, G. (2013). From self-assembly of electrospun nanofibers to 3D cm thick hierarchical foams. *Soft Matter*, 9(11), 3164-3172.
- Ajay, L. (2012). *Drishti: a volume exploration and presentation tool*. Paper presented at the Proc.SPIE.
- Akhtar, K., Khan, S. A., Khan, S. B., and Asiri, A. M. (2018). Scanning Electron Microscopy: Principle and Applications in Nanomaterials Characterization. In *Handbook of Materials Characterization* (pp. 113-145).
- Al-Abduljabbar, A., and Farooq, I. (2023). Electrospun Polymer Nanofibers: Processing, Properties, and Applications. *Polymers*, 15(1), 65.
- Alghoraibi, I., and Alomari, S. (2018). Different Methods for Nanofiber Design and Fabrication. In *Handbook of Nanofibers* (pp. 1-46).
- Alipoori, S., Torkzadeh, M. M., Mazinani, S., Aboutalebi, S. H., and Sharif, F. (2021). Performance-tuning of PVA-based gel electrolytes by acid/PVA ratio and PVA molecular weight. *SN Applied Sciences*, 3(3), 310.
- Apsite, I., Stoychev, G., Zhang, W., Jehnichen, D., Xie, J., and Ionov, L. (2017). Porous Stimuli-Responsive Self-Folding Electrospun Mats for 4D Biofabrication. *Biomacromolecules*, 18(10), 3178-3184.

- Arabi, A., Boggs, E., Patel, M. R., Zwiesler-Vollick, J., Maerz, T., Baker, K., . . . Li, Y. (2014). Surface modification of electrospun polycaprolactone fibers and effect on cell proliferation. *Surface Innovations*, 2(1), 47-59.
- Arican, F., Uzuner-Demir, A., Polat, O., Sancakli, A., and Ismar, E. (2022). Fabrication of gelatin nanofiber webs via centrifugal spinning for N95 respiratory filters. *Bulletin of Materials Science*, 45(2), 93.
- Askari, M., Afzali Naniz, M., Kouhi, M., Saberi, A., Zolfagharian, A., and Bodaghi, M. (2021). Recent progress in extrusion 3D bioprinting of hydrogel biomaterials for tissue regeneration: a comprehensive review with focus on advanced fabrication techniques. *Biomaterials Science*, 9(3), 535-573.
- Bain, S., and Koomsap, P. (2016). Preliminary Study on Solvent Effect in Fiber Fabrication in Near-Field Electrospinning.
- Bakhtiary, N., Pezeshki-Modaress, M., and Najmoddin, N. (2022). Wet-electrospinning of nanofibrous magnetic composite 3-D scaffolds for enhanced stem cells neural differentiation. *Chemical Engineering Science*, 264, 118144.
- Balaji T, P., and Choudhury, S. (2022). 7 - Separators for lithium-sulfur batteries. In *Lithium-Sulfur Batteries* (pp. 121-156).
- Balu, R., Kumar, T. S., and Ramalingam, M. (2011). Electrospun Polycaprolactone/Poly(1,4-butylene adipate-co-polycaprolactam) Blends: Potential Biodegradable Scaffold for Bone Tissue Regeneration. *Journal of Biomaterials and Tissue Engineering*, 1, 30-39.
- Baranowska-Korczyn, A., Warowicka, A., Jasiurkowska-Delaporte, M., GrzeŚkowiak, B., Jarek, M., Maciejewska, B. M., . . . Jurga, S. (2016). Antimicrobial electrospun poly( $\epsilon$ -caprolactone) scaffolds for gingival fibroblast growth. *RSC Advances*, 6(24), 19647-19656.
- Bell, C. (2015a). Delta Printer Hardware. In *3D Printing with Delta Printers* (pp. 39-70).
- Bell, C. (2015b). Introduction to Delta 3D Printers. In *3D Printing with Delta Printers* (pp. 1-37).

- Blakeney, B. A., Tambralli, A., Anderson, J. M., Andukuri, A., Lim, D.-J., Dean, D. R., and Jun, H.-W. (2011). Cell infiltration and growth in a low density, uncompressed three-dimensional electrospun nanofibrous scaffold. *Biomaterials*, 32(6), 1583-1590.
- Boyd, S. A., Su, B., Sandy, J. R., and Ireland, A. J. (2012). Cellulose Nanofibre Mesh for Use in Dental Materials. *Coatings*, 2(3), 120-137.
- Boys, C. V. (1887). On the Production, Properties, and some suggested Uses of the Finest Threads. *Proceedings of the Physical Society of London*, 9(1), 8.
- Bradley, R. S., Robinson, I. K., and Yusuf, M. (2017). 3D X-Ray Nanotomography of Cells Grown on Electrospun Scaffolds. *Macromolecular bioscience*, 17 2.
- Cai, S., Xu, H., Jiang, Q., and Yang, Y. (2013). Novel 3D Electrospun Scaffolds with Fibers Oriented Randomly and Evenly in Three Dimensions to Closely Mimic the Unique Architectures of Extracellular Matrices in Soft Tissues: Fabrication and Mechanism Study. *Langmuir*, 29(7), 2311-2318.
- Cao, K., Zhang, F., Zaeri, A., Zhang, Y., Zgeib, R., Calzolaio, M., and Chang, R. C. (2023). Advances in design and quality of melt electrowritten scaffolds. *Materials & Design*, 226, 111618.
- Cao, L., Si, Y., Yin, X., Yu, J., and Ding, B. (2019). Ultralight and Resilient Electrospun Fiber Sponge with a Lamellar Corrugated Microstructure for Effective Low-Frequency Sound Absorption. *ACS Applied Materials & Interfaces*, 11(38), 35333-35342.
- Carew, R. M., and Errickson, D. (2020). An Overview of 3D Printing in Forensic Science: The Tangible Third-Dimension. *Journal of Forensic Sciences*, 65(5), 1752-1760.
- Castejón, D., Alba-Tercedor, J., Rotllant, G., Ribes, E., Durfort, M., and Guerao, G. (2018). Micro-computed tomography and histology to explore internal morphology in decapod larvae. *Scientific Reports*, 8(1), 14399.
- Chainani, A., Hippensteel, K. J., Kishan, A., Garrigues, N. W., Ruch, D. S., Guilak, F., and Little, D. (2013). Multilayered Electrospun Scaffolds for Tendon Tissue Engineering. *Tissue Engineering Part A*, 19(23-24), 2594-2604.

- Charpashlo, E., Ghorani, B., and Mohebbi, M. (2021). Multilayered electrospinning strategy for increasing the bioaccessibility of lycopene in gelatin-based sub-micron fiber structures. *Food Hydrocolloids*, 113, 106411.
- Chen, H.-W., and Lin, M.-F. (2020). Characterization, Biocompatibility, and Optimization of Electrospun SF/PCL/CS Composite Nanofibers. *Polymers*, 12(7), 1439.
- Chen, S., John, J. V., McCarthy, A., Carlson, M. A., Li, X., and Xie, J. (2020). Fast transformation of 2D nanofiber membranes into pre-molded 3D scaffolds with biomimetic and oriented porous structure for biomedical applications. *Applied Physics Reviews*, 7(2).
- Chen, W., Xu, Y., Liu, Y., Wang, Z., Li, Y., Jiang, G., . . . Zhou, G. (2019). Three-dimensional printed electrospun fiber-based scaffold for cartilage regeneration. *Materials & Design*, 179, 107886.
- Chen, Y., Xu, W., Shafiq, M., Tang, J., Hao, J., Xie, X., . . . Mo, X. (2021). Three-dimensional porous gas-foamed electrospun nanofiber scaffold for cartilage regeneration. *Journal of Colloid and Interface Science*, 603, 94-109.
- Chi, H. Y., Chan, V., Li, C., Hsieh, J. H., Lin, P. H., Tsai, Y.-H., and Chen, Y. (2020). Fabrication of polylactic acid/paclitaxel nano fibers by electrospinning for cancer therapeutics. *BMC Chemistry*, 14(1), 63.
- Chieng, B. W., Ibrahim, N. A., Yunus, W. M. Z. W., and Hussein, M. Z. (2014). Poly(lactic acid)/Poly(ethylene glycol) Polymer Nanocomposites: Effects of Graphene Nanoplatelets. *Polymers*, 6(1), 93-104.
- Choi, D. Y., Bak, T. Y., Hwang, Y. H., Yang, S. W., Jung, S. C., Kook, M. S., and Kim, B. H. (2015). Preparation of O<sub>2</sub> Plasma Treated Polycaprolactone/Nano TiO<sub>2</sub> Composites and In Vitro Bioactivity. *J Nanosci Nanotechnol*, 15(8), 5653-5655.
- Chowdhury, S., Yadaiah, N., Prakash, C., Ramakrishna, S., Dixit, S., Gupta, L. R., and Buddhi, D. (2022). Laser powder bed fusion: a state-of-the-art review of the technology, materials, properties & defects, and numerical modelling. *Journal of Materials Research and Technology*, 20, 2109-2172.
- Cipitria, A., Skelton, A., Dargaville, T. R., Dalton, P. D., and Hutmacher, D. W. (2011). Design, fabrication and characterization of PCL electrospun scaffolds—a review. *Journal of Materials Chemistry*, 21(26), 9419-9453.

- Constante, G., Apsite, I., Alkhamis, H., Dulle, M., Schwarzer, M., Caspari, A., . . . Ionov, L. (2021). 4D Biofabrication Using a Combination of 3D Printing and Melt-Electrowriting of Shape-Morphing Polymers. *ACS Applied Materials & Interfaces*, 13(11), 12767-12776.
- Cooley, J. F. (1899). United States Patent No. February 4, 1902.
- Cosme, J., Silva, V., Nunes, R., and Picciani, P. (2016). Development of Biobased Poly(Lactic Acid)/Epoxidized Natural Rubber Blends Processed by Electrospinning: Morphological, Structural and Thermal Properties. *Materials Sciences and Applications*, 7, 210-219.
- Dalton, P. D. (2017). Melt electrowriting with additive manufacturing principles. *Current Opinion in Biomedical Engineering*, 2, 49-57.
- de Deus, W. F., de França, B. M., Forero, J. S. B., Granato, A. E. C., Ulrich, H., Dória, A. C. O. C., . . . Rodrigues, B. V. M. (2021). Curcuminoid-Tailored Interfacial Free Energy of Hydrophobic Fibers for Enhanced Biological Properties. *ACS Applied Materials & Interfaces*, 13(21), 24493-24504.
- Deegan, A. J., Cinque, G., Wehbe, K., Konduru, S., and Yang, Y. (2015). Tracking calcification in tissue-engineered bone using synchrotron micro-FTIR and SEM. *Analytical and bioanalytical chemistry*, 407(4), 1097-1105.
- Delfino, I., Ricciardi, V., and Lepore, M. (2022). Synchrotron FTIR Microspectroscopy Investigations on Biochemical Changes Occurring in Human Cells Exposed to Proton Beams. *Applied Sciences*, 12(1), 336.
- Dorota, P., and Malgorzata, C. (2021). Raman Spectroscopy in the Analysis of Textile Structures. In *Recent Developments in Atomic Force Microscopy and Raman Spectroscopy for Materials Characterization* (pp. Ch. 9).
- Du, X., Zhong, Y., Kang, G., Jiang, J., Wang, X., Li, W., and Zheng, G. (2023). Low-Temperature Self-Stacking Ink for Electrohydrodynamic Direct Writing. *ACS Applied Polymer Materials*, 5(7), 5314-5321.
- Duangkanya, K., Kopwitthaya, A., Chanhorm, S., and Infahsaeng, Y. (2022). Oxygen plasma treatment time induced hydrophilicity of polydimethylsiloxane (PDMS) thin films for liquid lenses application. *Materials Today: Proceedings*, 65, 2442-2445.

- Eatemadi, A., Daraee, H., Zarghami, N., Melat Yar, H., and Akbarzadeh, A. (2016). Nanofiber: Synthesis and biomedical applications. *Artificial Cells, Nanomedicine, and Biotechnology*, 44(1), 111-121.
- Elisabeta, E., Răpă, M., Popa, O., Mustatea, G., Popa, V., Mitelut, A., and Popa, M. (2017). Polylactic Acid/Cellulose Fibres Based Composites for Food Packaging Applications. *MATERIALE PLASTICE*, 54, 673-677.
- Elkaseer, A., Chen, K. J., Janhsen, J. C., Refle, O., Hagenmeyer, V., and Scholz, S. G. (2022). Material jetting for advanced applications: A state-of-the-art review, gaps and future directions. *Additive Manufacturing*, 60, 103270.
- Eom, S., Park, S. M., Hong, H., Kwon, J., Oh, S.-R., Kim, J., and Kim, D. S. (2020). Hydrogel-Assisted Electrospinning for Fabrication of a 3D Complex Tailored Nanofiber Macrostructure. *ACS Applied Materials & Interfaces*, 12(46), 51212-51224.
- Epp, J. (2016). 4 - X-ray diffraction (XRD) techniques for materials characterization. In *Materials Characterization Using Nondestructive Evaluation (NDE) Methods* (pp. 81-124).
- Esmail, A., Pereira, J. R., Zoio, P., Silvestre, S., Menda, U. D., Sevrin, C., . . . Freitas, F. (2021). Oxygen Plasma Treated-Electrospun Polyhydroxyalkanoate Scaffolds for Hydrophilicity Improvement and Cell Adhesion. *Polymers*, 13(7), 1056.
- Fang, F., Wang, H., Wang, H., Huang, W. M., Chen, Y., Cai, N., . . . Chen, X. (2021). Stimulus-Responsive Shrinkage in Electrospun Membranes: Fundamentals and Control. *Micromachines*, 12(8), 920.
- Fromager, B., Marhuenda, E., Louis, B., Bakalara, N., Cambedouzou, J., and Cornu, D. (2023). Recent Advances in Electrospun Fibers for Biological Applications. *Macromol*, 3(3), 569-613.
- Gade, H., Nikam, S., Chase, G. G., and Reneker, D. H. (2021). Effect of electrospinning conditions on  $\beta$ -phase and surface charge potential of PVDF fibers. *Polymer*, 228, 123902.
- Gai, Z., and Palasiatica, V. (2018). Synchrotron X-ray tomographic microscopy reveals histology and internal structure of Galeaspida (Agnatha). 56.

- Gao, Q., Gu, H., Zhao, P., Zhang, C., Cao, M., Fu, J., and He, Y. (2018). Fabrication of electrospun nanofibrous scaffolds with 3D controllable geometric shapes. *Materials & Design*, 157, 159-169.
- Garg, T., Rath, G., and Goyal, A. K. (2015). Biomaterials-based nanofiber scaffold: targeted and controlled carrier for cell and drug delivery. *Journal of Drug Targeting*, 23(3), 202-221.
- Ghobeira, R., Geyter, N. D., and Morent, R. (2017). *Plasma surface functionalization of biodegradable electrospun scaffolds for tissue engineering applications*.
- Gibson, I., Rosen, D. W., and Stucker, B. (2010). Introduction and Basic Principles. In *Additive Manufacturing Technologies: Rapid Prototyping to Direct Digital Manufacturing* (pp. 20-35).
- Gonçalves, R., Da Silva, F., Picciani, P., and Dias, M. (2015). Morphology and Thermal Properties of Core-Shell PVA/PLA Ultrafine Fibers Produced by Coaxial Electrospinning. *Materials Sciences and Applications*, 6, 189-199.
- Gorodzha, S. N., Surmeneva, M. A., and Surmenev, R. A. (2015). Fabrication and characterization of polycaprolactone cross- linked and highly-aligned 3-D artificial scaffolds for bone tissue regeneration via electrospinning technology. *IOP Conference Series: Materials Science and Engineering*, 98(1), 012024.
- Guo, Y., and Zhou, Y. (2007). Polyaniline nanofibers fabricated by electrochemical polymerization: A mechanistic study. *European Polymer Journal*, 43(6), 2292-2297.
- H. Yousefi, S., Tang, C., Tafreshi, H., and Pourdeyhimi, B. (2019). Empirical model to simulate morphology of electrospun polycaprolactone mats. *Journal of Applied Polymer Science*, 136, 48242.
- Haider, A., Haider, S., and Kang, I.-K. (2018). A comprehensive review summarizing the effect of electrospinning parameters and potential applications of nanofibers in biomedical and biotechnology. *Arabian Journal of Chemistry*, 11(8), 1165-1188.

- Haider, M. K., Ullah, A., Sarwar, M., Yamaguchi, T., Wang, Q., Ullah, S., . . . Kim, I.-S. (2021). Fabricating Antibacterial and Antioxidant Electrospun Hydrophilic Polyacrylonitrile Nanofibers Loaded with AgNPs by Lignin-Induced In-Situ Method. *Polymers*, *13*, 748.
- He, Z., Rault, F., Lewandowski, M., Mohsenzadeh, E., and Salaün, F. (2021). Electrospun PVDF Nanofibers for Piezoelectric Applications: A Review of the Influence of Electrospinning Parameters on the  $\beta$  Phase and Crystallinity Enhancement. *Polymers*, *13*.
- Hekmati, A. H., Rashidi, A., Ghazisaeidi, R., and Drean, J.-Y. (2013). Effect of needle length, electrospinning distance, and solution concentration on morphological properties of polyamide-6 electrospun nanowebs. *Textile Research Journal*, *83*(14), 1452-1466.
- Herrero-Herrero, M., Gómez-Tejedor, J. A., and Vallés-Lluch, A. (2018). PLA/PCL electrospun membranes of tailored fibres diameter as drug delivery systems. *European Polymer Journal*, *99*, 445-455.
- Huang, J. (2006). Syntheses and applications of conducting polymer polyaniline nanofibers. *Pure and Applied Chemistry*, *78*(1), 15-27.
- Hwang, T. I., Kim, J. I., Lee, J., Moon, J. Y., Lee, J. C., Joshi, M. K., . . . Kim, C. S. (2020). In Situ Biological Transmutation of Catalytic Lactic Acid Waste into Calcium Lactate in a Readily Processable Three-Dimensional Fibrillar Structure for Bone Tissue Engineering. *ACS Applied Materials & Interfaces*, *12*(16), 18197-18210.
- Islam, M. S., Ang, B. C., Andriyana, A., and Afifi, A. M. (2019). A review on fabrication of nanofibers via electrospinning and their applications. *SN Applied Sciences*, *1*(10), 1248.
- Janakiraman, S., Surendran, A., Ghosh, S., Anandhan, S., and Venimadhav, A. (2016). Electroactive poly(vinylidene fluoride) fluoride separator for sodium ion battery with high coulombic efficiency. *Solid State Ionics*, *292*, 130-135.
- Ji, D., Lin, Y., Guo, X., Ramasubramanian, B., Wang, R., Radacsi, N., . . . Ramakrishna, S. (2024). Electrospinning of nanofibres. *Nature Reviews Methods Primers*, *4*(1), 1.

- Jiang, J.-G., He, T.-h., Duan, H.-w., and Li, B. (2014). Electric Field Structure Analysis and Experimentation of Needle-plate Type Electrospinning Machine. *International Journal of Control and Automation*, 7, 369-378.
- Jiangling, L., Su, S., Kundrát, V., Abbot, A., Ye, H., Zhou, L., . . . Roberts, D. (2013). Carbon nanowalls grown by microwave plasma enhanced chemical vapor deposition during the carbonization of polyacrylonitrile fibers. *Journal of Applied Physics*, 113.
- Jin, L., Feng, Z.-Q., Wang, T., Ren, Z., Ma, S., Wu, J., and Sun, D. (2014). A novel fluffy hydroxylapatite fiber scaffold with deep interconnected pores designed for three-dimensional cell culture. *Journal of Materials Chemistry B*, 2(1), 129-136.
- Jing, X., Li, H., Mi, H.-Y., Liu, Y.-J., and Tan, Y.-M. (2019). Fabrication of Three-Dimensional Fluffy Nanofibrous Scaffolds for Tissue Engineering via Electrospinning and CO<sub>2</sub> Escaping Foaming. *Industrial & Engineering Chemistry Research*, 58(22), 9412-9421.
- Joy, N., Anuraj, R., Viravalli, A., Dixit, H. N., and Samavedi, S. (2021). Coupling between voltage and tip-to-collector distance in polymer electrospinning: Insights from analysis of regimes, transitions and cone/jet features. *Chemical Engineering Science*, 230, 116200.
- Jung, A., Lee, M. J., Lee, S. W., Cho, J., Son, J. G., and Yeom, B. (2022). Phase Separation-Controlled Assembly of Hierarchically Porous Aramid Nanofiber Films for High-speed Lithium-Metal Batteries. *Small*, 18(52), 2205355.
- Kasoju, N., Nguyen, L. T. B., Padalhin, A. R., Dye, J. F., Cui, Z., and Ye, H. (2018). 8 - Techniques for modifying biomaterials to improve hemocompatibility. In *Hemocompatibility of Biomaterials for Clinical Applications* (pp. 191-220).
- Keirouz, A., Wang, Z., Reddy, V. S., Nagy, Z. K., Vass, P., Buzgo, M., . . . Radacsi, N. (2023). The History of Electrospinning: Past, Present, and Future Developments. *Advanced Materials Technologies*, 8(11), 2201723.
- Kenry, and Lim, C. T. (2017). Nanofiber technology: current status and emerging developments. *Progress in Polymer Science*, 70, 1-17.

- Khajavi, R., and Abbasipour, M. (2017). 5 - Controlling nanofiber morphology by the electrospinning process. In *Electrospun Nanofibers* (pp. 109-123).
- Kim, J. I., Hwang, T. I., Aguilar, L. E., Park, C. H., and Kim, C. S. (2016). A Controlled Design of Aligned and Random Nanofibers for 3D Bi-functionalized Nerve Conduits Fabricated via a Novel Electrospinning Set-up. *Scientific Reports*, 6(1), 23761.
- Kim, J. I., Kim, J. Y., and Park, C. H. (2018). Fabrication of transparent hemispherical 3D nanofibrous scaffolds with radially aligned patterns via a novel electrospinning method. *Scientific Reports*, 8(1), 3424.
- Kolbuk, D., Guimond-Lischer, S., Sajkiewicz, P., Maniura-Weber, K., and Fortunato, G. (2015). The Effect of Selected Electrospinning Parameters on Molecular Structure of Polycaprolactone Nanofibers. *International Journal of Polymeric Materials and Polymeric Biomaterials*, 64(7), 365-377.
- Kostakova, E. K., Seps, M., Pokorný, P., and Lukas, D. (2014). Study of polycaprolactone wet electrospinning process. *Express Polymer Letters*, 8, 554-564.
- Kumarasinghe, H. U., Bandara, L. R. A. K., Bandara, T. M. W. J., Senadeera, G. K. R., and Thotawatthage, C. A. (2021). Fabrication of  $\beta$ -phase poly (vinylidene fluoride) piezoelectric film by electrospinning for nanogenerator preparations. . *Ceylon Journal of Science*, 50(5), 357-363.
- Kweon, O. Y., Lee, S. J., and Oh, J. H. (2018). Wearable high-performance pressure sensors based on three-dimensional electrospun conductive nanofibers. *NPG Asia Materials*, 10(6), 540-551.
- Lanceros-Méndez, S., Mano, J. F., Costa, A. M., and Schmidt, V. H. (2001). FTIR and DSC studies of mechanically deformed beta-PVDF films. *Journal of Macromolecular Science, Part B*, 40, 517-527.
- Landis, E. N., and Keane, D. T. (2010). X-ray microtomography. *Materials Characterization*, 61(12), 1305-1316.
- Lee, J., Moon, J. Y., Lee, J. C., Hwang, T. I., Park, C. H., and Kim, C. S. (2021). Simple conversion of 3D electrospun nanofibrous cellulose acetate into a mechanically robust nanocomposite cellulose/calcium scaffold. *Carbohydrate Polymers*, 253, 117191.

- Lee, S. H., Bang, J. H., Kim, J., Park, C., Choi, M. S., Mirzaei, A., . . . Kim, H. W. (2021). Sonochemical synthesis of PEDOT:PSS intercalated ammonium vanadate nanofiber composite for room-temperature NH<sub>3</sub> sensing. *Sensors and Actuators B: Chemical*, 327, 128924.
- Li, L., Li, H., Qian, Y., Li, X., Singh, G. K., Zhong, L., . . . Yang, L. (2011). Electrospun poly ( $\epsilon$ -caprolactone)/silk fibroin core-sheath nanofibers and their potential applications in tissue engineering and drug release. *International Journal of Biological Macromolecules*, 49(2), 223-232.
- Li, M. M., and Long, Y.-Z. (2011). Fabrication of Self-Assembled Three-Dimensional Fibrous Stackings by Electrospinning. *Materials Science Forum*, 688, 95-101.
- Li, X., Chen, W., Qian, Q., Huang, H., Chen, Y., Wang, Z., . . . Mai, Y.-W. (2021). Electrospinning-Based Strategies for Battery Materials. *Advanced Energy Materials*, 11(2), 2000845.
- Li, Y., Wang, J., Qian, D., Chen, L., Mo, X., Wang, L., . . . Cui, W. (2021). Electrospun fibrous sponge via short fiber for mimicking 3D ECM. *Journal of Nanobiotechnology*, 19(1), 131.
- Li, Y., Xu, M.-h., Xia, Y.-s., Wu, J.-m., Sun, X.-k., Wang, S., . . . Xiong, C.-x. (2020). Multilayer assembly of electrospun/electrosprayed PVDF-based nanofibers and beads with enhanced piezoelectricity and high sensitivity. *Chemical Engineering Journal*, 388, 124205.
- Liao, H.-S., Lin, J., Liu, Y., Huang, P., Jin, A., and Chen, X. (2016). Self-assembly mechanisms of nanofibers from peptide amphiphiles in solution and on substrate surfaces. *Nanoscale*, 8(31), 14814-14820.
- Lim, J. Y., Kim, S., and Seo, Y. (2015). Enhancement of  $\beta$ -phase in PVDF by electrospinning. *AIP Conference Proceedings*, 1664(1).
- Liu, X., Kuang, X., Xu, S., and Wang, X. (2017). High-sensitivity piezoresponse force microscopy studies of single polyvinylidene fluoride nanofibers. *Materials Letters*, 191, 189-192.
- Liu, Z., Ju, K., Wang, Z., Li, W., Ke, H., and He, J. (2019). Electrospun Jets Number and Nanofiber Morphology Effected by Voltage Value: Numerical Simulation and Experimental Verification. *Nanoscale Research Letters*, 14(1), 310.

- Loewner, S., Heene, S., Baroth, T., Heymann, H., Cholewa, F., Blume, H., and Blume, C. (2022). Recent advances in melt electro writing for tissue engineering for 3D printing of microporous scaffolds for tissue engineering. *Frontiers in Bioengineering and Biotechnology*, 10.
- Lu, T., Li, Y., and Chen, T. (2013). Techniques for fabrication and construction of three-dimensional scaffolds for tissue engineering. *International Journal of Nanomedicine*, 8, 337 - 350.
- Lukáš, D., Sarkar, A., Martinová, L., Vodsed'álková, K., Lubasová, D., Chaloupek, J., . . . Komárek, M. (2009). Physical principles of electrospinning (Electrospinning as a nano-scale technology of the twenty-first century). *Textile Progress*, 41(2), 59-140.
- Ma, J., Zhang, Q., Lin, K., Zhou, L., and Ni, Z. (2018). Piezoelectric and optoelectronic properties of electrospinning hybrid PVDF and ZnO nanofibers. *Materials Research Express*, 5(3), 035057.
- Mahesh Kumar, J., Rajeshwar Man, S., and Hem Raj, P. (2020). 3D Nonwoven Fabrics for Biomedical Applications. In *Generation, Development and Modifications of Natural Fibers* (pp. Ch. 6).
- Mahmood, H. S., and Jawad, M. K. (2019). Antibacterial activity of chitosan/PAN blend prepared at different ratios. *AIP Conference Proceedings*, 2190(1).
- Manoj Prabhakar, M., Saravanan, A. K., Haiter Lenin, A., Jerin leno, I., Mayandi, K., and Sethu Ramalingam, P. (2021). A short review on 3D printing methods, process parameters and materials. *Materials Today: Proceedings*, 45, 6108-6114.
- Marjuban, S. M. H., Rahman, M., Duza, S. S., Ahmed, M. B., Patel, D. K., Rahman, M. S., and Lozano, K. (2023). Recent Advances in Centrifugal Spinning and Their Applications in Tissue Engineering. *Polymers*, 15(5), 1253.
- Martins, A., Pinho, E. D., Faria, S., Pashkuleva, I., Marques, A. P., Reis, R. L., and Neves, N. M. (2009). Surface Modification of Electrospun Polycaprolactone Nanofiber Meshes by Plasma Treatment to Enhance Biological Performance. *Small*, 5(10), 1195-1206.

- Mecozzi, M., and Sturchio, E. (2017). Computer Assisted Examination of Infrared and Near Infrared Spectra to Assess Structural and Molecular Changes in Biological Samples Exposed to Pollutants: A Case of Study. *Journal of Imaging*, 3(1), 11.
- Mehta, P. P., and Pawar, V. S. (2018). 22 - Electrospun nanofiber scaffolds: Technology and applications. In *Applications of Nanocomposite Materials in Drug Delivery* (pp. 509-573).
- Mi, H.-Y., Jing, X., Napiwocki, B. N., Li, Z.-T., Turng, L.-S., and Huang, H.-X. (2018). Fabrication of fibrous silica sponges by self-assembly electrospinning and their application in tissue engineering for three-dimensional tissue regeneration. *Chemical Engineering Journal*, 331, 652-662.
- Monsores, K. G. d. C., Oliveira da Silva, A., Oliveira, S. d. S. A., Weber, R. P., and Dias, M. L. (2022). Production of nanofibers from solution blow spinning (SBS). *Journal of Materials Research and Technology*, 16, 1824-1831.
- Morehouse, A., Ireland, K. C., and Saha, G. C. (2023). An Investigation into the Effects of Electric Field Uniformity on Electrospun TPU Fiber Nano-Scale Morphology. *Micromachines*, 14(1), 199.
- Motchurova-Dekova, N., and A.T, H. (2010). Synchrotron radiation X-ray tomographic microscopy (SRXTM) of brachiopod shell interiors for taxonomy: Preliminary report. *Geološki Anali Balkanskog Poluostrva*, 71.
- Nain, A., Wong, J., Amon, C., and Sitti, M. (2006). Drawing suspended polymer micro-/nanofibers using glass micropipettes. *Applied Physics Letters*, 89, 183105-183105.
- Nain, A. S., Phillippi, J. A., Sitti, M., MacKrell, J., Campbell, P. G., and Amon, C. (2008). Control of Cell Behavior by Aligned Micro/Nanofibrous Biomaterial Scaffolds Fabricated by Spinneret-Based Tunable Engineered Parameters (STEP) Technique. *Small*, 4(8), 1153-1159.
- Nain, A. S., Sitti, M., Jacobson, A., Kowalewski, T., and Amon, C. (2009). Dry Spinning Based Spinneret Based Tunable Engineered Parameters (STEP) Technique for Controlled and Aligned Deposition of Polymeric Nanofibers. *Macromolecular Rapid Communications*, 30(16), 1406-1412.

- Nuansing, W., Frauchiger, D., Huth, F., Rebollo, A., Hillenbrand, R., and Bittner, A. M. (2013). Electrospinning of peptide and protein fibres: approaching the molecular scale. *Faraday Discussions*, 166(0), 209-221.
- O'Connor, R. A., Cahill, P. A., and McGuinness, G. B. (2021). Effect of electrospinning parameters on the mechanical and morphological characteristics of small diameter PCL tissue engineered blood vessel scaffolds having distinct micro and nano fibre populations – A DOE approach. *Polymer Testing*, 96, 107119.
- Owen, J. (1989). 21 - Ionic Conductivity. In *Comprehensive Polymer Science and Supplements* (pp. 669-686).
- Pocasap, P., Weerapreeyakul, N., Junhom, C., Phiboonchaiyanan, P. P., Srisayam, M., Nonpunya, A., . . . Barusrux, S. (2020). FTIR Microspectroscopy for the Assessment of Mycoplasmas in HepG2 Cell Culture. *Applied Sciences*, 10(11), 3766.
- Pokorny, M., Niedoba, K., and Velebny, V. (2010). Transversal electrostatic strength of patterned collector affecting alignment of electrospun nanofibers. *Applied Physics Letters*, 96(19).
- Radacsi, N., and Nuansing, W. (2020). Chapter 7 - Fabrication of 3D and 4D polymer micro- and nanostructures based on electrospinning. In *3D and 4D Printing of Polymer Nanocomposite Materials* (pp. 191-229).
- Rawson, S. D., Maksimcuka, J., Withers, P. J., and Cartmell, S. H. (2020). X-ray computed tomography in life sciences. *BMC Biology*, 18(1), 21.
- Recek, N., Resnik, M., Motaln, H., Lah-Turnšek, T., Augustine, R., Kalarikkal, N., . . . Mozetič, M. (2016). Cell Adhesion on Polycaprolactone Modified by Plasma Treatment. *International Journal of Polymer Science*, 2016, 7354396.
- Redondo, A., Jang, D., Korley, L. T. J., Gunkel, I., and Steiner, U. (2020). Electrospinning of Cellulose Nanocrystal-Reinforced Polyurethane Fibrous Mats. *Polymers*, 12(5), 1021.
- Refate, A., Mohamed, Y., Mohamed, M., Sobhy, M., Samhy, K., Khaled, O., . . . Mehanny, S. (2023). Influence of electrospinning parameters on biopolymers nanofibers, with emphasis on cellulose & chitosan. *Heliyon*, 9(6), e17051.

- Ren, L., Ozisik, R., Kotha, S. P., and Underhill, P. T. (2015). Highly Efficient Fabrication of Polymer Nanofiber Assembly by Centrifugal Jet Spinning: Process and Characterization. *Macromolecules*, 48(8), 2593-2602.
- Ren, Y.-K., Liu, S.-D., Duan, B., Xu, Y.-F., Li, Z.-Q., Huang, Y., . . . Dai, S.-Y. (2017). Controllable intermediates by molecular self-assembly for optimizing the fabrication of large-grain perovskite films via one-step spin-coating. *Journal of Alloys and Compounds*, 705, 205-210.
- Restuccia, A., Seroski, D. T., Kelley, K. L., O'Bryan, C. S., Kurian, J. J., Knox, K. R., . . . Hudalla, G. A. (2019). Hierarchical self-assembly and emergent function of densely glycosylated peptide nanofibers. *Communications Chemistry*, 2(1), 53.
- Rivera, M. L., and Hudson, S. E. (2019). *Desktop Electrospinning: A Single Extruder 3D Printer for Producing Rigid Plastic and Electrospun Textiles*. Paper presented at the Proceedings of the 2019 CHI Conference on Human Factors in Computing Systems, Glasgow, Scotland Uk.
- Roberts, K., Schluns, J., Walker, A., Jones, J. D., Quinn, K. P., Hestekin, J., and Wolchok, J. C. (2018). Cell derived extracellular matrix fibers synthesized using sacrificial hollow fiber membranes. *Biomedical Materials*, 13(1), 015023.
- SalehHudin, H. S., Mohamad, E. N., Mahadi, W. N. L., and Muhammad Afifi, A. (2018). Multiple-jet electrospinning methods for nanofiber processing: A review. *Materials and Manufacturing Processes*, 33(5), 479-498.
- Sankar, D., Mony, U., and Rangasamy, J. (2021). Combinatorial effect of plasma treatment, fiber alignment and fiber scale of poly ( $\epsilon$ -caprolactone)/collagen multiscale fibers in inducing tenogenesis in non-tenogenic media. *Materials Science and Engineering: C*, 127, 112206.
- Schmitt, B. M., Zirbes, C. F., Bonin, C., Lohmann, D., Lencina, D. C., and Netto, A. S. (2018). A Comparative Study of Cartesian and Delta 3D Printers on Producing PLA Parts. *Materials Research-ibero-american Journal of Materials*, 20, 883-886.
- Shechtman, O. (2013). The Coefficient of Variation as an Index of Measurement Reliability. In *Methods of Clinical Epidemiology* (pp. 39-49).

- Shepelin, N. A., Glushenkov, A. M., Lussini, V. C., Fox, P. J., Dicoski, G. W., Shapter, J. G., and Ellis, A. V. (2019). New developments in composites, copolymer technologies and processing techniques for flexible fluoropolymer piezoelectric generators for efficient energy harvesting. *Energy & Environmental Science*, 12(4), 1143-1176.
- Shkarina, S., Shkarin, R., Weinhardt, V., Melnik, E., Vacun, G., Kluger, P. J., . . . Surmenev, R. A. (2018). 3D biodegradable scaffolds of polycaprolactone with silicate-containing hydroxyapatite microparticles for bone tissue engineering: high-resolution tomography and in vitro study. *Scientific Reports*, 8(1), 8907.
- Si, Y., Yu, J., Tang, X., Ge, J., and Ding, B. (2014). Ultralight nanofibre-assembled cellular aerogels with superelasticity and multifunctionality. *Nature Communications*, 5(1), 5802.
- Šimko, M., and Lukáš, D. (2016). Mathematical modeling of a whipping instability of an electrically charged liquid jet. *Applied Mathematical Modelling*, 40(21), 9565-9583.
- Simons, A., Avegnon, K. L. M., and Addy, C. (2019). Design and Development of a Delta 3D Printer Using Salvaged E-Waste Materials. *Journal of Engineering*, 2019, 5175323.
- Singh, P., Borkar, H., Singh, B. P., Singh, V. N., and Kumar, A. (2014). Ferroelectric polymer-ceramic composite thick films for energy storage applications. *AIP Advances*, 4(8).
- Song, J., Zhu, G., Wang, L., An, G., Shi, X., and Wang, Y. (2017). Assembling of electrospun meshes into three-dimensional porous scaffolds for bone repair. *Biofabrication*, 9(1), 015018.
- Song, J. Y., Ryu, H. I., Lee, J. M., Bae, S. H., Lee, J. W., Yi, C. C., and Park, S. M. (2021). Conformal Fabrication of an Electrospun Nanofiber Mat on a 3D Ear Cartilage-Shaped Hydrogel Collector Based on Hydrogel-Assisted Electrospinning. *Nanoscale Research Letters*, 16(1), 116.
- Stanjek, H., and Häusler, W. (2004). Basics of X-ray Diffraction. *Hyperfine Interactions*, 154(1), 107-119.

- Sun, B., Li, J., Liu, W., Aqeel, B. M., El-Hamshary, H., Al-Deyab, S. S., and Mo, X. (2015). Fabrication and characterization of mineralized P(LLA-CL)/SF three-dimensional nanoyarn scaffolds. *Iranian Polymer Journal*, 24(1), 29-40.
- Sun, B., Long, Y.-Z., Yu, F., Li, M.-M., Zhang, H.-D., Li, W.-J., and Xu, T.-X. (2012). Self-assembly of a three-dimensional fibrous polymer sponge by electrospinning. *Nanoscale*, 4(6), 2134-2137.
- Sun, D., Chang, C., Li, S., and Lin, L. (2006). Near-Field Electrospinning. *Nano Letters*, 6(4), 839-842.
- Sun, F., Chen, J., Jin, S., Wang, J., Man, Y., Li, J., . . . Zuo, Y. (2019). Development of biomimetic trilayer fibrous membranes for guided bone regeneration. *Journal of Materials Chemistry B*, 7(4), 665-675.
- Sunthornvarabhas, J., Thumanu, K., Limpirat, W., Kim, H.-J., Piyachomkwan, K., and Sriroth, K. (2014). Assessment of material blending distribution for electrospun nanofiber membrane by Fourier transform infrared (FT-IR) microspectroscopy and image cluster analysis. *Infrared Physics & Technology*, 66, 141-145.
- Taddei, P., Di Foggia, M., Causa, F., Ambrosio, L., and Fagnano, C. (2006). In vitro Bioactivity of Poly( $\epsilon$ -Caprolactone)-Apatite (PCL-AP) Scaffolds for Bone Tissue Engineering: The Influence of the PCL/AP Ratio. *The International Journal of Artificial Organs*, 29(7), 719-725.
- Talukder, M. E., Hasan, K. M. F., Wang, J., Yao, J., Li, C., and Song, H. (2021). Novel fibrin functionalized multilayered electrospun nanofiber membrane for burn wound treatment. *Journal of Materials Science*, 56(22), 12814-12834.
- Tan, G. Z., and Zhou, Y. (2018). Tunable 3D Nanofiber Architecture of Polycaprolactone by Divergence Electrospinning for Potential Tissue Engineering Applications. *Nano-Micro Letters*, 10(4), 73.
- Tebyetekerwa, M., and Ramakrishna, S. (2020). What Is Next for Electrospinning? *Matter*, 2(2), 279-283.
- Thumanu, K., Wongchalee, D., Sompong, M., Phansak, P., Le Thanh, T., Namanusart, W., . . . Buensanteai, N. (2017). Synchrotron-based FTIR microspectroscopy of chili resistance induced by *Bacillus subtilis* strain D604 against anthracnose disease. *Journal of Plant Interactions*, 12(1), 255-263.

- Topuz, F., and Uyar, T. (2020). Electrospinning of Cyclodextrin Nanofibers: The Effect of Process Parameters. *Journal of Nanomaterials*, 2020, 7529306.
- Tzezana, R., Zussman, E., and Levenberg, S. (2008). A Layered Ultra-Porous Scaffold for Tissue Engineering, Created via a Hydrospinning Method. *Tissue Engineering Part C: Methods*, 14(4), 281-288.
- Undavalli, V. K., Ling, C., and Khandelwal, B. (2021). Chapter 6 - Impact of alternative fuels and properties on elastomer compatibility. In *Aviation Fuels* (pp. 113-132).
- Ura, D. P., Rosell-Llompart, J., Zaszczynska, A., Vasilyev, G., Gradys, A., Szewczyk, P. K., . . . Stachewicz, U. (2020). The Role of Electrical Polarity in Electrospinning and on the Mechanical and Structural Properties of As-Spun Fibers. *Materials*, 13(18), 4169.
- Urban, M. W. (1993). Fourier Transform Infrared and Fourier Transform Raman Spectroscopy of Polymers. In *Structure-Property Relations in Polymers* (Vol. 236, pp. 3-40).
- Vasireddi, R., Kruse, J., Vakili, M., Kulkarni, S., Keller, T. F., Monteiro, D. C. F., and Trebbin, M. (2019). Solution blow spinning of polymer/nanocomposite micro-/nanofibers with tunable diameters and morphologies using a gas dynamic virtual nozzle. *Scientific Reports*, 9(1), 14297.
- Vlassenbroeck, J., Masschaele, B., Cnudde, V., Dierick, M., Pieters, K., Van Hoorebeke, L., and Jacobs, P. (2006). Octopus 8: A High Performance Tomographic Reconstruction Package for X-ray Tube and Synchrotron micro-CT. In *Advances in X-ray Tomography for Geomaterials* (pp. 167-173).
- Vong, M., Diaz Sanchez, F. J., Keirouz, A., Nuansing, W., and Radacsi, N. (2021). Ultrafast fabrication of Nanofiber-based 3D Macrostructures by 3D electrospinning. *Materials & Design*, 208, 109916.
- Vong, M., Speirs, E., Klomkliang, C., Akinwumi, I., Nuansing, W., and Radacsi, N. (2018). Controlled three-dimensional polystyrene micro- and nano-structures fabricated by three-dimensional electrospinning. *RSC Advances*, 8(28), 15501-15512.

- Wang, H., Kong, L., and Ziegler, G. R. (2019). Fabrication of starch - Nanocellulose composite fibers by electrospinning. *Food Hydrocolloids*, 90, 90-98.
- Wellner, N. (2013). 6 - Fourier transform infrared (FTIR) and Raman microscopy: principles and applications to food microstructures. In *Food Microstructures* (pp. 163-191).
- Williams, G. R., Raimi-Abraham, B. T., and Luo, C. J. (2018). Electrospinning fundamentals. In *Nanofibres in Drug Delivery* (pp. 24-59).
- Xing, X., Wang, Y., and Li, B. (2008). Nanofiber drawing and nanodevice assembly in poly(trimethylene terephthalate). *Optics Express*, 16(14), 10815-10822.
- Yang, H., Sugita, N., and Nakane, K. (2019). Factors influencing the PVA polymer-assisted freeze-drying synthesis of Al<sub>2</sub>O<sub>3</sub> nanofibers. *Ceramics International*, 45(14), 16731-16739.
- Yeo, M., and Kim, G. (2014). Cell-printed hierarchical scaffolds consisting of micro-sized polycaprolactone (PCL) and electrospun PCL nanofibers/cell-laden alginate struts for tissue regeneration. *Journal of Materials Chemistry B*, 2(3), 314-324.
- Yousefzadeh, M., Latifi, M., Amani-Tehran, M., Teo, W.-E., and Ramakrishna, S. (2012). A Note on the 3D Structural Design of Electrospun Nanofibers. *Journal of Engineered Fibers and Fabrics*, 7(2), 155892501200700204.
- Yu, D.-G., Lu, P., Branford-White, C., Yang, J.-H., and Wang, X. (2011). Polyacrylonitrile nanofibers prepared using coaxial electrospinning with LiCl solution as sheath fluid. *Nanotechnology*, 22(43), 435301.
- Zargham, S., Bazgir, S., Tavakoli, A., Rashidi, A. S., and Damerchely, R. (2012). The Effect of Flow Rate on Morphology and Deposition Area of Electrospun Nylon 6 Nanofiber. *Journal of Engineered Fibers and Fabrics*, 7(4), 155892501200700414.
- Zeng, Y., Pei, Z., and Wang, X. (2009). *Numerical simulation of whipping process in electrospinning*.
- Zhang, Y., Jarosinski, W., Jung, Y.-G., and Zhang, J. (2018). 2 - Additive manufacturing processes and equipment. In *Additive Manufacturing* (pp. 39-51).

- Zhao, S., Wu, X., Wang, L., and Huang, Y. (2004). Electrospinning of ethyl–cyanoethyl cellulose/tetrahydrofuran solutions. *Journal of Applied Polymer Science*, *91*(1), 242-246.
- Zheng, Y., Meng, N., and Xin, B. (2018). Effects of Jet Path on Electrospun Polystyrene Fibers. *Polymers*, *10*(8), 842.
- Zhou, H., Shi, Z., Wan, X., Fang, H., Yu, D.-G., Chen, X., and Liu, P. (2019). The Relationships between Process Parameters and Polymeric Nanofibers Fabricated Using a Modified Coaxial Electrospinning. *Nanomaterials*, *9*(6), 843.
- Zhou, W., Apkarian, R., Wang, Z. L., and Joy, D. (2007). Fundamentals of Scanning Electron Microscopy (SEM). In *Scanning Microscopy for Nanotechnology: Techniques and Applications* (pp. 1-40).
- Zhu, P., Lin, A., Tang, X., Lu, X., Zheng, J., Zheng, G., and Lei, T. (2016). Fabrication of three-dimensional nanofibrous macrostructures by electrospinning. *AIP Advances*, *6*(5).
- Zlotnikov, I. D., Ezhov, A. A., Vigovskiy, M. A., Grigorieva, O. A., Dyachkova, U. D., Belogurova, N. G., and Kudryashova, E. V. (2023). Application Prospects of FTIR Spectroscopy and CLSM to Monitor the Drugs Interaction with Bacteria Cells Localized in Macrophages for Diagnosis and Treatment Control of Respiratory Diseases. *Diagnostics*, *13*(4), 698.

## APPENDIX F

### PUBLICATIONS AND PRESENTATIONS

#### F.1 Lists of publication

Atchara Chinnakorn, Yanawarut Soi-ngoen, Oratai Weeranantanapan, Phakkhananan Pakawanit, Santi Maensiri, Kriettisak Srisom, Pattanaphong Janphuang, Norbert Radacsi, and Wiwat Nuansing, “Fabrication of 3D Polycaprolactone Macrostructures by 3D Electrospinning”, ACS Biomaterials Science & Engineering, Accepted (2024), <https://doi.org/10.1021/acsbmaterials.4c00302>.

#### F.2 Lists of presentations

- |      |   |
|------|---|
| 2024 | Image mapping of biological assessment on electrospun fiber using synchrotron micro-FTIR (Poster presentation) in the 22 <sup>nd</sup> International Symposium on Eco-materials Processing and Design (ISEPD)         |
| 2022 | 3D imaging of <i>in vitro</i> cell ingrowth on electrospun architectures using X-Ray microtomography (Oral presentation) in 4D Materials Design and Additive Manufacturing Conference                                 |
| 2020 | Forming three-dimensional fibrous structure via 3D electrospinning (Oral presentation) in the 21 <sup>st</sup> International Union of Materials Research Societies – International Conference in Asia (IUMRS-ICA2020) |
| 2019 | Novel Three-Dimensional Fibrous Structure by Three-Dimensional Electrospinning (Oral presentation) in The Second Materials Research Society of Thailand International Conference                                      |

## CURRICULUM VITAE

**Name:** Atchara Chinnakorn

**Date of Birth:** 25<sup>th</sup> May 1995

**Place of Birth:** Rayong, Thailand

**Personal Address:** 325 Srisawat Damnoen Road, Talad Subdistrict, Muang District,  
Mahasarakham

**Nationality:** Thai

**Education:**

2017-2024 Ph.D. in Physics (M.Sc. and Ph.D. integrated programs)  
Suranaree University of Technology, Nakhon Ratchasima,  
Thailand  
Title: “Three-Dimensional Electrospinning of Polycaprolactone-  
Based Nanostructures for Biomedical Applications”  
Advisor: Dr. Wiwat Nuansing

2013-2017 B.Sc. in Physics (First Class Honours)  
Khon Kaen University, Khon Kaen, Thailand  
Title: “Optical Reflection Spectrum Model of Semiconductor  
Thin Film”  
Advisor: Asst. Prof. Thanusit Burinprakhon